Real-time assay of DNA damage by therapeutic radiation beams with silicon nano tweezers and microfluidic setup

Grégoire Perret

Numéro d'ordre 41965 Année 2015

THÈSE

Présentée à

L'Université de Lille I - Sciences et Technologies

pour obtenir le grade de

DOCTEUR DE L'UNIVERSITE

Spécialité: Micro et Nano Technologies, Acoustique et Télécommunications

REAL-TIME ASSAY OF DNA DAMAGE BY THERAPEUTIC RADIATION BEAMS WITH SILICON NANO TWEEZERS AND MICROFLUIDIC SETUP

Par

Grégoire PERRET

Soutenue publiquement le 14 Décembre 2015 devant le jury composé de

Dr. Xavier GIDROL	BIOMICS-INSERM U1038, CEA, Grenoble	Rapporteur
Dr. Liviu NICU	DR CNRS, LAAS-CNRS, Toulouse	Rapporteur
Pr. Lionel BUCHAILLOT	DR CNRS, IEMN, Lille	Examinateur
Dr. Anthony COLEMAN	DR CNRS, Laboratoire Multimatériaux et interfaces, Université Lyon 1	Examinateur
Pr. Hiroyuki FUJITA	DR CNRS, LIMMS/CNRS-IIS, Tokyo	Invité
Pr. Eric LARTIGAU	PU-PH, Universite de Lille-2, Centre Oscar Lambret, Lille	Invité
Dr. Dominique COLLARD	Université de Tokyo / IEMN	Co-directeur
Pr. Fabrizio CLERI	IEMN, Universite de Lille-1	Co-directeur

Order Number 41965 Year 2015

THESIS

Presented to

The University of Lille I – Sciences and Technology

To obtain the title of

DOCTEUR DE L'UNIVERSITE

Specialty: Micro and Nano Technologies, Acoustics and Telecommunications

REAL-TIME ASSAY OF DNA DAMAGE BY THERAPEUTIC RADIATION BEAMS WITH SILICON NANO TWEEZERS AND MICROFLUIDIC SETUP

by

Grégoire PERRET

Publicly defended on December 14th, 2015 in front of the jury:

Dr. Xavier GIDROL	BIOMICS-INSERM U1038, CEA, Grenoble	Reviewer
Dr. Liviu NICU	DR CNRS, LAAS-CNRS, Toulouse	Reviewer
Pr. Lionel BUCHAILLOT	DR CNRS, IEMN, Lille	Examiner
Dr. Anthony COLEMAN	DR CNRS, Laboratoire Multimatériaux et interfaces, Université Lyon 1	Examiner
Pr. Hiroyuki FUJITA	DR CNRS, LIMMS/CNRS-IIS, Tokyo	Invited
Pr. Eric LARTIGAU	PU-PH, Universite de Lille-2, Centre Oscar Lambret, Lille	Invited
Dr. Dominique COLLARD	Université de Tokyo / IEMN	Co-Supervisor
Pr. Fabrizio CLERI	IEMN, Universite de Lille-1	Co-Supervisor

Résumé

Dans les premières années de la radiothérapie, les mécanismes d'action et les effets secondaires des radiations ionisantes n'étaient que faiblement compris. La génétique moléculaire a clairement montré les dommages causés par ses radiations sur l'ADN des cellules. Cependant, le rayonnement ne distinguant pas les cellules saines des cellules tumorales, les plus grandes avancées modernes en radiothérapie sont concentrées sur l'amélioration de la précision de la dose délivrée. Avec un intérêt relativement bas pour la compréhension fondamentale des mécanismes de base des dégâts biologiques induits par irradiation.

Dans le 1er chapitre de cette thèse, l'état de l'art conduit à considérer le Silicon Nano Tweezers (SNT) comme un excellent candidat pour l'exploration des champs méconnus de la radiothérapie. Le 2nd chapitre présente le SNT et sa capacité à caractériser en temps réel les propriétés biomécaniques de l'ADN. Le 3ème chapitre montre le dispositif entourant le SNT et évalue sa capacité à mesurer les caractéristiques d'un faisceau d'ADN en milieu liquide subissant le rude champ électromagnétique généré par la machine de radiothérapie : le Cyberknife. Le 4ème chapitre explique le protocole spécialement développé pour la caractérisation par le SNT de l'ADN en milieu liquide. Le 5ème chapitre présente les résultats clés, obtenus dans diverses conditions, de caractérisations mécaniques en temps réel de faisceau d'ADN irradiés par le Cyberknife. La dernière partie conclue finalement sur les possibilités et les perspectives offertes par la technologie des Microsystèmes électromécaniques dans l'avancée de la recherche en radiothérapie et en plus largement en médecine.

Abstract

In the early days of radiotherapy, very little was known about the mechanism of action of ionizing radiation and its side effects. The understanding of molecular genetics has made it clear that radiation damages mainly the DNA of cells. However, since radiation does not distinguish between healthy and tumor cells, the largest improvement of the radiotherapy technology in modern days has concentrated on improving the precision of dose-deliver, with a comparatively lower interest in the fundamental understanding of the basic mechanisms of biological radiation damage.

In the first chapter of this thesis, the state of the art conducts to consider the Silicon Nano Tweezers (SNT) as an excellent candidate to explore unknown field of the radiotherapy treatment. The second chapter introduces the SNT and explains its ability to conduct real-time biomechanical characterization of a DNA bundle. The third chapter shows the surrounding SNT setup, and evaluates its capability to measure the biomechanical characteristic of a DNA bundle in liquid under the harsh electromagnetic environment generated by a radiotherapy machine: the Cyberknife. The fourth chapter explains the protocol developed for the DNA characterization in liquid by the SNT. The fifth chapter presents some key results of real-time mechanical characterization of DNA bundles under the Cyberknife irradiation in several conditions, followed by a discussion based on the theoretical model of a randomly damaged DNA bundle. The last part finally concludes on the capability and perspective offered by Micro-electromechanical technologies to push the research in radiotherapy and in medicine.

Acknowledgements

The research work presented in this thesis has been accomplished with the support from many people: mentors, colleagues, friends and family, to whom I would like to fully acknowledge. Their support, ideas, comments, and energy were essential in allowing me to successfully complete this thesis.

Firstly, I would like to express my sincere gratitude to my advisor Professors Dominique Collard and Fabrizio Cleri for the continuous support of my PhD study and related research, for their patience, motivation, and immense knowledge. Their education and their expertise have been essential in this research. Their guidance helped me in all the time of research and writing of this thesis. I was fortunate to learn from different scientific cultures and points of view.

Besides my advisors, I would like to thank Dr.Xavier Gidrol and Dr.Liviu Nicu, as part of the reading committee for their time, their comments and scientific inputs. I would like to thank also the members of my oral exam committee, Pr.Lionel Buchaillot, Dr.Anthony Coleman, Pr.Hiroyuki Fujita and Pr.Eric Lartigau, for their interest in the research of my thesis. It was a great honour and a privilege for me to have the chance to present my research work to them.

I would like to express all my gratitude to my great colleagues, especially Dr. Nicolas Lafitte, Dr. Mehmet Cagatay Tarhan, Dr. Momoko Kumemura and Dr. Laurent Jalabert, Dr. Yannick Tauran, Kou Hakuson who help me a lot during my research.
I am very much thankful to Thomas Lacornerie, I have been greatly aided by his knowledge and skills in the Physics of Radiotherapy. We spend a lot of time to perform experiments in the hospital in the evening after the treatment of patients.

I am also grateful for what I have received from every members of the laboratory of
Pr. Fujita and LIMMS laboratory. I appreciate the daily life with them, their friendship and their permanent support. I would like to extend my gratitude to the secretaries in IEMN and LIMMS which make everything possible and the life easier for us.

I would like to thanks all my close friends for their unconditional love and encouragement. And especially Sequoya Yiaueki for his substantive help to enhance English expression of the thesis.

And finally and the most important, I would like to thank my parents Christine and Frédéric Perret, my sisters and brothers. They were always supporting and encouraging me with their best wishes.

Table of Contents

Table of Figures

General introduction and motivation

In the early days of radiotherapy, very little was known about the mechanism of action of ionizing radiation and its side effects, leading to sometimes disastrous effects. The understanding of molecular genetics has made it clear that radiation damages mainly the DNA of cells, mostly causing oxidative damage [1]. However, since nuclear radiations do not distinguish between healthy and tumor cells, the largest improvement of the radiotherapy technology in modern days has concentrated on improving the precision of dose-delivery in space and time, with a comparatively reduced interest in the fundamental understanding of the basic mechanisms of biological radiation damage.

Since the refinement of space-time protocols is reaching, or will soon reach, its practical limits, even including sophisticated features such as the real-time following of patient respiration and involuntary movements, the need for a deeper understanding of the direct, molecular-scale correlations between radiation dose and biological damage, becomes urgent. Such an endeavor will open the way to a better efficiency of treatment and a customized, patient-specific radiation treatment.

Gas chromatography with ion-selective mass spectrometry [2], high-performance liquid chromatography (HPLC) [3], as well as gel micro electrophoresis ('Comet') [4], are among the main experimental tools adopted up to now to study RDD of irradiated DNA at the molecular level. All such methods, however, are based on chemical treatments carried out on DNA **after** irradiation. Typically, DNA samples are irradiated by a known dose, stored for some time, and subsequently hydrolyzed and derivatized. The resulting solution contains the individual DNA bases, both damaged and undamaged, to be analyzed by one of the above methods. The link between radiation damage and DNA molecular structure, in this case, is very indirect (chemical signatures correlated to the damage are observed) and subject to the variable conditions of subtle shifts in the oxidation paths (differential recombination [5]).

Alternative strategies can be found, for example by looking at electrical or mechanical properties of the DNA. Notably, the direct mechanical characterization of DNA is possible. This is traditionally performed by expensive biophysical instruments such as the Atomic Force Microscope [6], Optical Tweezers [7] or Magnetic Tweezers [8]. These instruments are extremely accurate and can achieve single-molecule level detection; nevertheless, they are expensive, bulky and cannot operate in confined areas and harsh environment. Moreover, the radiation damage is a statistical process; therefore the measurement must involve a meaningfully large sample, instead of just one molecule at the time. It is our central hypothesis that to fulfill the needs of mass screening with molecular resolution, DNA manipulation by

means of a tiny, stable, low-cost, easily fabricated device, the technology of Micro Electro Mechanical Systems (MEMS) is an appropriate approach.

The aim of this thesis is **to evaluate the capability of MEMS-based Silicon Nano tweezers to perform a real-time characterization of DNA damage** under a radiotherapy treatment.

In short, we will employ a sophisticated nanoscale electromechanical device, the Electro-Mechanical Silicon Nanotweezer (SNT) [9], to directly measure the rate of breaking of DNA molecules, placed under a controlled radiation beam. DNA bundles of known sequence, with length in the μm range, will be trapped and held straight in parallel strands between the tips of the SNT device. Such nanoscale vibrating tips can measure with extreme accuracy the elastic modulus and viscosity of the DNA bundle, [10] immersed in physiological water in a sealed microfluidic chamber. During the irradiation, under well-known and fully characterized conditions by means of different machines typical of clinical radiotherapy, the individual DNA strands will break, thus progressively reducing the bundle. Correspondingly, the SNT device will measure the dynamical variation of the mechanical response of the bundle, with a time-constant characteristic of the type of damage. Experimental results will be eventually compared with a theoretical model of a randomly damaged DNA bundle [11].

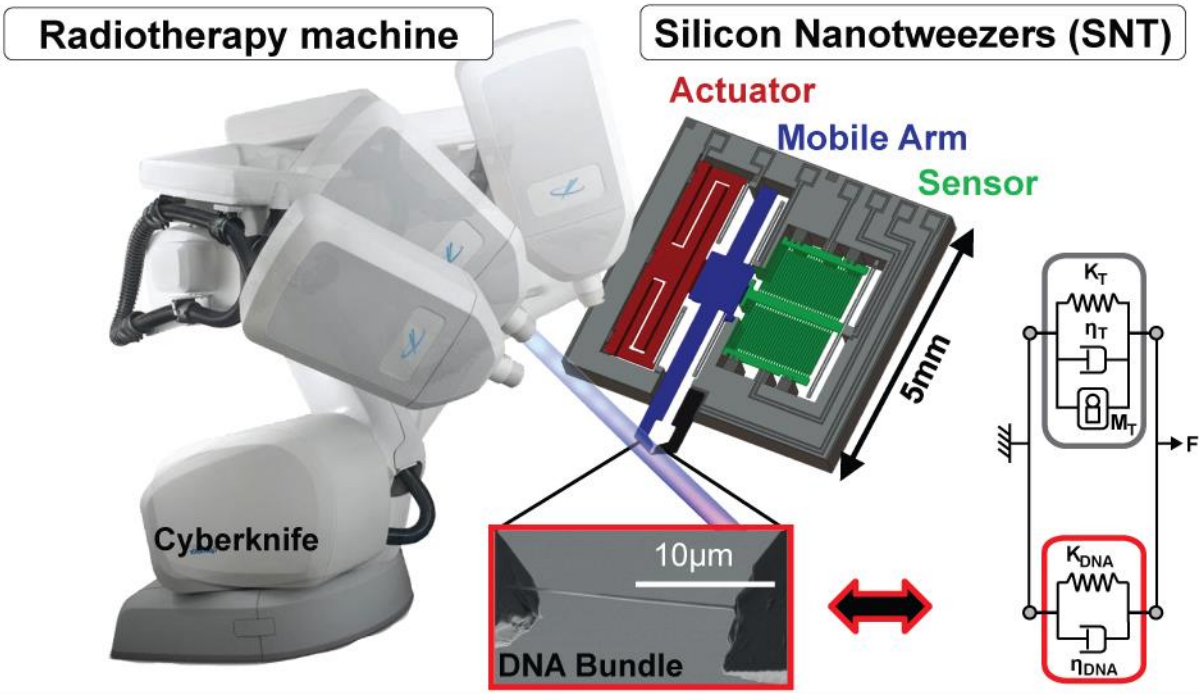

Figure 0.1: Real-time mechanical characterization of a DNA bundle under radiotherapy treatment.

This thesis is divided in five chapters. The first chapter synthetically presents the state of the art in radiation damage of DNA, which conducted to consider the Silicon Nano Tweezers as the best candidate to explore the unknown field of the radiotherapy treatment. The second chapter introduces the Silicon Nano Tweezers, and explains its ability to conduct real-time biomechanical characterization of a DNA bundle. The third chapter details the key devices of the surrounding SNT setup, and evaluates its capability to measure the biomechanical characteristic of a DNA bundle in liquid under the harsh electromagnetic environment generated by one of the most advanced radiotherapy machines: the Cyberknife. The fourth chapter explains the original protocol developed for the DNA characterization in liquid by the SNT. Finally, the fifth chapter presents some key results of real-time mechanical characterization of DNA bundles under the ionizing γ-ray beam of the Cyberknife in several conditions, followed by a discussion based on the theoretical model of a randomly damaged DNA bundle. The last part finally concludes on the capabilities and perspectives offered by Micro-electromechanical technologies, to push the research in radiotherapy and in medicine.

The work described in the following pages was carried out jointly in the laboratories of Laboratory for Integrated Micro-Mechatronics (LIMMS, CNRS UMI 2520), based at the Institute for Industrial Sciences of the University of Tokyo (Komaba), where the candidate spent about 1 full year, to develop the basic technology of the SNT; in the *Centre de Lutte Contre le Cancer "Oscar Lambre*t" of Lille, where all the irradiation sessions took place; and in the *Institut d'Electronique, Microelectronique and Nanotechnologie* of Lille (IEMN, CNRS UMR 8520), where data analysis and theoretical developments were mostly performed.

Chapter 1: State of the Art in Radiotherapy and DNA damage analysis

1.1 Radiotherapy treatments

1.1.1 Introduction

Every source used in radiotherapy emits a radiation of particles (electrons, protons, ...) or electromagnetic waves (photons). While propagating in matter, the radiation deposits energy along its path. This deposit is not homogeneous but may show peaks at more or less deep sites in the irradiated volume. When radiation passes through a healthy or tumor tissue, this energy chiefly damages the genetic material (DNA) of the cells, as well as other cell structures (membranes, organelles). Several types of DNA lesions may occur, the worst ones being the so-called *double-strand break* (DSB) of the DNA double helix. Since the cell repair mechanisms for this defect are much slower and faulty than for any other type of defect, this type of injury leads to errors in the copying of chromosomes, eventually prevents cells from dividing, and leads to cell death. The study of radiation effects at the cellular level is the field of radiobiology.

Radiotherapy remains one of the most effective elements in the fight against cancer and is perfectly integrated in existing multidisciplinary therapeutic strategies. For 70% of patients with cancer, radiation therapy is one of the treatments used. Although a local-only treatment can sometimes be sufficient, the radiotherapy treatment is most often associated with surgery and/or chemotherapy.

So, as of today radiotherapy is usually required for one or more of the following reasons:

- As a stand-alone treatment to cure cancer.
- To shrink a cancer before surgery.
- To reduce the risk of a cancer coming back after surgery.
- To complement chemotherapy.
- To control symptoms and improve quality of life if a cancer is too advanced to cure.

1.1.2 History

1.1.2.1 Birth of radiotherapy

The end of 19th century was marked by the discovery of new physical phenomena that would have revolutionized the medicine in the next century. In 1895, Wilhelm Conrad Roentgen projected the electrons accelerated by an electric field on a tungsten target in a vacuum tube. A radiation was emitted. Roentgen gave it the name of 'X-ray' because of its unknown nature. Radiology was born and radiology services were to be installed in hospitals already in 1897. In 1896, Henri Becquerel reported for the first time a phenomenon later called 'natural radioactivity' by Marie Curie and Pierre Curie, who discovered in 1898 the properties of Radium and Polonium. In 1903, they shared the Nobel Prize for this major discovery.

Quickly, the medical treatments by X-ray and Radium-radiotherapy knew their early developments. Already by 1900, the Radium radiations were tested to treat many diseases resistant to known therapies. (Not too surprisingly, by about 1910 radioactivity was also considered as a kind of panacea for any medical disease, by many charlatans and quack doctors.) Early in the 20th century, Marie Curie was convinced that X-rays and radiation of radioactive substances could cure cancer. But to prove it, there was need for researchers, hospitals and money. With Dr. Claudius Regaud, they managed to gain the support of the University of Paris, the Institut Pasteur and many donators, to create a foundation for this purpose. This initiative originated the Institut Curie, which can be considered the birthplace of radiotherapy in the world. Since then, much progress has been made to optimize the effectiveness of radiation therapy while minimizing its side effects.

1.1.2.2 From Cobalt to particle accelerator

Very powerful sources of Cobalt-60 could be manufactured by the end of WWII. The "Cobalt revolution" started in 1955, when commercial Cobalt-therapy machines were developed. The sources of Cobalt-60 produce more effective and more penetrating high-energy radiation than radium or X-rays. The spatial definition of the emerging beam is more accurate. With "Cobalt bombs", the maximum dose is not delivered to the surface but some 5 mm below: penetration is much better and the field margins are better defined. Irradiation to the normal tissue is limited. However, Cobalt-therapy machines had the disadvantage that the beam energy is fixed to relatively low values of 1.17-1.33 MeV; moreover, the natural radioactive decay of the isotope ^{60}Co makes it necessary to replace the source, about every four years, with attending problems of nuclear waste disposal.

In the late 60s, a new step was reached with the introduction of linear particle accelerators (electrons, protons, etc.). These high-energy radiation generators are more efficient and flexible

than radioisotopes. The radiation beams obtained are extremely fine, which makes it possible to orient and focus them with great accuracy. The risk of material activation and radioactive waste disposal is much reduced.

The most common such machines are electron accelerators. When used directly in external irradiation, the electron beam is absorbed in the first centimeters of tissue, before being completely stopped, depending on its energy. These limits can be precisely chosen by the user. However, electron accelerators allow also generating further irradiation by passing first thorough a heavy target (Tungsten, Copper, Gold…), which in turn emits X or γ rays, whose energy is deposited more deeply in the tissues. By combining photon beams from different directions, the dose can be maximized at any desired depth down to about 15cm, while sparing most superficial tissues. The contours of these beams can be defined with greater precision, and enable compliance with healthy organs surrounding the tumor.

1.1.3 State of art in radiotherapy

Today, radiation therapy is often associated with surgery or chemotherapy so as to obtain optimum results. It can be performed prior to surgery, to reduce tumor size, or after, to remove residual tumor cells, thus reducing the risks of recurrence. It can be administered externally or internally. Radiation therapists have many techniques from which they may select the best for each tumor. The linear accelerator is generally preferred to all other in case of deep cancer; Cobalt-therapy machines (Gamma-knife) are still used in some cases, for the treatment of breast cancer and for specific locations in ear-nose-throat (ENT) cancers, but they are increasingly being replaced by small accelerators, more adaptable and efficient.

1.1.3.1 Medical imaging

Imaging by such tools as the X-ray tomographic scanner (CT Scan), and magnetic resonance (MRI), have greatly improved the treatment of tumors. The CTScan, in particular, plays a key role in tumor diagnosis. It has become an indispensable examination tool of the pre-therapeutic assessment, since it allows to accurately determining the volume, expansion and relations of the tumor with the surrounding healthy tissue.

On each of the graphical sections obtained from the scanner, the radiation oncologist delineates tumor and healthy organs. Nowadays, this crucial step remains largely manual because of the limitations of automatic recognition programs. Radiotherapists establish the 3-dimensional volume of the tumor and surrounding organs. From this reconstruction, a "virtual patient", they determine for each case the irradiation volume at the millimeter scale, seeking the best compromise between efficiency and potential toxicity. Margins are then added to this volume

to take into account cancer cells that are not visible on the image, and the movements of the tumor volume due to breathing and a potential different positioning of the patient during successive sessions. Radiation therapists are thus forced to increase the volume of irradiation, thereby exposing a higher proportion of healthy tissue to irradiation.

1.1.3.2 Sophisticated particles accelerators

Radiotherapy machines have undergone many changes over the years. Today multiple separate radiation beams produced by the same machine are commonly used. The head of the particle accelerator rotates around the patient, stopping in the position pre-established for delivering in each case a part of the irradiation (see the Cyberknife). The cumulative action of these beams produces a homogeneous dose even in a volume with a complex shape. The concurrent use of a plurality of beams can increase the effectiveness of radiation therapy to the tumor, while limiting the effects in healthy tissues. Taken separately, the micro-beams do not have sufficient energy to cause tissue damage but their combined action allows the maximum damage to the cells. Therefore, the energy and direction of the beams are determined to localize their concurrent action on the tumor. At this stage, computer simulation is essential to allow the physician to quickly specify certain parameters.

On modern linear accelerators a collimator, a variable aperture that can deliver radiation for a variable time, delimits each beam. Modern “multi-leaf” collimators can be composed of 80 to 120 metal leaves, each independently set in motion by a micro-motor, itself controlled by a computer. The quality of the positioning is checked with X-ray films of high sensitivity, as well as by "imaging beam" systems. By releasing the radiotherapist from the constraints of building heavy lead masks for each different treatment, these collimators enabled the development of the “conformal” irradiation.

Conformal radiotherapy in 3D is an important step in the evolution of radiotherapy since it allows a better adaptation of the beam to the tumor volume and limiting the exposure of healthy organs. The irradiation volume being better defined, the dose can be increase, and thereby increasing the efficacy of radiotherapy.

1.1.3.3 Enhanced dosimetry

The dose is the amount of energy deposited by the radiation in a given volume of tissue. It is expressed in Gray (1 Gy=1 J/kg), and its accurate measurement is the field of the dosimetry.

The success of a radiation therapy depends on the accuracy with which the radiation dose is delivered to the tumor: a dose 5-10% lower than the optimum dosage may produce an incomplete removal of the tumor cells, and possibly a recurrence. By contrast, a too large dose,

only 5-10% above prescribed, can lead to severe complications. The dose must also be perfectly homogeneous within each single beam: variations should not exceed ±3%. The radiotherapist plans the total dose, fractionation (number of sessions) and spreading (total treatment time), whose delivery to the patient is then assured by a medical physicist. Several factors are involved in dose planning. The dose depends on the age of the patient, his health status, the location and nature of the tumor. Not all tumors respond to radiations in the same way; they may be more or less radiosensitive. The average dose per session is generally between 1.8 Gy and 2.5 Gy. The technique of splitting the radiation dose over several weekly sessions and spread them over several weeks (generally 6 to 8 weeks) allows healthy tissue to restore. The calculation of the dose distribution in 3D in the tumor and the body requires sophisticated computer programs, a long and demanding process.

1.1.4 Side effects

Side effects occurring during treatment are mainly due to the irradiation of healthy tissue. They depend on individual sensitivity of patients and the irradiated area. They appear in a delayed manner, usually from the 3rd or 4th week treatment, and can persist up to a month after the last one.

The most common are skin reactions similar to sunburn, fatigue, nausea. Other specific effects of the irradiated part of the body may occur: vomiting and lack of appetite in case of abdominal radiation, hair loss in case of irradiation in the brain, for dry mouth and throat cancers language. All of these effects are transient and disappear gradually.

But, in the longer term (several years), other effects such as tissue fibrosis, telangiectasia (purple spots) may appear, and in some cases, a secondary cancer may develop. One of the major challenges is to limit these phenomena. The main strategy up to now is to better define the tumor area, to better target the radiation level in the region, and to choose the most appropriate dose.

1.1.5 Conclusion

Radiotherapy has experienced in recent years much progress: The advent of 3D conformal radiotherapy, targeted, preserving at maximum the body and with fewer side effects. The modulated intensity is now possible to propose a treatment truly "sculpted" to the shape of the tumor and also the respiratory-gated radiotherapy developed recently. The irradiation volume is better defined and surrounding healthy tissue is better preserved.

With further research in physics, radiobiology and imaging, radiation therapy may in the future be optimized and personalized for each patient. Genomics is widely expected to participate in the growth of this radiation "custom" adapted to the tumor, but also to the radiation sensitivity of patients. This step is also closely associated with the parallel development of DNA chips, which will allow establishing the genetic profile of tumors. However, a necessary preliminary step should include **a test assessing the individual response to radiation**. Only then it will be possible to speak of "customized treatment".

In this thesis, the Silicon Nano Tweezers is introduced as a new method for the direct characterization of the **DNA response to radiation**. Coupled with a microfluidic system, the DNA may be immerged in any kind of medium, to mimic **the patient cell**, or to test the role of drugs such as **radiosensitizers**.

1.2 Ionizing radiation interactions with DNA

1.2.1 Introduction

As described in the previous Section 1.1, a radiotherapy treatment is based on the irradiation of a tumor with ionizing radiations. This section gives a synthetic summary of the radiation interactions with matter, and more specifically with DNA.

1.2.2 Sources of ionizing radiation

The radioactive decay of an unstable nuclide, either natural or artificially produced, is a process that is initiated by the emission of an α or a β particle, and produces a variety of secondary consequences, specifically the emission of γ-rays, as well as that of further α and β. This chain of subsequent emission of secondary radiations occurs because the unstable nuclide turns into a daughter nucleus that that may be in an excited state; de-excitation takes the daughter nucleus to lower energy states, down to its ground state, and the corresponding energy is emitted in form of γ rays, as well as further radioactive (α and β) decays, which in turn give origin to another daughter nucleus and so on, until a stable ground state is reached (see example in Figure 1.1). The de-excitation of excited nuclear levels by emission of electromagnetic energy in the form of γ-rays parallels that observed in atomic electrons, whereby the shift to lower atomic levels produces instead visible light quanta.

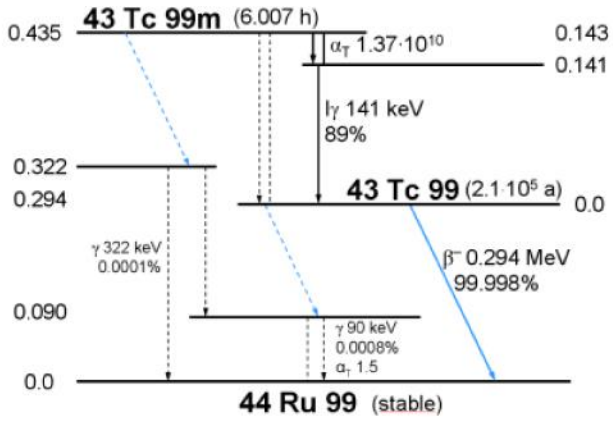

Figure 1.1: Example of a radioactive decay sequence. The principal decay modes are indicated by thick lines; minority modes by dashed lines. Gamma and internal conversion electrons in black, β^- decay in blue. Right branch: the metastable nuclide ^{99m}Tc decays with high efficiency from its level at 143 keV to 141 keV by internal conversion, then a principal gamma ray of 141 keV is emitted, going to the ^{99}Tc ground state. From here, radioactive β^- decay of 294 keV gives the ^{99}Ru stable nuclide. A minor path includes emission of 143 keV γ, and β^- decay to the 90 keV excited state of ^{99}Ru. Left branch: with small probability, Tc^{99m} can undergo β^- decay to an excited state at +322 keV of ^{99}Ru; hence, a 322 keV γ-ray can take to ground state, or an intermediate 294 keV γ to a lower excited state; from here, a 90 keV γ or internal conversion electron takes ^{99}Ru to the ground state.

Natural radiation from radioactive nuclides, cosmic rays and solar radiation, is a permanent feature of the natural environment. Therefore living organisms are constantly being exposed to such radiation. Human activity, such as medical practices, radioisotopes in health care, as well as commercial and industrial practices, such as the production of electricity in nuclear reactors and other nuclear techniques, as well as military applications as exemplified by weapons testing, represent important secondary sources of exposure to radiation. Despite the human activity, natural sources are the prevalent cause of irradiation; including cosmic rays and radionuclides present in the Earth's crust, in the food, water and air we ingest, as well as in the human body itself, accounts for 90% of human exposure to radiation. This separation of radiation into human and man-made sources (Table 1.1) highlights the constant exposure faced by man to radiation. This may be compared to the dose delivered in a medical framework and specifically during radiotherapy treatment.

Table 1.1 Average annual affective dose of ionizing radiation to individuals (in 2000)

Source	Dose (mSv)	Range (mSv)
Natural background		
External exposure		
Cosmic	0.4	0.3-1.0
Terrestrial	0.5	0.3-0.6
Internal Exposure		
Inhalation (mainly radon)	1.2	0.2-10
Ingestion	0.3	0.2-0.8
Total	2.4	1-10
Man-made (artificial)		
Medical	0.4	0.04-1.0
Nuclear power production	0.0002	Decreasing trend
Total	**2.8**	**1-10**

1.2.3 Radiation beams from particle accelerators

Since the early days of radiotherapy, the technology of artificial sources was aimed towards ever-higher photon and electron beam energies and intensities. During the first 50 years of radiotherapy the technological progress was relatively slow and mainly based on X-ray tubes, (electrostatic) van de Graaf generators, and magnetic-field betatrons. The development in the '50s of linear electron accelerators (medical LINACs), already introduced in the 1930s' aside of the first circular accelerators, moved to increasingly sophisticated machines and became the most widely used radiation source in modern radiotherapy. With its compact and efficient design, the LINAC offers excellent versatility for use in radiotherapy and provides either electrons, or megavoltage X-ray therapy, with a wide range of energies. In addition to LINACS, electron and X ray radiotherapy is also carried out with other types of accelerator, such as betatrons and microtrons. More exotic particle beams, such as protons, neutrons, heavy ions, and negative π mesons, all produced by special accelerators, are also sometimes used for radiotherapy.

Clinical X-ray beams typically range in energy between 10 kV and 50 MV, and are produced when electrons with kinetic energies between 10 keV and 50 MeV are suddenly decelerated by

hitting special metallic targets. Most of the electron kinetic energy is transformed in the target into heat, but a small fraction of the energy is emitted in the form of X-ray photons, characteristic X-rays from the target metal, and *bremsstrahlung* X-rays (from the German word meaning 'radiation from deceleration'). These latter are the most important component, and result from Coulomb interactions between the incident electron and the nuclei of the target material: the incident electron is suddenly decelerated, and loses part of its kinetic energy by irradiating an amount *P* of electromagnetic power, a situation well approximated by the physics of relativistic dipole emission:

Equation 1.1

$$P = \frac{e^2 a^2 \gamma^6}{6\pi\epsilon_0 c^2}$$

with e=1.6x10^{-19} C the electron charge, a the deceleration equal to v/t for a typical collision time t ~10^{-14} s, and γ=(1-v^2/c^2)$^{-1/2}$ the relativistic mass factor (the particle mass according to the theory of relativity increases as γm for a velocity v).

This basic principle is applied both in the older X-ray tubes, in which the fast electron beam was produced by a hot filament and a series of accelerating grids (pretty much like in a thermionic valve or a cathode ray tube of old TVs), as well as in modern linear electron accelerators, in which the electron beam is created by injecting an electron current in a complex combination of alternating electric fields and electromagnetic resonant cavities. No matter how the primary electron beam is generated, after hitting on a heavy-*Z* target (Tungsten, Copper, Gold, etc) it is subsequently converted into an intense beam of *bremsstrahlung* photons, with an energy spectral distribution of the type shown in Figure 1.2.a. The photon spectrum is continuous, extending from some E_{min} fixed by the plasma frequency of the target metal, to the maximum electron energy E_{max}, with a maximum of intensity peaked roughly at about E_{max}/25 (keV). If the maximum electron energy allows it, also characteristic X-ray lines can appear superposed to the continuous spectrum, resulting from the direct collisions of projectile electrons with atomic electrons. The angular distribution of the emitted photon beam is rather isotropic at the lowest electron beam energy, and becomes increasingly forward peaked as the initial electron energy is increased. As shown in Figure 1.2.b, already for E_{max}=500 keV, the photon beam is strongly forward peaked. At the typical beam energies of a medical CLINAC, E_{max}=5-20 MeV, the photon beam is sharply directed in the forward direction with a minimal lateral dispersion.

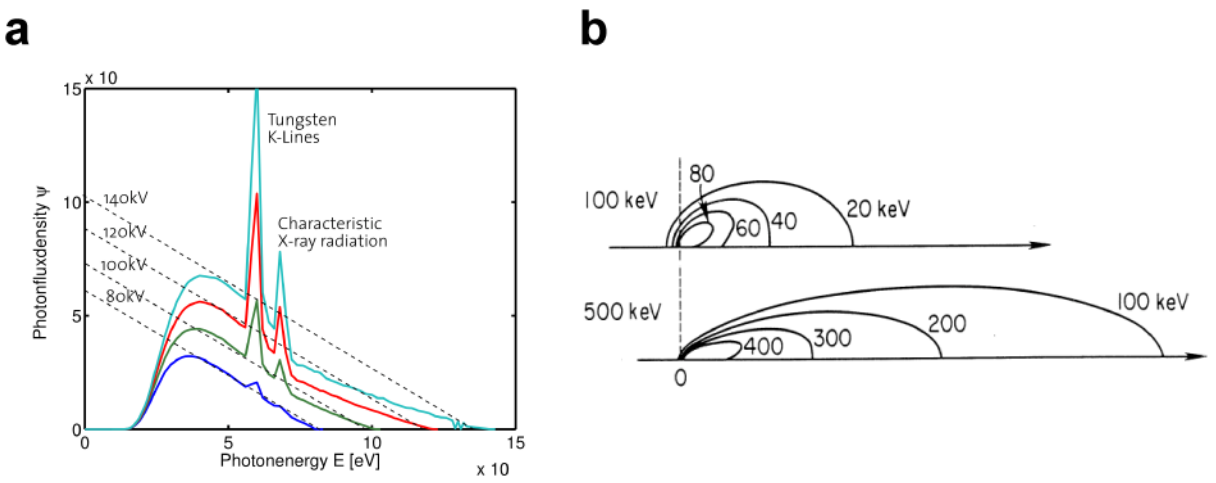

Figure 1.2: a. the spectrum of photon radiation emitted by a monochromatic beam of electrons with energies of 80 to 140 keV. The maximum energy of each bremsstrahlung spectrum ends at the electron energy. Note the characteristic X-ray lines of the Tungsten target at 59 and 67 keV. **b.** angular curves of isointensity of the emitted photon beam from electrons of 100 and 500 keV on a W target.

1.2.4 Types of ionizing radiations

In order of increasing frequency and decreasing wavelength, the electromagnetic spectrum spans radio waves, microwaves, visible light, ultraviolet light, X-rays and γ-rays (Figure 1.3). According to the quantum theory of radiation, the energy E of the electromagnetic wave is connected to its frequency ν and wavelength λ by Planck's equation:

Equation 1.2

$$E = h\nu = \frac{hc}{\lambda}$$

where h=6.62x10^{-34} J s, is Planck's constant. The wave velocity is $c = \lambda\nu$, equal to the speed of light in vacuum c=3x10^{8} m/s. The idea that radiation is quantized, despite having a continuous spectrum of allowed energies, defines the concept of *photon*, the equivalent of an ideal monochromatic wavepacket. Quantum theory predicts that photons of any wavelength also demonstrate **particle-like** behavior, and carry a wavevector **k**=**p**($2\pi/h$) associated to the relativistic momentum **p** of a massless particle. However it is only at the highest frequencies, and smaller wavelengths, when the radiation energy is comparable to the energy levels of atoms and molecules, that such particle-like properties become readily observable. The absorption of electromagnetic photons in matter depends on the energy of the photons and on the absorbing material atomic number Z.

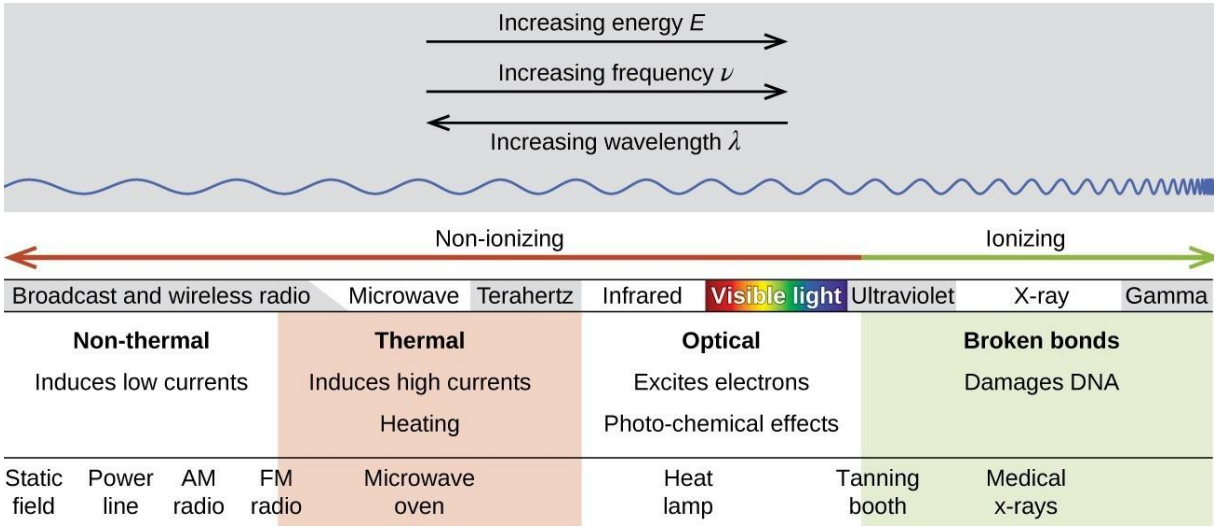

Figure 1.3: Schematic of the electromagnetic spectrum [12]

Low-energy electromagnetic radiation can at most excite vibrations and rotations of molecules (infrared frequencies). Low-energy, or non-ionizing, wavelengths are commonly understood to have minimal effects on biological and chemical structures, and are therefore considered harmless, outside the effect caused by heating, in biological tissue. Most of the technological objects we use in everyday life, including cellphones, microwaves, and radio transmitters make use of the lower energy-wavelengths of the electromagnetic spectrum. This being said, it is important to note that continuing research varies at the exact line of demarcation between ionizing and non-ionizing radiation, considering that certain molecules require very little energy to be ionized and can therefore wavelengths such as UV can sometimes create affects similar to X and γ-rays.

At the highest end of the spectrum, X and γ-ray photons possess sufficient energy to cause atoms through which they pass to eject an electron from its orbit. This capacity to break apart electrons from the orbit of atoms is the process of **ionization**. Typical binding energies of orbital electrons are in the range of tens of eV (1 eV=1.6x10^{-19} J). Therefore, a photon energy of at least the same order or higher is necessary, corresponding to frequencies $\nu=E/h > 10^{15}$ s^{-1} and wavelengths $\lambda=c/\nu < 10^{-7}$ m, or 1000 Ångstroms (visible light). Photons of even higher energies, such as **X-rays** (E ~ 0.1-100 keV, λ ~ 1-100 Å, ν ~ 10^{16}-10^{18} s^{-1}) and **γ-rays** (E > 100 keV, λ < 1 Å, $\nu > 10^{19}$ s^{-1}) can produce many such events of ionization, giving off some fraction of their energy at each ionization event. As a rough estimate, a 1 MeV γ-ray in water can produce about 30,000 ion pairs over a path length of about 10 cm.

When an atom is ionized, the loss of one of its electrons leaves behind a charged atom, the ensemble being understood as an ion pair (a negative electron and a positively charged ion). Ions traveling in the material can interact with other species, and if not recombined with negative charge, can produce highly reactive **free radicals**. For example, one ionized water molecule H_2O^+ can interact with a normal water molecule, and give

$$H_2O^+ + H_2O \rightarrow H_3O^+ + OH^*.$$

The hydronium ion (H_3O^+) would be normally present in water at neutral pH, because of dissociation equilibrium. The OH^*, however, is not normally found in water, and is called a free radical. This is a special molecule that is not ionic (it has zero charge), however it has one unpaired electron, indicated by the '*'. This unpaired electron represents a danger for other chemical species, in that the free radical seeks to attach to any other electron receptor species, typically acids. And, remember, DNA is 'deoxyribonucleic acid'. Attachment of a free radical to DNA is indeed at the origin of the most severe damages.

Direct ionization is among the many effects electromagnetic radiation can have when passing through matter. In the range of energies typically used for radiotherapy and imaging applications (from a few keV to some tens of MeV), photons passing through matter transfer their energy to target atoms and molecules through the following three main processes: photoelectric absorption, Compton scattering, and pair production, as shown in Figure 1.4.

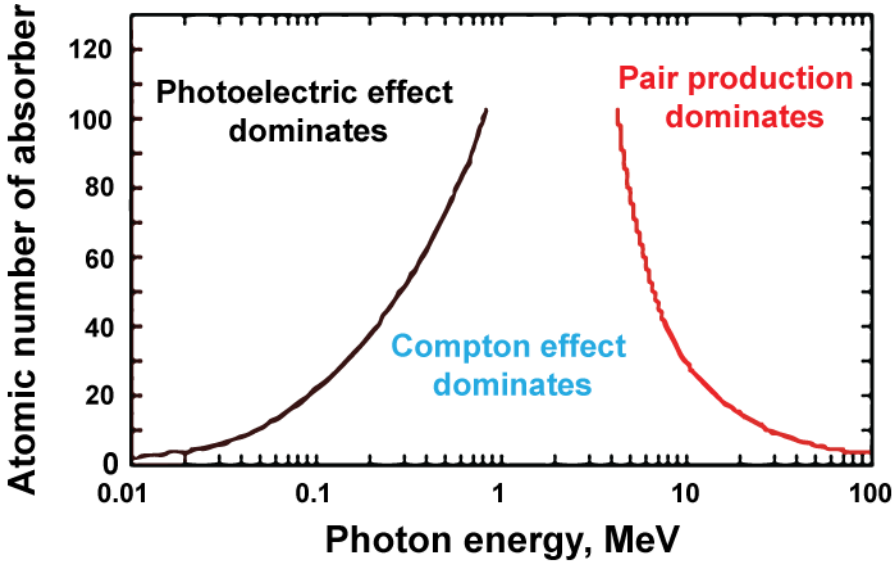

Figure 1.4: Dominant types of interactions as a function of the atomic number Z of the absorber and the energy of the photon radiation [13]

- Photoelectric effect: The photon travelling through a medium is absorbed by an atom, causing ejection of this electron and disappearance of the photon. The electron has a kinetic energy equal to the photon energy minus the *work function* of the solid, or the *ionization energy* of the atom (in both cases, the energy necessary to extract the electron into free space) and usually a random wavevector **k**.
- Compton scattering: The photon is scattered from an atomic electron of the medium (electron considered as free), which leads to the atom ionization. The electron receives part of the photon energy and momentum, and the photon is scattered with a lower energy and momentum, as well as change in the direction of **k**.
- Pair production (or materialization): when a high-energy photon enters in the Coulomb field of a nucleus (possibly of an electron), it can materialize into a positron/electron pair. The incident photon energy must be higher than or equal to 1.022 MeV, the positron and electron receive the extra energy as kinetic energy and their momenta are in (almost) collinear opposite directions.

High-energy photons are not the only radiations capable of promoting ionization. All charged particles can induce ionization, such as electrons, protons, ions (notably alpha particles, which are just Helium atoms stripped of both electrons, therefore ^{4}He nuclei). However, in the case of charged particles the ionization density per unit path length is so high that it is not useful to consider individual interaction events (such as photoelectric, Compton, pair-production in the case of photons). Instead, the average energy loss *dE* is considered to be practically continuous over any infinitesimal distance *dx*, and grouped in what is called the stopping power, *dE/dx*, of the material for a particular charged particle (see Figure 1.5). Due to the much higher ionization density, charged particles of comparable energy travel much shorter paths in a material, compared to photons or neutrons. To give an order of magnitude, a 1 MeV γ-ray travels ~10 cm in water, a 1 MeV electron (beta-ray) about 1 cm, a 1 MeV proton a few 10^{-3} cm, and a 1 MeV α-particle about 10^{-4} cm.

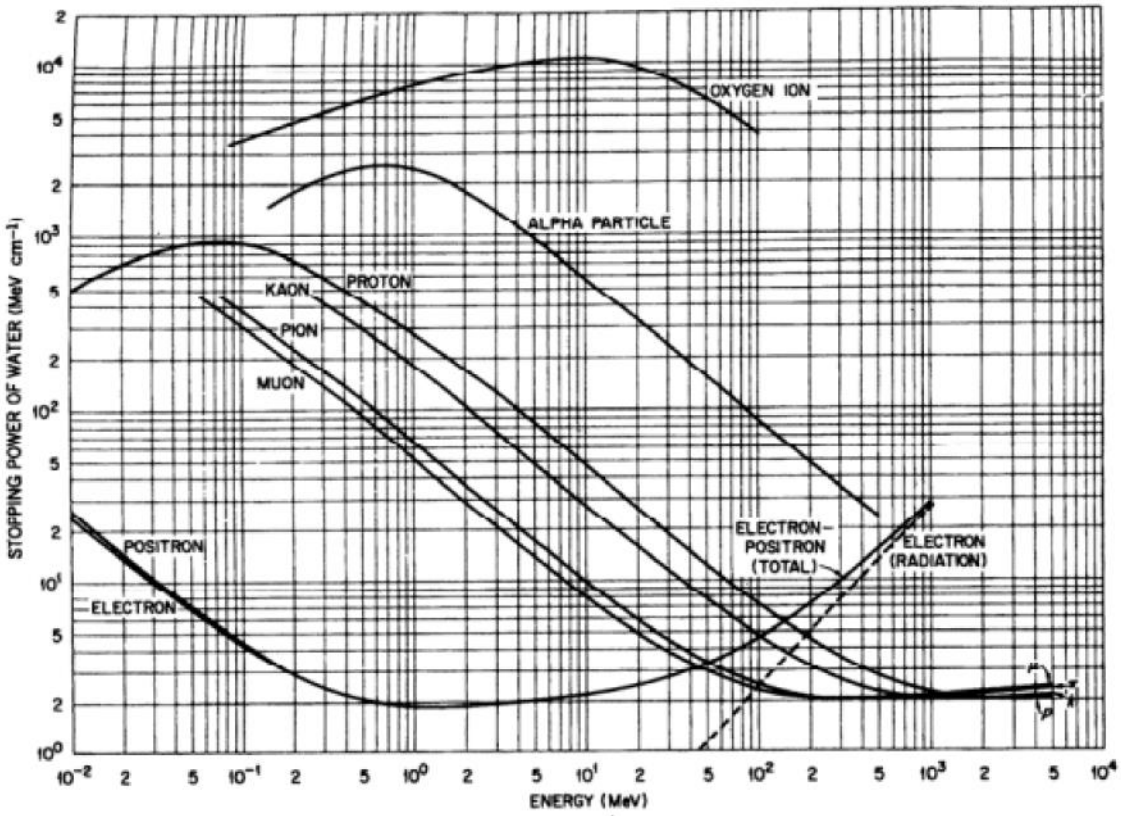

Figure 1.5: Comparison of the calculated stopping power (*dE/dx*, in MeV/cm), for various light and heavy charged particles. The shape of the curves (from the Bethe-Bloch formula [14]) is always very similar, only being shifted to higher energies as the mass and charge of the projectile increase. For electrons, the Bethe-Bloch formula is modified by additional terms.

1.2.5 Linear energy transfer

The linear energy transfer (LET) has been introduced to reflect the spatial density of ionization. It allows giving a rough characterization of the quality of a radiation by a single number, without having to describe each type of particle and its energy. The LET is defined as being equal to the amount of energy *dE* transferred to the material by radiation traveling a distance *dx*, and is usually expressed in keV per micrometer ($keV.\mu m^{-1}$):

Equation 1.3

$$LET = -\frac{dE}{dx}$$

The LET is increasingly large when the radiation loses much energy over a short distance; the ionization caused by the passage of a low-LET particle will therefore be much more scattered than the ionization caused by high-LET particle. For charged particles, the LET increases linearly with the density of the medium and, for a given environment, it increases as the square of the charge of the particle and is inversely proportional to its kinetic energy over a large

energy interval [15]. Radiations are categorized into low- and high-LET, with charged particles usually being high-LET radiations, whereas X- and γ-rays are considered low-LET radiations due to their sparse ionization density (Table 1.2). For low LET radiations the energy deposition events along the track of the photon are sparse relative to the dimensions of biomolecules such as DNA, with the result that photons may pass through such a molecule without depositing any energy.

A practical formula for estimating the ionization density, *ID* as (ion pairs)/micron, in biological tissues is:

$$ID = \frac{LET\ (keV/\mu m)}{34}$$

Table 1.2: Typical let values of ionizing radiation [12]

Radiation Linear Energy Transfer, KeV/μm	
CO-60 and **γ rays**	0.2
250 kVp X rays	2.0
10 MEV protons	4.7
150 MeV protons	0.5
14 MeV neutrons	12
2.5 MeV α particles	166
2 GeV Fe ions	1000

1.2.6 Radiation dose and units

The biochemical changes produced by ionizing radiations are the fundamental events leading to radiation damage in tissues. Radiation is measured either as exposure or as absorbed dose. The absorbed dose is the amount of energy absorbed in a system and generally regarded as the best way to quantify the radiation absorption. Various types of radiation dose units are used in radiobiology and Table 1.3 presents some of the frequently used dose units for measuring these radiation quantities.

1.2.6.1 Exposure

The radiation exposure is a measure of radiation based on its ability to produce ionization in air under standard temperature and pressure. This is the quantity measured by many radiation detectors, such as ionization chambers. The (S.I.) unit for exposure is Coulombs/kg in air (or Roentgen R in old units: 1 R = 2.58 x 10-4 C/kg air). The unit of exposure is only defined for

air and cannot be used to describe dose to tissue. Nevertheless ionization chambers are widely used to calibrate medical radiation devices and conversion factors to calculate the absorbed dose from exposure have been carefully documented for different radiation energies and tissues.

1.2.6.2 Absorbed dose

The amount of energy absorbed per mass is known as radiation dose. Radiation dose is the energy (Joules) absorbed per unit mass of tissue and has the (S.I.) units of Gray (1 Gy = 1 J/ kg). In the past the rad (radiation absorbed dose) was used, where 100 rad = 1 Gy (1 rad = 1 cGy).

1.2.6.3 Equivalent dose

As discussed above, the biological effectiveness (RBE) of each type of radiation varies greatly, depending largely on LET. For radiation protection and occupational exposure purposes the term 'equivalent dose' is used to compare the biological effectiveness of different types of radiation to tissues. The (S.I.) dose equivalent (H_T) in Sievert (Sv) is the product of the absorbed dose (D_T) in the tissue multiplied by a radiation-weighting factor (WR), often called the quality factor.

Equation 1.4

$$H_T = \sum W_R x D_T$$

Table 1.3: Summary of radiation units [12]

Dose	SI unit	Old unit	Conversion factor
Exposure	C/kg air	Roentgen	1 R = 2.58 x 10-4 C/kg air
Absorbed dose	Gray (Gy)	Rad	100 rad = 1 Gy
Equivalent dose	Sievert (Sv)	Rem	100 rem = 1 Sv

1.2.7 Penetration of photon beams into a phantom or patient

The intensity of a point-like photon source emitting in air or a vacuum decreases according to the inverse square law of the distance from the source; the beam from a LINAC can usually considered point-like, even with a small divergence [16]. On top of this, the intensity of a photon beam propagating through a phantom or patient, is altered by the attenuation and scattering from the biological tissues of the patient, or the biological-like material of the phantom. These combined effects make the dose deposition in a phantom or patient a

complicated process, and its precise determination is a complex task. A direct measurement of the dose distribution inside the patient is essentially impossible, yet for a successful outcome of patient radiation treatment it is imperative that the dose distribution in the irradiated volume be known precisely and accurately. This is usually achieved through the use of several transfer functions that link the dose at any arbitrary point inside the patient to the known dose at the beam calibration (or reference) point in a phantom.

The transfer functions are usually measured with suitable radiation detectors distributed in tissue equivalent phantoms. The dose or dose rate at the reference point is determined for, or in, water phantoms for a specific set of reference conditions, such as depth, field size and source to surface distance (SSD). A typical dose distribution on the central axis of a megavoltage photon beam penetrating a patient is shown in Figure 1.6. Several important points and regions may be identified. The beam enters the patient on the surface, where it delivers a certain surface dose D_s. Beneath the surface, the dose first rises rapidly (build-up), reaches a maximum value at depth z_{max} and then decreases almost exponentially until it reaches a value D_{ex} at the patient's exit point. The build-up is an important feature of high-voltage (above a few MeV) photons, since it allows creating a relatively sharp maximum of dose at some depth (a few cm) inside the patient, thus aiming more precisely at the tumor mass, while reducing the dose on the surface (skin-sparing effect).

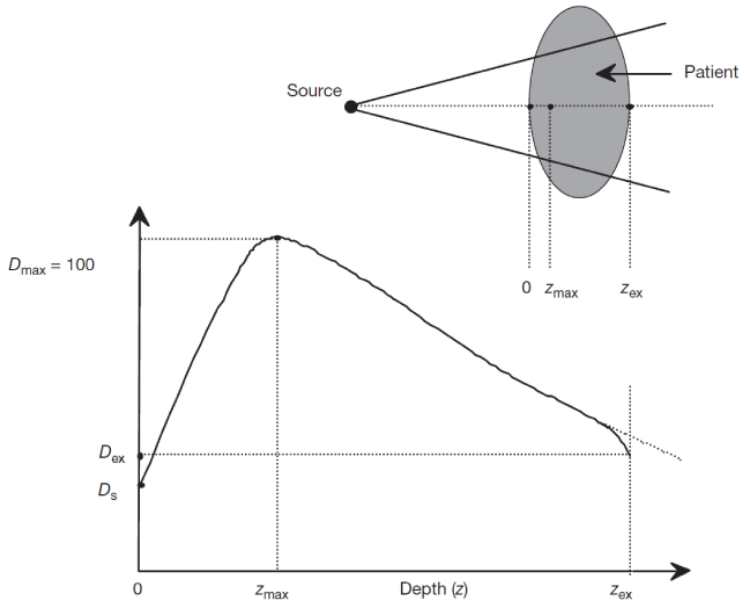

Figure 1.6: Dose deposition from a megavoltage photon beam in a patient. Ds is the surface dose at the beam entrance side, D_{ex} is the surface dose at the beam exit side. D_{max} is the dose maximum often normalized to 100, resulting in a depth dose curve referred to as the percentage depth dose (PDD) distribution. The region between z = 0 and z = z_{max} is referred to as the dose buildup region.

The depth of maximum dose (z_{max}) beneath the patient's surface depends on the beam energy and beam field size. The beam energy dependence is the main effect, whereas the field size dependence is often ignored because it represents only a minor effect. Nominal values for z_{max} range from z_{max}~0 for superficial and orthovoltage X ray beams (with accelerating energies below 500 keV), z_{max} = 1.5 cm for **6MeV (Cyberknife)**, to z_{max} = 5 cm for 25 MeV beams, as shown in Table 1.4.

Table 1.4: Typical depths of dose maximum zmax for various photon beam energies and a field size of 5 × 5 cm2

Photon beam energy	Superficial	Orthovoltage	CO-60	4MeV	**6MeV**	18MeV	25MeV
Zmax (cm)	0	0	0.5	1	**1.5**	3.5	5

1.3 Biological analysis methods of DNA damage

1.3.1 Introduction

During the cell life, DNA is constantly worn by endogenous or exogenous agents [17]. The action of these chemical or physical agents leads to varied chemical modifications of the cellular DNA. Physical agents include **ionizing radiation (X and γ rays)** explained in the previous sub-chapter and ultraviolet light (UV). DNA damages have some complex **biological consequences** and a better understanding of the phenomena is essential to optimize the dose delivery during a radiotherapy treatment. Nowadays, the DNA damage study is mainly performed by biological methods described below.

1.3.1.1 The DNA molecule

1.3.1.1.1 DNA: the carrier of genetic information

The current molecular-scale knowledge of biology comes from several disciplines: genetics, cytology, chemistry, molecular physics, biochemistry. Molecular genetics was born when Avery, McLeod and McCarthy showed in 1943 that deoxyribonucleic acid (DNA) is the molecular support of genetic information [18]. However, this discovery was regarded with skepticism, because at that time most scientists thought that genetic information should have a protein nature. Final acceptance of the theory of Avery would come only with the elucidation of the DNA structure, by James Watson and Francis Crick in 1953 [19] (Figure 1.7.a), based on the X-ray DNA diffraction patterns of crystallographers Maurice Wilkins and Rosalind Franklin. This discovery earned the three men the Nobel Prize for Medicine in 1962. (Unfortunately excluding Rosalind Franklin, the only chemist in the group, who had actually performed all the X-ray diffraction experiments and identified in the first place the helical structure of the molecule.)

The existence of a genetic code for translating the information contained in DNA in a sequence of amino acids has been firstly described by Khorana and Nirenberg 1961 [20]. With the advent of genetic engineering in 1970s, the genes of the most complex organisms could be decoded and directly analyzed, until in 2003 the entire human genome was decoded.

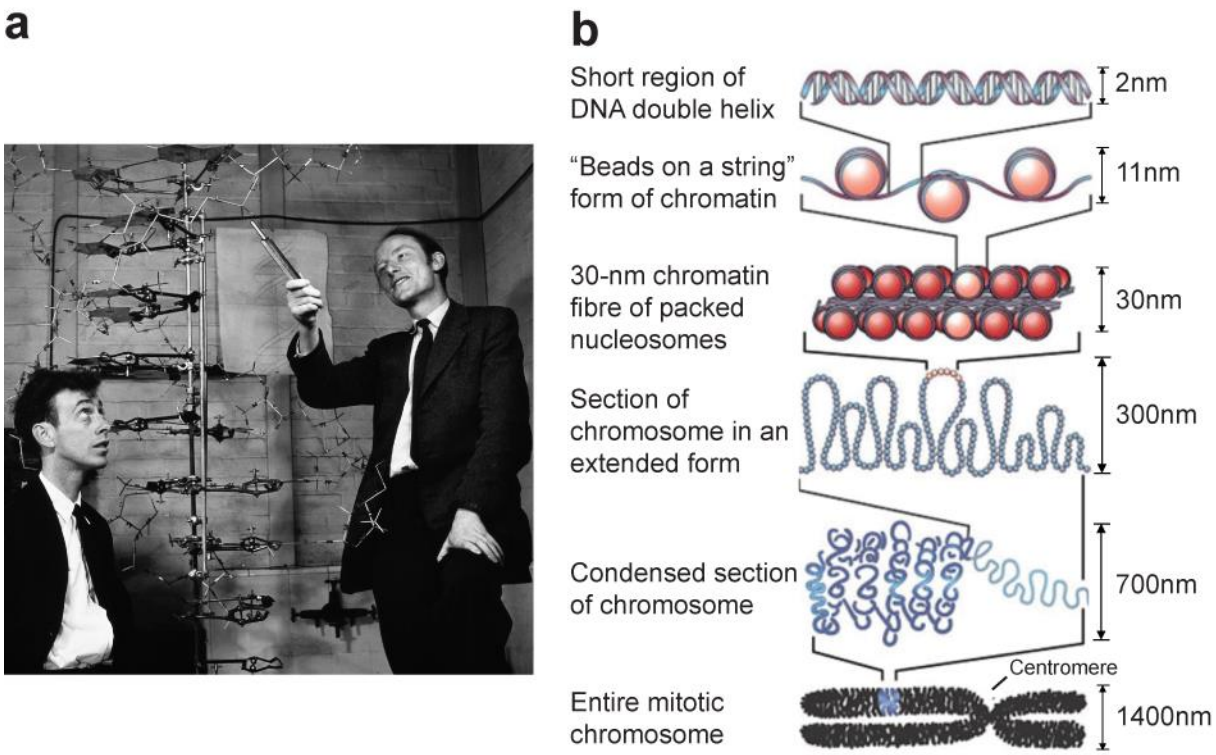

Figure 1.7: a. DNA 3D model by Watson and Crick's in 1953. b. Scale of the DNA structure

1.3.1.1.2 DNA structure

The DNA macromolecule is a polymer formed by two oligonucleotide antiparallel strands wound helically around each other in double helix, as shown in Figure 1.7.b and Figure 1.8. A strand DNA consists of a series of four basic units, the nucleotides. They bear each one of the four different nucleobases: adenine (A), guanine (G), cytosine (C) and thymine (T). Each base is attached to a 2-deoxyribose by a N-glycoside bond, to form a nucleoside. When a nucleoside is linked to at least one phosphate, it becomes a nucleotide. A and G are called purine bases, while C and T pyrimidine bases. Subsequently, many phosphate-sugar groups can attach to each other, by losing one OH and one H each, respectively, which is liberated as a H_2O molecule. In this way, a long polymer of many nucleotides can be formed, a single-strand DNA (ssDNA). Since the OH terminus of the sugar is indicated by the symbol 3', and the CH_2 terminus (where the PO_4 sits) is indicated as 5', the order of bonding in the single-strand polymer is said to proceed in the 3'-to-5' progression. However, when DNA is being 'read' in the transcription stage, the enzyme RNA-polymerase always proceeds in the 5'-to-3' direction.

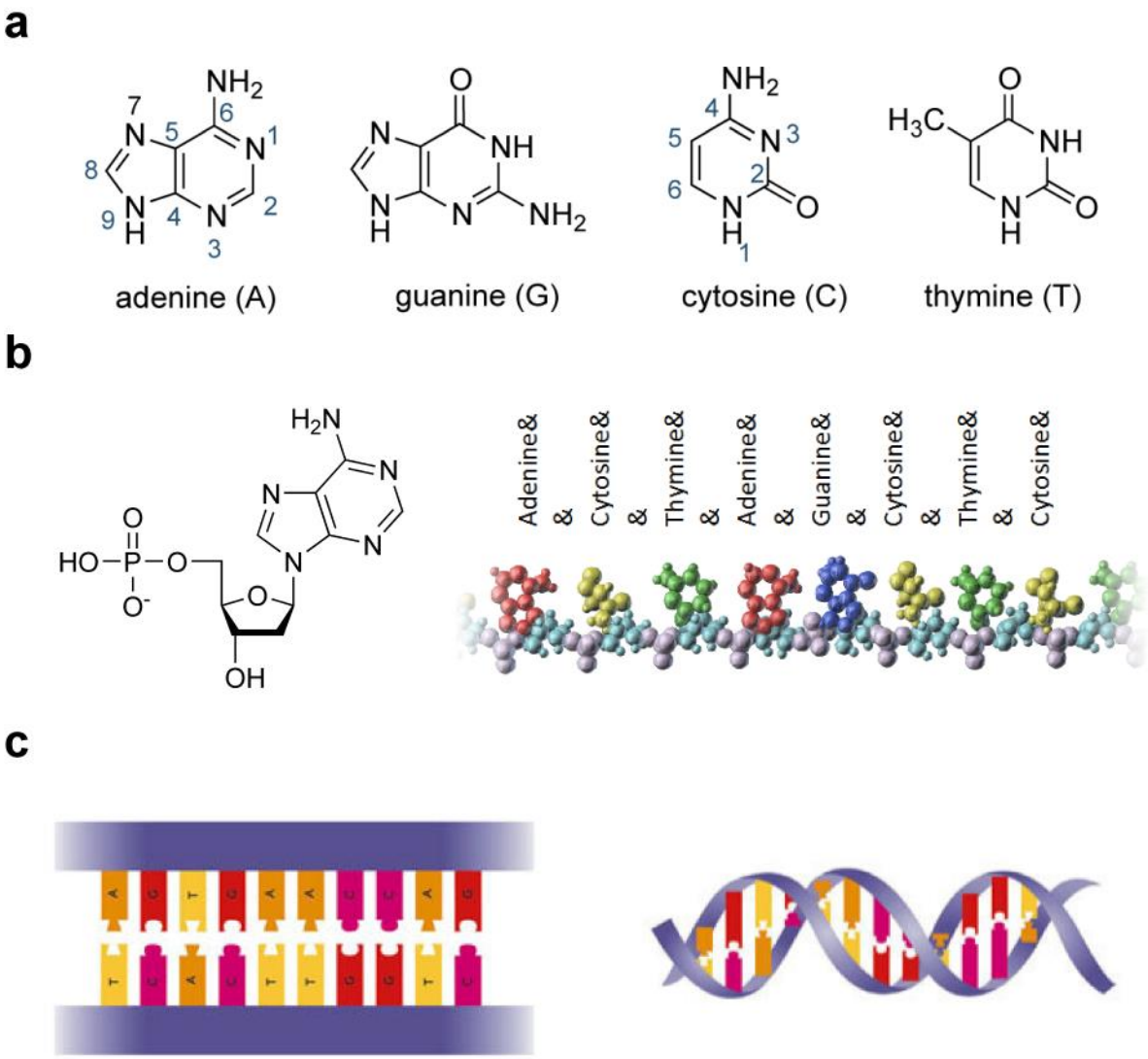

Figure 1.8: Assembly of the DNA structure. **a.** Molecular structure of the four DNA bases: Adenine (A), Thymine (T), Cytosine (C) and guanine (G). **b.** nucleotides (left) are formed when a base (in this case, A) binds to a ribose sugar (pentagon), linked to a phosphate group. Since the ribose has lost one Oxygen in the binding, the nucleoside is called a deoxyribo-nucleoside, and becomes a deoxyribo-nucleotide when the phosphate (PO_4H) is attached. A polymer holding many bases (example on the right) is formed when a nucleotide phosphate loses the OH group, and can bind to the -OH hanging group of a ribose from another nucleotide; this ribose loses its H, which forms a H_2O molecule with the other OH, and the phosphate-sugar-phosphate-sugar… backbone of a single-strand DNA is thus formed. **c.** Since A and T can form each two hydrogen bonds, while G and C can form three, two sequences of single-strand DNA can come together, if their respective sequences are complementary, pairing at every site two bases A-T or G-C on either side of the double backbone (left). Structural energy minimization, together with water and ion interactions in the nucleoplasm, force the paired double-polymer to assume the characteristic twisted double-helix shape (right), which won the Nobel prize to Wilkins, Watson and Crick.

As shown in the Figure 1.8, two single strands of DNA can come together and form a double-strand polymer (dsDNA). Because of their hydrogen-bond forming ability, A can pair with T (two H-bonds each), but not with C or G; and C can pair with G (three H-bonds each), but not A or T. If the two single polymer strands have complementary sequences on either side, for example:

… A – T – G – G – A – C – T – G …

… T – A – C – C – T – G – A – C …

hydrogen bonds can be formed, and the antiparallel (i.e., with ends and heads reversed) double strand becomes a real DNA:

5’ … A – T – G – G – A – C – T – G … 3’
|| || ||| ||| || ||| || |||
3’ … T – A – C – C – T – G – A – C … 5’

Antiparallel here means that one strand is attached in the 3’-to-5’ sense and the other in the 5’-to-3’ sense. The spacing between each nucleotide is 0.34 nm, and the average twist at each base pair is about 35 degrees, so that a complete turn of the helix requires about 10.5 base pairs, and a helix pitch of 3.6 nm; the bases also have a slight tilt by about -1 deg towards the 3’ direction. A human DNA can contain about 3 billion base pairs, making for about 1 m of length (2 m if considered each strand separately), all packaged in the cell nucleus of about 1 μm diameter. These are the canonical Watson-Crick base pairings. In principle, other pairs may form (and are indeed observed in DNA, and more often in RNA) with “non standard” couplings, for example C≡C, since both cytosines can form three hydrogen bonds. However, such non standard pairs are comparatively quite rare, since their formation energy is higher than for standard pairs: they represent defects in the coding structure, and are called *mismatches*.

The characteristic double-helical DNA shape comes about from the molecular interactions besides the hydrogen bonding, notably: (1) a stacking interaction, of Van der Waals type, between the nearly parallel, twisted bases lying on top of each other along each side of the helix; (2) an electrostatic screening of the negative PO_4^- charges (counterions) along the backbone, mostly from the Na^+ ions in the physiological solution; (3) interaction with water molecules, surrounding and stacking along and inside the helical grooves. (4) Elastic torsion and twisting energy of the backbone bonds. The sum of all these interactions makes the helical structure to be preferred with respect to the straight parallel strands. Upon forming the helix, it can also be noted (see again Fig. 1.8 above) that the grooves are not equal, but alternate in a ‘major’ and a ‘minor’ groove, of width respectively 0.22 and 0.12 nm. Structural water molecules (micro-

hydration) tend to nest preferentially along the grooves, while counterions may also bind close to the center of the helix. Divalent cations (Ca^{2+}, Mg^{2+}) have a higher affinity for the DNA grooves than monovalent ones (Na^{+}, K^{+}).

1.3.1.2 Radiation damage in DNA

While many biological compounds are sensitive to radiolysis, DNA is a critical target for ionizing radiation and cellular damage with lethal consequences (cell death due to replication blockage) or pro-mutagenic (non-repaired lesions inducing replication errors) for the cell.

Any ionizing radiation may act on the DNA by **direct and indirect effects**, described below. Various lesions may be detected in the DNA after irradiation: base alterations, base cross-linking, and base losses, backbone sugar modifications, DNA-proteins bridges, and most notably **single strand break (SSB) or double strand break (DSB)**.

The number and distribution of these damages depend on the radiation LET, structure of DNA and certain physico-chemical parameters such as temperature, oxygen level, and presence of protector or sensitizer compounds [21], [22].

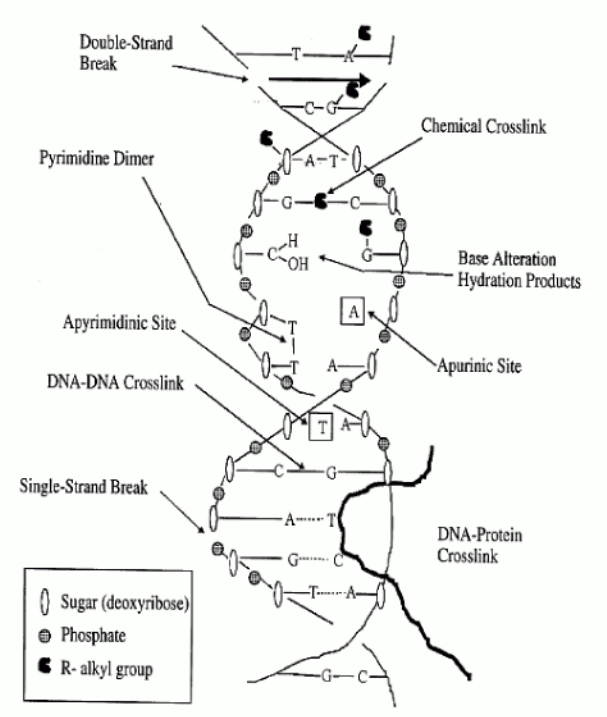

Figure 1.9: Types of DNA damage by ionizing radiations.

The preceding Figure 1.9 gives a summary of the main types and locations of radiation induced damages to the DNA molecule. The estimated average numbers of lesions induced in the DNA of a cell by a dose of 1-2 Gy are approximately: base damages > 1000; single strand breaks (SSB) ~1000; double strand breaks (DSB) ~40.

1.3.1.3 Direct and indirect effects

Figure 1.10 below summarizes both the **direct** and **indirect** effects of ionizing radiation on a DNA molecule. Namely, the direct interaction of the ionizing radiation with the DNA molecule, as opposed to the interaction with the surrounding water molecules, which subsequently produce reactive species capable of attacking indirectly the DNA.

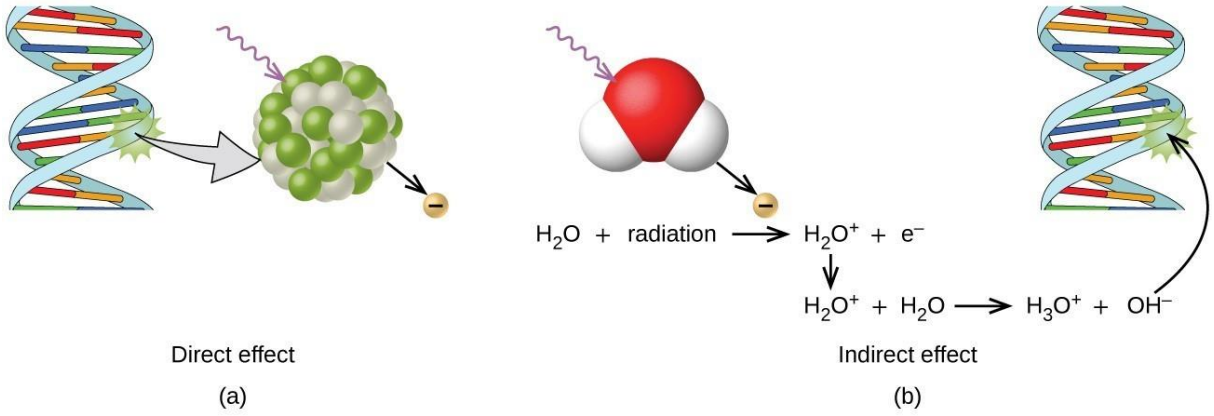

Figure 1.10: Direct versus indirect action [12]

1.3.1.3.1 Direct effects

Ionizing radiation can act directly, by impacting on biological molecules (RH, representative of hydrocarbons) causing ionization and excitation, as described in the previous paragraphs. One or more chemical bonds may be broken, resulting in atoms of the backbone or of the nucleotides with unpaired electrons (free radicals), which are very reactive and have a short life. The formation of these radicals occurs in the picosecond time range after the passage of the radiation, and leads to structural changes of the DNA.

It is estimated that about **one third of biological damage by γ radiation is caused by direct effects**. This process becomes even more dominant with high-LET radiation, such as protons or α particles.

1.3.1.3.2 Indirect effects – Water Radiolysis

The absorption of energy depends on the proportions and density of material in the path of the radiation. Water is the most predominant molecule in living organisms (about 80% of the mass of a living cell is water). Therefore, a major proportion of radiation energy deposited will be absorbed in cellular water. A complex series of chemical changes occurs in water after exposure to ionizing radiation (Figure 1.11). This process is called **water radiolysis,** a very complex network of electron-transfer reactions whose relative yields depend on the pH and LET of the radiation. The understanding of chemical changes in water is essential in order to study radiation effects on DNA, since the products of water radiolysis attack the DNA, thus providing an **indirect** effect of the radiation.

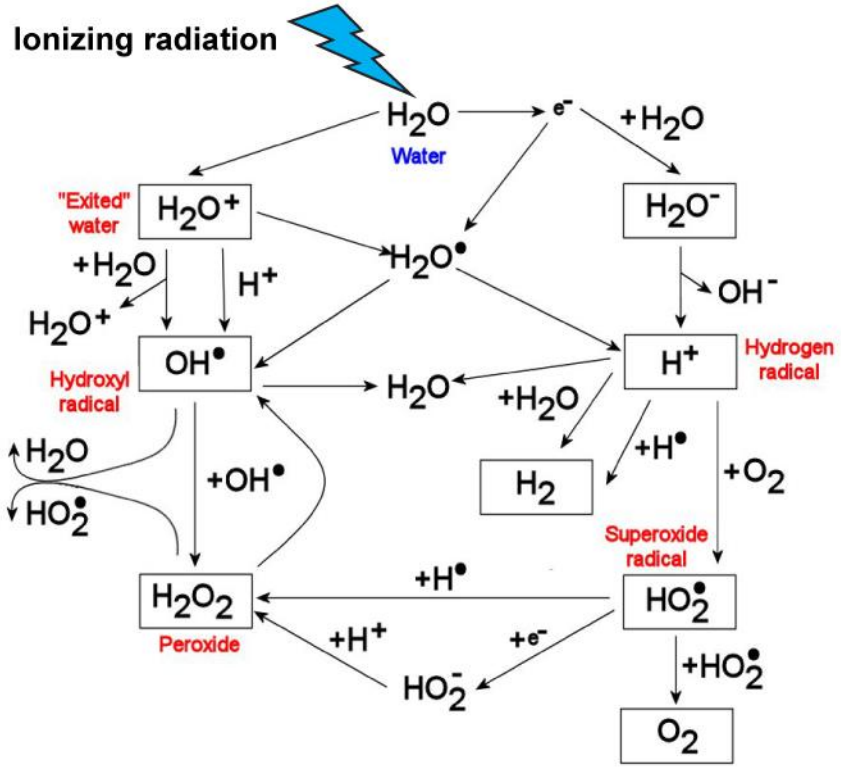

Figure 1.11: Radiolysis of intracellular water (H_2O) [23]

Free radicals have a typically short life, of the order of 10^{-9} seconds, and can diffuse to relatively short paths in water. The diffusion coefficient of the radical OH^* is about 7 $x10^{-5}$ cm^2/s (somewhat higher than those of the H_2O molecule and the OH^- ion), giving a typical RMS range of 65 Å. However, when attached to other molecular species, in a complex, radicals can survive much longer, and travel longer distances. When a free radical, isolated or in complex, reaches in proximity of the DNA, it can attach to several different places on the backbone, and transfer the unpaired electron(s) to the DNA itself. This is the origin of a chain of chemical events

leading to the formation of various defects in the DNA. Among these, the most relevant for cell survival are certainly single- and double-strand breaks.

Single strand break (SSB) results from one broken bond of the DNA backbone, on one strands of the double helix. The rate of production of SSB varies linearly with the dose and is lower when the LET radiation increases. SSBs are quite easily repaired by the cell, in the space of a few hours. Reparation can be divided into four stages: the recruitment of repairing enzymes and their attachment to the damaged DNA, the restoration of the 3' and 5' normal extremity on either side of the failure, the replacement of the missing nucleotide, and finally the ligation of the DNA [24].

Double strand break (DSB) result from the two DNA strands on each side of the helix being cut within less than *h* nucleotides apart, the number *h* depending on the stability of hydrogen connections between the two strands, and being usually <10. Therefore, the amount of DSB produced by a given dose is lower for high ionic force and low temperature. A DSB is called homologous if it occurs at the same base pair and heterologous otherwise. A DSB may be produced by the action of a single radical OH^* on the 2-deoxyribose [25] with the transfer of the radical on the second strand, or by attack of multiple radicals in neighboring areas [26]. Figure 1.12 gives an example of a possible mechanism of creation of a DSB by a single radical, aided by the action of two oxygen molecules (an example also of the great importance and sensitivity of radiotherapy to oxygenation of the cell). However, it must be noted that a DSB is NOT the sum of two adjacent SSBs, since its chemistry is different, as also proved by the fact that the cell recruits entirely different enzymes to start the repairing action.

These lesions are considered to be among of the most damaging and are lethal for the cell, if they are not, or poorly, repaired. There are two major DSB repairing systems [27]: homologous recombination reparation and strand pairing reparation. Recent studies on mouse have shown that the absence of such systems lead to genome instability, including oncogenic translocations [28].

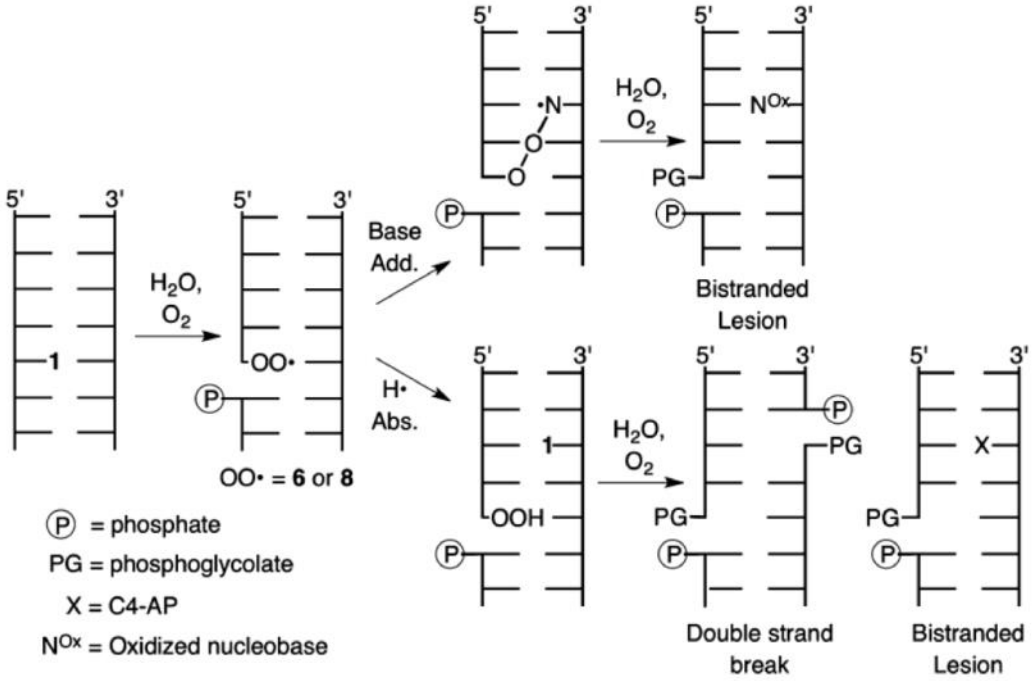

Figure 1.12: A proposed model for DSB formation helped by oxygen. From the left to the right: formation of an initial radical at a T nucleotide (indicated as 1); adduction of O_2 breaks the phosphate backbone (SSB) and incorporates an O_2^* radical; this can remove a H atom from a T on the opposite strand (lower path), reforming the radical 1 on the other strand; adduction of a second O_2 molecule breaks the phosphate also on this strand, thus producing a DSB, from one single free radical + 2 O_2 [29].

1.3.1.4 Biological consequences of DNA damage

Damage to cellular DNA is involved in mutagenesis and the development of cancer. The DNA in a human cell undergoes several thousand to a million damaging events per day. Changes to the cellular genome can generate errors in the transcription of DNA. Errors in repair, in addition to generate small insertion or deletion mutations, can also result in chromosomal rearrangements [Varga & Aplan 2005] and genome instability [Elliott & Jasin, 2002; Thompson & Schild, 2002].

Once cells lose their ability to effectively repair damaged DNA, there are three possible responses (Figure 1.13):

- The cell may become apoptotic. Sufficient DNA damage may trigger an apoptotic signaling cascade, forcing the cell into programmed cell death.
- The cell may become senescent, i.e., "irreversibly" dormant. In 2005, multiple laboratories reported that senescence could occur in cancer cells in vivo as well as in vitro, stopping mitosis and preventing the cell from evolving further.[30], [31]

- The cell may become malignant, i.e., develop immortal characteristics and begin uncontrolled division.

DNA damage analysis is essential to understand the transformation of a healthy cell to an apoptotic, senescent or cancer cell.

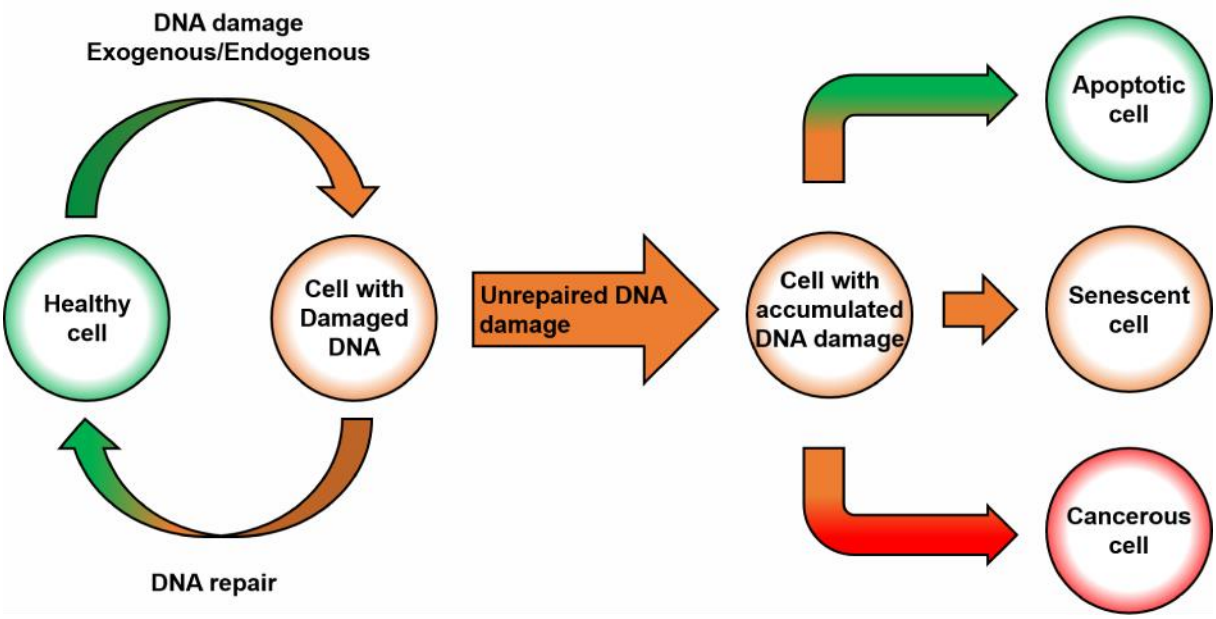

Figure 1.13: The pathways of cellular DNA damage and repair that leads to senescence, apoptosis, or cancer cells

1.3.2 Chromatography

The most commonly used approach and the oldest to measure damage to DNA bases is based on the use of direct chemical methods. The first work in this area dates back to the 70s [32]. These methods rely on immunochemical techniques, post-labeling techniques, liquid (LC) or gas (GC) chromatographic analysis, coupled with mass spectrometry detection, or electrochemical detection. The quantification of the damage is done on the DNA base, the modified nucleoside or nucleotide. Measuring the cellular damage level requires a prior cellular DNA extraction step. The extracted DNA is then hydrolyzed to monomers, bases, nucleosides or nucleotides, before damages can be finally analyzed.

1.3.2.1 Post-labelling method

The post-labelling method has been used for three decades ([33], [34]) for measuring various DNA adducts. The use of a radioactive signal makes it a very sensitive tool (1 adduct per 10^8 normal nucleotides) that may be very suitable for the measurement of radiation-induced damage of bases. Another advantage of the method is that it requires a very small amount of DNA (a few micrograms).

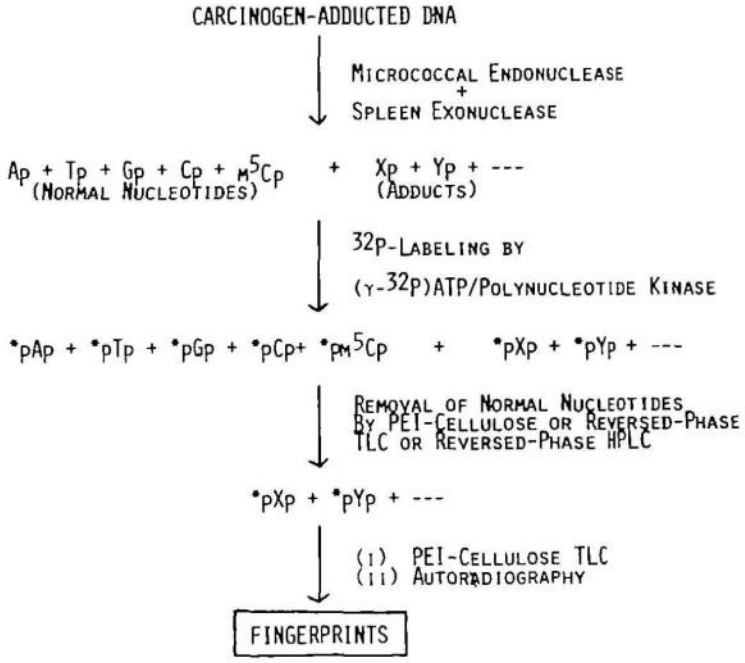

Figure 1.14: Principle of the ^{32}P post-labelling [33]

The methodology is an enzymatic hydrolysis of the DNA as a 3'-monophosphate nucleosides (with a micrococcal nuclease and a calf spleen phosphodiesterase). One (T4 polynucleotide) kinase allows to introduce a radioactive phosphate group using the [γ-32P] ATP as donor, on the 5'-OH function of the nucleoside 3'-monophosphate (Figure 1.14). Chromatographic separation on thin layer cellulose anion exchange will separate normal nucleotides and modified before the quantification.

1.3.2.2 Immunological method

The method is based on the use of poly or monoclonal antibodies directed against DNA changes. A key challenge is to obtain specific antibodies to a given oxidative damage. To prepare an antigenic system, one strategy is to attach the modified nucleoside to a protein that will be recognized by the immune system of a host system. The difficulty of obtaining antibodies is related to the variability of responses among individuals, the choice of the hapten and the potential cross-reactions. This explains the almost total absence of sufficient specific antibody for the measurement of oxidized DNA bases. An exception is the monoclonal antibody directed against the thymidine diol [35].

The first poly- and monoclonal antibodies directed against thymine diols (Tg) were obtained by West et al. [36] and Leadon and Hanawalts [37]. Other antibodies were prepared using a thymidine diol (Tg) monophosphate coupled to a protein, as hapten. Detection limits showed low specificity of 1 Tg for 10^4 [38], and 1 Tg for 10^3 base pairs that helped highlight Tg residues in DNA isolated exposed to 20 [39] and 10 Gy [40]. However, this sensitivity is insufficient to measure the basal level of Tg estimated between 1 and 20 for 10^6 normal nucleotides [41].

1.3.2.3 Gas chromatography with ion-selective mass spectrometry

The use of mass spectrometry (MS) allowed, in the last thirty years, the measurement of many DNA lesions. This is today the main technique for detecting oxidative-induced DNA damage in cancer [42]. Coupled with gas chromatography, the (GC-MS) method allows the determination of basal level, the rate formation and the repair kinetics of the modified bases in a DNA sample. Several of these lesions are produced by gamma irradiation ([43], [44],[45]).

Mass spectrometry (MS) allows the determination of the masses of fragments after ionization of the molecule. Thus, information on the nature and structure of these molecules are collected. It involves the ionization of the analyzed compound to submit charged species thus obtained to an electric or magnetic field. Each ion product is selected as a function of its mass/charge ratio and appears in the mass spectrum. This detection method is particularly specific, and allows the detection of several modified bases in DNA.

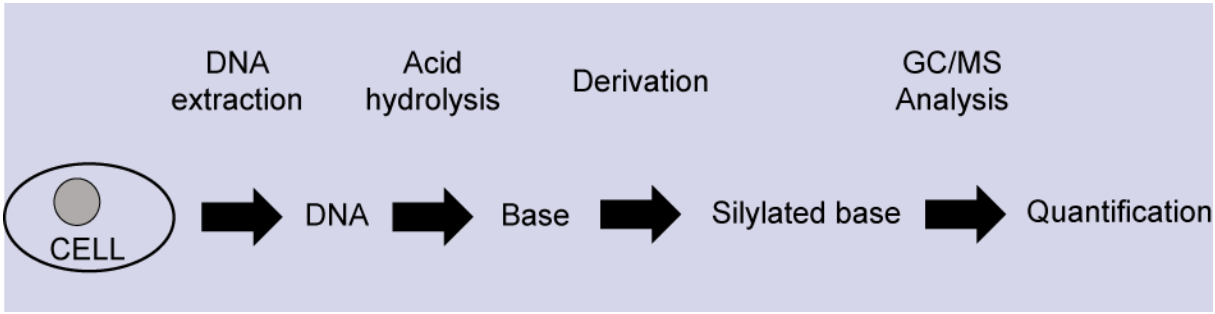

Figure 1.15: Preparation of DNA sample for GC/MS analysis

The method is applicable only to bases or nucleotides thermo-stable after a derivation step. Measurements made on the cellular DNA require a cellular **DNA extraction** as a first step.

Subsequently an enzymatic **hydrolysis** (P1 nuclease/alkaline phosphatase and/or acid) is carried out to release the nucleosides or bases. Some nucleoside can be directly analyzed after a derivation step [46]. However, acid hydrolysis leading to the liberation of the lesions in the form of bases is commonly used (Figure 1.15).

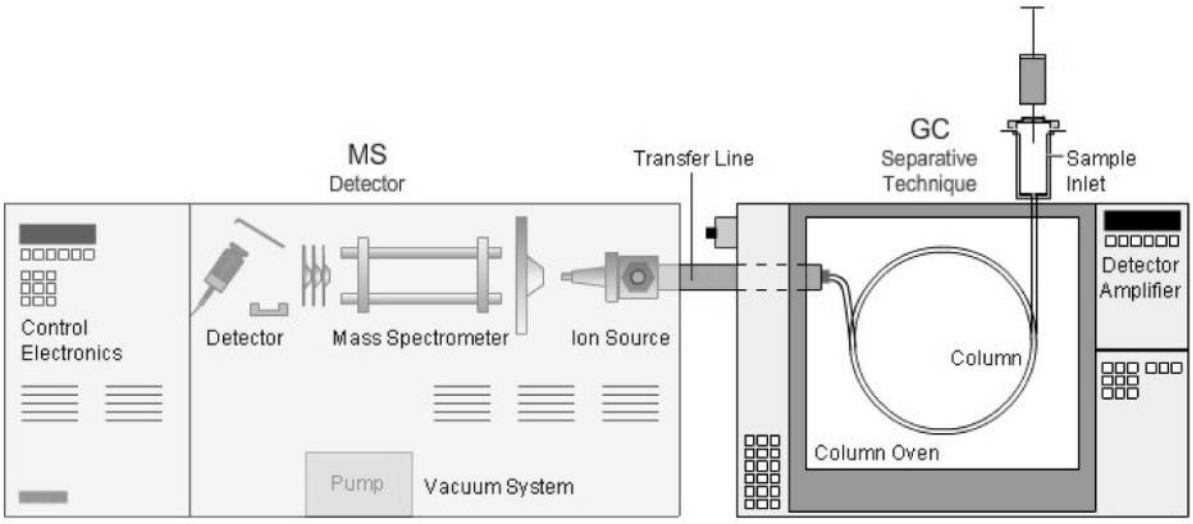

Figure 1.16: Schematic diagram of GC/MS [47]

Once the hydrolysis is completed, the compounds must be **derivatized** to make them volatile. This is a critical step for the sample preparation. Main derivatization methods involve silylation of alcohols, amine and enol function of the bases of the trimethylsilyl groups ([48], [49]). Derivatizing agents may be used such as N-tertbutyldiméthylsilyl-N-methyl-trifluoroacetamide (MTBSTFA) or N,O-Bis(trimethylsilyl)trifluoroacetamide (BSTFA) and the derivatization requires heating for a period of 20 to 30 min at 130 ° C.

Volatile compounds for the derivation are injected onto a capillary column of silica (coated with a film methylsiloxane substituted with 5% of phenylmethylsiloxane) flushed with helium. The injection port and the **GC-MS** interface are maintained respectively at 250 ° C and 290 ° C (Figure 1.16). Dropping of the compounds is carried out by a gradient increasing of the column temperature. The compounds are thus released with time and detected at the column outlet by the mass spectrometer. Ionization is usually done by electron impact with a SIM type detection mode ("Single Ion Monitoring"). The SIM mode versus SCAN mode (which allows you to view all the ions from the fragmentation of the parent ion) is much more sensitive.

1.3.2.4 High-performance liquid chromatography (HPLC-MS/MS)

High performance liquid chromatography technique coupled with mass spectrometry detection in tandem (HPLC-MS / MS) is the analytical method proposed most recently. HPLC is also the most common separation method to study biological samples by MS or MS/MS, because the majority of biological samples are liquid and nonvolatile. LC columns have small diameters (e.g., 75μm; nanoHPLC) and low flow rates (e.g., 200nL/min), which are ideal for minute samples [50]. Additionally, "in-line" liquid chromatography (LC linked directly to MS) provides a high-throughput approach to sample analysis, since multiple analytes that elute through the column at different rates can be immediately analyzed by MS (Figure 1.17).

Practically, all samples require some form of preparation prior to study by MS to remove detergents, reduce the complexity of the sample when focusing on specific proteins and/or tag proteins for identification/quantitation. Proper sample preparation is critical for MS analysis, because the quality and reproducibility of sample extraction and preparation significantly impact results from MS instruments. Sample preparation encompasses a wide range of techniques that includes lysate preparation, protein or peptide enrichment, sample clean-up and protein digestion.

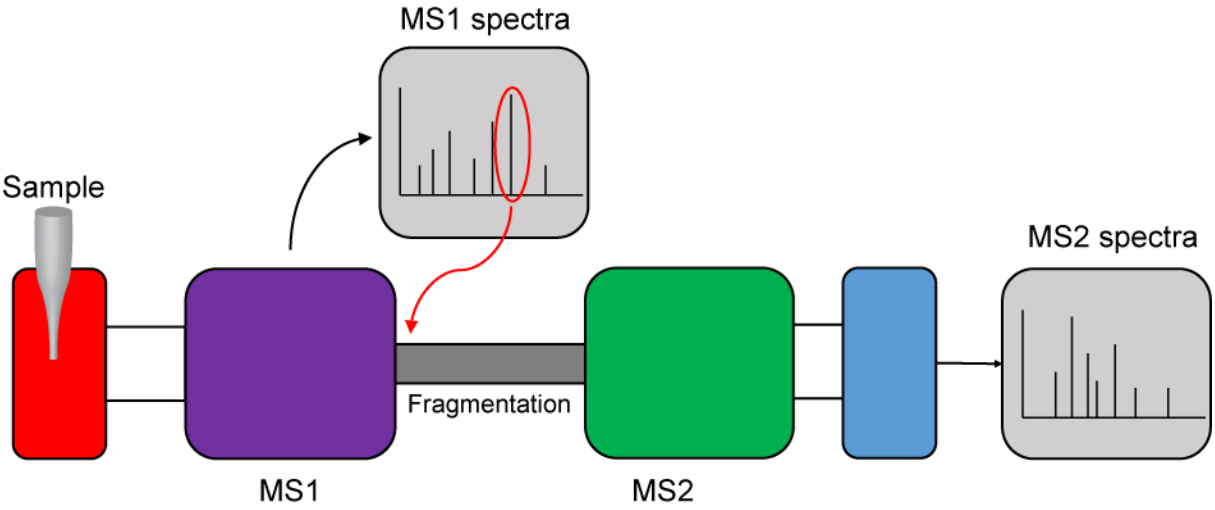

Figure 1.17: Diagram of tandem mass spectrometry (MS/MS). A sample is injected into the mass spectrometer, ionized and accelerated and then analyzed by mass spectrometry (MS1). Ions from the MS1 spectra are then selectively fragmented and analyzed by mass spectrometry (MS2) to give the spectra for the ion fragments.

Due to the recent accessibility HPLC-MS/MS technique, there is limit number of DNA damage measurement [51]. However, there are some studies of xenobiotics action on the isolated DNA [52]. This mode of analysis is particularly suitable for the detection of thermolabile compounds and opens new perspectives.

1.3.3 Strand-break length studies

Measurements of single-strand break (SSB) and double-stranded (DSB) have been the subject of numerous studies due mainly to the strong involvement of DSB in the radiation-induced lethality. On the other hand, the techniques involved in the determination of DSB have been adapted for measuring other damage [53]. Several methods have been proposed over the last fifty years. We briefly present their principle and compare their sensitivity with the gel microelectrophoresis method in single cell.

1.3.3.1 Sucrose gradient centrifugation

Initially used to determine the size of the DNA molecules, the centrifugation method on a sucrose gradient was then used to determine the number of single-stranded breaks [54]. The method had to face several methodological problems, such as the effect of the sedimentation rate on long DNA fragments, instability of the gradient, etc. In addition, the sensitivity of this technique, due to the existence of background noise generated by the manipulation of cells [55], is relatively low.

1.3.3.2 DNA relaxation

The principle relies on the observation that the presence of DNA breaks accelerates the electrophoretic migration of the molecule in an agarose gel in an alkaline medium [56]. After irradiation, cell membranes are lysed in a basic medium. The solution is then neutralized and a chromatography on hydroxyapatite column separates DNA fragments containing SSBs and DSBs.. The method was used by Rydberg and Johansson in 1978 on individual cells [57]. A DNA staining with ethidium bromide is used to estimate the relative proportions of intact and fragmented DNA.

1.3.3.3 Pulsed-field gel electrophoresis

Cells are included in agarose wells and their plasma and nuclear membranes are then lysed. After suitable treatment (protease and RNAse), DNA molecules move under the action of an electric field in an agarose gel. Smallest is the size of DNA molecule higher is its displacement. DNA molecules are previously labeled by cell incubation in presence of ^{3}H or ^{14}C precursors. This method is particularly used for the measurement of the DSB and is suitable for large DNA molecules. Several methodological steps of the technique were upgraded such as the use of reversed or perpendicular fields [58].

1.3.3.4 Elution filter

Elution filter is one of the easiest method. It is based on the polycarbonate filter used for DNA fragments size discrimination. The method can be used for the measurement of DNA-protein bridges, SSB, DSB and alkali-labile sites. Cells included in a lysis solution are deposited on a filter and most of the cellular contents, except DNA, are removed off by gravity. An alkaline solution is then fed under the action of a pump and the eluent is collected as various fractions. Elution of DNA fragments which are removed from the filter shows a semi-logarithmic relationship with the mass [59], [60]. Despite the very high sensitivity of the method, various studies have shown the influence of extrinsic factors such as the lysis pH [61], the composition of the used buffers [62] and the phase of the cell cycle [63]. Performed under neutral conditions, it is nevertheless particularly suitable for the measurement of DSB generated by low doses of gamma radiation [64].

1.3.3.5 Gel microelectrophoresis (Comet)

In 1978, Rydberg and Johanson proposed the comets method. They incorporated cells in an agarose gel placed on a microscope slide. The plasma and nuclear membranes are then lysed in

mild alkaline medium, before the DNA is stained with orange acridine. The observed red or green fluorescence, as acridine is linked to the single or double-stranded DNA, allows to estimate the proportion of the two classes of breaks. To increase the sensitivity of the method, Ostling and Johanson (1984) [4] introduced an electrophoresis step under neutral conditions. Their hypothesis was that the DNA fragments migrate especially fast the smaller they are, and that they are even more numerous once the DNA is cut. In 1988, Singh introduce the electrophoresis in alkaline medium [65]. The method allows the detection of DNA strands break. Allowing the detection of 1 SSB for 6.10^7 bases, the method is much more sensitive than most of the techniques used previously (Table 1.5).

Another advantage of this technique is the cell-by-cell damage analysis. It is thus possible within a population to distinguish subpopulations, which is not the case of global analyzes of DNA modifications. Requiring only a very small number of cells, it is particularly suitable for clinical studies [66], [67].

Table 1.5: Sensitivity of different measurement method of Single Strand Break

	Refences	**Sensitivity**
Gradient sucrose centrifugation	[68]	1 break/ 6-15 10^5 bases
DNA relaxation	[69]	1 break/ 2-3 10^7 bases
Pulsed-field gel electrophoresis	[70]	1 break/ 1 10^7 bases
Elution filter	[71]	1 break/ 0,6-1 10^7 bases
Gel microelectrophoresis (Comet)	[72]	1 break / 6 10^7 bases

1.3.4 Conclusion: Need for alternative methods of damage detection

Biological DNA analysis provides a rich panel of method to characterize DNA damage with a high accuracy. Nevertheless, these methods invariably require some chemical agents, complex processes, and cannot be performed in real-time during the DNA damaging process, most unlikely online during the irradiation. Moreover, DNA damage mechanisms are coupled with fast DNA damage reparation by a host of cellular proteins [73], which may start working already during, or immediately after, the irradiation, thereby altering the results of the subsequent chemical manipulations. Consequently, biological DNA analysis do not allow to observe the fundamental DNA damage mechanism, namely the microscopic mechanism which transform a healthy DNA molecule into a strongly damaged DNA by irradiation of cellular DNA.

Alternative methods to biochemical assays should be therefore investigated, to complement and improve the biochemical ones, based on the fact that the radiation damage chiefly induces a **structural** damage to the DNA molecule in the first place.

Since DNA is, after all, a strongly polar molecule immersed in a multiple electrolyte solution, one first idea could be that of measuring its electrical properties, mostly looking at possible variations of its electrical conductivity with increasing damage. However, the question of DNA conductivity has been long and bitterly debated [74], some claiming it to be a superconductor, others believing DNA would not conduct electricity at all. Biologists struggled for long time about how conductivity might affect DNA function. The overall consensus is now that although DNA can transport electrons over a length of a few base pairs, it fails to conduct over longer distances. Moreover, nearly all measurement of high conductivity were eventually discredited as pertaining mostly to the conductivity of the backbone-adsorbed water molecules [10].

A second alternative way to biochemistry, definitely much more promising, may however come from the measurement of DNA mechanical properties. The basic mechanics of DNA under traction, compression, twisting has been well characterized in the past decades, by a number of sophisticated experimental tools with single-molecule resolution, displacement resolution in the sub-nm, and force resolution in the pN range [75], [76]. The theory of mechanical response of DNA under applied stress is well developed, and provides a solid basis to analyze and interpret the mechanical experiments conducted on isolated DNA molecules of pre-defined sequence[77], [78]. By comparison, not much has been done yet on the mechanics of DNA with defects, and especially radiation induced defects, although theoretical developments indicate that meaningful mechanical signatures could be identified, for both single molecules and bundles of parallel DNA molecules [11], [79].

Therefore, this thesis proposes a novel approach, based on the detection of DNA damage by **force spectroscopy**, to observe in **real-time** the mechanical properties of a DNA bundle, under ionizing radiation beams from a radiotherapy machine. Different existing devices for the mechanical characterization of molecules will be described in the next Section, before introducing the Silicon Nano Tweezers based on MEMS technology that is at the heart of the present work.

1.4 Force spectroscopy

1.4.1 Introduction

The Silicon Nano Tweezers (SNT) have been developed as a new integrated device for direct bio-molecular manipulation and sensing. The motivation towards molecular manipulation is to reduce the uncertainty of conventional biological assay technique like tube assay by performing the detection by directly interrogating the molecule in real-time [80].

Molecular manipulations are traditionally performed by biophysical instruments, such as Atomic Force Microscope (AFM, [6]), Optical Tweezers(OT, [7]) or Magnetic Tweezers(MT, [8]). This Section 1.4 describes and compares these three technologies, introduces the idea of SNT, and motivates the choice of the SNT for the DNA characterization under radiotherapy treatment.

1.4.2 Optical tweezers

Since their proof of principle in 1986 [81], optical traps have been widely applied to a variety of biological systems such as DNA molecules [82], [83], kinesin motors [84], [85], viruses [86] or whole cells [87]. In a typical experiment, biological polymers, membranes, cells, microtubules are attached in between two optically trapped beads or a trapped bead and a glass surface (Figure 1.18), powered by a single, or split Nd:YAG laser beam at 1064 nm (at this frequency most biological material have a minimum absorbance). Then the rheological properties of these objects are probed through the motion of the trapped bead by measuring the deflection forces with steering optics. The force is deduced from the measurement of the relative motion of the bead with respect to the trap center and force. Nanometer-scale displacements and pN forces can be detected. Since the typical Young's modulus of biomolecules are in the range of E~10-100s MPa, with sizes in the 1-10 nm, this technique is particularly appropriate for studying forces and displacement at the single-molecule level (by using $F \sim (EL)\Delta x$). Although the full theory of the optical trap is quite complex, it is well demonstrated in the first report of the principle [81] and in the detailed paper [88]. Practical features are described in the extensive reviews by Neuman and Block [89] and by Ritort [90].

The measurement is carried out in the following manner (see Figure 1.18 below). An optical trap is formed by tightly focusing a laser beam with an objective lens of high numerical aperture. Dielectric particles in the vicinity of the focus experience a three-dimensional restoring force directed toward the focus. Typically for small displacements (< 150 nm) of the polarized

particle from its equilibrium position, the force gradient is linearly proportional to the displacement, and the optical trap is well approximated as a linear spring.

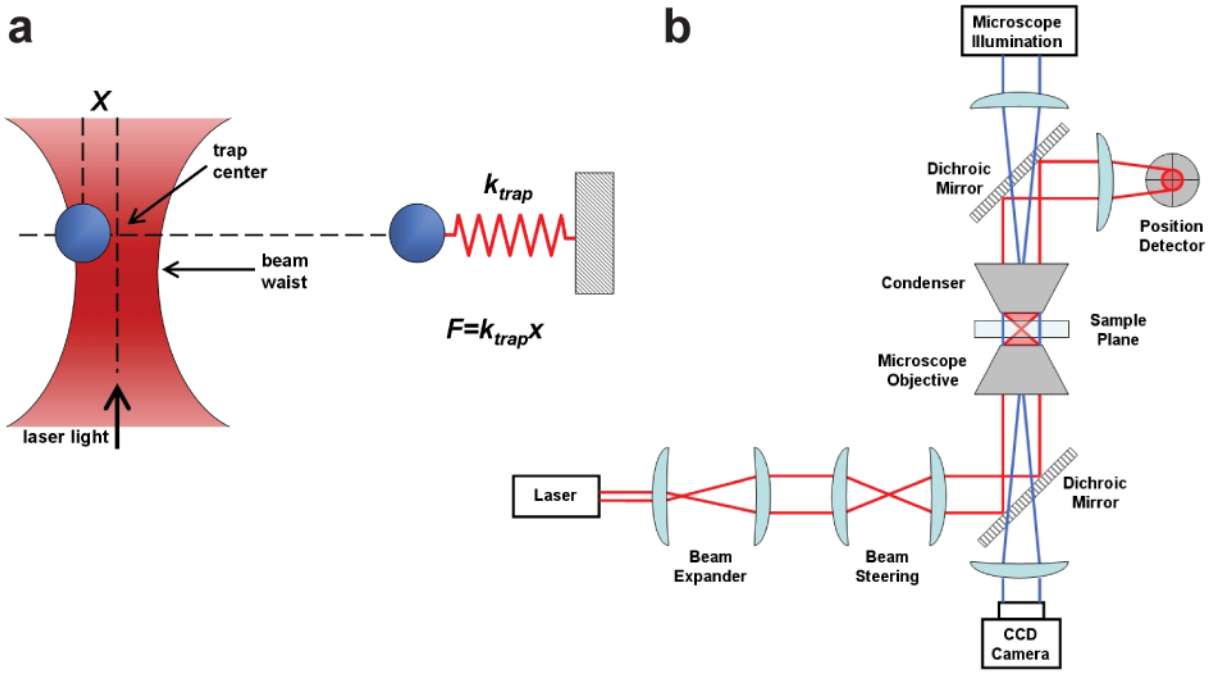

Figure 1.18: Optical tweezers principle for DNA analysis. **a.** Force calculation. **b.** Schematic implementation

The spring constant, or stiffness, depends on the steepness of the optical gradient (how tightly the laser is focused), the laser power, and the polarizability of the particle.

Therefore, measurements require a preliminary calibration of the position and the force. Usually, the effective spring constant *k* is identified from the characterization of Brownian motion, or by moving the probe through a known distance. Accordingly, the force measurement is deduced from the Hooke's law, $F=-kx$. The review [89] detailed the method for calibration and measurements.

The limitations of this technique arise from the use of a laser to form the optical trap. A possible heating of the solution and the generation of local convection currents may influence the measurements of enzymatic activity for example. Furthermore, a laser in the near-infrared wavelengths is usually used to minimize photodamage of the specimens without eliminating all the risks. With this technique, the range of applied forces is 0.1 - 100 pN. The low limit is set by the lowest stiffness needed to ensure trap stability, while the upper limit is set by the maximum laser power. The range of displacement is usually limited to the linear range of the trap, i.e. ~150 nm. For larger displacements, the experimental setup may be enhanced by

incorporating actuation and control mechanisms of the optical stage. Experimental results of spatial and temporal resolution reportedly are below the nanometer and millisecond levels.

1.4.3 Magnetic tweezers

The concept of magnetic tweezers (MT) is similar to that of optical tweezers. Single molecule can be manipulated by attaching it to an electromagnet with a paramagnetic core material and operating in a high magnetic field gradient (Figure 1.19). One distinctive feature of the MT is that it can be used to both stretch and twist the molecules. These characteristics are ideally suited to the study of DNA enzymes such DNA topoisomerases which unwind ds-DNA [91] or rotary motors such as F0F1ATPase [92].

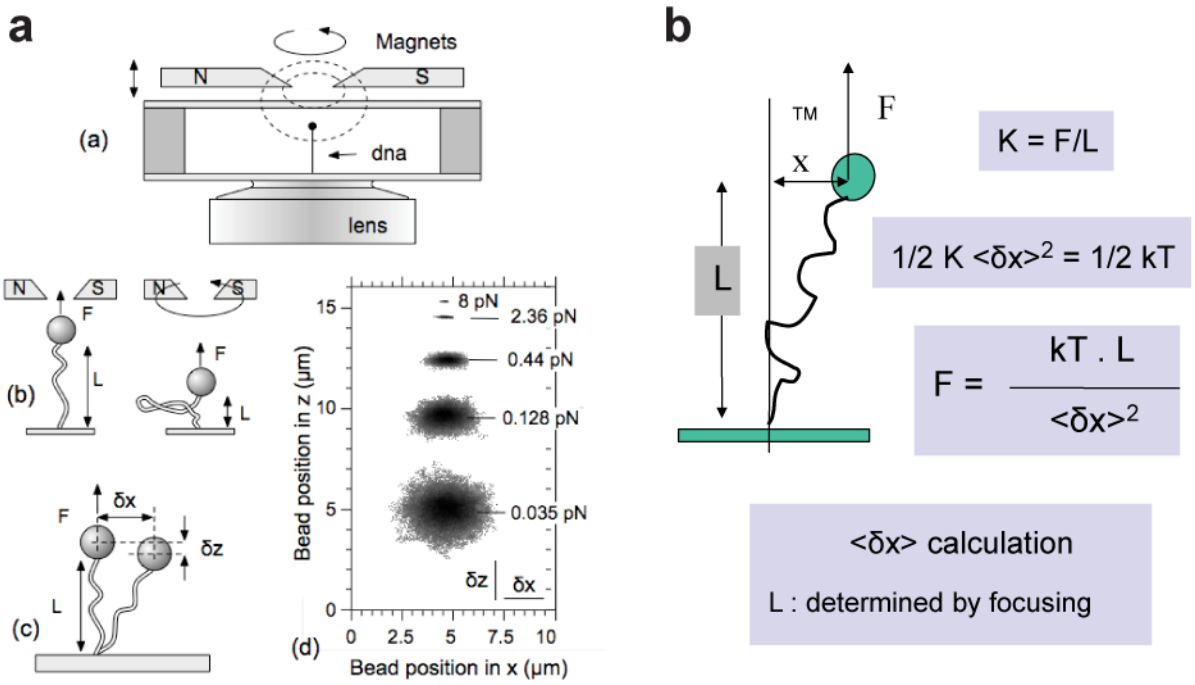

Figure 1.19: Magnetic tweezers principle for DNA analysis **a.** Schematic implementation. **b.** Force calculation [93]

The measurement is carried out in the following manner. The MT are placed above the sample holder of an inverted microscope, and biological polymers (typically DNA) are attached in between a controllable magnetic bead and a glass surface. Forces are proportional to the gradient of the square of the magnetic field. However forces can be important and roughly constant in between the magnets, resulting in a very low effective stiffness (reported 10^{-6} pN=nm). Experiments are usually performed at a constant force (at force clamp). The sample is illuminated through the gap in the magnets, and interference fringes between unscattered and scattered light produce a well-defined pattern, which permits the measurement of the height position of the bead. The lateral motion of the particle is measured by centroid tracking. The MT are capable to exert forces in excess of 1 nN (with electromagnets) or 200 pN (with small permanent magnets). As mentioned before, one of the distinctive feature of the MT is that

torque experiments can be applied to molecules. Estimates of the applied torque for a 1 μm magnetic bead are in excess of 10^3 pN.nm, which is nevertheless much larger than molecular torques (for example, the torque produced by ATP-synthase is 27-45 pN.nm; the maximum plateau torque supported by straight DNA is about 10 pN.nm). MTs are up to now the unique tools to enable torque experiments on single molecules. However, the large applied torque limits the use of this feature and moreover the direct measurement of the rotation requires special labeling of the molecule [94].

Finally, as for optical tweezers, sensitivity is limited by the video-based detection, which prevent the direct measurement of very fast or very small displacements. This technique also allows full 3D manipulation, but this requires cumbersome feedback system in addition to the sophisticated setup.

1.4.4 Atomic force microscopy

AFM is very versatile tool widely used for imaging, measuring, and manipulating matter at the nanoscale. Binning discovered the principle in 1986 [95] after the development of Scanning Tunneling Microscope (STM). Basically, the AFM consists of a micron-sized cantilever with a sharp tip at its end that is usually used to scan surfaces for topography at sub-nanometer resolution (thousand times better than the optical diffraction limit). When the tip is brought into proximity of a sample surface, forces between the tip and the surface lead to a deflection of the cantilever according to the stiffness of the cantilever. Depending on the studies, the forces that are measured with an AFM include mechanical contact force, van der Waals forces, capillary forces, chemical bonding, electrostatic forces, magnetic forces and Casimir forces for instance.

The AFM also allows measurements of inter and intra-molecular interaction forces at the piconewton-level. Similar to the OT and MT setup, in order to measure the mechanical properties of the sample molecule, the two ends of the biological molecule need to be prepared to specifically attach respectively the AFM probe and the surface (Figure 1.20). Therefore many methods of attachment were developed using antibodies, streptavidin-biotin bonds, avidin-biotin bonds but anyhow the contribution of the attachment must be considered in the elastic response of the system.

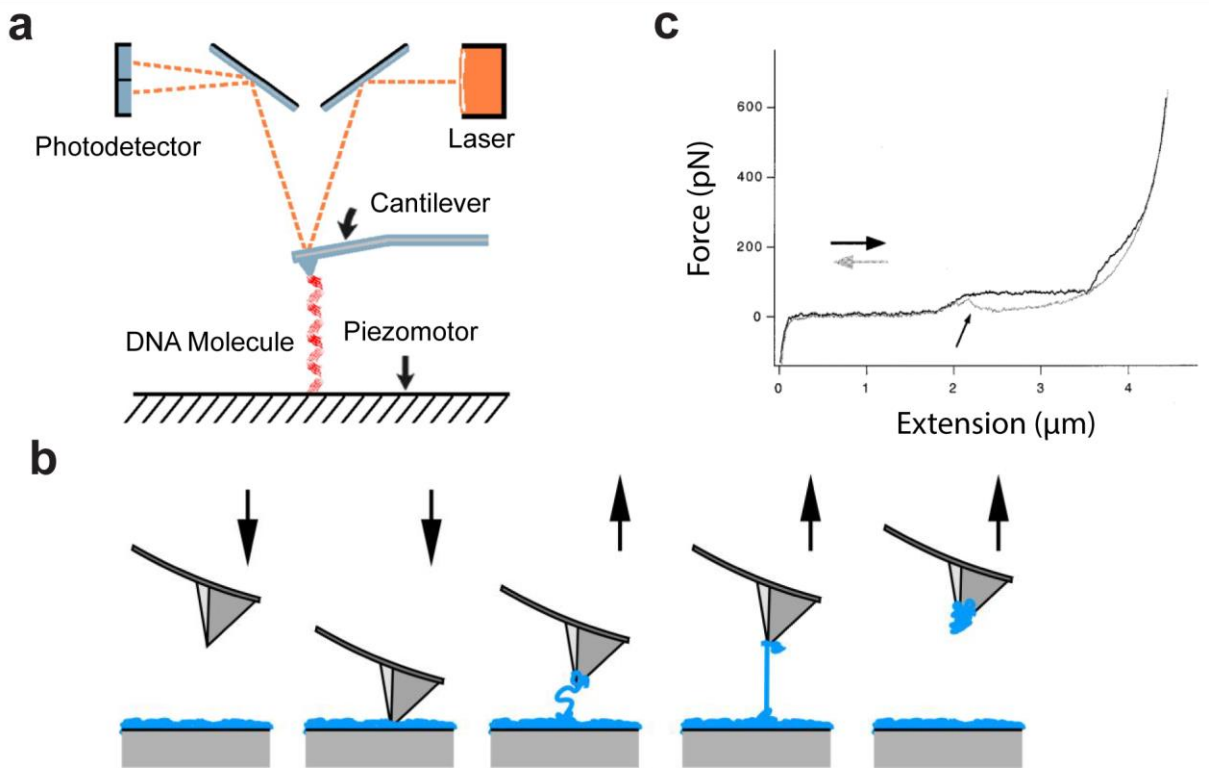

Figure 1.20: Atomic Force Spectroscopy principle for DNA analysis **a.** Atomic force microscopy principle for DNA analysis. **b.** Molecule stretching by AFM tip.[96] **c.** Melting force of ds-DNA [97] Single-molecule extension is commonly obtained by the z-displacement of the piezo-actuated stage, and forces are generally calculated from the bending of the cantilever with a known spring constant. Molecules of interest are described as springs that generate a restoring force when they are mechanically stretched. Therefore the extension is the distance between the anchoring points, i.e. between the cantilever tip and the glass surface.

AFM-based force spectroscopy has emerged as a very popular tool to study pico- to nanonewton-level forces, such as the rupture of molecular bonds (covalent bonds, ligand-receptor binding, or enzyme-DNA interactions) ([98], [99], [100], [101], [102], [103]). Commercial AFM are available from several suppliers, but usually customized experimental setups are built, in which the cantilever is customised and functionalized with respect to the target analysis. The accuracy of the measurements is determined by the quality of the piezoelectric displacement detector stage and the implementation of closed-loop position feedback control. The main limitations of AFM stem from the large size of the cantilever probe, which imposes high stiffness (~1 N m) and implies important losses in liquid environment (resonance quality factor flattening to 1 in liquid). Besides the forces associated with many biological processes are difficult to study with AFM. On the other hand, surface functionalization and bio-liquid preparation are required to avoid nonspecific molecule binding, undesirable interactions with the surface and subsequent artifact in data measurement. It can be

difficult to distinguish interactions of the tip with the molecule of interest from nonspecific interactions or inappropriate contacts with the molecule of interest.

1.4.5 Conclusion

Force spectroscopy methods evidently opened the way for new types of experiments in molecular biology. Direct measurement of forces at the molecular level has enabled to detect, quantify and understand forces governing the interactions between the molecules in the cell. Nevertheless these techniques still show some particularities and limitations, which are summarized in Table 1.6. Indeed, one specificity of these methods is the need to attach the ends of the molecule to a probe (which can be a bead or a tip).

Table 1.6: Comparison of single-molecule force spectroscopy techniques

	Optical tweezers	Magnetic tweezers	AFM
Displacement resolution (nm)	$0.1 - 2$	$2 - 10$	$0.5 - 1$
Temporal resolution (s)	10^{-4}	10^{-2}	10^{-3}
Stiffness (N/m)	$10^{-6} - 10^{-3}$	$10^{-9} - 10^{-6}$	$0.1 - 100$
Force range (pN)	$0.1 - 100$	$0.001 - 200$	$10 - 1000$
Displacement range (nm)	$0.1 - 10^5$	$0.1 - 10^4$	$0.1 - 10^4$
Probe size (µm)	$0.1 - 10$	$0.1 - 10$	$100 - 250$
Features	3D manipulation High resolutions	Rotation Constant-force assays	High-force assays "Simple" setup
Limitations	Photodamage Heating Complex setup	Complex setup	High stiffness Large minimal force

These instruments are extremely accurate and can achieve single-molecule level detection, nevertheless they are expensive, bulky and cannot operate in confined areas and harsh environment. It is indeed difficult to imagine a 'delicate' machine like an OT or an AFM to be operated in a clinical setting on a daily basis, requiring rapidity of set up for any new measurement, no need of a constant recalibration nor special time- and money-consuming functionalization of the samples, stable and repeatable results. Moreover, the statistical nature of the radiation damage process requires performing the measurement on a meaningful sample of molecules, not just one by one. To fulfill the need of molecular manipulation with a tiny and low-cost device, instead Micro Electro Mechanical Systems (MEMS) could be a more appropriate approach, as they integrate accurate molecular-level engineering tools, and can be cheaply produced with parallel processes. Moreover, with their tiny size in the range of a few mm^2, they can be inserted in small areas, and their basic silicon-based technology and electro

mechanical operations can endure high temperatures and **intense electromagnetic environments, such as γ irradiation.**

1.5 Introduction to MEMS technology

Born more than 30 years ago [104], [105], Micro-electromechanical systems (MEMS) integrate mechanical and electrical components and have feature sizes ranging from micrometers to millimeters and merge at the nano-scale into nano-electromechanical systems (NEMS). They may be fabricated using methods similar to those used to construct integrated circuits (IC) and they have the potential of providing significant cost advantages when batch fabricated. The development of the MEMS technology benefited of the fast-growing IC industry and subsequent progress on materials and techniques for micro-manufacturing such as microsystems have nowadays spread numerous fields ranging from fundamental nanosciences to applications in biology or biochemistry with the manipulation of molecules and the emergence of Lab-On-Chip systems. A broad range of devices, architectures and operations have been investigated for studies dedicated to the micro- and the nanometer scales. Besides passive mechanisms and sensors, several active devices such as turbines [106], linear and rotative motors[107], [108], resonators [109],switches [110], grippers (see further) and fingers [111] have been successfully accomplished at the micro scale.

Suitable actuation is achieved taking advantages of the specificities of the micro world. Beyond the decrease of the weight in L^3 (length cubed), the downscaling benefits to some actuations based on physical principle, such as electrostatic forces, which are inappropriate at the macroscale. Among the family of new devices, microgrippers focused much interest. A first motivation rose from the ability to handle micro-size objects for their positioning or assembling. Forces and dimensions of the microgrippers are usually the more appropriate for the safe manipulation of micro-objects. The second reason comes from the reduced size of the grippers itself that allows performing these manipulations in tiny areas. Accurate manipulation of micro-sized objects is an important concern that need to be solved and improved. In terms of applications, a large segment is open with the manipulation and the assembly of objects always smaller, which requires more precision and force control (besides accuracy and speed of operations). In early works, some studies investigated several types of actuation and integration for manipulation. Every actuation suitable at the micro-scale work were studied: electrostatic [112], [113], magnetic [114], thermal [115], [116], piezoelectric [117] and SMA [118], [119]. Additionally, several devices aiming improved force/displacement control characteristics has been demonstrated with different designs and mechanisms. Some mechanical solutions for the amplification of the displacement [120] or for linear displacement through mechanical feedback [9] were successfully adopted from the macro-scale to the micro-scale. The trend followed by the new family of grippers is to develop monolithical or all-integrated microgrippers.

Electrostatic comb-drive and differential capacitive sensor seem to be the techniques the more used and the more suitable for batch-fabrication, low consumption with good performances.

The combination of MEMS and nano-bio technology is especially beneficial to improve the quality of life in the future society by providing better understanding of biological processes and developing new medical diagnosis tools [121].

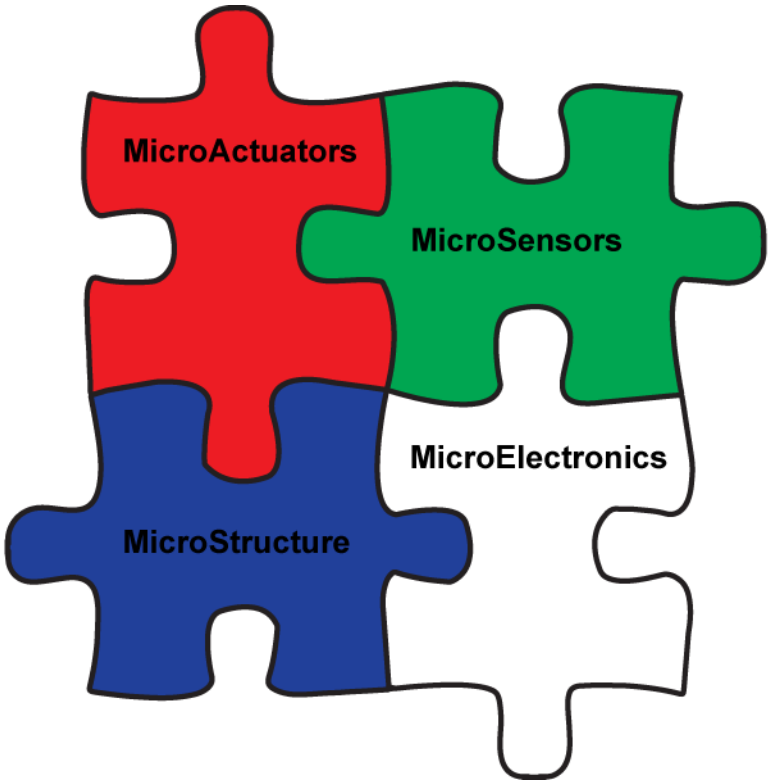

Figure 1.21: The integration of MEMS components

Chapter 2: Silicon Nano Tweezers

2.1 Introduction and SNT Principle

Silicon Nano Tweezers have been developed since 2005, as a versatile tool to perform biomechanical characterization of biomolecules and whole cells. This thesis is based on a specific design of the SNT, optimized for DNA characterization in liquid.

Figure 2.1 shows a 3-D illustration of the Silicon Nano Tweezers. It consists of a MEMS device whose overall dimensions are 4.5 × 4.5 × 0.5 mm. The SNT integrates all the functions needed for biomechanical assays:

- molecule trapping and manipulation
- visualization of the assay
- mechanical stimulation(s)
- capacitive sensor reading of the molecule response.

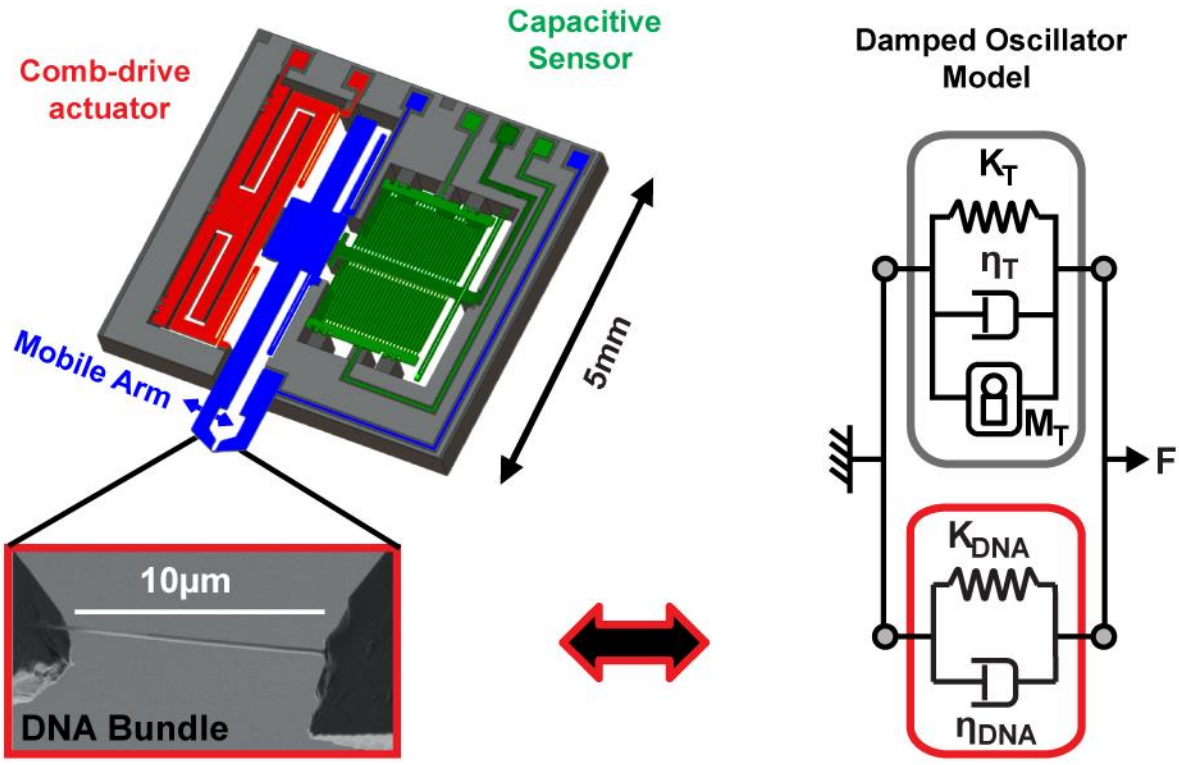

Figure 2.1: 3-D view of the SNT. The two arms are shown in blue, the actuator of the mobile arm in red, and the displacement sensor in green. A DNA bundle is trapped between the two tips of the SNT. The damped oscillator model of the SNT+DNA is illustrated on the right of the figure.

The SNT is comprised of two parallel arms ending with sharp opposing tips. These tips also act as electrodes to trap the molecules by Dielectrophoresis (DEP). One of the arms can be fixed,

or both mobile in a more general case, and are displaced by electrostatic actuators. The comb-drive type actuators are tuned by a voltage difference applied between the two actuation voltage ports (Figure 2.2). The real displacement of this arm is measured by a displacement sensor, thus the bio mechanical characteristics of the trapped molecules can be measured in real-time.

Therefore, the device consists of the following three parts:

- Two sharp tips at the end of parallel arms. One arm fixed for the Single-Actuators SNT (S-A SNT) and both arms mobile for the Double Actuators Silicon Nano Tweezers (D-A SNT).
- A series of comb-drive actuators.
- A differential capacitive sensor.

These different elements must be electrically insulated, while being mechanically linked to each other. This is achieved by using SOI technology. Indeed, the handling substrate is used for the mechanical connection, and the intermediate oxide layer serves as an electrical insulator.[9]

2.2 The design and microfabrication

The actual design and fabrication of the SNT is based on previously existing technology [9],[122]. However, in this Section, the design and the features are summarized and a new version, the Double-Actuators SNT, is presented.

2.2.1 The Single-Actuators SNT

2.2.1.1 The comb-drive actuators

Actuation is provided by electrostatic forces in an interdigitated comb architecture (Figure 2.2). This means of providing force is one of the most widely used in the design of submicrometer-size systems ([109], [123]–[126]). Although the interdigitated comb architecture has a shorter total stroke compared to parallel plate architecture, it is nonetheless privileged because the force is exclusively dependent on the actuation voltage (and not on the electrode position), which allows for simpler control of the actuation. The design of a comb drive actuator requires the study of electrostatic forces generated between the two electrodes. The electrostatic field between the two electrodes is commonly described by a simple planar model (i.e., the electric fields are confined to the cross-sections of the individual comb fingers). Force corrections, studied in [127], take into account the interactions in unengaged regions. Here, a simple model is considered to evaluate the order of magnitude of the force.

Local forces are obtained by applying the principle of virtual work. According to the notion of energy preservation EC, the invested mechanical work (W_{es}) will increase the electrical energy stored within the capacitance with $dW_{es} = F_x dl$. The electrostatic force F_x acting on the mobile electrode of the capacitance C compound by the comb fingers is given by the Equation 2.1.

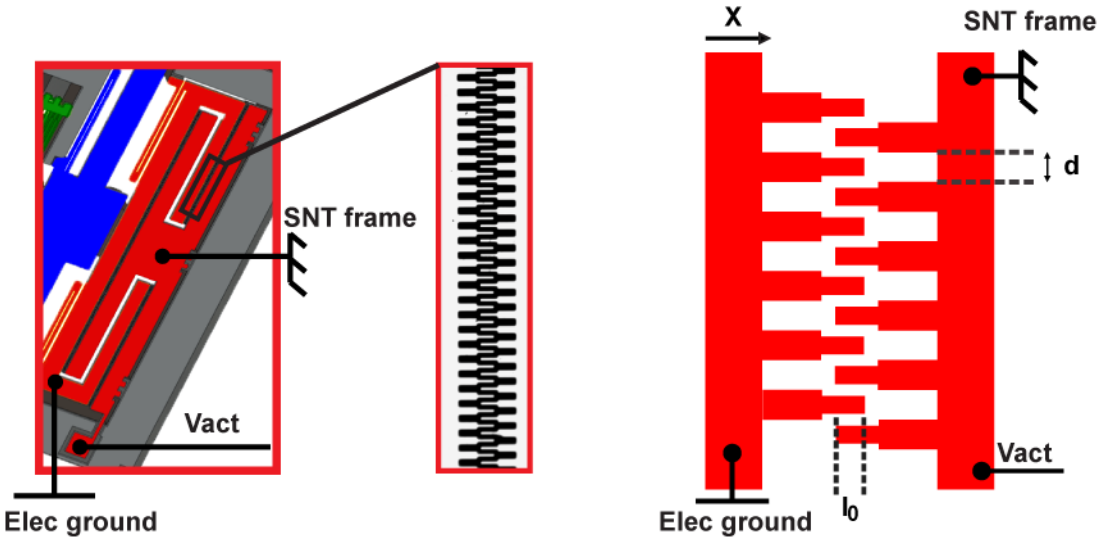

Figure 2.2: Schematic of the comb drive actuators

Equation 2.1

$$F_x = \frac{\partial W_{es}}{\partial x} = \frac{\partial E_C}{\partial x} = \frac{1}{2}\frac{\partial C V^2}{\partial x} = \frac{1}{2}V^2\frac{\partial C}{\partial x} = \frac{1}{2}V^2\frac{\partial}{\partial x}\left(\varepsilon_0\varepsilon_r\frac{N(l_0+\Delta x)t}{d}\right)$$

with ε_0 the vacuum permittivity, ε_r the relative permittivity of Silicon, and V the potential difference between the electrodes (i.e. the actuation voltage V_{act}). N is the number of fingers on both sides of electrodes, l_0 the overlapping length of the fingers for V=0; t the thickness of the fingers; d the gap between the opposite fingers. Finally, the electrostatic force equation in comb actuators is expressed by Equation 2.2:

Equation 2.2

$$F_x = \varepsilon_0\frac{Nt}{2d}V^2 = \alpha_1 V^2$$

The force depends on the square of the actuation voltage *V*. However, this force acting in the x-direction or along the length *l* of the fingers is independent of ($l_0 + \Delta x$), that is to say that the force is independent on the displacement.

2.2.1.2 The capacitive sensor

The tip displacement of the SNT is measured by a differential capacitance sensor which is suitable for bulk micromachining and compact integration [128]. The sensor is designed with a tri-plate configuration and transverse combs [129].

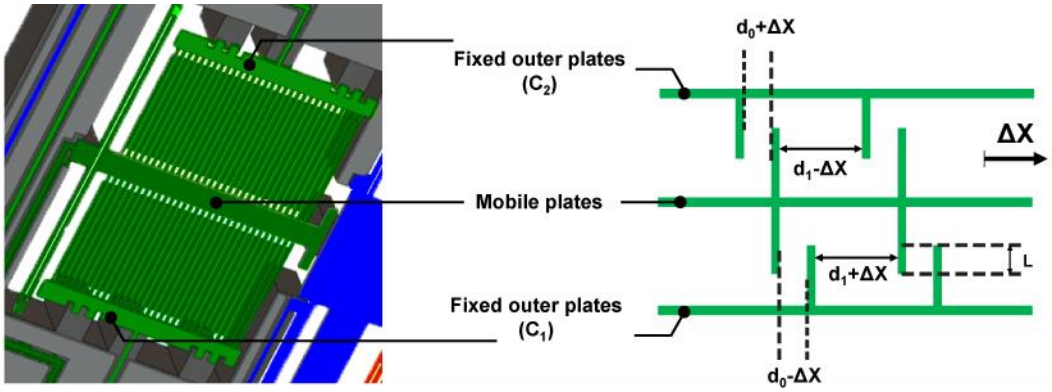

Figure 2.3: Close-up of the differential capacitive sensor. The right schematic illustrates displacement sensing through C1 and C2 capacitance variations. [9]

A central electrode is mechanically connected to the mobile tip and moves in between two fixed electrodes creating two differential capacitances C_1 and C_2 whose difference, ΔC,

Equation 2.3

$$\Delta C = C_1 - C_2$$

is related to the displacement, Δx (see also Figure 2.3), as:

Equation 2.4

$$\Delta C = \varepsilon_0 N_b L t \left[\left(\frac{1}{d_0 - \Delta x} + \frac{1}{d_1 + \Delta x}\right) - \left(\frac{1}{d_0 + \Delta x} + \frac{1}{d_1 - \Delta x}\right)\right]$$

Again, ε_0 is the vacuum permittivity; N_b the number of capacitance electrodes in opposition; t the device thickness; L the electrode length; d_0 and d_1 the initial distances between repeating

combs. For small displacements such as $\Delta x \ll d_0 < d_1$, a first order approximation of the Equation 3.5 gives a linear relationship between ΔC and Δx :

Equation 2.5

$$\Delta C \approx 2\varepsilon_0 N_b L t \left(\frac{1}{{d_0}^2} - \frac{1}{{d_1}^2}\right) \Delta x = \alpha_{CS} \Delta x$$

In theory, C_1 and C_2 are equal so that the differential sensing is zero when there is no actuation. Additionally, according to Equation 2.5 the relation between the motion and the differential capacitance is linear. The capacitances are measured through the measurement of the current flowing through C_1 and C_2.

2.2.1.3 The mechanical structure

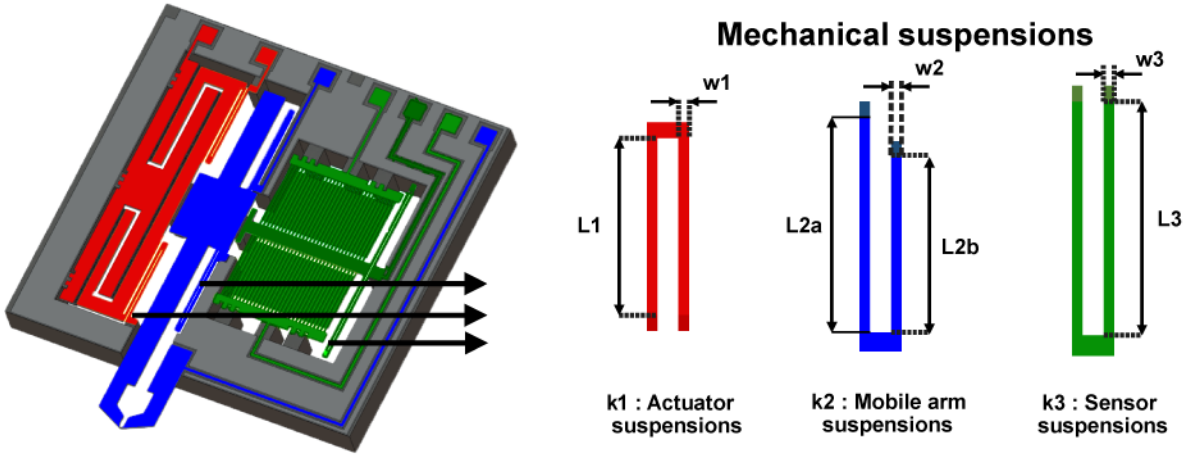

Figure 2.4: Schematic of the mechanical structure of the SNT. Design of the three sets of suspensions, k1 for the actuators polarization, k2 for the mobile arm, and k3 for the central sensor plate.

The mobile part of the SNT is linked to the Silicon frame by flexible suspensions (Figure 2.4)[130]. Commonly integrated in mechanical microsystems [124], [125], folded suspension springs are designed to minimize suspension areas, which decrease their mechanical stiffness and enhance displacement ranges [126]. In the SNT design of Figure 2.4, three sets of folded suspensions support the mobile part of the system (the comb-drive actuators, the mobile tip, and the capacitive sensor) and provide the electrical connections for the actuation and the sensor

readings. The springs are arranged symmetrically along the actuation and sensing axis to minimize any rotation, and their sum gives the total stiffness k_T of the device.

To sense the mechanical characteristics of trapped molecules on the tweezers response a highly compliant system is required. On the other hand, a minimum stiffness is mandatory to endure the fabrication processes and manipulations, supporting the mobile system weight, and preventing sticking due to attractive surface forces between the comb-drive actuators and the capacitive sensor electrodes.

2.2.1.4 The sharp tips

In the case of DNA characterization, the design of the tips of the SNT incorporate highly sharpened points, to focus the electrical field during DEP, and to precisely localize the DNA attachment.

This structure can be obtained by a process combining an anisotropic wet etching in silicon (KOH or TMAH etching) and local oxidation of silicon techniques as sketched in Figure 2.5 and reported in [131]. The complete fabrication process is detailed in chapter 2.2.3. Finally, a thin aluminum film is evaporated on the front side of the SNT. The addition of the aluminum film allows both the creation of electrical connections and the optimization of the attachment of DNA to the tips of the SNT (cf. Chapter 4.2 for DNA trapping protocol).

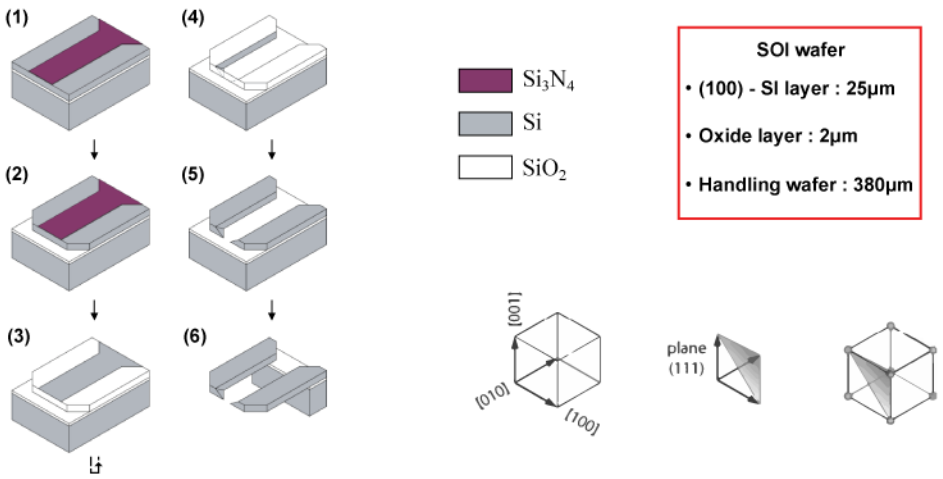

Figure 2.5: Fabrication process of the sharp Silicon Nano Tweezers using Silicon-On-Insulator technology. The crystallographic orientation is indicated with Miller indices.[9]

2.2.2 The Double-Actuators SNT

The Double-Actuators Silicon Nano Tweezers (D-A SNT) has been developed to overcome an unexpected challenge encountered in the characterization of DNA inside different media. Indeed, the DNA environment has a strong impact on the length of the DNA molecule. Therefore, by trapping a DNA bundle inside a certain medium, its length changes in other media. The D-A SNT allows controlling the gap between the two sharp tips of the SNT, which allows stretching the trapped DNA bundle as the right-hand part of the SNT measures its mechanical properties at the same time.

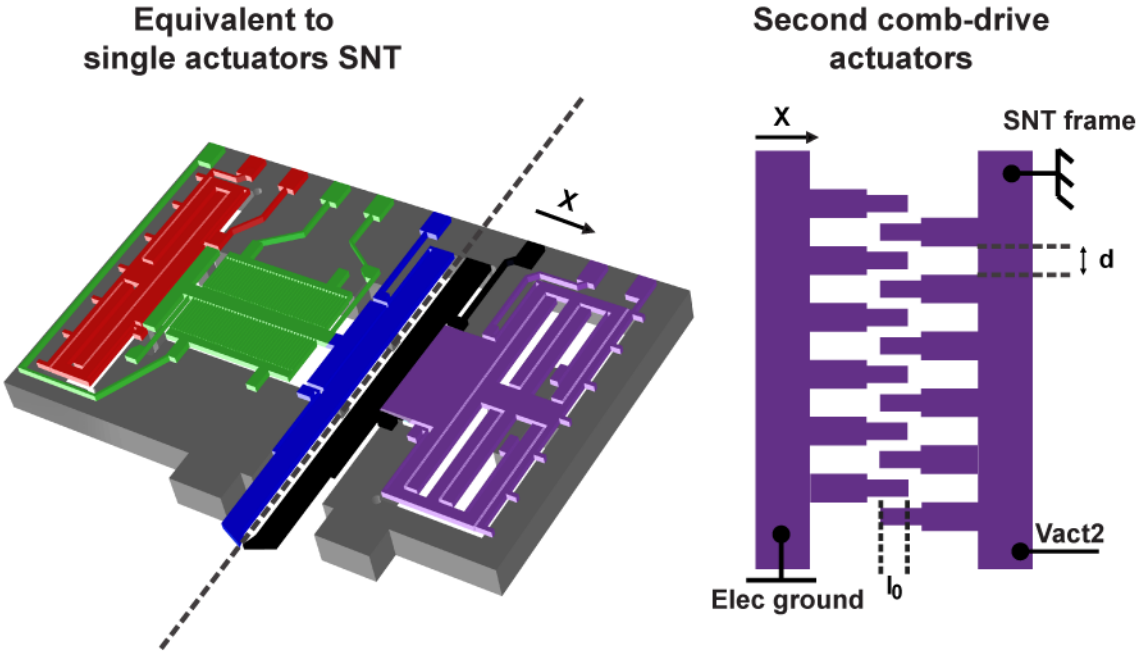

Figure 2.6: Schematic of the double actuators SNT

The Double-Actuators Silicon Nano Tweezers (Figure 2.6) is evidently based on the same design of the Single-Actuators SNT (S-A SNT). The initial mobile arm (blue) has the same structure in the D-A SNT and the S-A SNT. This arm is moved by comb drive actuators (red) and its displacement is recorded by a capacitive sensor (green). The second arm (black) is fixed on S-A SNT and become mobile in the D-A SNT generation. The same technology (comb drive actuators) is used to move both arms. Nevertheless, the second comb driver actuators (purple) is designed with a larger actuating surface, to generate a higher force on the second arm and allow a larger displacement. The force is still proportional to the number of fingers and inversely proportional to the gap (d) between fingers (see Equation 2.2). In the case of the S-A

SNT, a compromise is found for the gap width, in order to obtain sufficient force and minimize the risk of sticking during the fabrication process, transport of the device, and experiments. The only way to increase the force in the D-A SNT is therefore to increase the number N_2 of fingers. Moreover, the D-A SNT has been designed to have a maximum stroke in the 10 µm range. Therefore, a free space between each line of fingers is reserved for displacement. The mechanical suspension design is calculated to allow large displacement (10µm) under a maximal tension of 100V. Nevertheless, the global stiffness of the actuating arm of the D-A SNT (k_{T2}) should be large enough to minimize the coupling effect (described Chapter 2.3.2.2) between the right and the actuating arm when a molecule is trapped between them. The second arm is always used in static mode ($\sum F = 0$) and the displacement law is given by the following equation:

Equation 2.6

$$k_{T2}\Delta x_2 = \alpha_2 {V_{act2}}^2$$

Δx_2 is the displacement of the second arm, V_{act2} the voltage between the two electrodes of the second comb-drive actuators and α_2 a constant which depend on the design of the comb-drive actuators. So the displacement of the second arm is linear with ${V_{act2}}^2$.

2.2.3 Overview of the fabrication process

2.2.3.1 Introduction

The fabrication process of Single and Double-Actuators SNTs is almost identic. The only part of the process that changes is the masks. This is one advantage of microtechnologies.

The addition of gaps to the design allows for the displacement of movable structures of an SNT (comb drives, capacitive sensor) along with the width/height ratio of suspended structures, which define the spring stiffness. For SNT performance, precise fabrication of the device with given dimensions is therefore critical. Moreover, for better integration in clinical application without compromising the MEMS performance, SNTs immersion in liquid needs to be able to be minimized. Consequently, sharp and protruding tips are essential.

MEMS is fabricated (Figure 2.7) from (100) oriented SOI wafer (Ultrasil) either type Nor P, having resistivity between 0.01 and 10 Ω.cm. SOI layer thicknesses are 30 µm, 2 µm and 400 µm for the top silicon layer, the buried oxide (BOX) and the handle wafer respectively.

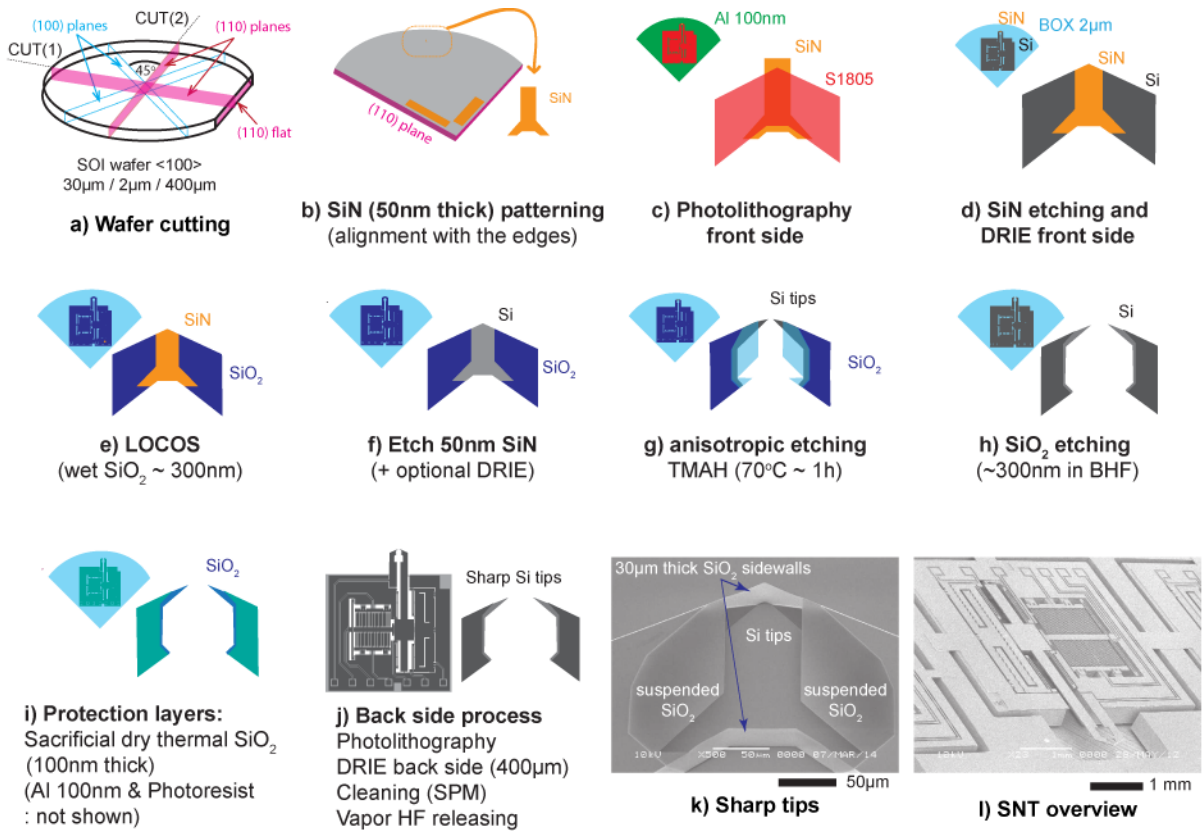

Figure 2.7: Overview of the microfabrication process of sharp tip SNT [132]

The first step of the SNT microfabrication is cutting the SOI wafer along the (110) planes. Then, the fabrication is divided in two parts, the front-side, and the back-side process [133].

2.2.3.2 Front side process

1. Nitride deposition: After standard SPM cleaning (H_2S0_4: H_20_2 mixture), a 50 nm-thick silicon nitride layer is deposited by Low Pressure Chemical Vapor Deposition (LPCVD) at 800°C silane and ammonia gas reaction.
2. Defining crystallographic alignment structures: As sharp tips are formed through the wet etching of silicon, the nitride patterns are aligned along the (110) planes and in order to have a symmetric the alignment of these planes with the (100) plane is extremely important. The crystallographic alignment can be achieved by the cutting/dicing of the silicon wafer or performing dummy TMAH (tetramethylammonium hydroxide) etching to reveal the planes.
3. Photolithography (mask #1) to pattern nitride layer for LOCOS: After a photoresist (Shipley S1805) is patterned, the nitride is etched by Inductively Coupled Plasma Reactive Ion Etching (ICP-RIE) by mixing SF6 with C4Fs (5:1) in a chamber with a pressure of 5 mTorr. Directional etching is obtained by setting RF platen and coil powers at 50W and 600W respectively. Later, the residual polymers are removed by oxygen plasma ashing.

4. Photolithography (mask #2) to achieve sensors and actuators: Al thin film (100 nm deposition by evaporation) is used as a mask for Deep Reactive Ion Etching (DRIE). After patterning a photoresist (Shipley S1805), the Al layer is wet-etched using a commercial Al etchant.
5. DRIE front side: Overhanging nitride film surrounding the Al patterns on the tip area is removed by ICP-RIE, followed by plasma oxygen before the DRIE process. The deep RIE process consists of repeating sequences of isotropic etching of silicon (SF6/02 gas) followed by a passivation step based on a Tef1on-like coating on the sidewalls (C_4F_8 gas). Finally, plasma oxygen removes the passivation layers. Increasing the pressure to 20 mTorr performs multi-directional ashing. After cleaning, the sacrificial mask is removed by immersion in the commercial aluminum etchant. Finally, a LOCOS (LOCal Oxidation of Silicon) process of 350 nm is performed by wet oxidation (H_2O/O_2) at 1100°C for 90 min.
6. Sharp tips fabrication and gap control: The 50 nm-thick nitride on the tip area is etched by ICP-RIE similarly to step (f). The initial nitride width and the top silicon layer thickness define the dimension of the final gap. Interestingly, the gap can be controlled by the over-etching depth of the top Silicon layer, using the same mask. The gap adjustment can be performed before or after the TMAH wet etching [132]). The anisotropic etching is performed in TMAH (15%, at 70°C for ~60 min depending on the remaining silicon top layer thickness). The thick oxide sidewalls (from LOCOS) act as an etch barrier. Later, the remaining sacrificial oxide is removed in buffered HF. Before working on the backside of the wafer, the top silicon structures are protected by: (1) conformal thermal oxidation (at 1050°C for 30 min resulting in sharpening the tips during the final step), (2) evaporating a thin Al film (100 nm) and (3) spin coating 2 µm thick photoresist baked on a hot plate (at 130°C for 30 min). Silicon Nano Tweezers for molecules and cells manipulation and characterization

2.2.3.3 Back side process

7. Photolithography (mask #3) **and backside** DRIE: A 100 nm-thick Al film is evaporated on the backside before photolithography. After patterning and wet Al etching, the bulk silicon (400 µm thick) is etched by DRIE. Remaining aluminum is removed by wet etching (40°C) and a final SPM cleaning is performed (110°C, 10 min).
8. Releasing in vapored HF: The vapored HF process is performed to remove the buried and sacrificial oxides. The isotropic vapored HF process generates 1-2 µm under etching preventing short-circuits in cases requiring Al coating on the front side to perform electrical manipulation/measurements.

2.2.3.4 Electrical connection and packaging

After the micro-fabrication process, SNT are released from the wafer through manual manipulation under a microscope. Then SNT are mounted and wire bonded on the Printed Circuit Board (PCB) (Figure 2.8.b). SNT are glued on the PCB with epoxy glue to create a rigid mechanical contact. And the wire bonding bridges the micro electrical connectors of the SNT and the macro connectors of the PCB. SNT are finally packaged in clean and safe boxes ((Figure 2.8.d) before characterizations and experiments.

PCBs are designed to provide the appropriate connections to the fixed stage (Figure 2.8.c). During experiment, the PCB is placed on a fixed stage that includes a specially designed spring pin-connection system and necessary connections to electronic equipment. Screwing the PCB on the fixed stage is enough to complete the electrical connections (< 1 min).

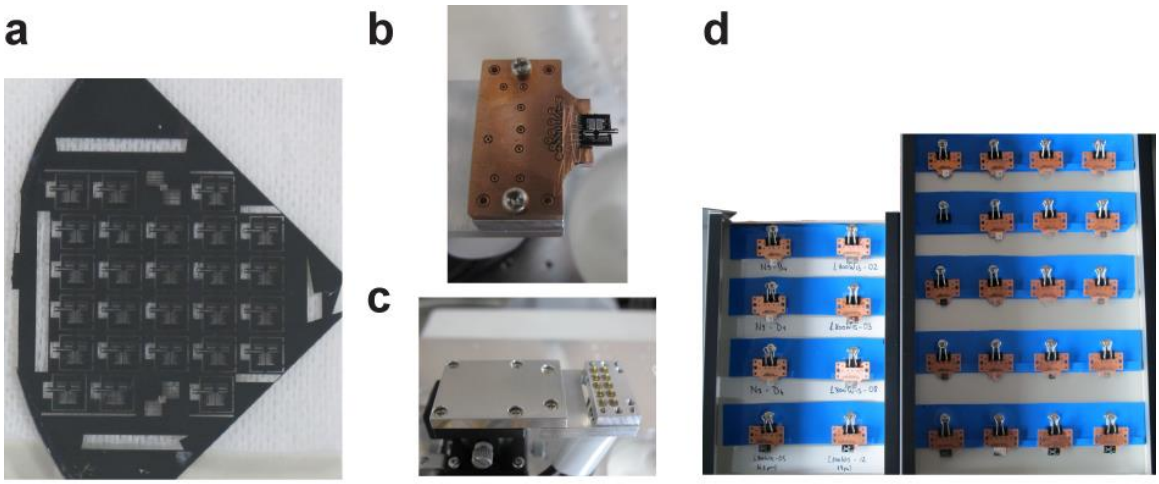

Figure 2.8: a. Quarter of wafer after SNT fabrication. **b.** SNT released from the wafer, mounted, and wire bonded on PCB. **c.** 2 boxes of SNT prepared for travelling from Japan to France for in-hospital experimentations.

2.3 SNT measurements

The experimental setup in its environment (the Oscar Lambret radiotherapy center in Lille) with all the required equipment and instruments is illustrated in Figure **3.34**, next Chapter 3.

The actuation of the tip is relatively straightforward. A voltage is required to generate a force. However, a high current is possible when a contact occurs and may cause the destruction of the device. So protection resistance is used to avoid similarly destructive situation.

Measurements of the differential capacitance ΔC are used to produce sensor readings of the motion (Equation 2.3). Hereafter, an instrumentation chain is introduced to perform dynamic measurements. This strategy creates alternate currents through the capacitances C_1 and C_2 of the capacitive sensor. The key point is to measure very small currents, around a picoampere, with low-noise capability provided by a lock-in amplifier.

By applying a constant voltage (3V) on C_0, dynamic currents (i_1 and i_2) are generated by the capacitance variation (Equation 2.7 and Equation 2.8). The resulting currents flowing through the capacitances C_1 and C_2 are converted into voltages V_1 and V_2, respectively, by two low-noise current-to-voltage (A/V) preamplifiers from Signal Recovery (model 5182, http://www.signalrecovery.com). The preamplifier's low-input impedance (virtual ground) ensures an accurate current conversion. Lastly, a lock-in amplifier from Signal Recovery (SR 7230, http://www.nfcorp.co.jp) allows an accurate measurement to perform the magnitude-phase detection of the differential inputs ($V_1 - V_2$) at the reference frequency.

2.3.1 Single-Actuators Silicon Nano Tweezers (S-A SNT)

2.3.1.1 Dynamic Measurement Principle

During the dynamic mode, the cenAtral electrode C_0 of the sensor moves with the SNT tip while a constant voltage V_0 is applied at C_0 and creates dynamic currents i1 and i2 related to motion dynamics. The sensor readings of the capacitive currents is related to the motion:

Equation 2.7

$$i_1 - i_2 = \frac{dQ_1}{dt} - \frac{dQ_2}{dt} = \frac{d(C_1V_0)}{dt} - \frac{d(C_2V_0)}{dt}$$

Equation 2.8

$$i_1 - i_2 = V_0 \frac{d\Delta C(t)}{dt} = V_0 \times \alpha_{CS} \frac{d\Delta x(t)}{dt}$$

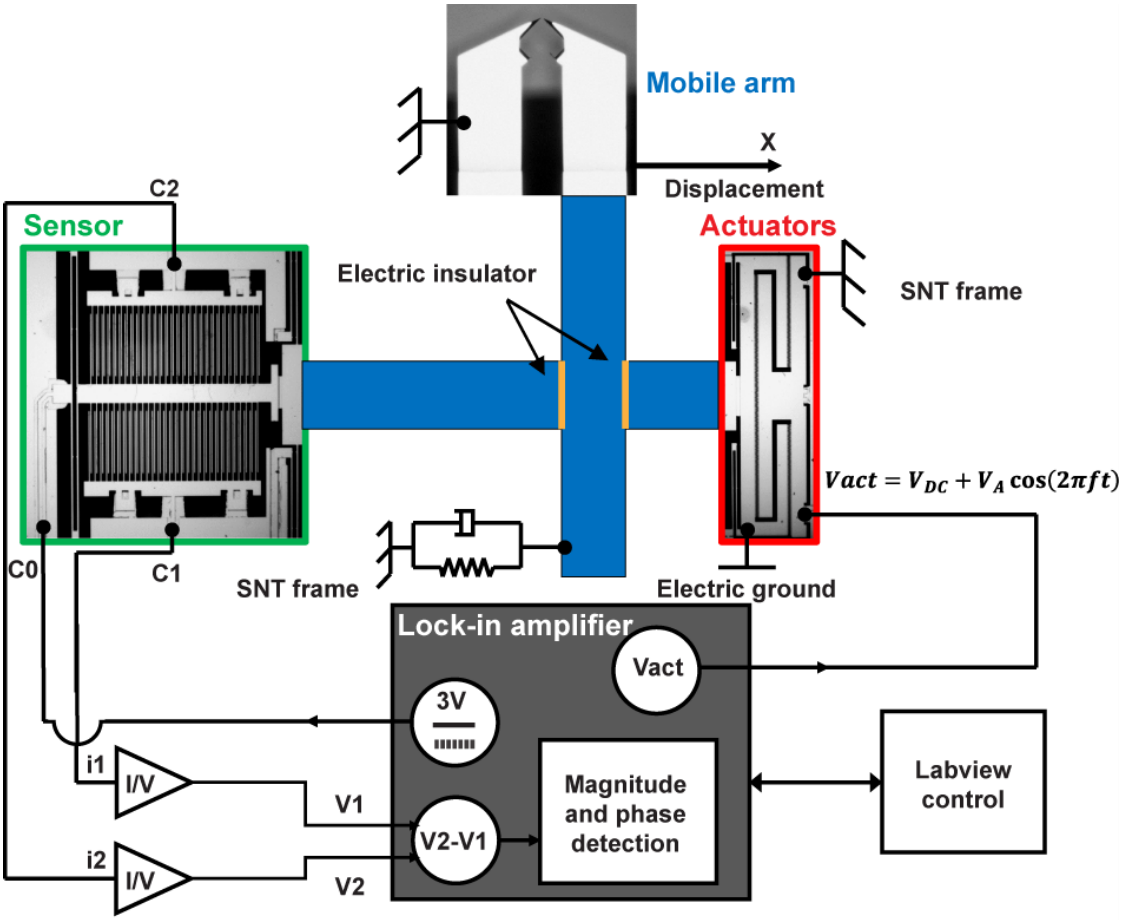

Figure 2.9: Schematic of the dynamic measurement with Single-Actuators SNT

Q_1 and Q_2 are respectively the charges of the capacitances C_1 and C_2, and $\Delta x(t)$ the displacement of the tip. Consequently, within the limits of sensor approximations, the output current is related to the tip displacement velocity.

2.3.1.2 The frequency response

2.3.1.2.1 Bare Silicon Nano Tweezers

The harmonic analysis of the SNT is performed with the measurement configuration in Figure 2.9. The actuation signal, V_{act}, is directly provided by the internal oscillator of the lock-in amplifier. A DC voltage, V_0 = 3 V, is supplied to the central plate of the capacitive sensor. Because the displacement has a quadratic dependence with the actuation voltage caused by the generated force, the amplitude and phase of the SNT oscillations are measured using the second harmonic mode detection (i.e. at the frequency 2*f*):

Equation 2.9

$$F_x = \alpha_{CD} \times {V_{act}}^2 = \alpha_{CD} \times \left(V\sqrt{2}\sin(2\pi ft)\right)^2$$

Equation 2.10

$$F_x = \alpha_{CD} \times V^2 \times (1 - \cos(2\pi(2f)t))$$

A constant force is generated related to $\alpha_{CD} \times {V_{act}}^2$, but sensor readings are not produced since they do not generate AC currents. The harmonic force at $2f$ produces a sensor reading and the sensor output is a function of $\alpha_{CD} \times {V_{act}}^2$as well. This technique eliminates the fundamental mode of the direct coupling capacitive current between the actuators and the sensor electrodes, thus enabling better characterization of the mechanical motion.

_

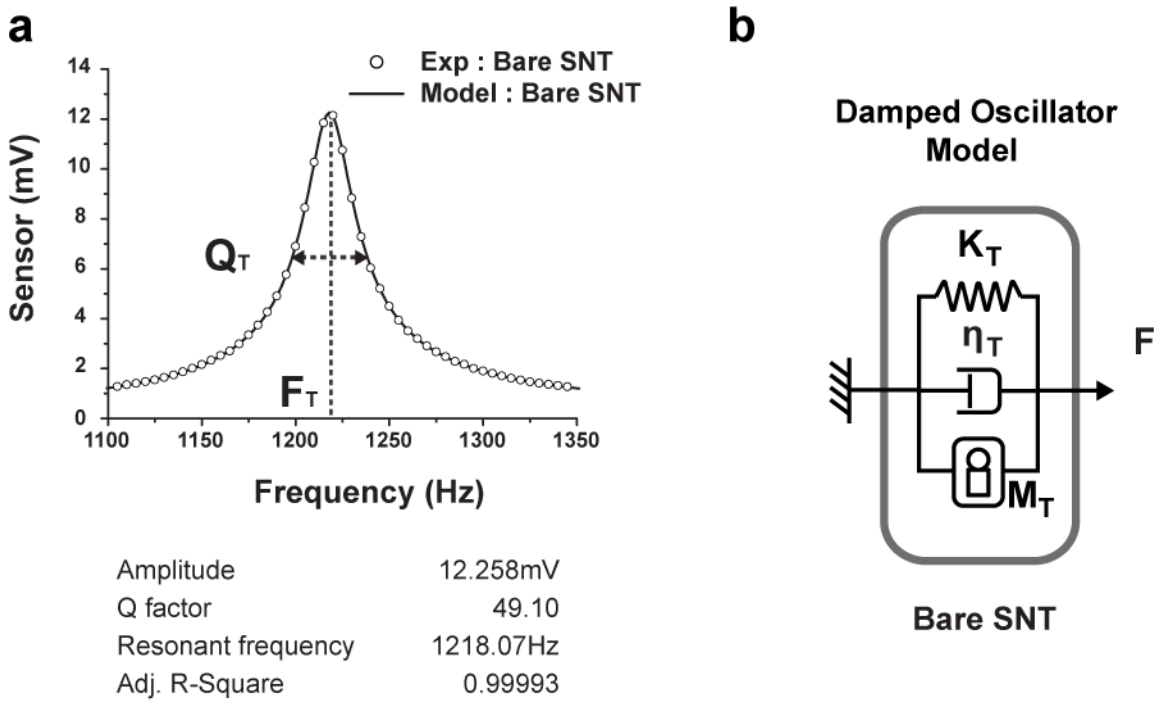

Figure 2.10: a. Frequency response of the bare Silicon Nano Tweezers **b.** Damped oscillator model of the bare SNT

Figure 2.10 shows the frequency response of the device and outlines the mechanical resonance at 1218 Hz. This main resonance is fitted by a 2nd-order differential equation, stemming from a damped oscillator model system:

Equation 2.11

$$M_T \frac{d^2x}{dt^2} + \eta_T \frac{dx}{dt} + k_T x = F_x = \alpha_{CD} \times {V_{act}}^2$$

where M_T is the mass of the mobile part, k_T the mechanical stiffness, η_T the viscous losses related parameter, $F_x = \alpha_{CD} \times {V_{act}}^2$ the electrostatic force.

Firstly, an approximate identification is performed by a reverse calculation of the resonance frequency of the bare SNT (F_T) and its quality factor (Q_T) equations (Equation 2.12 and Equation 2.13):

Equation 2.12

$$F_T = \frac{1}{2\pi}\sqrt{\frac{k_T}{M} - \frac{1}{2}\frac{v^2}{M^2}}$$

Equation 2.13

$$Q = \frac{\sqrt{k_T M}}{v}$$

Then, the frequency response curve is accurately fitted with the least mean square algorithm.

Equation 2.11 is transformed into a transfer function to allow a magnitude/phase plot of the velocity $\frac{\partial x}{\partial t}$ with measurement data:

Equation 2.14

$$T(j\omega) = \frac{1}{k_T}\frac{j\omega}{1 + \frac{M}{k_T}(j\omega) + \frac{M}{k_T}(j\omega)^2}$$

and finally the following equations give amplitude (A) and phase (φ):

Equation 2.15

$$A = G \times V_{C0} \times \alpha_{CS} \times |T(j\omega)| \times \alpha_{CD} \times V^2$$

Equation 2.16

$$\varphi = angle(T(j\omega))$$

where G is the amplification gain of the A/V preamplifiers. The preamplifiers are intended to be used with a bandwidth such that the gain is constant in the experiment

frequency range with no phase shift. Figure 2.10 demonstrates a high accuracy within the identified model according to the behavior of the SNT.

2.3.1.2.2 Silicon Nano Tweezers + DNA bundle

When a DNA bundle bridges between the 2 tips, the SNT resonance experiences a change due to the added mechanical component brought by the molecules. Figure 2.11 demonstrates the changes of the frequency response caused by the DNA bundle properties. In black, the bare SNT resonates at 1218.07 Hz. After DNA trapping by DEP, the resonance frequency of the systems increased to 1229.86 Hz. In accordance, the quality factor is about 49 for the bare SNT and 37 for measurements with DNA.

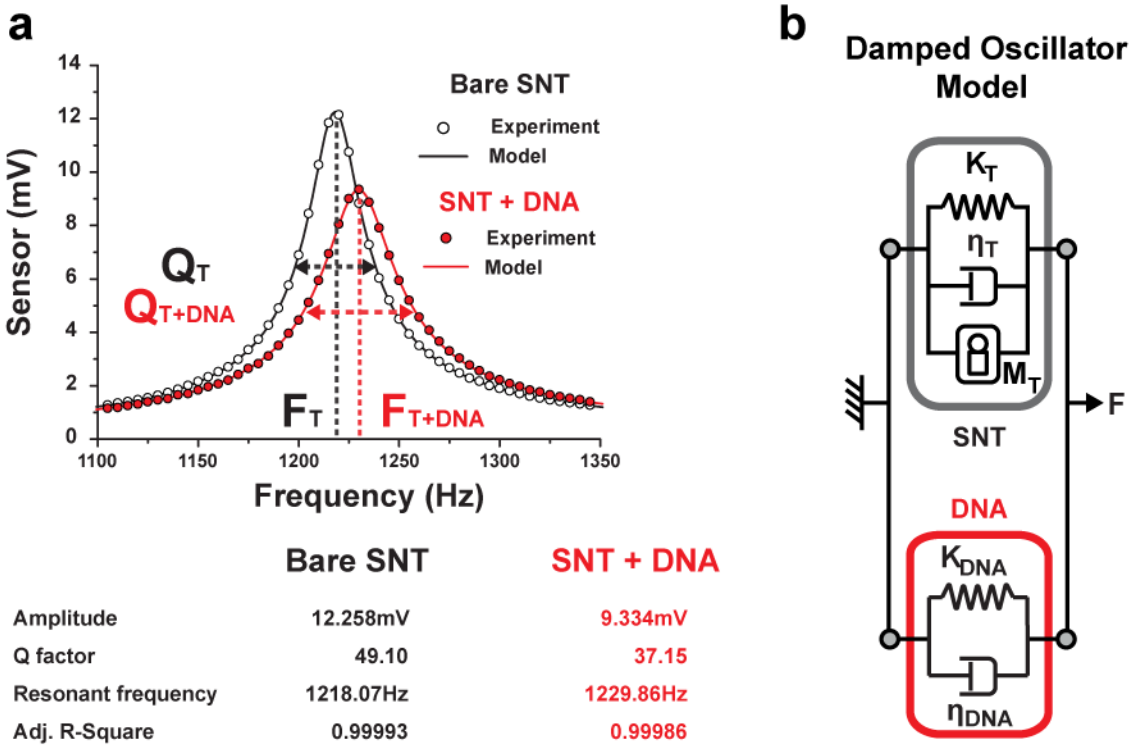

	Bare SNT	SNT + DNA
Amplitude	12.258mV	9.334mV
Q factor	49.10	37.15
Resonant frequency	1218.07Hz	1229.86Hz
Adj. R-Square	0.99993	0.99986

Figure 2.11: a. Comparison of the frequency response of the bare SNT and SNT after DNA trapping **b.** Damped oscillator model of the SNT after DNA trapping

2.3.1.3 Real-time measurement

The design of SNT is devoted to the sensor readings of the mechanical properties of molecules. The following paragraph details the principle of measurement.

The dynamic model of the device allows measurement of the mechanical properties of a trapped object by monitoring the changes in the frequency response and in amplitude. Basically, SNT are characterized as a mechanical mass-spring system integrating transducers for actuation and sensor readings. Figure 2.11 sums up the features of the model of the Silicon Nano Tweezers. Changes in the resonance frequency (F_{T+DNA}) and quality factor (Q_{T+DNA}) of the SNT are detected by performing dynamic measurements after DNA trapping, which is the consequences of the changes in mechanical properties of the trapped object:

Equation 2.17

$$F_{T+DNA}(t) = \frac{1}{2\pi}\sqrt{\frac{k_T + k_{DNA}(t)}{M_T}}$$

Equation 2.18

$$Q_{T+DNA}(t) = \frac{1}{2\pi}\frac{\sqrt{M_T(k_T + k_{DNA}(t))}}{\eta_T + \eta_{DNA}}$$

The equations of F_{T+DNA} and Q_{T+DNA} (Equation 2.17 and Equation 2.18) are simply updated from the bare SNT model by adding the DNA stiffness and viscosity, which are considered in parallel to the mechanical suspension of the SNT, as illustrated in Figure 2.11.b.

The mechanical properties of the DNA bundle (stiffness and viscosity) are calculated from the resonance frequency and the quality factor of the overall system, as:

Equation 2.19

$$k_{DNA} = k_T \frac{{F_{T+DNA}}^2 - {F_T}^2}{{F_T}^2}$$

Equation 2.20

$$\eta_{DNA} = \frac{k_T + k_{DNA}}{Q_{T+DNA} \times 2\pi \times F_{T+DNA}}$$

From [75] (and the force-extension plot of the paper), the stiffness of a single λ-DNA molecule (i.e. 48.5 kbp) can be deduced as approximately 30×10^{-6} N/m in solution. Accordingly, an equivalent number of molecules which compose the bundle can be presumed during experiments in solution.

One of the objectives of this work is to achieve real-time monitoring of biological processes with a high temporal resolution. As previously shown, the dynamic characterization of the SNT by the frequency sweep characterizes the resonance amplitude peak and phase.

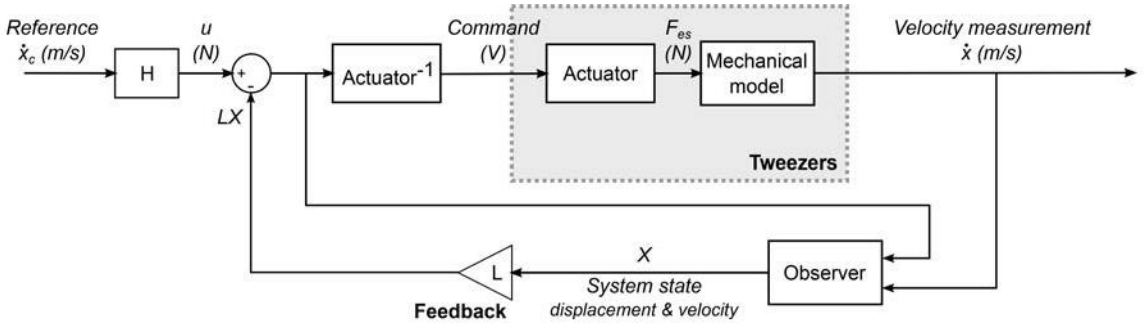

Figure 2.12: Phase-locked loop schematic principle for real-time measurement of the resonance frequency and amplitude of the SNT, with or without trapped DNA[130].

In order to perform fast characterization of the resonance frequency, a Phase-Locked Loop (PLL) algorithm, based on the injective phase function of a 2nd order model, is implemented (Figure 2.12). The PLL produces a signal in the form $Vact=A\times\sin(2\pi F_R t)$ and monitors the system response, adjusting the drive frequency to maintain a phase $\varphi=0^\circ$ for the velocity $\dot{x}$ measurement compared to the drive signal, i.e. at the system resonance. The velocity is transformed into an electrical intensity by the capacitive sensor, which is in turn transformed into a voltage by the trans-impedance amplifier. The lock-in amplifier allows accurate measurement of the magnitude and phase φ of the electrical output signal at the reference frequency, and enables implementing the algorithm through prototyping and development software such as *LabVIEW*.

The graph in Figure 2.13 plots the real-time measurement of the resonance frequency and oscillation amplitude of the SNT. The first two parts of the graph measure the intrinsic mechanical characteristics of the SNT in air and in DI water. The decrease of the resonance frequency (F_R) in solution is due to added liquid mass, while the decrease of the amplitude (A) is due to the viscous damping of the solution. The third portion of the graph measures the

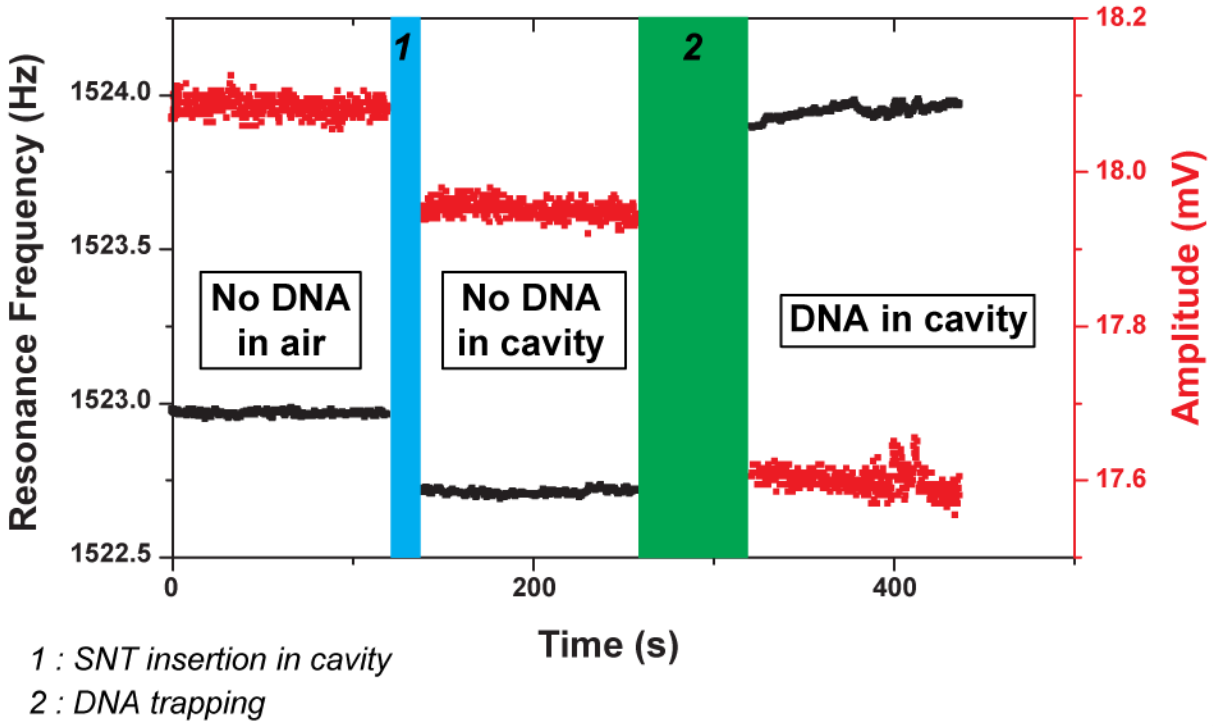

Figure 2.13: Real-time measurement of the resonance frequency and the amplitude of the single actuators Silicon Nano Tweezers. Measurements are conducted by the same SNT, in air without DNA and in cavity filled by DI water before and after DNA trapping.

mechanical characteristics of the SNT after DNA trapping inside DI water. It can be seen that the presence of trapped DNA increases F_R due to extra stiffness and decreases A due to added friction. By knowing the mechanical properties of the SNT, the mechanical properties of the DNA are calculated.

2.3.2 Double-Actuators Silicon Nano Tweezers (D-A SNT)

2.3.2.1 Measurement principle of the D-A SNT

The measurement principle for the bare D-A SNT is exactly the same as that for the bare S-A SNT. The capacitive sensor is positioned on the right side of the SNT to free space for the actuating arm. Nevertheless, there is no significant change in the mechanical properties of sensing arm mobility.

The principal difference between the two SNT designs is generated by the coupling effect between the two arms. In theory, this coupling appears when a mechanical link exists between the sensing and the actuating arms. This link is the force of the meniscus when the tips are immerged inside a microfluidic cavity, or the force of a trapped molecule (DNA). A thorough experimental characterization of the coupling effect is performed in chapter 3.7.

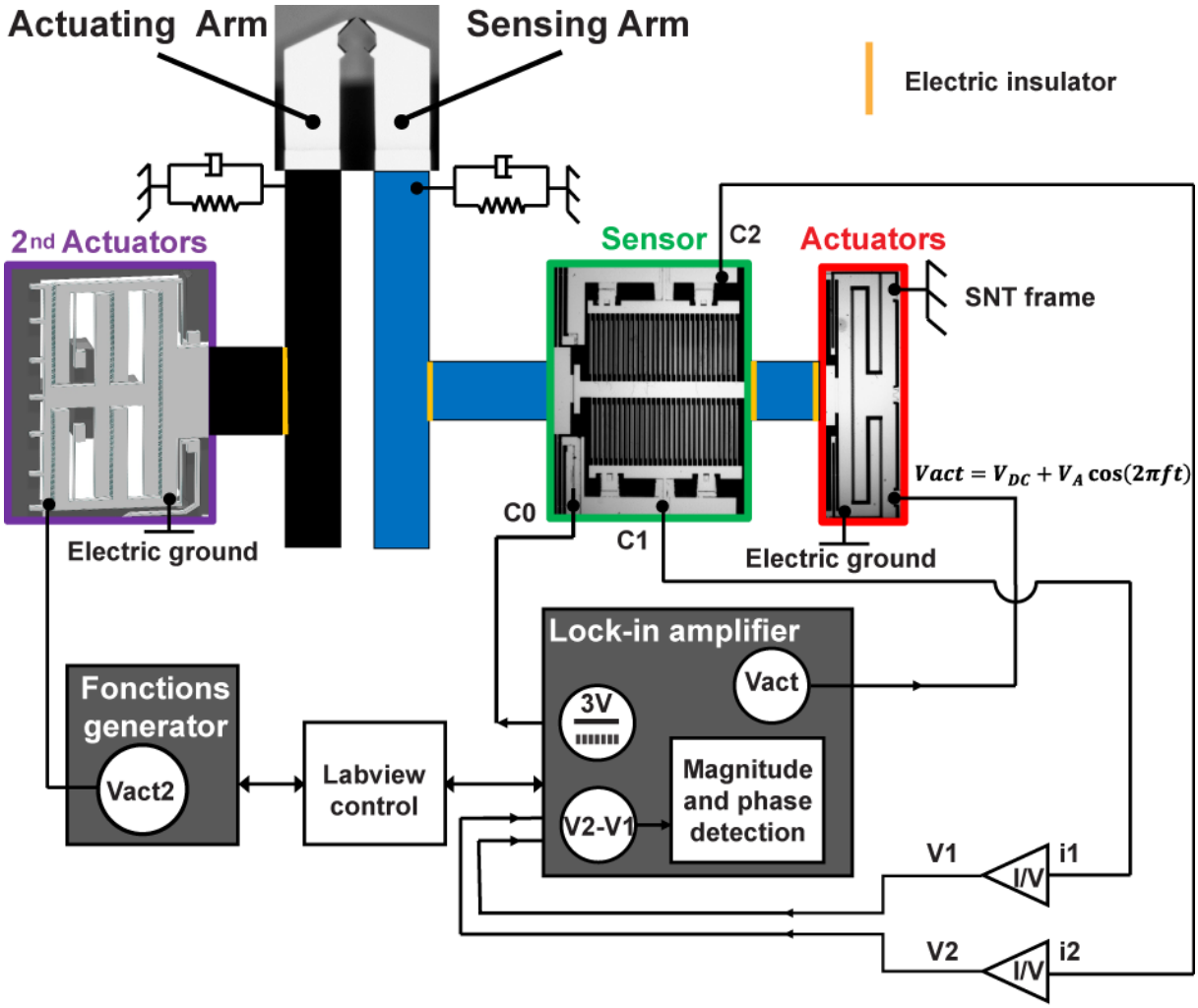

Figure 2.14: Measurement principle schematic of the Double-Actuators SNT

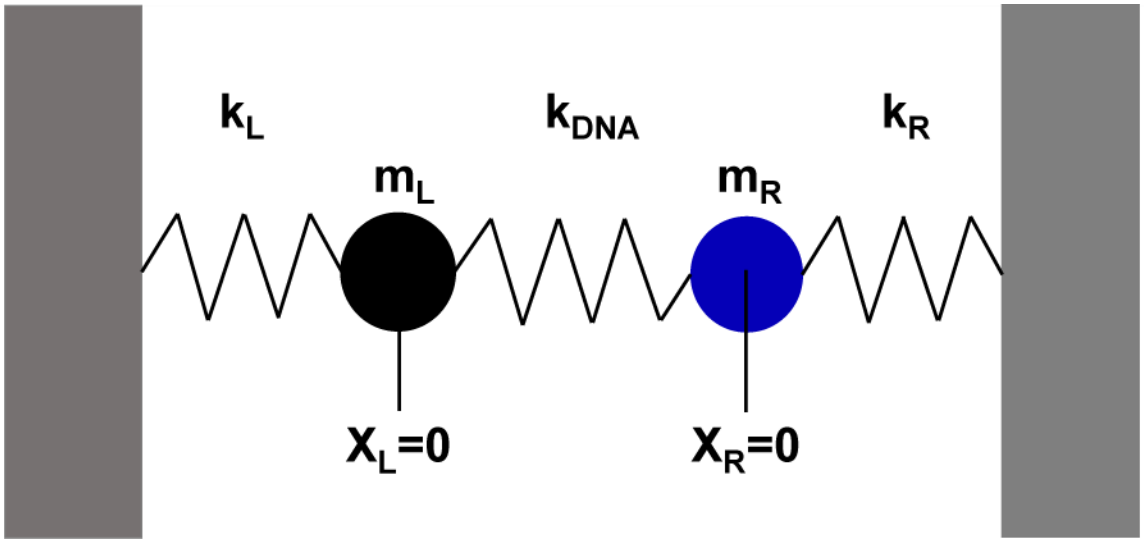

Figure 2.15: Simplified oscillator model of a DNA bundle trapped by Double Actuators Silicon Nano Tweezers

2.3.2.2 Coupled oscillator model

The Double Actuators Silicon Nano Tweezers has been designed to minimize the coupling effect (described below) between the two arms of the D-A SNT. In this paragraph, in order to explain the coupling effect phenomenon, the damped oscillator model is simplified. The model considers mechanical interactions as a pure spring without any viscous losses. The Figure 2.15 illustrates this simplified model.

To simplify the calculation, the system is also simplified by considering $M_L=M_R=M_T$ and $k_R=k_L=k_T$ as a specific symmetrical case which allows straightforward analytical calculation. The positions of the two arms are given by $x_R(t)$ and $x_L(t)$ and the Newton's second law is applied to the two-mass system to obtain two second-order differential equations describing the motion of the masses.

Equation 2.21

$$M_T \frac{d^2 x_L}{dt^2} + k_T x_L - k_{DNA}(x_R - x_L) = 0$$

Equation 2.22

$$M_T \frac{d^2 x_R}{dt^2} + k_T x_R - k_{DNA}(x_L - x_R) = 0$$

By adding and subtracting Equation 2.21 and Equation 2.22, the following equations are deduced with the same form as that of the single spring oscillator model:

Equation 2.23

$$\frac{d^2(x_L + x_R)}{dt^2} + \left(\frac{k_{DNA}}{M_T}\right)(x_L + x_R) = 0$$

Equation 2.24

$$\frac{d^2(x_L - x_R)}{dt^2} + \left(\frac{k_T + 2k_{DNA}}{M_T}\right)(x_L - x_R) = 0$$

The complete system has two resonance frequencies, and x_L and x_R are coupled:

Equation 2.25

$$f_1 = \frac{1}{2\pi}\sqrt{\frac{k_{DNA}}{M_T}}$$

Equation 2.26

$$f_2 = \frac{1}{2\pi}\sqrt{\frac{k_T + 2k_{DNA}}{M_T}}$$

The coupling effect has been demonstrated in a basic case, and becomes more complicated to calculate in non-symmetric and real (adding losses) systems. In order to simplify the calculations of the mechanical properties of the DNA bundle trapped between the tips of a Double-Actuators SNT, the mechanical suspension of the actuating arm is designed to have a global stiffness k_{T2} much higher than the sensing arm. In this case, the actuating arm can be considered fixed in a first approximation of the model. Nevertheless, the results reported in Figure 2.16 show that this model is far from real conditions when the DNA bundle stiffness is too high (in air).

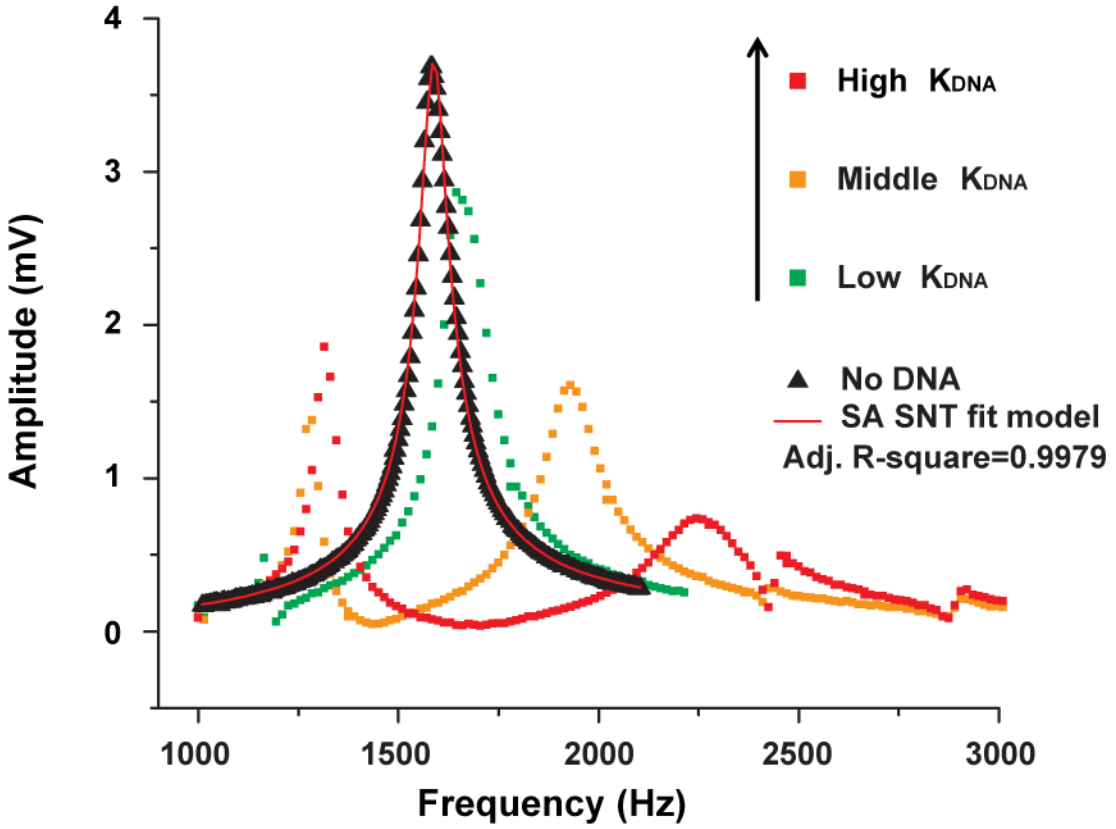

Figure 2.16: Frequency response for 3 different DNA bundles, each with a different stiffness, on the same Double-Actuators Silicon Nano Tweezers (color points). The frequency response of the bare D-A SNT is the red curve fitting the black points.

2.3.2.3 The frequency response

The frequency response of a Double-Actuators SNT is obtained experimentally in Figure 2.16, for three DNA bundles with different stiffness. All curves are obtained with the same D-A SNT in air. The DNA bundle stiffness changes are obtained by placing the same DNA bundle at different humidity levels.

The frequency response of the bare D-A SNT is the curve of reference for the ulterior experiments, and is plotted in black triangles. In this configuration, the D-A SNT and S-A SNT have an identical model for the sensing arm. The black curve shows only one resonance frequency and can be fitted using the same Equation 2.15 of the Single-Actuators SNT model. The green curve shows a resonance frequency with a very similar shape as the black one. Nevertheless, a second peak of resonance at a lower frequency appears due to the coupling effect. The amplitude of this second peak increases as the DNA stiffness increases. For the red points, the amplitude of the lower frequency peak is even higher than the second one (that is the main for the green data). As DNA bundle stiffness increases, the simplified model diverges too much from the real conditions, to be able to extract a quantitative value of DNA bundle

stiffness. This is the reason why the mechanical suspension design is used to minimize the coupling effect. In our case study, the DNA is inserted in liquid, and quantitative experiments are performed with low equivalent bundle stiffness. Therefore, a small resonance frequency shift (under 10Hz) is obtained. For merely qualitative results, however, the system can be used also with several hundred Hz of frequency resonance shift.

2.3.2.4 Real-time measurement

Real-time measurements of the stiffness are performed by the sensing arm of the D-A SNT. As already mentioned, the sensing arms are identical in both SNT types. During real-time measurement by the sensing arm, the actuating arm can be independently displaced by applying a DC voltage V_{act2} on the second comb-drive actuators. Note that, if the two arms of the SNT are not mechanically linked, the motion of the actuating arm has no influence on the real-time measurement, as illustrated in the Figure 2.17.

On the other hand, when a molecular bundle bridges the two arms, the motion of the actuating arm stretches the bundle, and this mechanical change is sensed by the other arm. In the case study, the actuating arm stretches a DNA bundle after its immersion in liquid. The Figure 2.18 shows the ability of D-A SNT to simultaneously stretch a DNA bundle and measure its mechanical property changes.

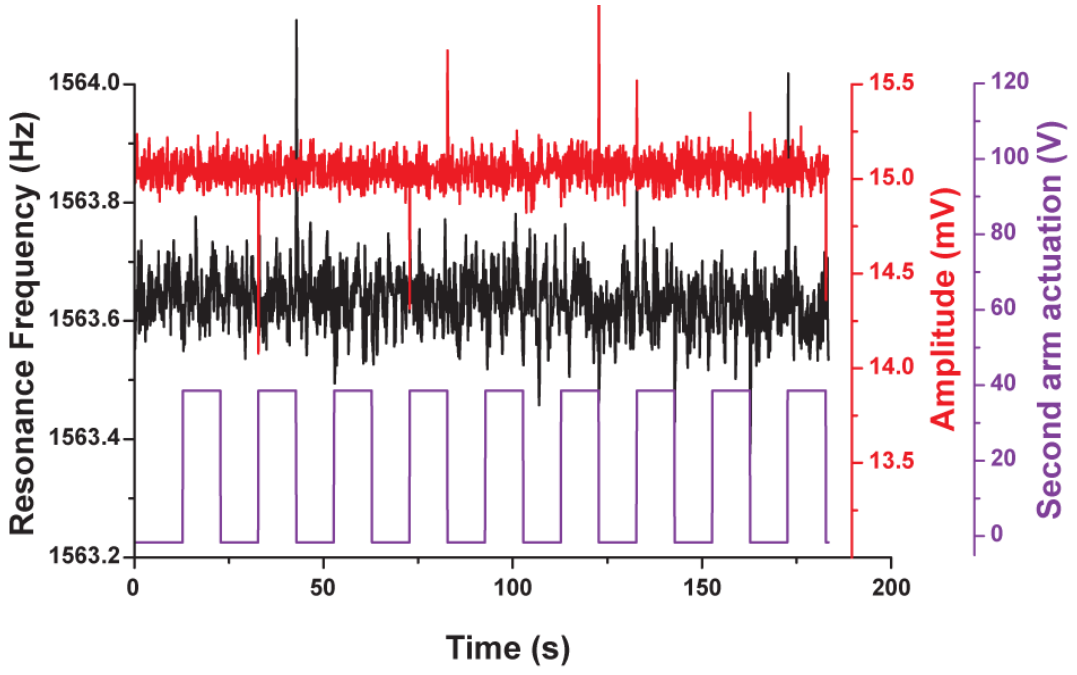

Figure 2.17: Real-time measurement by D-A SNT without any mechanical bridge between sensing and actuating arms. Influence of the actuating arm motion limited to some spikes due to abruptly applied voltage.

The displacement generated by the comb-drive actuators is proportional to $(V_{act2})^2$. Therefore, a square root signal cycle must be applied to the second comb-drive, in order to obtain a linear displacement as a function of time. Different amplitudes of the square root signal were tested. The resonance frequency of the sensing arm follows the displacement of the actuating arm, the higher the displacement, the higher the amplitude. This displacement has but a minor influence on the amplitude of the sensing arm. As a result, it is now possible to calculate the stiffness of a DNA bundle as a function of its elongation.

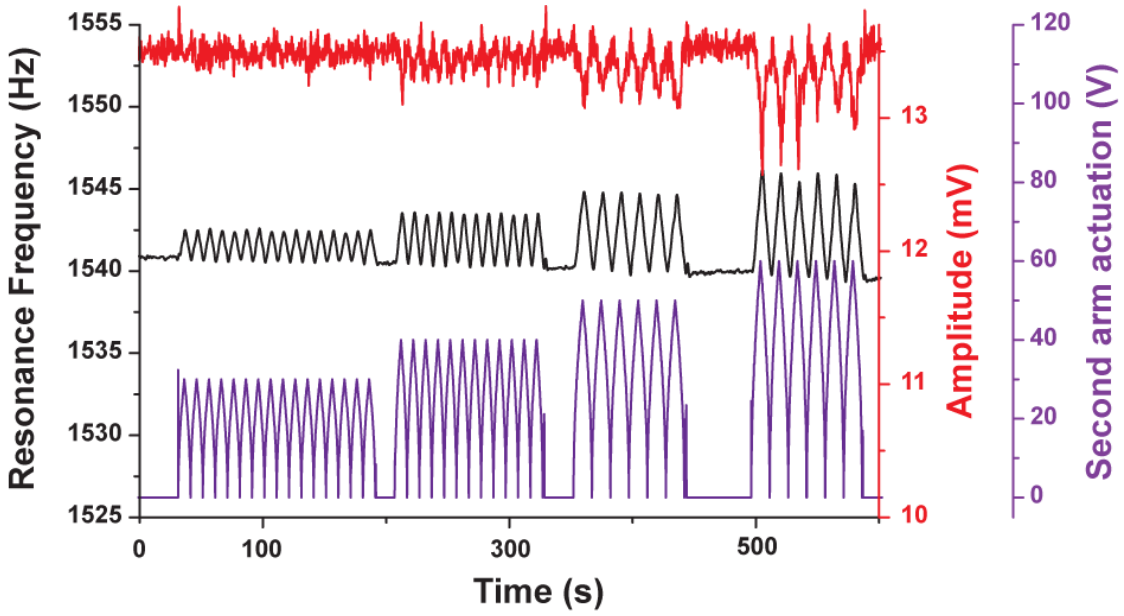

Figure 2.18: Real-time measurement of the amplitude and resonance frequency of a D-A SNT after DNA trapping and immersion in DI water. Influence of the actuating arm motion on the sensing arm.

2.4 Conclusion

Silicon Nano Tweezers allows the real-time measurement of the mechanical properties of a DNA bundle in air and in liquid. By immerging the DNA bundle in different media its length may increase drastically and the S-A SNT may no longer be able to get a sensor reading of it. To solve this geometrical problem, a D-A SNT has been developed and shows itself highly capable of stretching DNA bundles before and during the real-time measurement of its mechanical properties. In this study, the dedicated use of the SNT is inside a hospital environment under ionizing radiation. The following chapter introduces and evaluates the complete setup involved in the SNT.

Chapter 3: Setup

3.1 Introduction

In the early study realized at the *Centre Oscar Lambret* in 2012, a portable **SNT set-up** was prepared to perform real-time biomechanical characterization of a DNA bundles in air under ionizing radiation for the first time. The experimental setup, illustrated in Figure 3.1, integrates the SNT as well as a glass plate attached to a micromanipulator for DNA trapping onto a mobile platform. With this "simple" setup, a proof of concept was demonstrated and paved the way for the more complex experiments in liquid.

During the last three years, the SNT setup has been largely improved, to allow complex DNA mechanical characterization in a microfluidic cavity, with a maximum of control of the environment. This chapter explains in detail the key points of the setup, and the characterization of its capability to measure the DNA mechanical properties in liquid under ionizing radiation in a hospital environment.

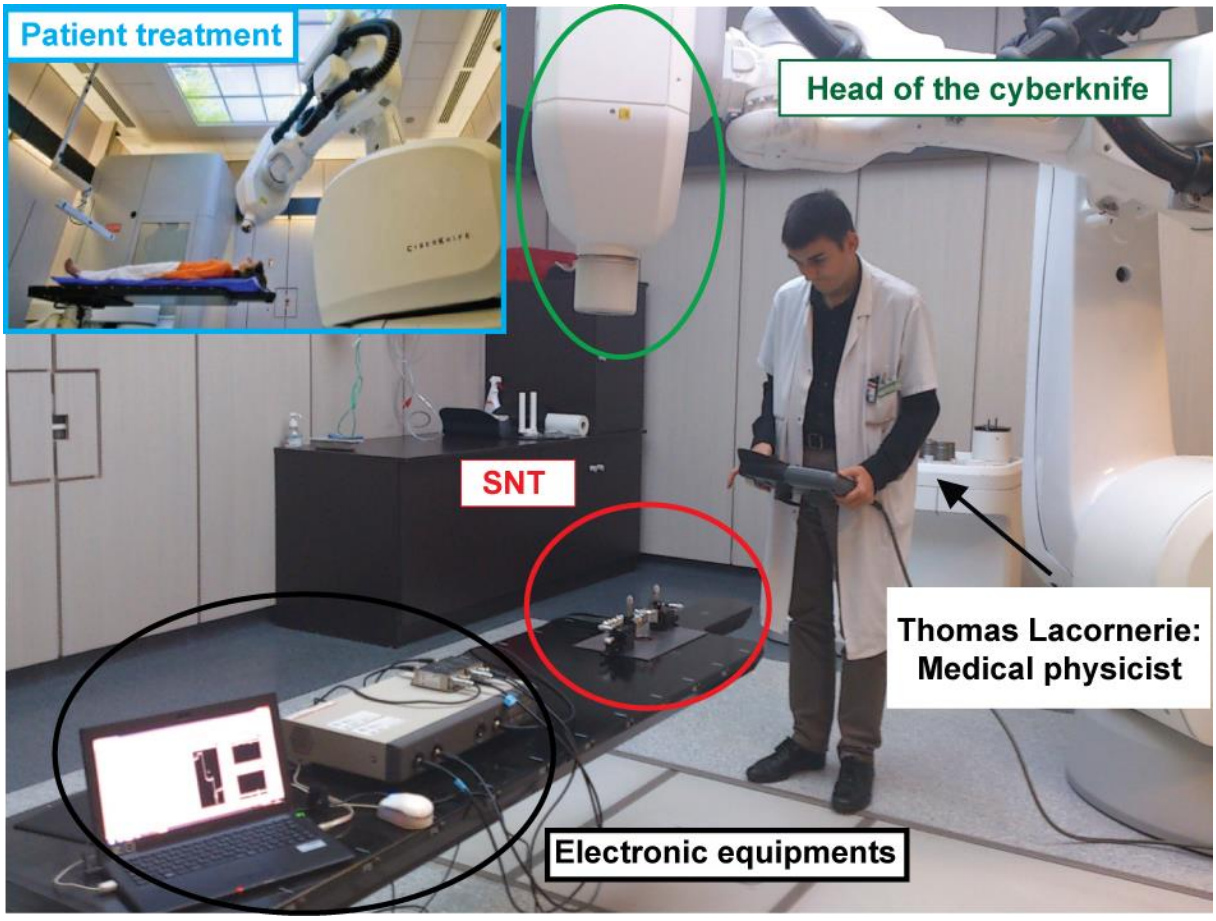

Figure 3.1: First Setup for DNA characterization under Cyberknife (2012)

3.2 The radiotherapy machine

3.2.1 The Cyberknife

The Department of Radiation Therapy at the *Centre Oscar Lambret* allowed the usage of an advanced Cyberknife machine, for this joint research purpose. The Cyberknife, composed of a LINAC attached to a robotic arm, uses circular collimators between 5 and 60 mm (Figure 3.3) and delivers an intense and collimated photon flux at adjustable energy. In our studies we always used 6 MeV energy, that is typical in radiotherapy applications. The advantage of using collimated beams, is to control and monitor the irradiation of the SNT during the experiment. Therefore, the SNT electronic noise can be evaluated during the experimental procedure. To limit the noise, the electronic equipment is put 1m away from the beam. In addition, the 3D-robotized movement of the Cyberknife simplifies the positioning of the setup under the beam.

The Cyberknife radiotherapy system configuration is illustrated in Figure 3.2. The treatment room, which contains the irradiation machine, is surrounded by a wall made of a 1.5 m thick high-density concrete for radioprotection. The operators are installed in the nearby control room, which is shielded from ionizing radiation. Finally, electronic equipment for Cyberknife control (robot, LINAC, imaging system and patient positioning system) is in a dedicated room, protected against irradiation and under temperature control with air conditioning.

The Cyberknife uses about one hundred incident beams of 6 MeV γ-rays that can partially or entirely treat the target. The LINAC head uses circular collimators between 5 and 60 mm (Figure 3.3), and is capable of delivering up to 6 Gy per minute. The robotic arm moves in a well-defined path around the patient, aiming the beam at different inclinations. One single beam can deliver up to 0.5 Gy of γ-ray dose. The imaging system, made up of two kV-X-ray tubes associated with two planar silicon detectors, is used not only for the setup of the robotic couch before treatment, but also to control and correct movement during treatment. The extra dose of ionizing radiation due to kV images is about 1 mGy. For the irradiation machine, the dose per session can reach up to 20 Gy.

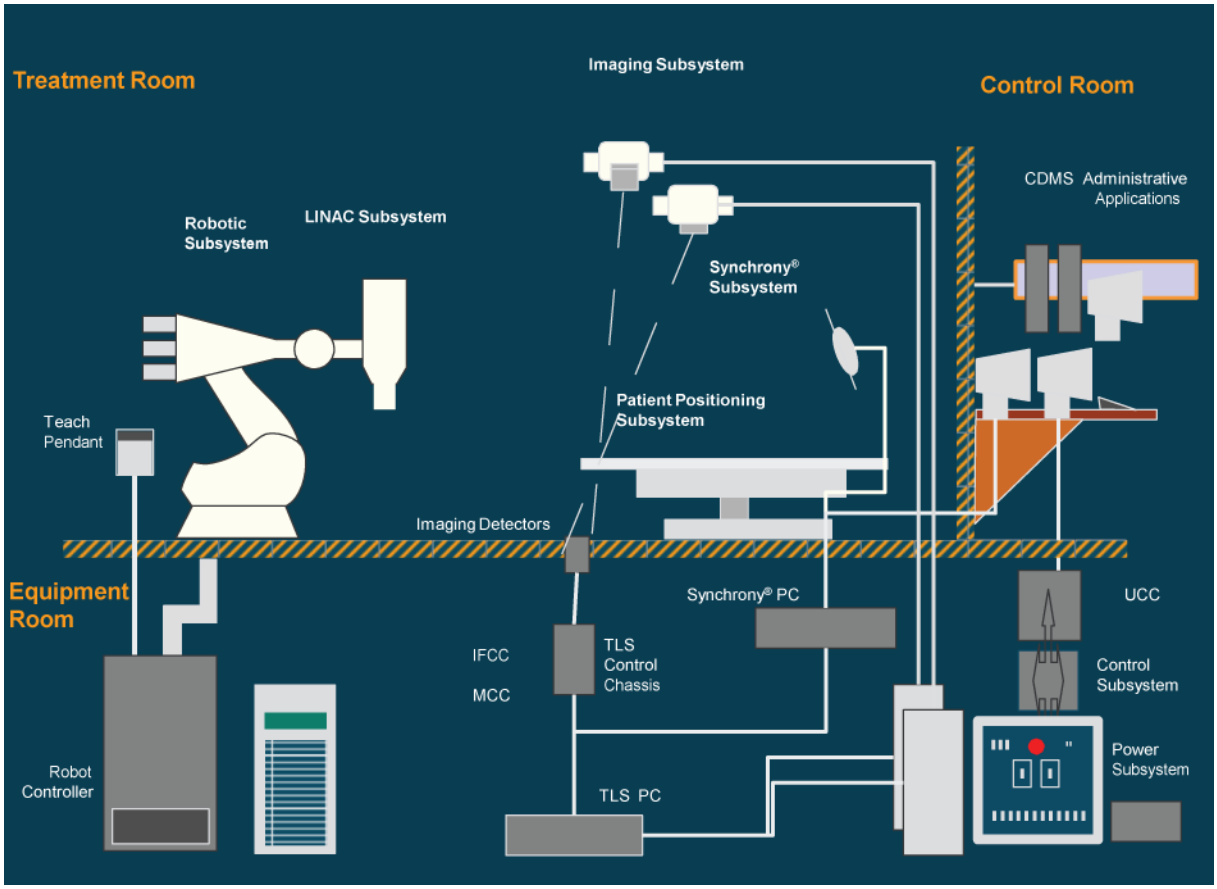

Figure 3.2: Cyberknife radiotherapy system configuration.

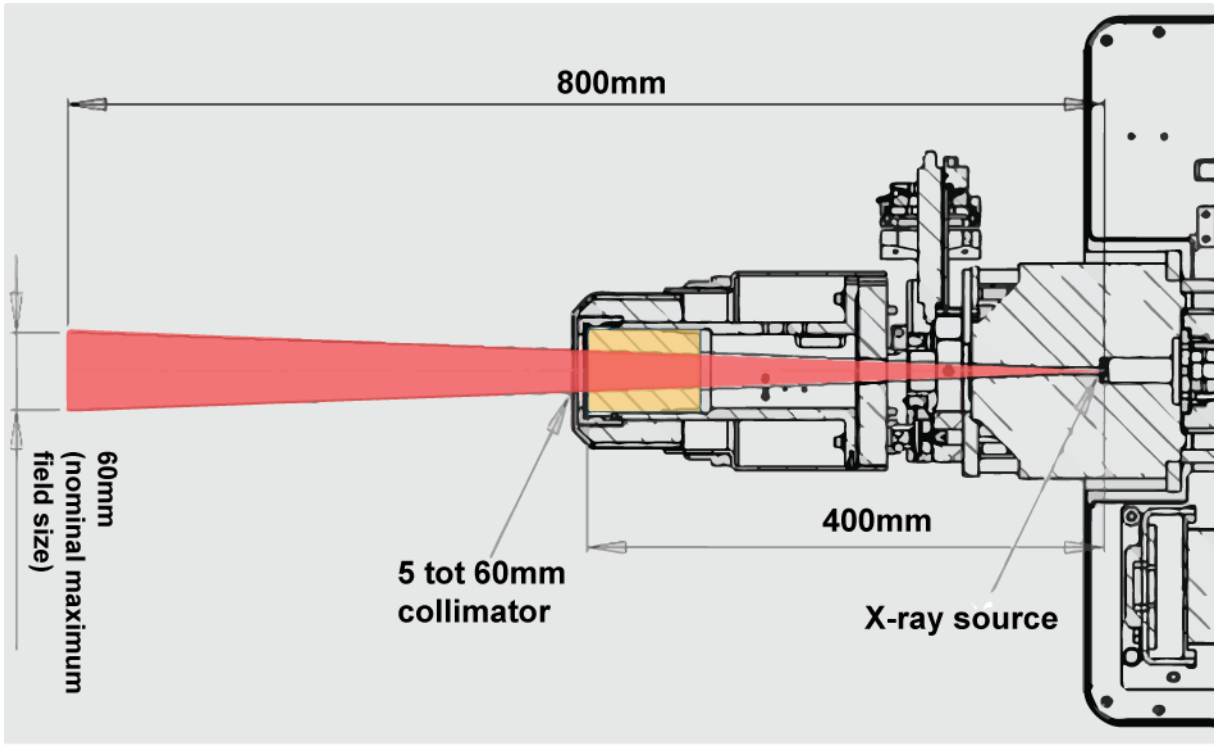

Figure 3.3: Collimator assembly of the LINAC accelerator on the head of the Cyberknife.

3.2.2 The phantom

The γ-ray beam produced from the Cyberknife's LINAC accelerator is focused on the DNA bundle trapped between the tips of the SNT. However, in real radiotherapy treatment, the radiation beam passes through the patient's skin before reaching the area of treatment. The process of dose absorption depending on the photon energy beam was summarily described in chapter 1.2.7. In the case of the Cyberknife (6 MeV), the maximum dose (build-up) is obtained at a 1.5 cm depth. To mimic the thickness of biological tissue corresponding to electronic equilibrium [16], a piece of plastic material with equivalent water density (called a *phantom* in radiotherapy) was designed, to be fitted on top of the SNT. The spherical geometry of the phantom ensures that the application of γ radiation, independently of the angle of incidence of the beam, passes through it the material at a uniform thickness.

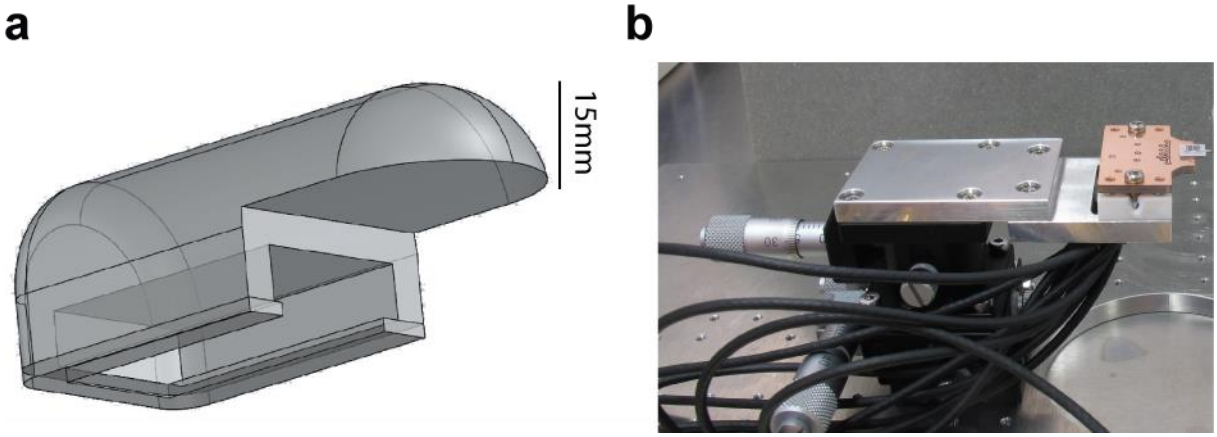

Figure 3.4: a. Design of the phantom (equivalent water density). **b.** SNT on micromanipulator, the phantom is fitted over the top of SNT.

3.3 The microfluidic cavity

3.3.1 Introduction

During the irradiation in aqueous medium, a strong predominance of indirect damage has been demonstrated when compared to direct damages [134] as is explained in more details in Chapter 1.3.1.3. To generate both types of damage during an experiment, and also because the measurement in absence of water would be little relevant to biological conditions, our DNA is placed inside an aqueous solution, to simulate the way in which DNA is damaged by water radiolysis products generated during ionizing irradiation in human cells. Moreover, additional oxygen reactive agents, pH-tampons, etc., can be introduced in the solution, in order to observe the agent's effects. To facilitate stable application of the solution, two types of microfluidic cavity have been developed (Figure 3.5 and Figure 3.6) in order to introduce the SNT into the liquid before and during DNA irradiation:

- A simple microfluidic cavity, called a "**static microfluidic cavity**" that allows keeping the same solution for the entire experiment. This type of cavity is filled by pipetting at the beginning of the experiment.

- A more complex microfluidic system, called a "**dynamic microfluidic cavity**" has been mainly developed by M. C. Tarhan in Tokyo (ref) and allows exchanging the liquid by means of a microfluidic pump at any time during an experiment, even if the SNT is already inserted inside it.

3.3.2 The static microfluidic cavity

The static microfluidic cavity is composed of two glass coverslips separated by a PDMS spacer 0.5mm thick. The design of the cavity, shown in Figure 3.5 is defined by a small aperture (1mm) on the front of the cavity and a large aperture (20mm) on its back. This design geometry, emphasizing the larger rear aperture, minimizes the evaporation from the front aperture, thereby also minimizing the displacement of the meniscus. This design allows pinning the meniscus to the front side of the cavity and obtaining a stable interface for the DNA characterization, even during irradiation experiments lasting up to an hour.

The geometry of the static cavity allows introducing liquid through the front aperture of 1mm. The SNT tips gripping the molecule bundle are then introduced into this front cavity. The shape of the meniscus is a 1x0.5 mm^2 rectangle. After the insertion of the SNT tips, no more liquid can be injected and the experiment should finish before the level of evaporation is too important

on both the meniscus shape and the concentration of the liquid. For these reasons, the duration of the experiment in these conditions is limited, and may not exceeded 1 hour.

The purple part of Figure 3.5 is a small independent cavity (DNA cavity) in the corner of the static microfluidic cavity's frame. For the DNA trapping in cavity (see Chapter 4.2) the SNT tips are firstly immersed in the DNA cavity containing a λ-DNA solution. The small distance (a few mm) between the two cavity apertures allows the automation of all the displacements (DNA trapping followed by SNT immersion) by the robot (see Chapter 3.4).

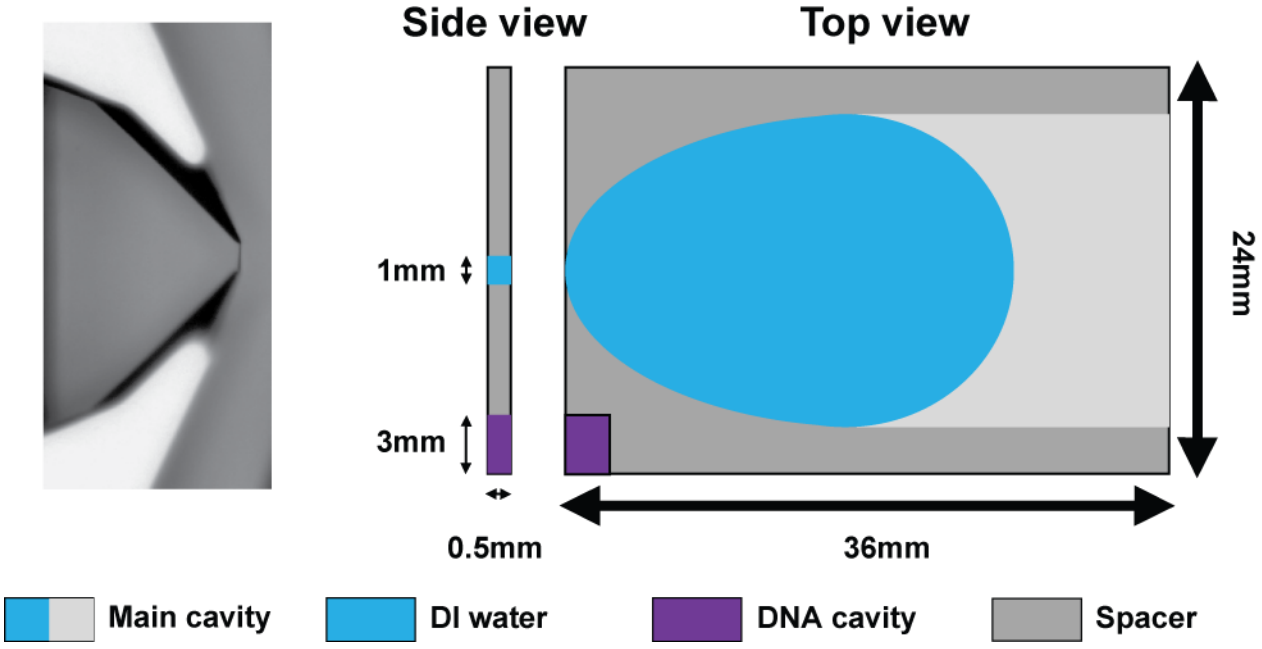

Figure 3.5: Design of the static microfluidic cavity. The blue is the main cavity inside which the irradiation experiment is carried out. A smaller cavity area (purple) is designed to contain the DNA solution for the DNA trapping.

3.3.3 The dynamic microfluidic cavity (DMC)

3.3.3.1 The global design of the dynamic microfluidic cavity

The dynamic microfluidic cavity was introduced to allow exchanging the liquid by means of a microfluidic pump at any time during an experiment. The meniscus displacement due to evaporation is controlled by the pump, therefore this cavity can be used for longer experiments (more than 10h, see Section 3.7.1.3.5)

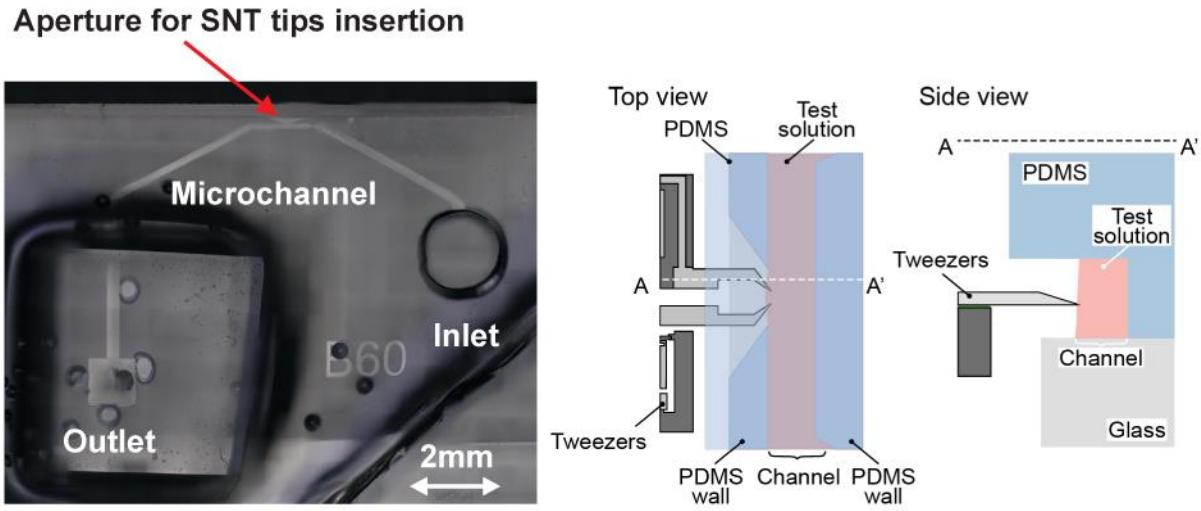

Figure 3.6: Design of the dynamic microfluidic cavity **a.** Photograph of the DMC **b.** Top and side view of the DMC schematic. [135]

The design of the dynamic microfluidic cavity is illustrated in Figure 3.6. The cavity is realized by placing a PDMS slab on a glass coverslip. A micro-channel with an inlet, an outlet and a side opening is molded into the PDMS slab. In order to obtain high resolution PDMS dimensioning, the mold is built by SU8 lithography. A set of devices with different geometries, different channel heights (varying from ~50µm to ~250µm) and different side openings widths (varying from ~50µm to ~200µm) are fabricated, with the same channel width of 100µm. The inlet and outlet holes are punched into the PDMS slab with 1-mm and 0.5-mm width diameters respectively. The inlet hole is designed to stock a droplet of a given liquid, which will be attracted in the channel by the difference of pressure generated by the pressure pump, connected to the outlet with peek tubing.

The PDMS slab is manually placed on a coverslip using a microscope (with 20x magnification). The edge of the coverslip is aligned with the PDMS wall (width of 300µm) keeping the brimming part of the PDMS slab (>500 µm) hanging over the coverslip (Figure 3.6.b). The PDMS rim region is crucial for insertion protocol.

3.3.3.2 The dynamic microfluidic setup

Figure 3.7 is a schematic of the microfluidic setup surrounding the dynamic microfluidic cavity. To test the effect of different solutions, liquid is injected into the channel via the microfluidic device inlet. The outlet is connected to a pressure pump (Elveflow AF1 Dual) for inducing flow when required. The flow is detected with a microfluidic flow sensor (Elveflow MFS). The

pressure pump is controlled by modules written with LabVIEW software, therefore a feedback on the pressure control can be applied depending on the flow detection.

In this configuration, the inlet droplet must be manually placed, and changed on the top of the inlet hole. For better control and automation of the liquid change, a multi-inlet device will need to be developed. Such a higher level of control could not be implemented in the experiments described in the remainder of this work. In order to compensate for the conditions of a single inlet, a simplified solution was used in order to minimize the effect of evaporation during longer experiments, and a syringe-pump was used to feed the inlet automatically.

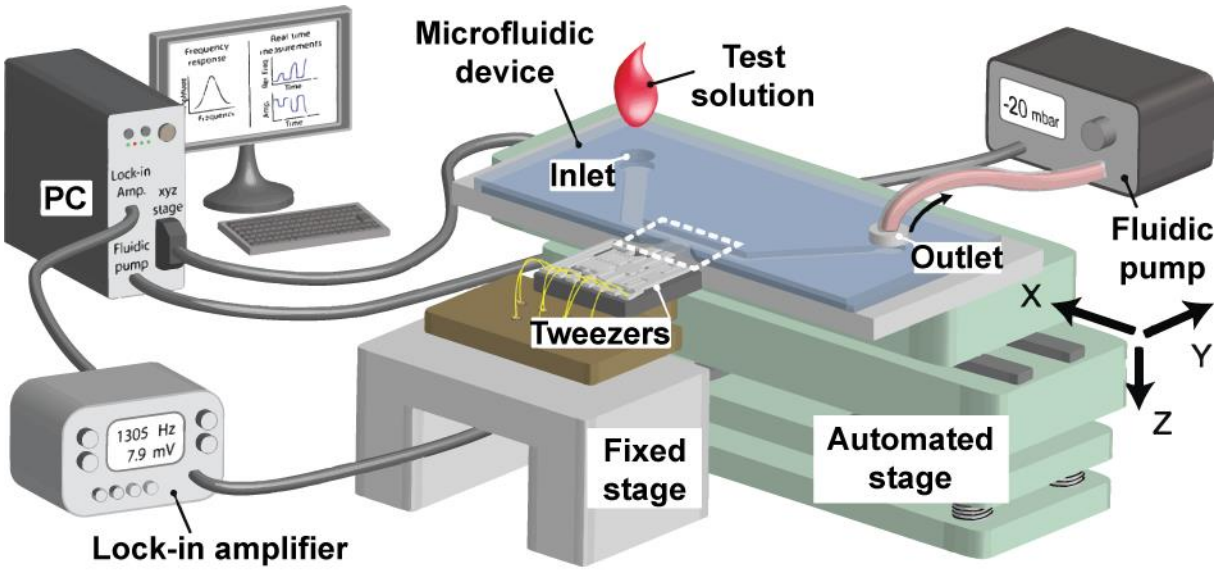

Figure 3.7: The dynamic microfluidic setup ([135])

3.4 The positioning robot

The relative SNT and microfluidic cavity positioning requires a high degree of precision, and need to be automatized to optimize the runtime and the repeatability of an experiment. A technological solution was developed here, by using a robot with high precision positioning.

The robot is a 3D positioning micro-machine based on piezoelectric elements, which provide a nanometer accuracy in displacement and a semi-automated manipulation. The robot is composed of 3 linear degrees of freedom, based on linear piezo-motors in the (x,y,z) directions. Piezo-motors are connected to a controller, which can be manually manipulated or

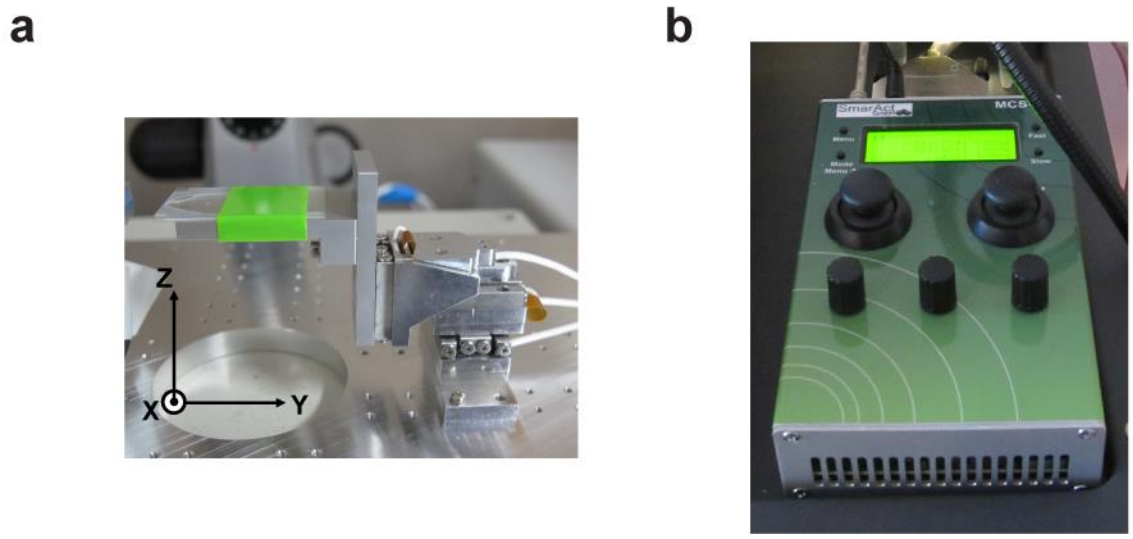

Figure 3.8: a. Picture of the 3D positioning-robot **b.** Picture of the positioning robot controller

connected to a PC to automatize both the displacement of the robot and the recording of its position.

In our study case, the robot was connected to the PC and controlled by the LabVIEW program. Its position is known with a nanometer precision, and can be recorded at any time, by the user or automatically. By combining the recorded position with the corresponding mechanical characteristics of the SNT, the robot position is automatized to detect the aperture of both types of microfluidic cavity and to trap DNA (in the case of DNA trapping protocol in cavity Chapter 4.2).

3.5 The controlled environment chamber

The surrounding environment (humidity, temperature, air-conditioning wind) should be controlled, to evaluate and minimize its effect on experimental measurements. The SNT setup was put under a closed box (Figure 3.9) to avoid sudden changes of the environment around the SNT. Nevertheless, the SNT setup requires electrical and fluidic connections and the user still needs a microscope feedback, to install and have a better understanding of the experiments. For these reasons, the controlled chamber should be transparent at least on the top and customized to have a good isolation in spite of the cable wiring.

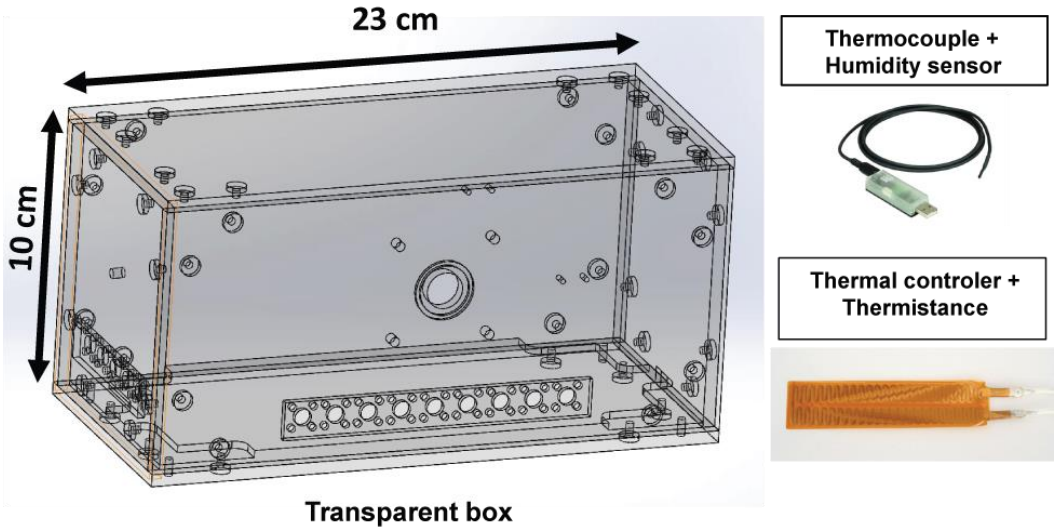

Figure 3.9: Design of the humidity and temperature controlled chamber.

Thermocouple and humidity sensors are installed inside the box and connected to the LabVIEW program. The temperature and humidity are recorded all along experiments.

Since this set up aims at manipulating biological elements, it is relevant to provide an experimental environment with a higher temperature than ambient. Therefore, a thermistor is glued on the aluminum body of the setup and is controlled by LabVIEW. A proportional-integral-derivative controller (PID controller) program allows a high accuracy control of a programmed temperature, for example 37.5°C to mimic the body temperature as illustrated below in Figure 3.10.

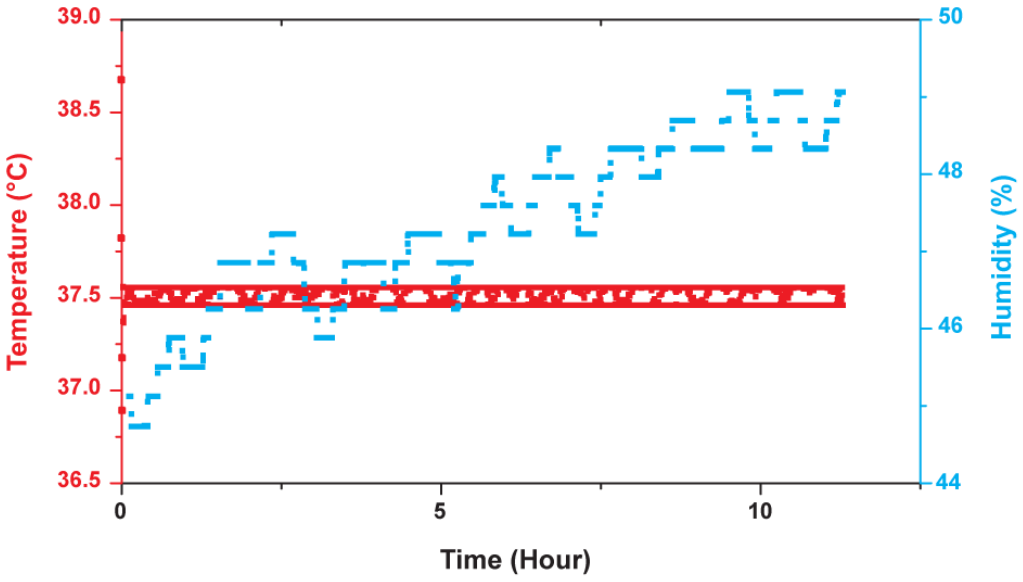

Figure 3.10: Recording of the temperature and relative humidity inside the isolated box of the SNT setup. The temperature is kept constant at the human body temperature (37.5°C).

3.6 The LabVIEW program

In order to automatize the experiments, the complete set-up is conceived to be fully controlled by LabVIEW. All instruments composing the set-up are connected to the PC, and have LabvVIEW's drivers. The LabVIEW program is composed of two windows: (1) the control window, and (2) the data window.

3.6.1 The control window

The first window (shown in Figure 3.11) is dedicated to the control of the instruments and the interaction between them. This window is mainly used during the installation of the set-up inside the Cyberknife room.

1. The black left panel allows to turn on the instruments that will be used for the specific experiment.
2. The green panels are related to the positioning robot control and the microfluidic positioning.
3. The purple panels are more related to the lock-in amplifier and are used to perform Frequency Response and Phase locked loop on the Silicon Nano Tweezers.
4. Panels related to the DEP signal for DNA trapping and to actuating arm actuation for Double-Actuators SNT.
5. Control of the microfluidic pump: pressure and flow control inside the microfluidic cavity
6. Temperature and humidity control inside the controlled chamber.

3.6.2 The data window

The data window of the LabVIEW program Figure 3.12 is fully dedicated to the visualization of the data, acquired during the preparation of the set-up and the experiment. The separation of the control and the visualization of data in two different windows simplify the experiment and provide a comfortable visualization of data outside of the Cyberknife room, during the irradiation.

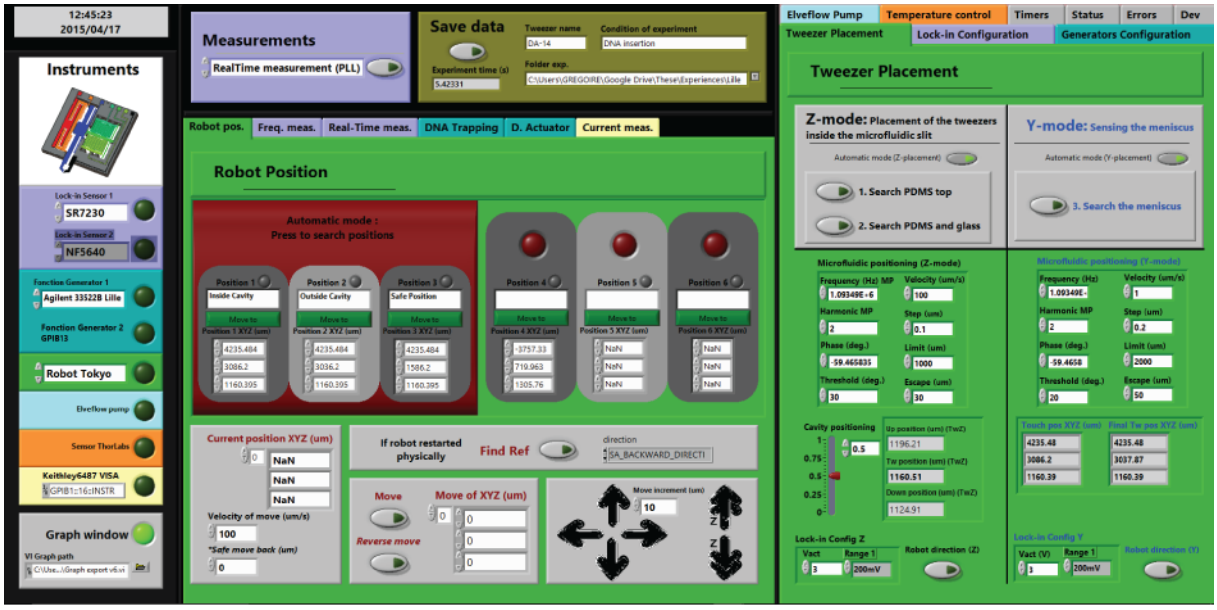

1 : Intruments switches

2 : Positioning robot control and microfluidic positioning

3 : Frequency Response and PLL

4 : DNA trapping and D-A SNT control

5 : Microfluidic pump : pressure and flow control

6 : Temperature and humidity control

Figure 3.11 Control window of the LabVIEW program for the installation of experiments

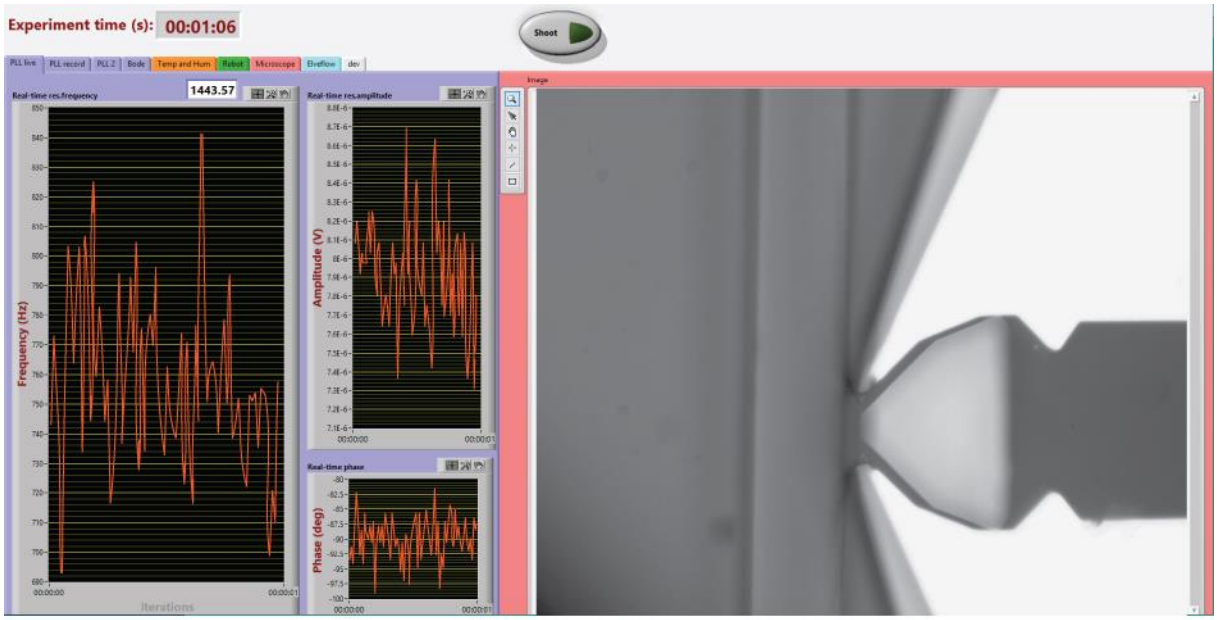

1 : Microscope

2 : Positioning robot position

3 : Frequency Response and PLL

4 : Switch to record irradiation period

5 : Pressure and flow inside the microfluidic cavity

6 : Temperature and humidity control

Figure 3.12: Data window of the LabVIEW program

3.7 Evaluation of the setup

The developed setup aims to perform real-time mechanical characterization under γ-ray irradiation. Before carrying out the irradiation experiment, a complete characterization of the setup is here proposed, dealing with: (1) air environment on bare SNT; (2) insertion parameters of SNT tips in either the passive or dynamic microfluidic cavity with bare SNT; (3) bombardment of the bare SNT with ionizing radiation in air and in liquid; (4) test of several aqueous mediums on SNT after DNA trapping.

3.7.1 Bare SNT

A complete characterization of the response of the bare SNT under experimental condition was performed before trapping any DNA molecules. This step was essential to uncorrelate the impact of the environment on the SNT itself, and/or on a future DNA bundle.

3.7.1.1 In Air

For real-time mechanical characterization of a DNA bundle, the sharp tips of the SNT can be immersed in liquid. Nevertheless, to have a precise mechanical measurement (and also because the SNT is not electrically isolated), the body of the SNT is kept in ambient air during the experiment. So, the influence of the air in the environment on the mechanical properties of the bare SNT itself has to be quantified. Thus, the effect of the environment on the SNT/liquid interface and/or on the DNA bundle will be more easily discriminated.

3.7.1.1.1 Influence of humidity

The relative humidity can be recorded but not monitored in the setup. So in order to evaluate the effect of humidity on the bare SNT, a small amount of water is introduced inside the closed box. The temperature is controlled to be constant at 37.5 °C and the variation of the humidity as well as the resonance frequency and amplitude of a bare SNT is recorded for more than 10h. The plot in Figure 3.13 gives the time variation of the resonance frequency and amplitude together with the monitored temperature and the recorded humidity.

The plot Figure 3.14 represents the resonance frequency (F_R) and amplitude (A) of the SNT versus humidity, from the scatter plot of the same data in Figure 3.13. Since the temperature is constant, its effect can be neglected. In a first approximation, the relation between F_R and the relative humidity can be considered linear in the range of the experiment, with a slope equal to -20mHz/%. The relation between the amplitude A and the relative humidity can as well be considered linear, with a slope equal to -0.01mV/Hz. The decrease of F_R and A are due to the added mass to the SNT by condensation.

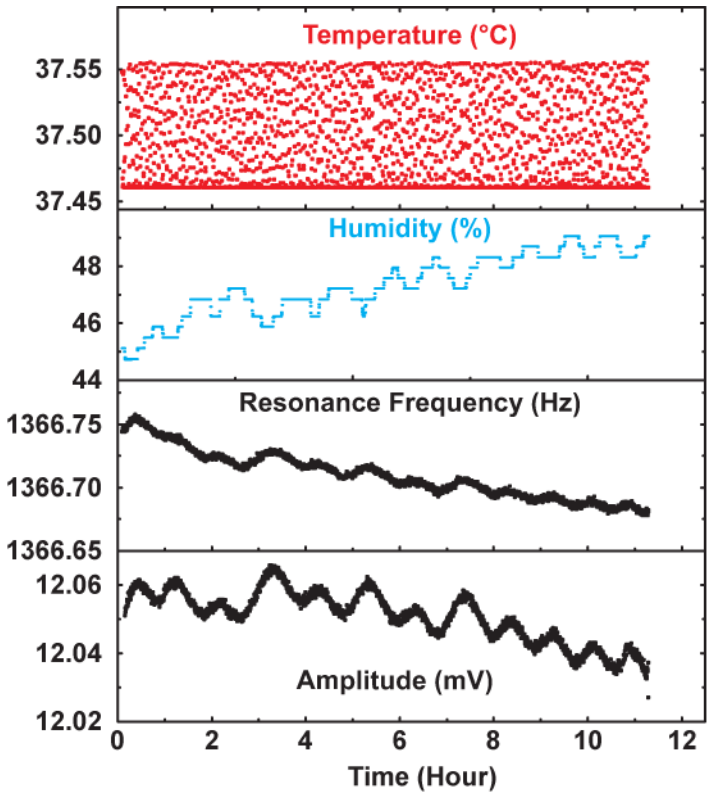

Figure 3.13: Variation of humidity, resonance frequency and amplitude of a bare SNT at constant temperature

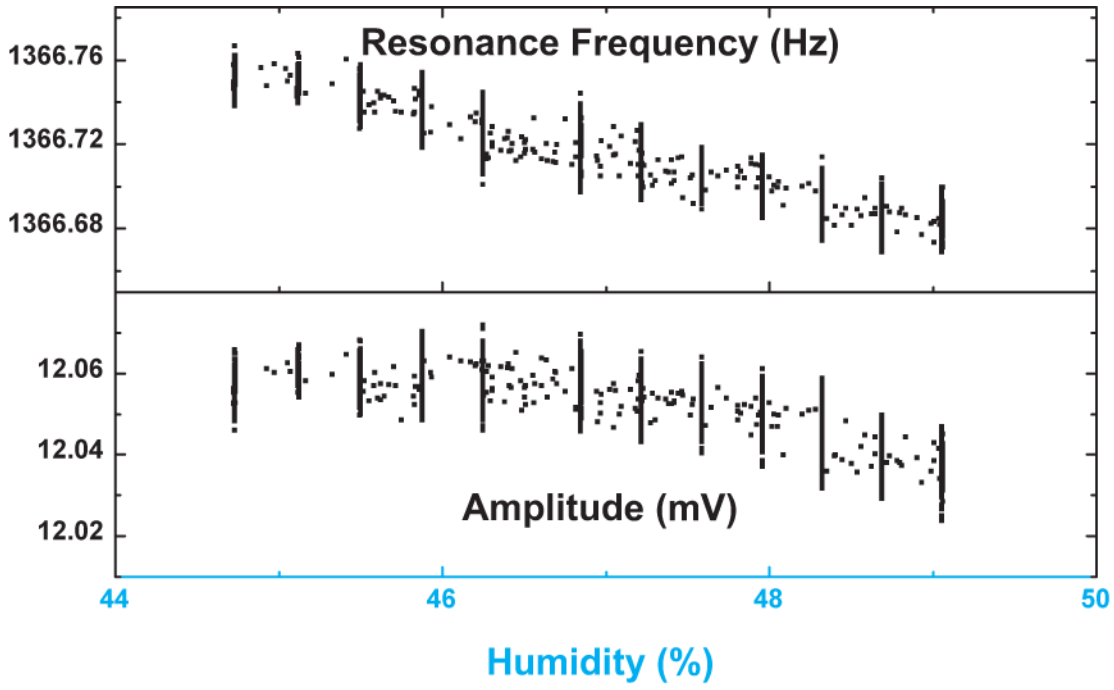

Figure 3.14: Influence of humidity on the mechanical properties of a bare SNT

3.7.1.1.2 Influence of temperature

The chamber allows to monitor the temperature from ambient up to 70°C. Temperature cycles were programmed in the chamber and the corresponding F_R and A are plotted in the Figure 3.15. The effect of the temperature on the mechanical properties of this SNT is evaluated.

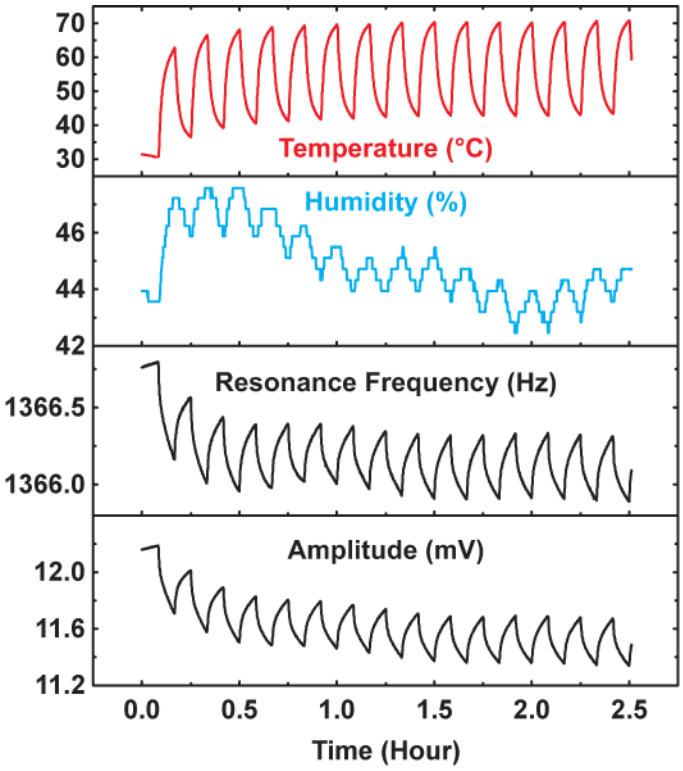

Figure 3.15: Temperature cycle from room temperature to 70°C and its effect on humidity and resonance frequency and amplitude of a bare SNT

The graph Figure 3.16 plots the resonance frequency and amplitude of a bare SNT versus temperature. These data correspond to the second scan in Figure 3.15 (between 0.25 and 0.5h time), the temperature increasing from 35 to 65 C, with an attending variation in relative humidity of about 2%. To correct for humidity variation, fractions of 40 mHz and 0.02 mV must be respectively subtracted from the curves for F_R (above) and A (below).

In a first approximation, both can be considered linear with the temperature, with a slope equal to -15mHz/°C for the resonance frequency, and a slope equal to -0.01mV/°C for the amplitude. The decrease of the resonance frequency is due to a softening and elongation of the springs.

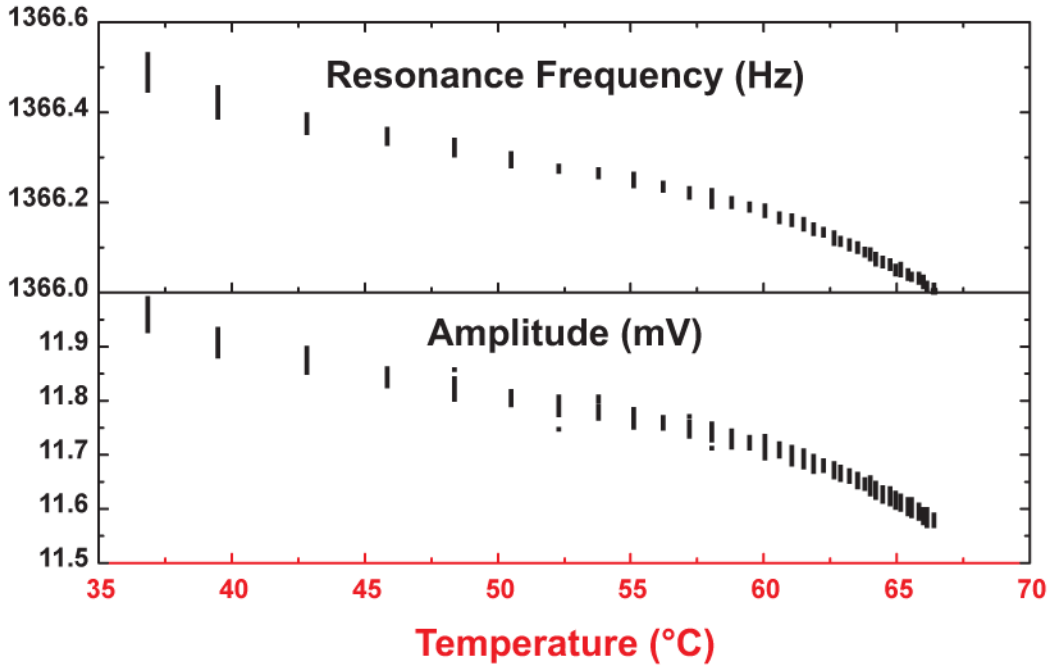

Figure 3.16: Influence of the temperature on the mechanical properties of a bare SNT in air.

3.7.1.2 In passive microfluidic cavity

In this characterization phase, the passive microfluidic cavity was always filled with DI water. In fact, the high instability of the meniscus with other mediums did not allow to obtain relevant measurements. In order to solve this problem, some modifications of the passive microfluidic cavity fabrication (PDMS molding, coating of parylene) have been tried, but without enough success. Therefore, in the further experiments, the dynamic microfluidic device was always preferred.

In this setup, with the passive microfluidic cavity, the depth insertion cannot be controlled with a high precision, because the relatively hydrophilic property of the SNT surface tends to attract the DI water during the insertion of the SNT tips.

The geometry of the cavity is symmetrical, therefore the highest stability is obtained when the tips are inserted in the middle of the meniscus (determined by the insertion protocol in passive cavity, Chapter 4.3). So only this configuration is reported in the graph of the Figure 3.17. The resonance frequency and the amplitude of the SNT are seen to slowly decrease linearly after the insertion of the tips of the SNT. For this specific experiment, the slope of F_R versus time is equal to 0.1Hz/hour and the slope of A versus time is equal to 0.25mV/hour. Nevertheless, these values are not perfectly repeatable for different cavities and SNT. For every experiment in the passive microfluidic cavity, the meniscus effect is determined just after the insertion. When stabilization is reached, other experimental actions can be processed.

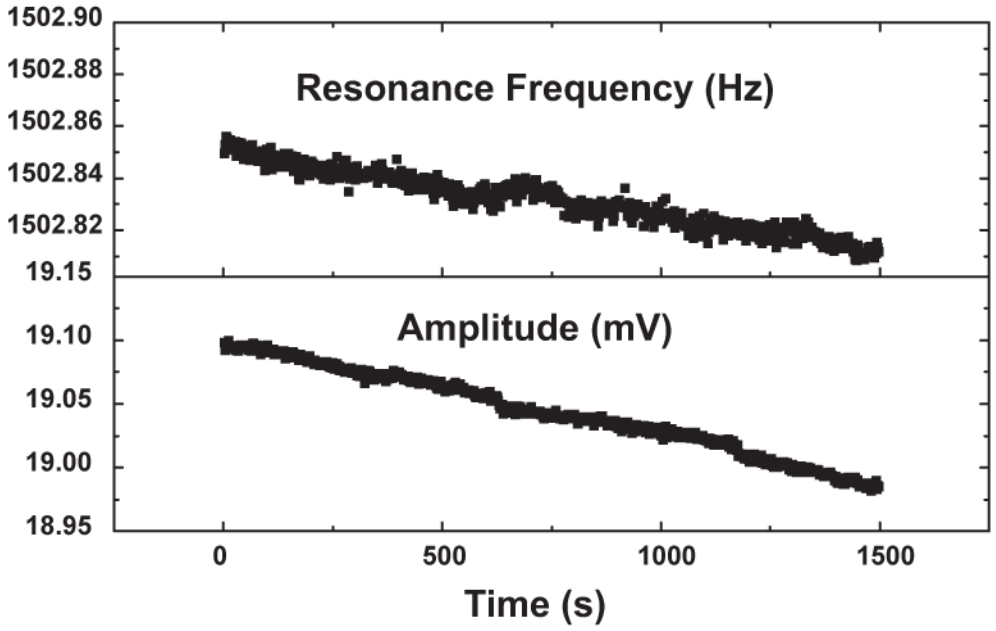

Figure 3.17: Stability of the resonance frequency and amplitude of a bare SNT with its tips immerged in passive microfluidic cavity filled by DI water

3.7.1.3 In dynamic microfluidic cavity

The dynamic microfluidic cavity was developed to solve the problem of instability relative to the passive microfluidic cavity, as well as to allow changing the liquid composition during the real-time measurement of the DNA mechanical properties by the SNT. Firstly, the shape of the meniscus must be determined in this non-symmetrical system. Secondly, the position of the tips of the SNT inside the meniscus is evaluated, according to the stability of the SNT/liquid interface. This stability is characterized at different positions, and the most favorable one is chosen for next experiments. Third, the repeatability of the insertion of the SNT tips at the optimal position is plotted. And fourth, the long term stability of the SNT/DI water interaction at the most stable position is monitored and plotted for more than 10 hours.

3.7.1.3.1 Shape of the meniscus

The shape of the meniscus is not symmetrical due to the difference of hydrophilic character between glass and PDMS. In order to determine the shape of the meniscus, the air/liquid interface is sensed by the SNT with the same protocol used for the SNT insertion (protocol description Chapter 4.4.2). The position of the air-liquid interface changes slightly closer to the glass surface due to the hydrophilic surface (Figure 3.18). 30 µm above the glass surface resulted in <0.5 µm changes in the air-liquid interface position.

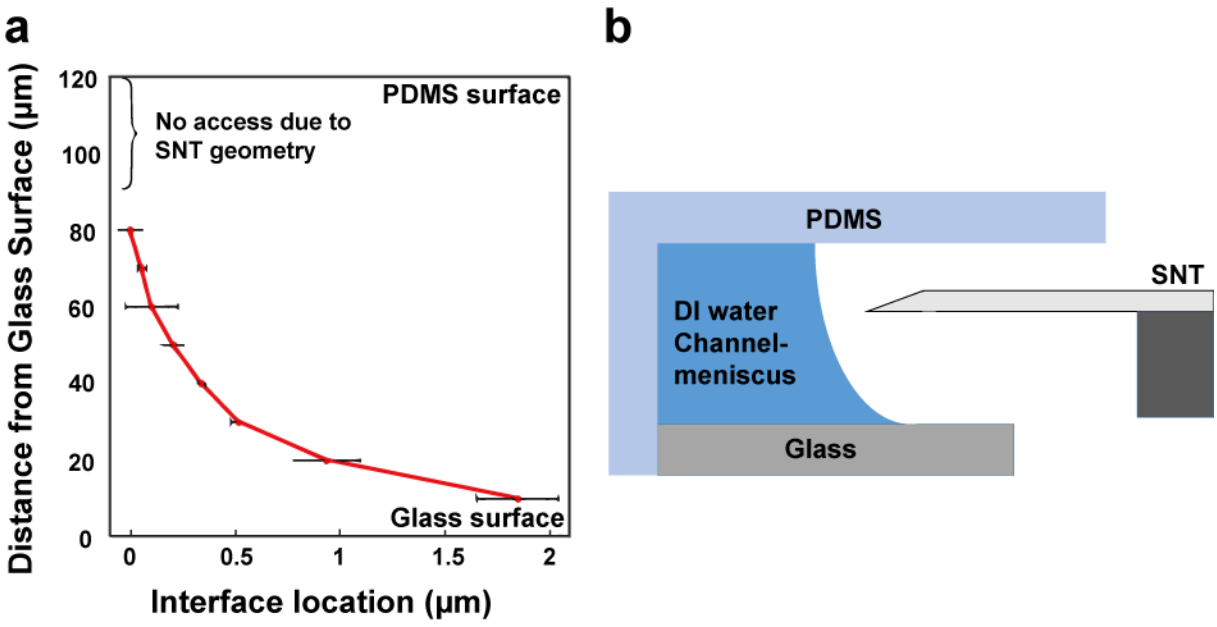

Figure 3.18: Shape of the meniscus of the dynamic microfluidic cavity **a.** Experimental detection of the meniscus by the SNT. **b.** Schematic of the meniscus

3.7.1.3.2 Insertion height

The non-symmetrical shape of the meniscus was discussed in the previous paragraph. The stability of the SNT at different heights (the position of bottom of the tips of the SNT is measured) is reported in Figure 3.19. The SNT is inserted into the channel (t = 0 min) at different heights (from 10 µm to 70 µm above the glass surface for a device with aperture height equal to 115 µm and aperture width equal to 108 µm). The initial immersion depth was 5 µm for all the cases. However, insertion at 10-µm height caused solution to go out under the SNT because of the capillary effect between the glass surface and the bottom of the SNT, the graph 3.19b shows the SNT stability. The graph 3.19c defines the working region for an acceptable stability of the SNT/liquid interaction along the time. In order to have repeatable experiment, the SNT will be always placed in the middle of this working region in the next experiments

3.7.1.3.3 Insertion depth

The insertion depth of the tips of the SNT inside the liquid of the microfluidic cavity is optimized to protect the future DNA measurement from two undesirable effects. First, both tips should be immersed inside the liquid, an incomplete insertion induces instability. Second, if the tips are too much immersed, the capillarity force is too high and the liquid can continuously rise on the tips. The SNT/liquid interaction is unstable in this condition.

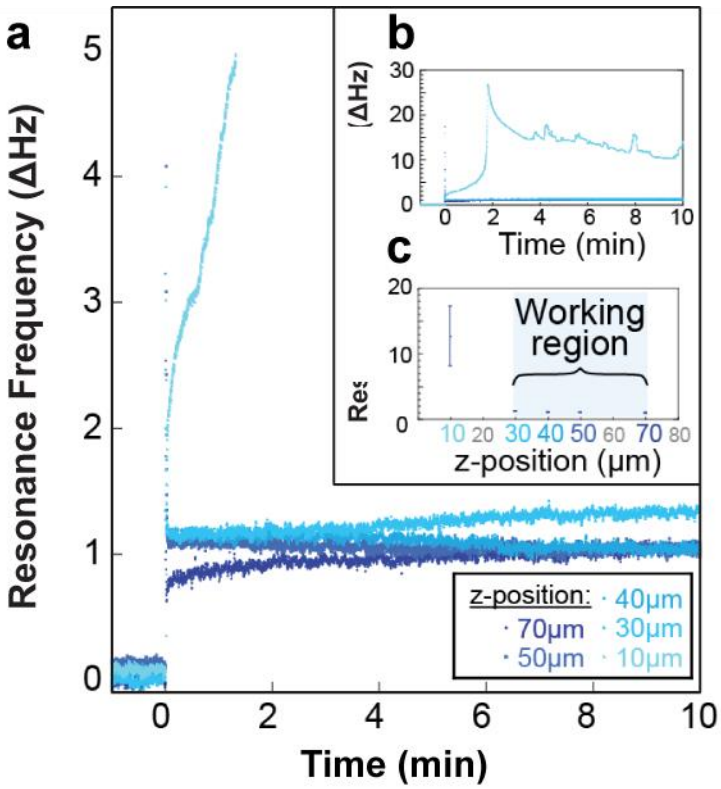

Figure 3.19: a. Stability of the resonance frequency of a bare SNT for different insertion Height. **b.** Overview of the instability for insertion height lower than 30µm. **c.** Working region with acceptable stability.[132]

The SNT is inserted into the channel (from an opening of h= 115µm, w= 108µm) at different immersion depth Figure 3.20. Between each step, the SNT is taken out to a position 3 µm away from the air-liquid interface. The position of each step with respect to the air-liquid interface is shown in the inset, and defines the working area with good enough stability. For an immersion depth of 5µm, the DNA is always fully immersed and the risk of instability by capillarity is extremely low. In order to have repeatable experiment, the immersion depth will always be kept at 5µm in the next experiments.

3.7.1.3.4 Multiple insertions in DI water

The stability of the setup is now tested with respect to the repeatability of the insertion of the tips of the SNT inside the microfluidic cavity, reported Figure 3.21. The graph measures the resonance frequency (F_R) and the amplitude (A) of the SNT during a cycle of insertion and removal of the tips of the SNT from air to DI water. The tips are inserted 5µm inside DI water for 5min and brought back in air for 5min, and this sequence is repeated for 4 hours. The repeatability of F_R and A shifts proves the stability of the system.

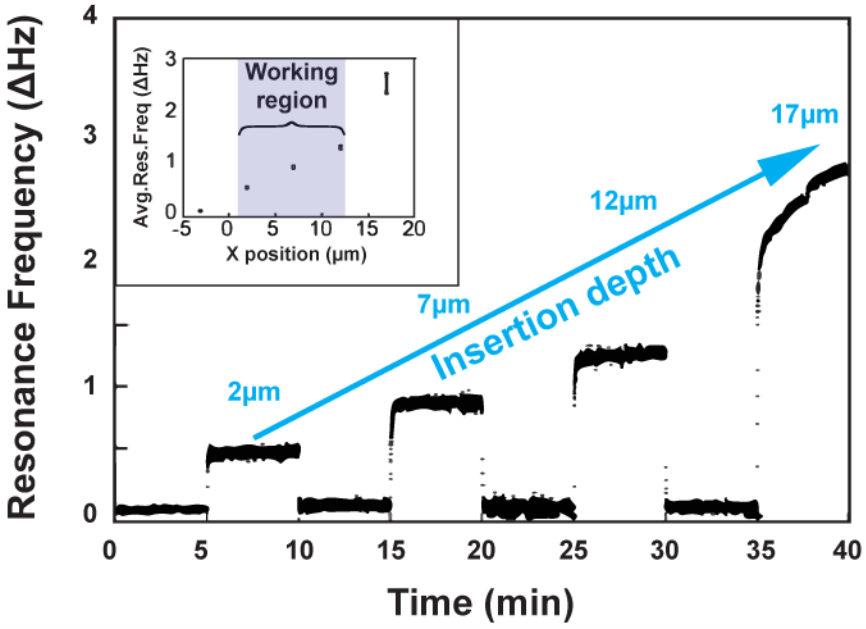

Figure 3.20: Stability of the resonance frequency of a bare SNT for different insertion depth.[132]

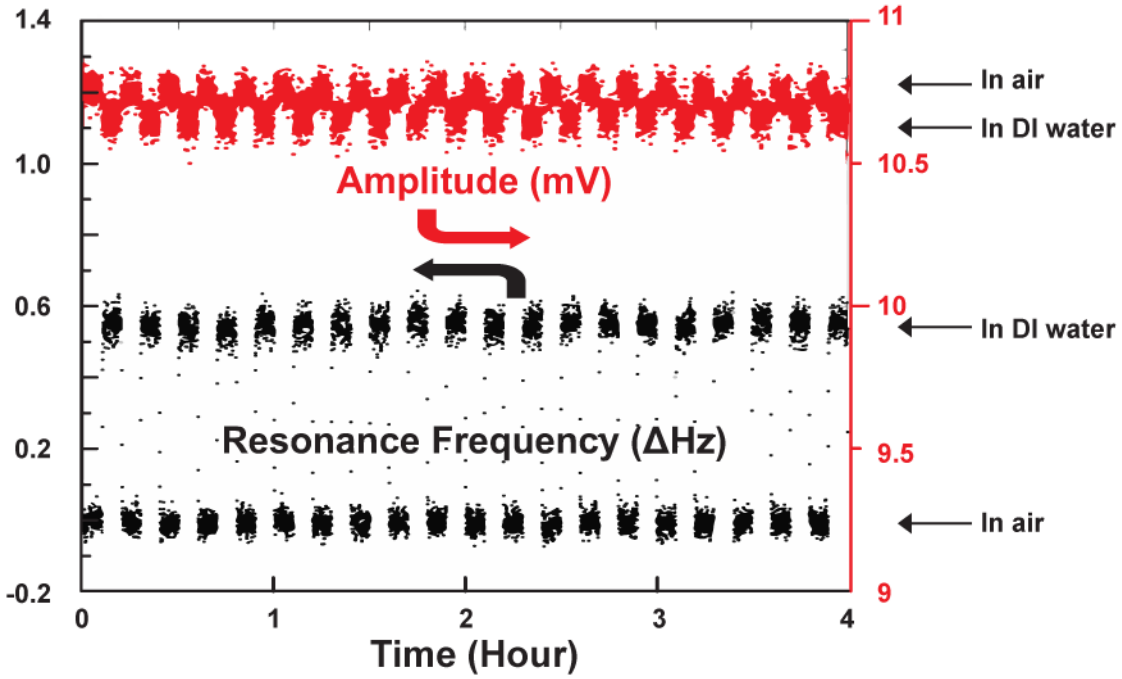

Figure 3.21: Insertion repeatability inside the dynamic microfluidic cavity.[132]

3.7.1.3.5 Long time stability in DI water

The stability of the bare SNT inside the dynamic microfluidic cavity is finally tested over a long period of 10 hours (Figure 3.22). The drift of both the resonance frequency and the amplitude is negligible during the experiment. This proves that the bare SNT is perfectly stable inside the dynamic microfluidic cavity filled with DI water.

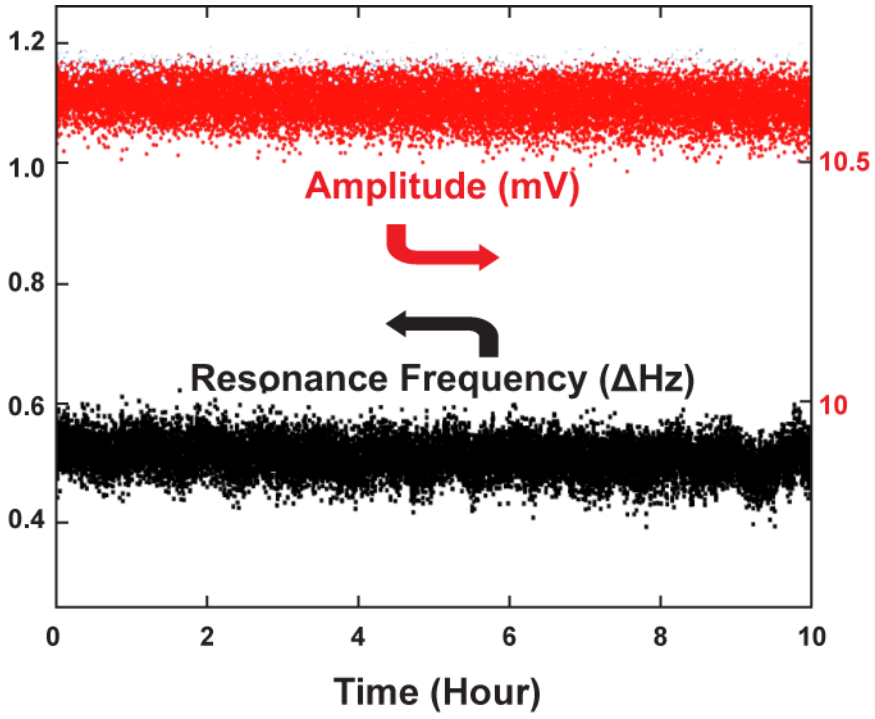

Figure 3.22: Long time stability of bare SNT inside the dynamic microfluidic cavity filled with DI water.[132]

3.7.1.3.6 Buffer exchange

One important advantage of the dynamic microfluidic cavity is the ability to change the liquid solution during the experiments, even if the SNT is already inserted inside the cavity. This capability is tested in the experiment reported in Figure 3.23. The SNT is firstly inserted in a phosphate-buffered saline (PBS) solution. After 5min, the liquid is changed to DI water by means of the vacuum pump (Chapter 3.3.3.2). The liquid flow generated for the liquid change temporarily modifies the air/liquid interface. This phenomenon is characterized a the strong decrease of the resonance frequency, during the liquid change. Eventually, it can be said that

the operation of changing liquid induces but a slight changes of the resonance frequency of the bare SNT.

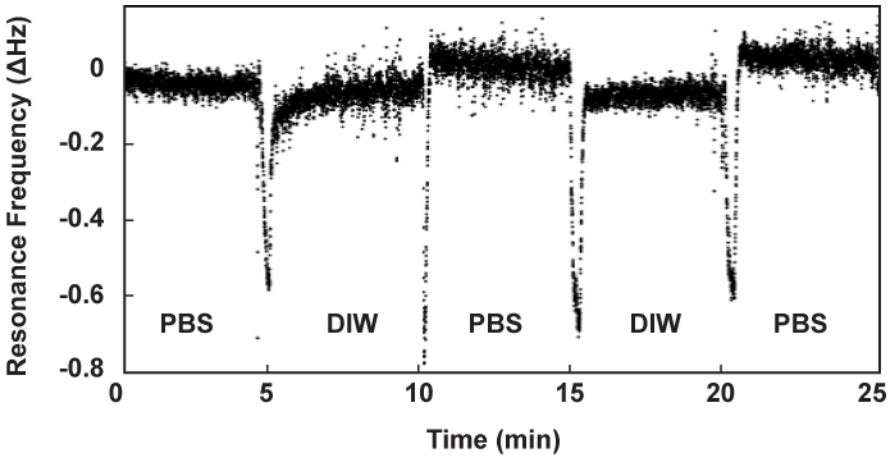

Figure 3.23: Effect of the liquid change (PBS/DI water) on the resonance frequency of a bare SNT inserted inside a dynamic microfluidic cavity. [132]

3.7.1.4 Noise and stability under ionizing radiation

The novelty and the key challenge of this work are to perform **real-time** DNA mechanical characterization **under the ionizing radiation** of a radiotherapy machine. Conventional methods do not support the harsh electromagnetic field of the ionizing radiation, and are not adapted to real-time measurement.

To minimize the effect of the ionizing radiation on the SNT measurement, the electronics are placed at 1m distance from the beam that will irradiate the SNT. In addition, the body of the SNT is grounded to help the evacuation of charges. Nevertheless, the γ-ray beam generates an extremely harsh electromagnetic environment, and could affect the electromechanical characteristics of our global system.

So, a set of controlled experiments on the bare SNT is necessary to analyze later the effect of the irradiation on the mechanical properties of a DNA bundle. The effect of a strong ionizing radiation dose (around 30 Gy which is about ten times the quantity used during a session of a radiotherapy treatment) on the resonance frequency, F_R, of a bare SNT was quantified in several conditions (Figure 3.24 and Figure 3.25).

In the Figure 3.24, the ionizing radiation beam is constrained by a collimator with a large aperture (40mm) and is focused on the tips of the SNT. Graphs **a** and **b** compare the effect of the ionizing radiation on a bare SNT respectively immersed or not in DI water. In both cases, different conditions are tested:

- With or without a phantom (see Chapter 3.2.2) on top of the SNT.
- With or without an additional DC voltage on the comb drive actuators, to stress the SNT. This stress mimics the additional force applied by the DNA bundle on the SNT.

First, in every condition the noise level of the F_R measurement does not change during the irradiation, while F_R itself increases by less than 0.1Hz. Second, the effect of the irradiation is lower in DI water (the most interesting condition) than in air. Third, the phantom amplifies the effect of the irradiation, particularly in air. And fourth, the DC voltage on the comb drive actuators has a negligible effect.

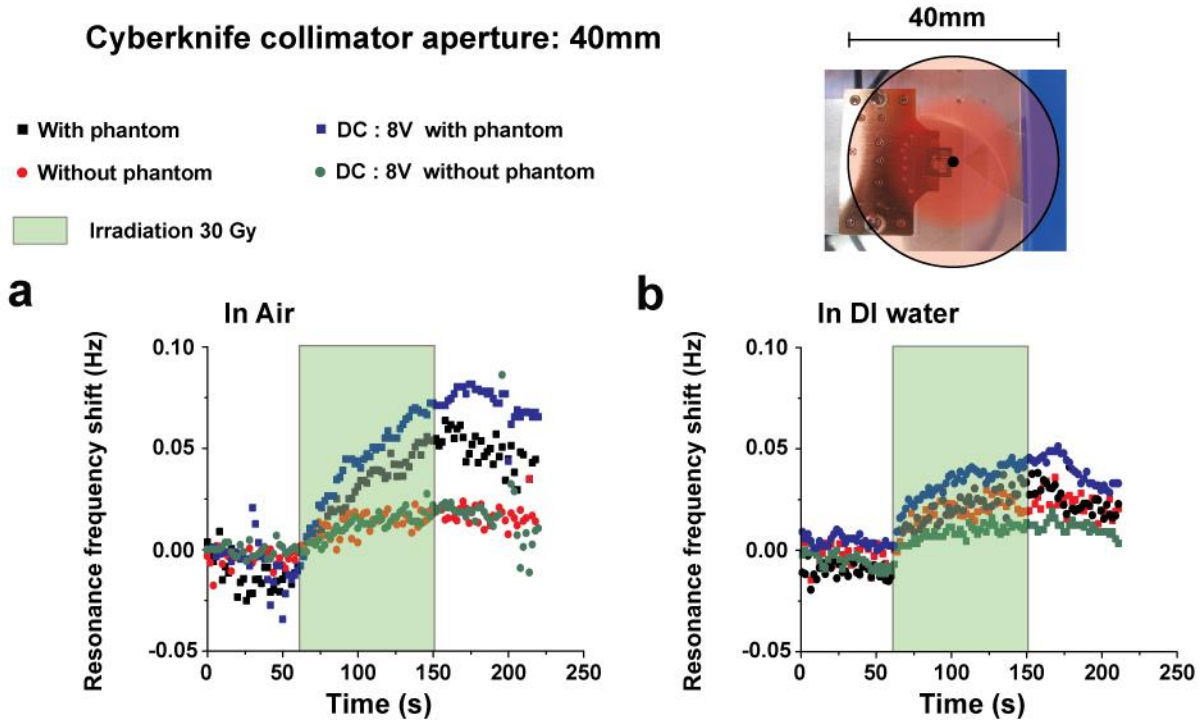

Figure 3.24: Control experiments to quantify the effect of ionizing irradiation on the resonance frequency of a bare SNT in several conditions. The irradiation beam (40mm aperture) is aligned with the tips of the SNT. **a.** The tips of the SNT are in Air **b.** The tips of the SNT are in DI water.

An advantage of the Cyberknife, compared to older linear accelerators machines, is to allow a small collimator aperture. A 5mm collimator aperture is used in the Figure 3.25, in order to minimize the irradiation effect. The radiation beam is focused on different elements of the SNT to have better understanding of the sensitivity of these elements to the irradiation. For every experiment, the resonance frequency is very stable during the irradiation. This 5mm aperture is used for the mechanical characterization of DNA bundle under irradiation.

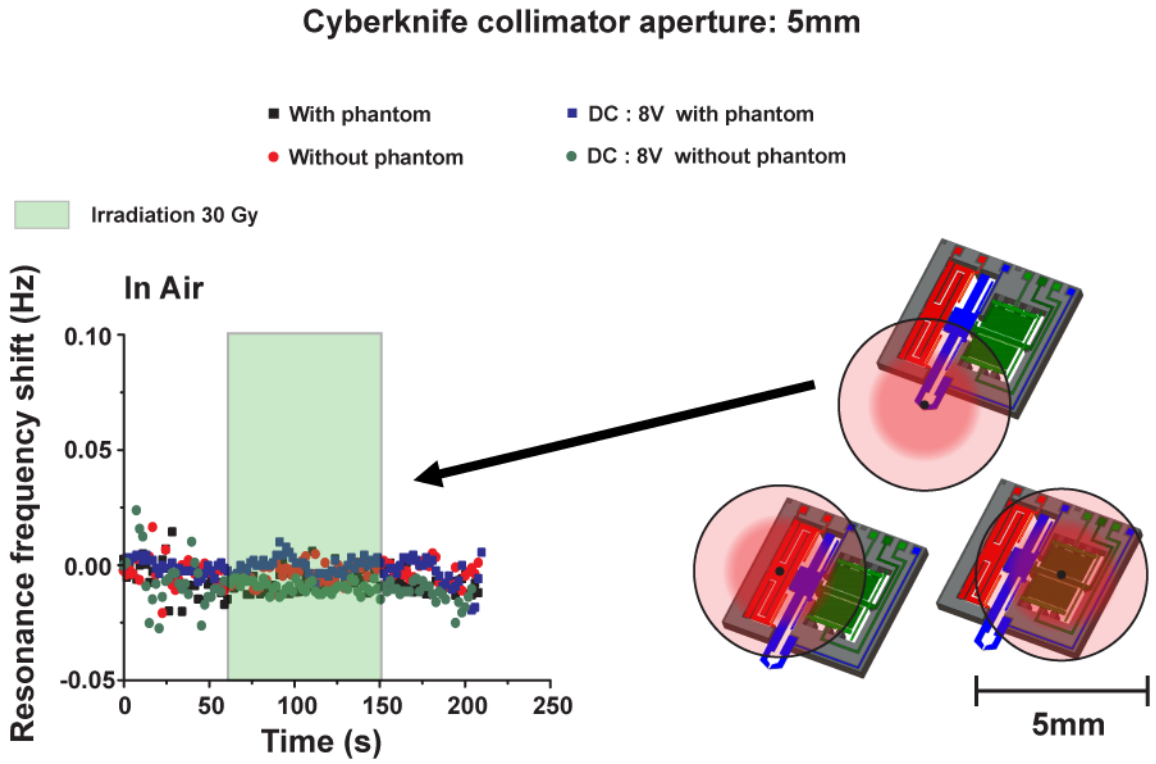

Figure 3.25: Control experiments to evaluate the effect of ionizing irradiation on the resonance frequency of a bare SNT in air. The collimator aperture of the Cyberknife is equal to 5mm, and the irradiation beam is focused on different parts of the SNT. The graph plot the "Resonance frequency of the SNT" vs "Time" when the irradiation beam is focused on the tips of the SNT. Similar results are obtained with a focus on the sensor and the actuator of the SNT.

These results fully support the choice of the Silicon Nano Tweezers for the real-time DNA mechanical characterization under therapeutic radiation beams, importantly justified by its capability to endure the ionizing radiation of the radiotherapy machine while still retaining molecular level accuracy.

3.7.2 SNT and trapped DNA

In this part, the stability of SNT with trapped DNA is evaluated. After applying the DNA trapping protocol (see Chapter 4.2), the effect of the environment on the DNA is quantified in air, in DI water, and in mediums with different pH. The conformation of the DNA molecules (and so the effective length of the DNA bundle) can change depending on the medium. If the DNA bundle is too long, the Single-Actuator SNT is no more able to sense it. The last part of this chapter quantifies the effect of the Double-Actuators SNT on the DNA elongation in DI water and in TRIS buffer, where the S-A SNT is not able to sense DNA.

3.7.2.1 Insertion in DI water

The stability of the bare SNT in air and in DI water has been previously quantified. So, for the next experiments (after DNA trapping), any new effects should be solely ascribed to the change of the DNA mechanical action on the SNT.

The experiment reported in Figure 3.26 starts by the DNA trapping in cavity (Chapter 4.2).

The SNT tips are then removed from the trapping cavity, and placed at 1mm from the meniscus of the passive microfluidic cavity. The resonance frequency F_R increases from around 1500Hz to 2000Hz, and the amplitude A increases from 7.5mV to 16.5mV. The large variation of F_R and A reveals the effect of an additional stiffness and viscous loss on the SNT, due to the adsorbed DNA bundle. The DNA bundle effect on the SNT is extremely instable in air for three main reasons. Firstly, the DNA bundle is extremely sensitive to environment vibration. Secondly, air movement easily moves the DNA bundle, especially out of the controlled chamber (because of air conditioning). Third, the mechanical properties of the DNA bundle depend strongly on the relative humidity (Chapter 4.3.3).

After 15min in air, the DNA bundle is approached to the meniscus of the passive microfluidic cavity and then inserted in DI water. The DNA bundle recovers its initial mechanical properties in solution as soon as the humidity increases, during the approach phase (see the rapid drop immediately before the purple region in the plot). When the DNA bundle is finally inserted inside DI water, F_R and A stabilize around 2Hz and 1mV above their initial value. This shows that the order of magnitude is the same when DNA is adsorbed and fully hydrated, getting close to the bare SNT values.

After 15 min in DI water, the DNA bundle is removed from the cavity and repositioned at 1mm from the meniscus. This time, F_R and A do not recover their value in air (i.e., the values just after the DNA trapping). This indicates that the mechanical properties of the DNA bundle have somewhat changed during the insertion or/and the removing of the SNT tips inside the DI water. The DNA bundle is probably being rearranged or damaged during this protocol, which should not be repeated during the real experiments. These phenomena also show the limits of the non-specific aluminum/DNA adhesion.

The zoom of the Figure 3.26.b illustrates the stability of F_R and A when the DNA bundle is immersed in DI water. The DNA bundle could be indeed completely trapped only after the combing protocol (Chapter 4.2), when the SNT is removed from the DNA solution.

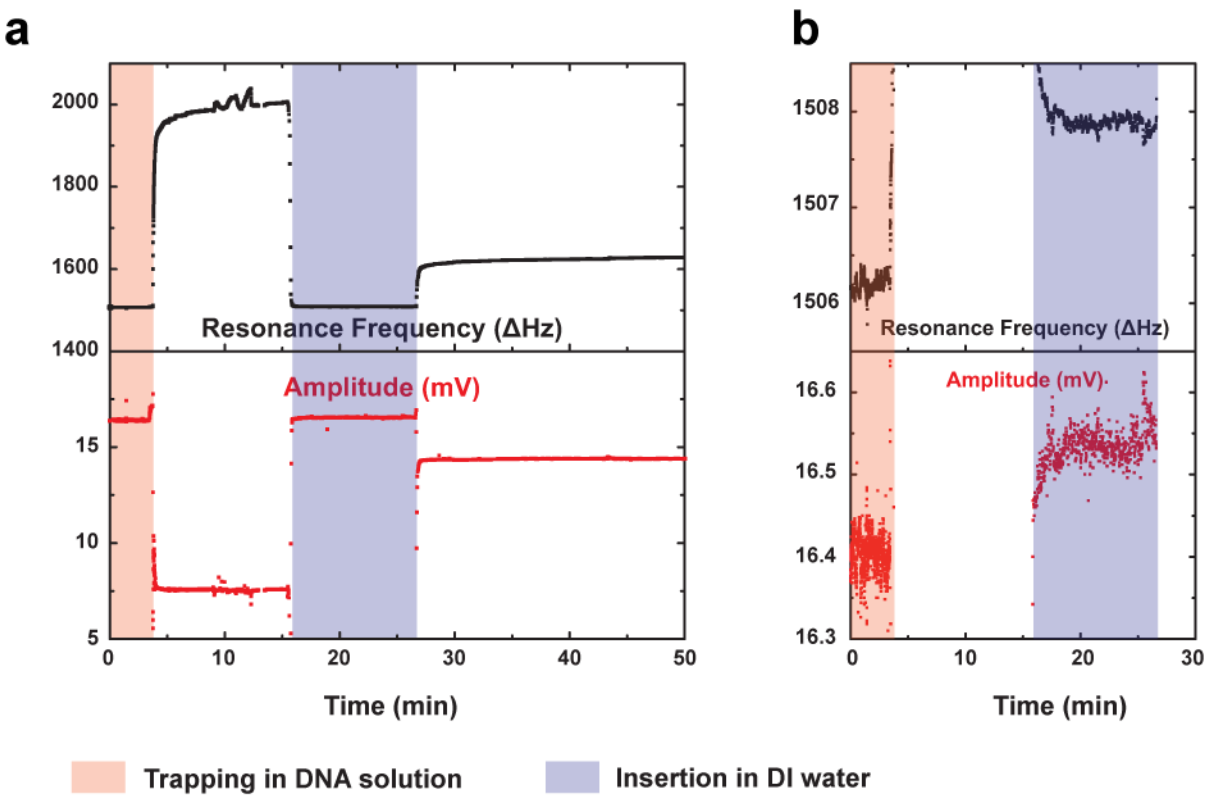

Figure 3.26: DNA insertion inside passive microfluidic cavity filled by DI water. **a.** F_R and A during DNA trapping, and after the trapping, in air and in DI water. **b.** Zoom on the graph **a** to illustrate the stability of the DNA mechanical properties in DI water.

The experiment Figure 3.27 summarizes the effect of the DI water on the SNT before and after DNA trapping. In the passive microfluidic cavity, and before the DNA trapping, F_R and A decrease when the SNT tips are immersed in DI water. This effect is due to the additional force gradient applied by the meniscus on the SNT.

The key point of the experiment is to compare, before and after the DNA trapping, F_R and A once the SNT tips are immersed in DI water (purple regions of the plot). F_R increases by 1.3Hz, and A decreases by 0.38mV. This variation is purely due to the additional stiffness and losses of the DNA bundle bridge between the two sharp tips of the SNT.

The signal measured during the insertion in cavity (1) and the DNA trapping (2) has been subtracted from the graph for two reasons. Firstly, large displacements of the robot generates sometimes enough noise to "unlock" the phase locked loop (PLL), and the signal is lost until the operator restarts the PLL. Secondly, the key idea of this graph is to underline the DNA effect on the SNT inside DI water (and the noisy signal in (1) and (2) do not help).

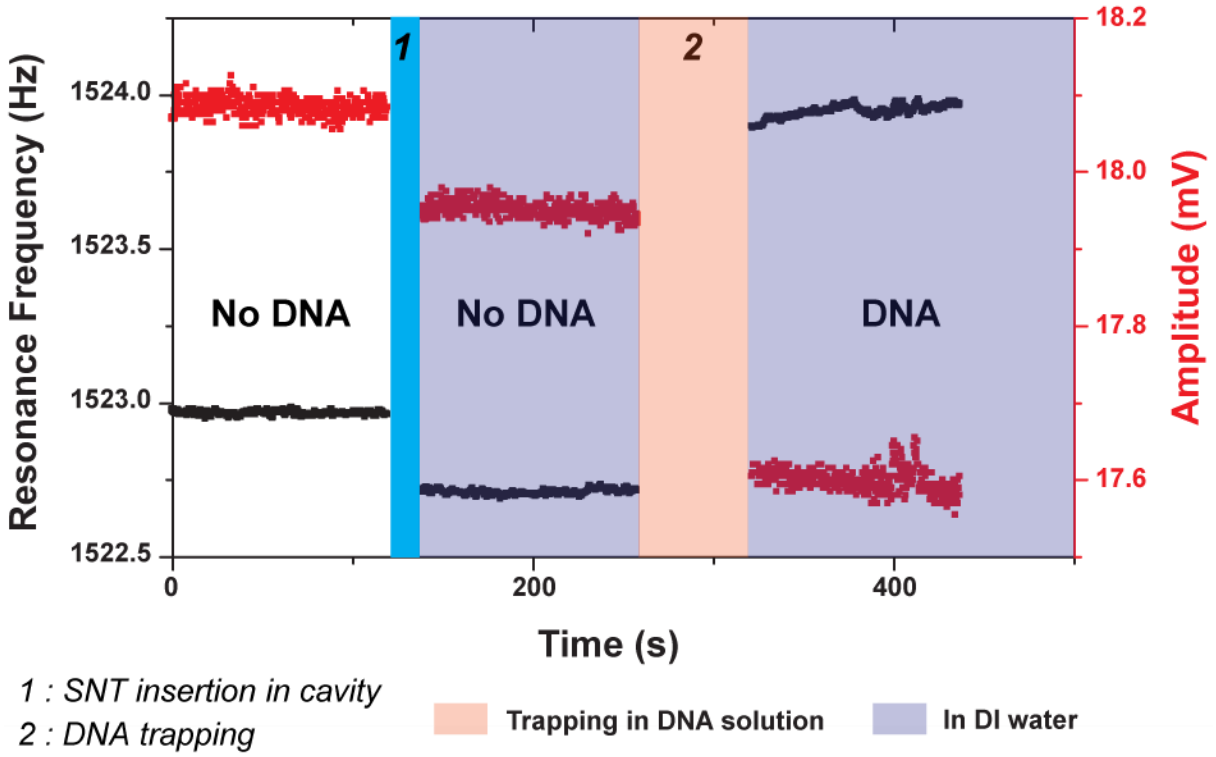

Figure 3.27: F_R and A measurements comparison in three cases: Bare SNT in air, bare SNT in DI water and SNT in DI water after DNA trapping.

3.7.2.2 pH effect on the DNA bundle

The previous paragraph shows the stability of DNA bundles inside DI water. The dynamic cavity allows to change liquid during the experiment and thus to reveal the effect of the pH on the mechanical properties of the DNA bundle.

After inserting the DNA bundle into the channel, pH effects are examined (Figure 3.29) using repetitive acid/buffer cycles: HNO_3 solution (pH 2.1) followed by 10 mM Tris•HCl solution (pH 6.8). After 20 s of flow, 6 min of incubation period (no flow) is performed to monitor the pH effect. Decreasing pH to more acidic values increases F_R and decreases A. By contrast, when adding the buffer the DNA returned to its initial condition. Changes in F_R and A depend on the amount of captured DNA and SNT characteristics. For better characterization of the bundle, we calculated the stiffness and viscous losses of the bundle to subtract the individual SNT effect from the results (see Equation 2.17 and Equation 2.18). In this way, the effect of decreasing the pH (from 6.8 to 2.1 in 7 steps using HNO_3) on the DNA bundle in real-time can be examined (Figure 3.30.a). In order to reverse the pH effect between each step, the acid was changed successively by two runs of Tris buffer solution (10 mM Tris•HCl for 3.5 min followed by 10 µM Tris•HCl for 1.5 min) thanks to the microfluidic pump. Decreasing pH caused an apparent increase in the stiffness and viscous losses (Figure 3.30.b) at proportional levels.

In these experiments, different effects of the pH on the DNA bundles can be hypothesized. A lower pH results in protonation of DNA, leading to a decrease in the negative charges along the phosphate backbone, although this may also be associated with a conformational shift [136]. Depurination and denaturation of DNA has been reported in the literature under acid pH. Moreover, DNA molecules could begin to repel less each other, and may form a tighter bundle with increased intermolecular interaction (Figure 3.28).

The overall observed result is that both the stiffness and the viscous losses increase with decreasing pH, i.e. with higher protonation. For our project, it may be relevant to try to use low pH values, to modify the stiffness of the DNA present between the tips, during and at the end of the experiment.

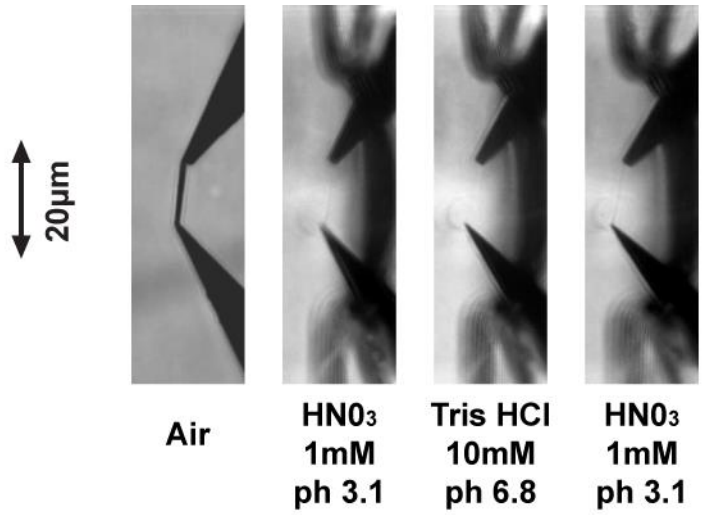

Figure 3.28: Picture of trapped DNA in air, nitric acid, and Tris•HCl buffer.[132]

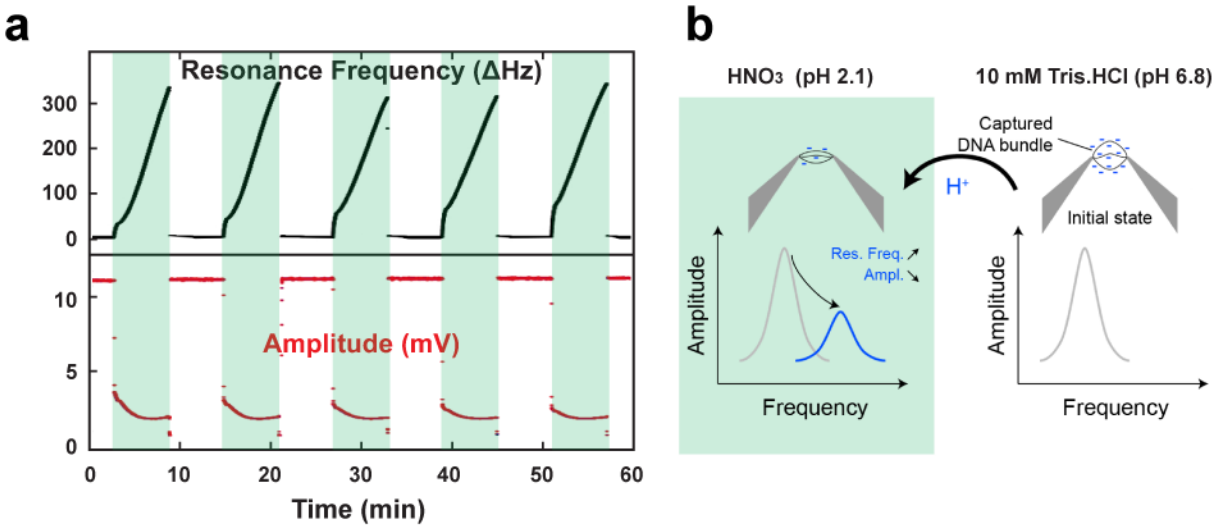

Figure 3.29: pH effect on DNA mechanical properties. Reversible effect of the acid by Tris•HCl. [132]

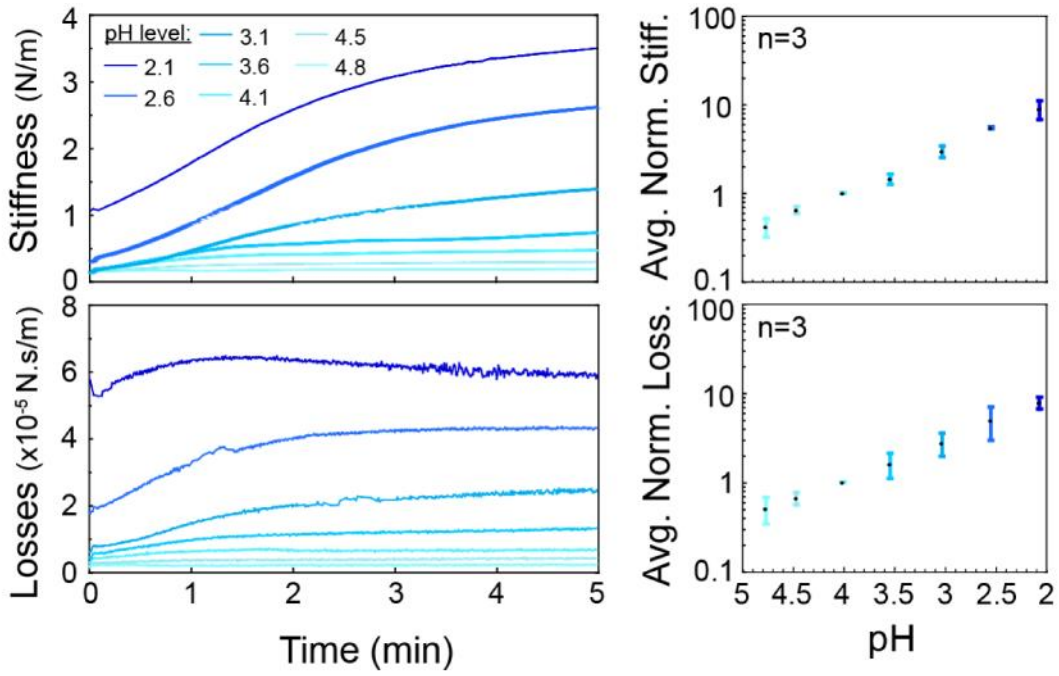

Figure 3.30: pH effect on the stiffness and viscous losses of a DNA bundles. [132]

3.7.2.3 Double-Actuators SNT

The pH effect on the DNA bundle mechanical structure was described in the previous part. The DNA bundle mechanical characterization requires less sensitivity for lower pH as the additional stiffness and viscous losses largely increase. This advantage is however hampered by a relative instability of the mechanical properties of the DNA bundle at low pH.

The DNA bundle is elongated inside Tris•HCl buffer, and the SNT is no longer able to sense it. The frequency response of the SNT is the same as for the bare SNT. To solve this problem, an idea is to open the gap between the two tips of the SNT to stretch the DNA in between the 2 tips. The advantage to use the Double-Actuators SNT is very clear in this case.

Firstly, a control experiment was performed inside DI water without trapped DNA, to evaluate the effect of the actuating arm actuation on the sensing arm measurements (Figure 3.31.a). The second arm is actuated by a cycle of square-root signal (V_{act2} from 0V to 40V) to generate a displacement linear in time (Equation 2.6). The noise generated by the second arm displacement is negligible and does not create instabilities of the air/liquid interface.

The same experiment is performed in Figure 3.31.b in Tris.HCl buffer after DNA trapping. The resonance frequency of the sensing arm increases while the amplitude decreases, upon increasing V_{act2}. The effect of V_{act2} on the amplitude is very small compared to the noise level

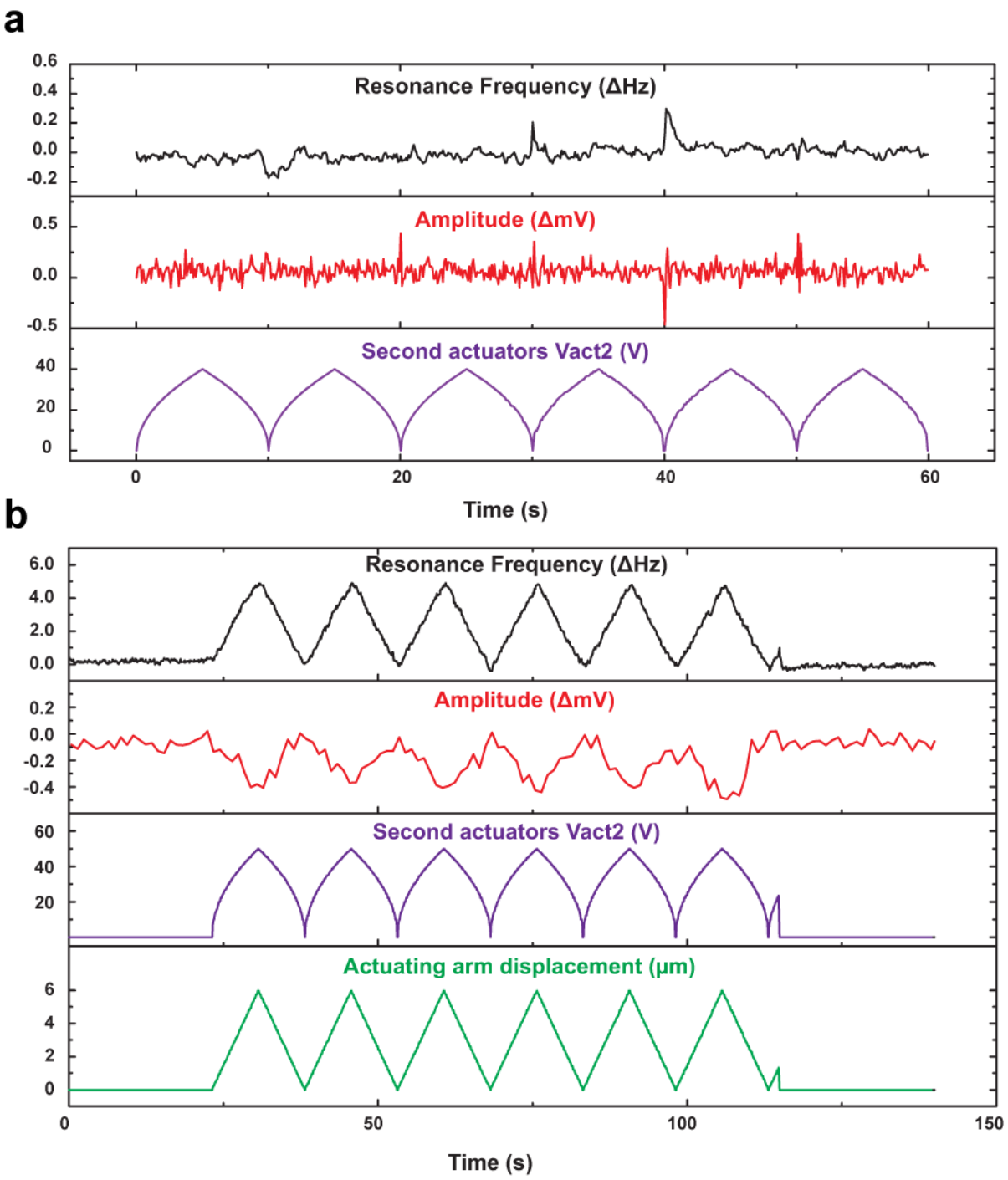

Figure 3.31 Effect of a cycle of second arm actuation (Vact2) on the sensing arm measurements, with SNT tips inside liquid. **a.** Before DNA trapping inside DI water **b.** After DNA trapping inside Tris.HCl buffer.

of the signal, therefore the amplitude measurement must be averaged (average 10 points of measure) to observe its variations.

The Figure 3.32 displays the same experimental data as Figure 3.31.b in a different way. The DNA bundle elongation is calculated from V_{act2}, and the resonance frequency is plotted versus

the DNA elongation, for every value measured during the six cycles of gap opening/closing (from 14µm to 20 µm) of the SNT tips. The DNA bundle properties are not constant when it undergoes elongation. A linear law links the DNA bundle stiffness to the DNA elongation, and the linear fit gives the slope (26.5 $mN.m^{-1}/\mu m$).

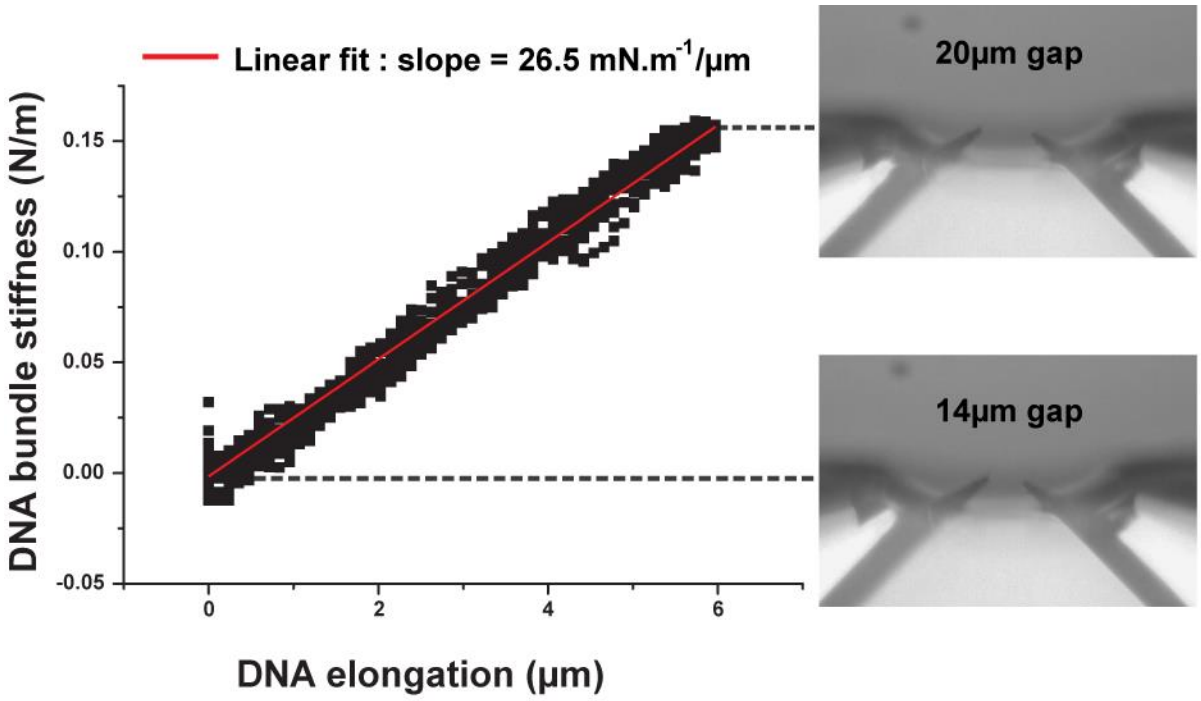

Figure 3.32 Effect of the DNA elongation on DNA bundle stiffness (D-A SNT immersed inside Tris.HCl buffer).

The stability and noise of F_R and A after the DNA elongation is also evaluated in Figure 3.33. A is not strongly changed by the DNA elongation, unlike F_R which increases by about 4Hz during the elongation, and then decreases slightly. The experiment can be read in terms of the stiffness and viscous losses of the DNA bundle. In these terms, the DNA bundle elongation has a small effect on its viscous losses, while the DNA bundle is stressed and its stiffness increases. Finally, some internal relaxation is also observed after the DNA elongation.

The D-A SNT is able to elongate the DNA bundle, thus increasing the resonance frequency shift of the SNT after DNA trapping. The D-A SNT is thus capable of sensing the DNA bundle inside Tris•HCl (i.e., at close-to-neutral pH) and opens the way of DNA mechanical characterization in a complex medium.

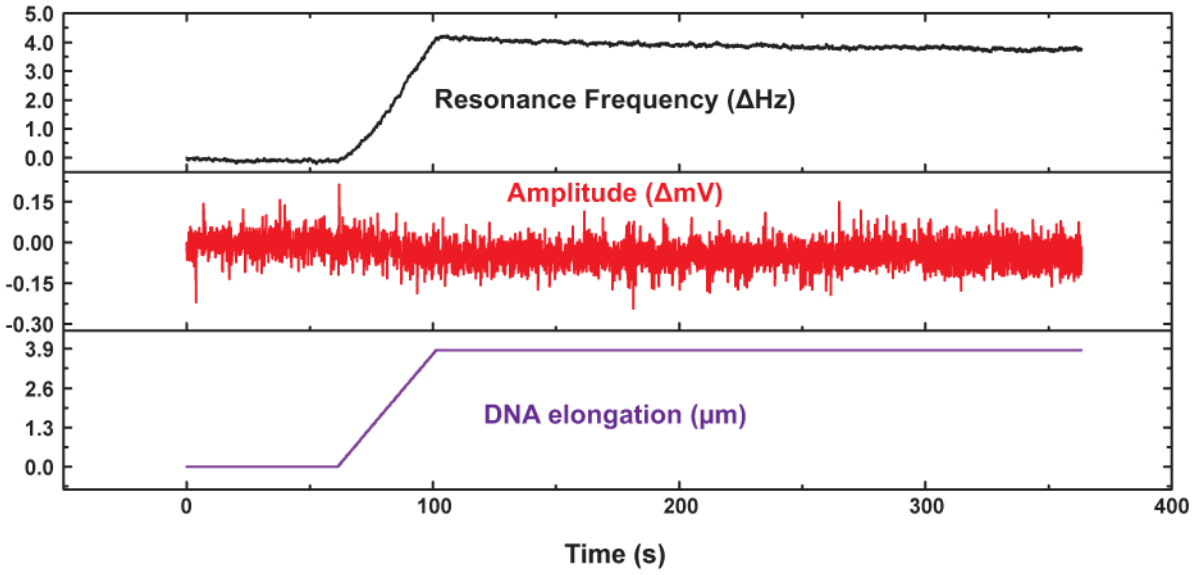

Figure 3.33: Stability and noise of F_R and A, before and after DNA elongation.

3.8 Conclusion

A complete experimental setup has been developed to allow the real-time DNA mechanical characterization under radiotherapy treatment. The ionizing radiation effect on the bare SNT is quantified, and the capability of the setup to characterize DNA bundle, in air, in DI water, and also in others mediums thanks to the dynamic microfluidic cavity and the D-A SNT, is demonstrated. The stability of the setup has been quantified in this chapter and allows uncorrelating the effect of the ionizing radiation on the DNA bundle in the next experiments.

The Figure 3.34 is a picture of the new complete setup installed in the Cyberknife's room of the *Centre Oscar Lambret*. The setup is built on trolleys, to optimize its installation at the beginning of the short time (about 2h) allocated for research experiments, after daily patient treatments.

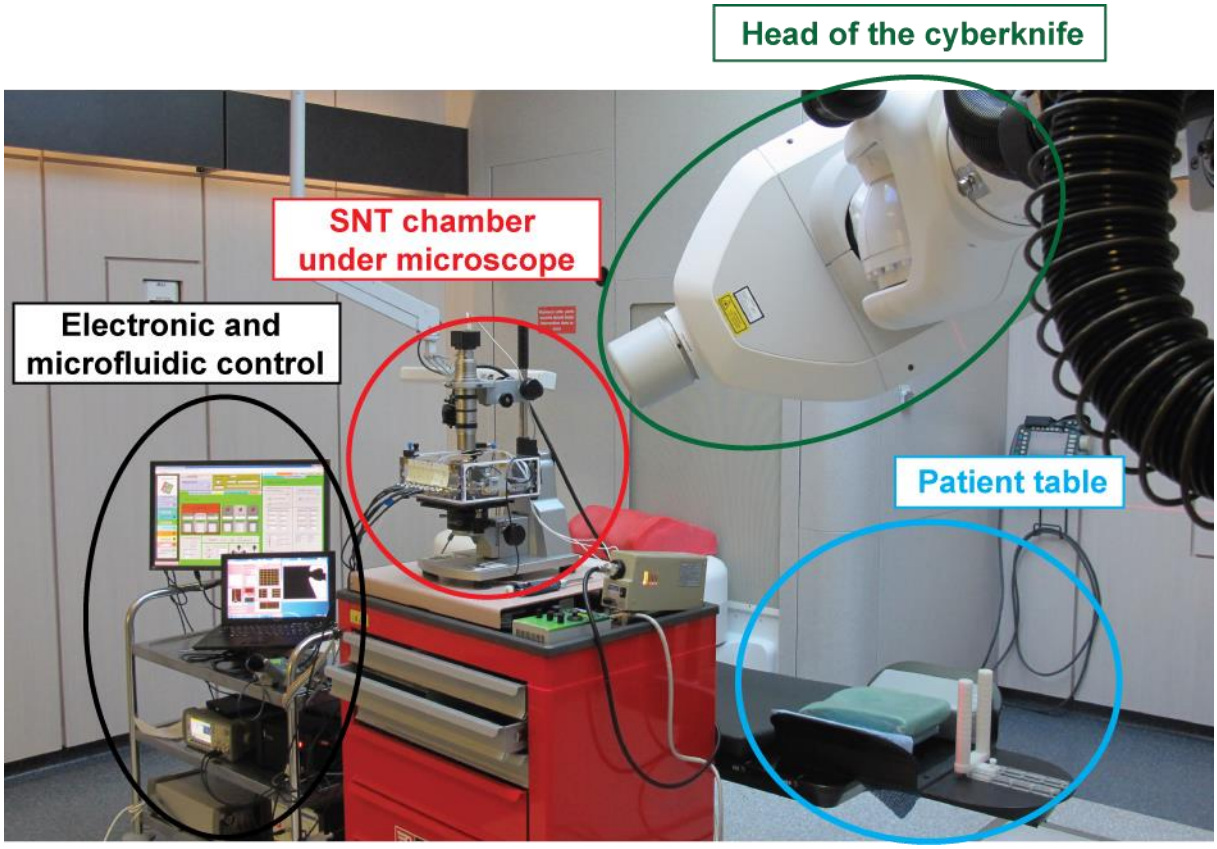

Figure 3.34: The complete setup in *Centre Oscar Lambret* hospital in Lille.

Chapter 4: Experimental Protocol

4.1 Introduction

The experimental protocol is automatized as much as possible, for two main reasons. Firstly, the repeatability of the experiments is improved by the automation of the key steps of the protocol. Secondly, the protocol is developed to optimize the runtime of the experiments under real daily hospital conditions. The priority of the radiotherapy center is obviously the treatment of the patients, so time is critical.

The key steps of the experimental protocol are detailed in the following paragraphs: DNA trapping, and SNT insertion both in the passive and dynamic microfluidic cavity. Finally the complete experimental protocol is summarized.

4.2 DNA trapping

In this paragraph, the objective is to briefly describe the DNA trapping method. For more detailed explanations on DNA trapping by dielectrophoresis (DEP) and its theoretical background, the reader should refer to the pioneering work of Washizu and Kurosawa [137].

Two different protocols are used, with similar results. In every case, a solution of double-stranded λ-DNA (48.5 kbp, 16-µm-long) is diluted in deionized water. The DNA trapping protocol is based on dielectophoresis and combing.

The DNA can be trapped in a dedicated **DNA cavity**. Around 3µL of the prepared DNA solution is introduced inside the DNA cavity, which is housed on the side of the passive microfluidic cavity (see again Figure 3.5). With the help of the positioning robot, the tips of the SNT are inserted approximately 30µm inside the DNA solution. The DNA cavity then makes a lateral movement of 2mm at 20µm.s^{-1} while applying a high frequency electric field (around 1MV/m, 1 MHz). In this way, DNA strands are "combed" by the meniscus. DNA strands are attracted by DEP around the aluminum tips of the SNT ([138],[131]). Upon reaching the end of the cavity, the positioning robot slows down to 1µm.s^{-1}, to optimize the combing of DNA from the right to the left tip. Then the actuating arm of the SNT, which is fixed, is extracted from the cavity and absorbs the capillarity force without damaging the new DNA bundle. One advantage of this protocol is the possibility of **fully automating** the DNA trapping, since the position of the DNA cavity is fixed. Another advantage is that the combing effects by the meniscus help the DNA bundle retrieval from solution.

In the case of a Double-Actuators SNT, the actuating arm is not fixed. Capillary force can therefore move the arm, and strongly increase the gap between the tips once these tips are

removed from the DNA solution. For this reason, DNA trapping in the DNA cavity with a Double-Actuators SNT cannot be recommended. In this case, the DNA is separately trapped in a **droplet** of prepared DNA solution, as illustrated in Figure 4.1. The protocol between the trapping in the cavity and the trapping in the droplet is similar. In the case of the droplet, the tips of the SNT are inserted and moved manually by an operator, following the curved shape of the droplet. The first tip is removed from the droplet in the same manner as from the cavity. Then, the second tip is moved to generate a force perpendicular to the mobile arms. In this way, the gap between the tips remains stable, and the DNA bundle is saved.

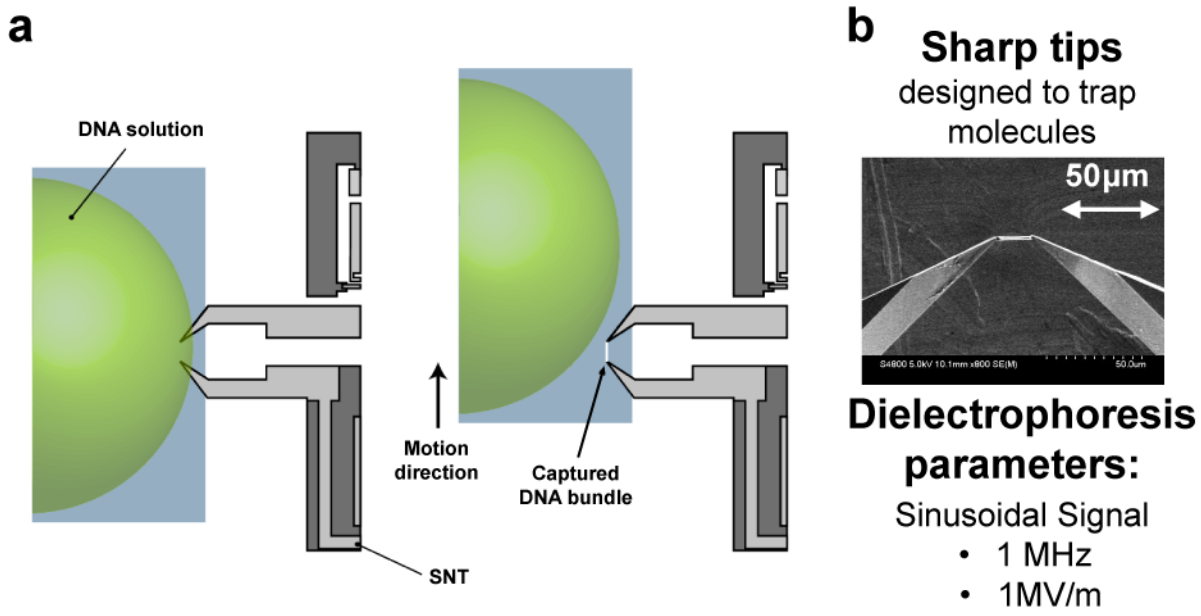

Figure 4.1: a. Schematic of the DNA trapping protocol. **b.** Picture of DNA trapped between sharp tips of the SNT and dielectrophoresis parameters.

4.3 SNT insertion inside a passive microfluidic cavity

4.3.1 Introduction

After SNT insertion inside a liquid, an additional force gradient is applied to the mobile arm by the meniscus' surface tension. In order to measure the mechanical properties of the DNA, this interface force must be minimized and subtracted from our measurements. To minimize the force, the SNT is placed in the middle of the meniscus, so as to make the system symmetrical. Then, a measurement of the mechanical properties of the bare SNT is recorded at this position, allowing for the subtraction of this force.

The electrical and mechanical properties of a DNA bundle correlate strongly to the relative humidity of the ambient environment. These properties are described in detail below, and will be moreover used to automatically locate the center of the opening window, to get the symmetric configuration pointed out before. By using the SNT after DNA trapping, it is possible to measure the relative humidity close to the aperture of the microfluidic cavity. Notably, such a tool can be used in a more general way to create a 3D humidity image in a micro-environment as illustrated in Figure 4.2.

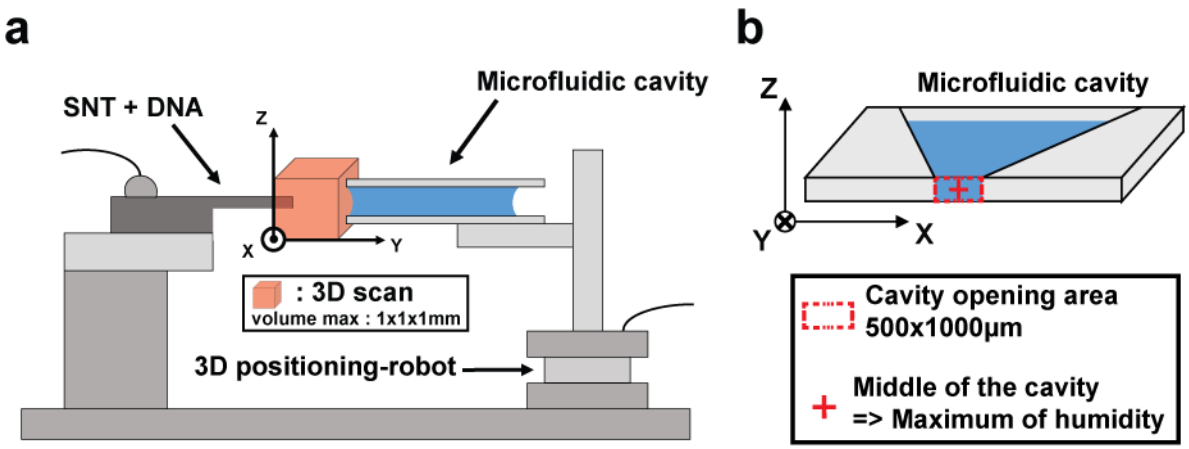

Figure 4.2: Humidity imager Set-up. **a.** Microfluidic cavity on the top of the positioning-robot front of the SNT after DNA trapping. Scanning accessibility in red **b.** Schematic of the middle of the opening of a passive microfluidic cavity.

4.3.2 DNA bundle conductance vs. humidity

Besides its mechanical capabilities, the SNT enables also to carry out electrical experiments on DNA bundles. The DNA bundle conductance shows an exponential dependence on the relative humidity, as shown in Figure 4.3. An explanation for this dependence is reviewed by Yamahata and al [10]. That work suggests that the conductivity of DNA is due to water adsorption on the molecule. The exponential dependence of the conductivity with the relative humidity can then be explained by the change of permittivity arising from this adsorption.

This well-established exponential relationship between DNA bundle conductance and the relative humidity will be used in the following paragraph, to establish the relationship between DNA bundle stiffness and relative humidity.

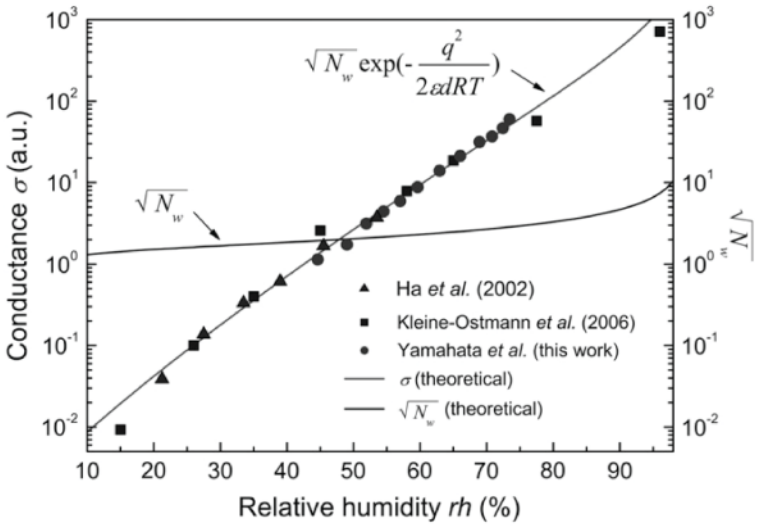

Figure 4.3: Comparison between experimental data found in the literature and the theoretical model of conductance. The other experimental data are extracted from the articles published by Ha et al. [139] and Kleine-Ostmann et al. [140]. An arbitrary unit is used because the slope of the curves is subject of interest. For the comparison, $\sqrt{\mathbf{Nw}}$ is also plotted: It clearly shows that the increase of ε (permittivity) with *rh*, rather than with the fraction of adsorbed water (N_w), is the dominating parameter that explains the increase of σ. [10]

4.3.3 DNA bundle stiffness vs ambient humidity

First, the conductance and the stiffness of the DNA bundle are plotted for different distances of the DNA bundle from the meniscus of the passive microfluidic cavity, taken to define the *y*-direction (Figure 4.4.a). The microfluidic cavity provides a source of humidity, and the moisture diffusion process is modeled by a Fick's system (1D model along *y*). The result is an exponential distribution of the relative humidity *rh*. The logarithm of the conductance is then linear with the humidity [10], therefore log(Conductance) and the relative humidity have the same decay length x_0, fitted in Figure 4.4.a. The "relative humidity" vs. "distance to the meniscus" is calculated and plotted in Figure 4.4.b, by knowing the room temperature and the position of the air/liquid interface. Lastly, the "DNA bundle stiffness vs relative humidity" is plotted in Figure 4.5, and exhibits a logarithmic dependence.

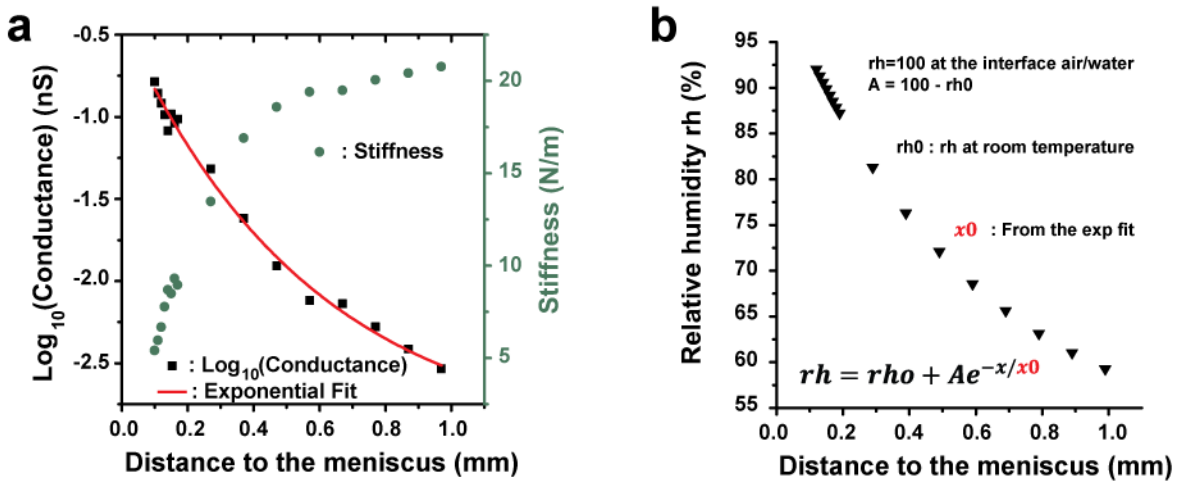

Figure 4.4: a."log(DNA bundle conductance) and DNA bundle stiffness" vs "Distance of the DNA bundle to the meniscus. **b.**"Relative humidity" vs "Distance to the meniscus"

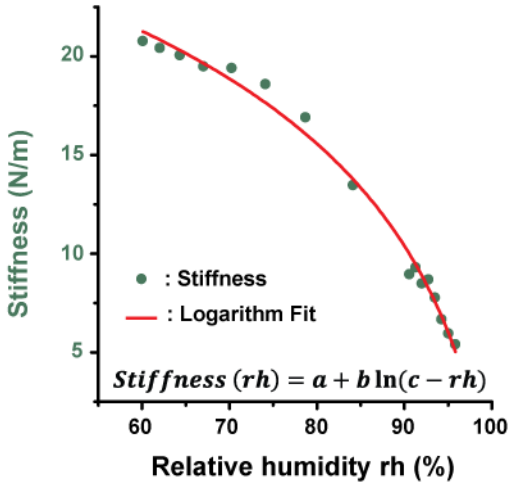

Figure 4.5: "DNA bundle stiffness" vs. "relative humidity".

4.3.4 3D humidity imager

The ability of the SNT to measure the relative humidity can be used to build a 3D humidity imager in confined environment, e.g. around the aperture of microfluidic cavity. The microfluidic cavity of interest is mounted on a 3D positioning robot in front of the SNT with trapped DNA (Figure 4.2). The humidity sensor (SNT with trapped DNA) scans the volume in front of the microfluidic cavity with a controlled speed (from 1µm/s to 100µm/s) and, at a set of programmed positions, records the DNA bundle stiffness. Finally, the humidity image is extracted from the bundle stiffness thanks to the established relationship (Figure 4.5).

The 2D scans of the humidity around the cavity are then plotted for four different distances in Figure 4.6. The robot moved at a continuous speed (10µm/s) in the *x*-direction and the humidity was recorded in steps at every 20µm. The robot displaced the cavity of 20µm in the *z*-direction for every 800µm in the *x*-direction. The result is a 3D image of the humidity distribution around the opening of the cavity.

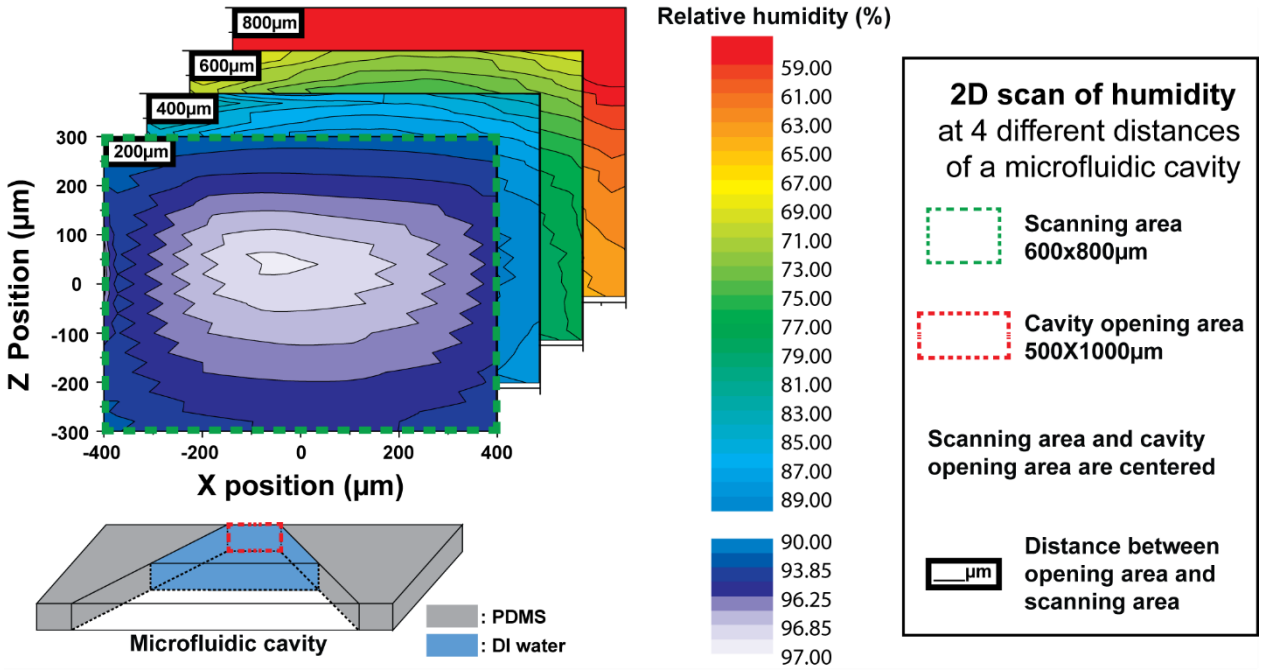

Figure 4.6 : 3D image of humidity around the opening of a microfluidic cavity

4.3.5 Automatic insertion of DNA in microfluidic cavity

The 3D humidity imager provides an accurate method of positioning the SNT. The SNT itself, after the DNA trapping, is used as a humidity sensor with acute precision, for an automatic detection of the cavity center (i.e., the highest humidity value) shown in Figure 4.2.

The stiffness measurement of the DNA bundle is plotted in Figure 4.7 during a 2D scan of the entire cavity with a high and continuous speed (100µm/s). To obtain the middle position of the meniscus, only two scans are necessary in the *x*- and *z*-directions. The minimum DNA bundle stiffness gives the position of the middle of the cavity, corresponding to the position with the highest value of humidity. At this position, together, the SNT and the DNA bundle are inserted into the meniscus at a constant, slower speed (5µm/s) and their position is recorded. When the tips barely touch the meniscus, DI water is attracted by the capillary force, thus the insertion

depth depends on the surface properties of the SNT tips. The irradiation experiments can then be performed. After the irradiation, DNA is washed away and the SNT characteristics are checked again at the same position inside the microfluidic cavity, to verify that the bare SNT is recovered.

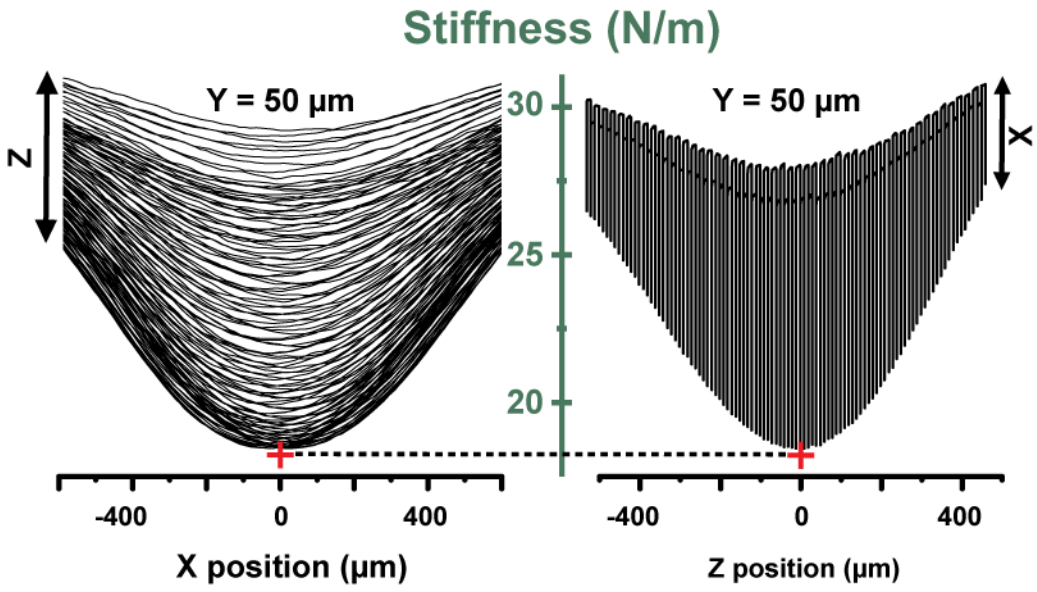

Figure 4.7 : Automatic detection of the middle of a microfluidic cavity.

4.3.6 Conclusion

This new method correlates for the first time the DNA bundle stiffness variation with humidity. This model allows using the SNT itself to measure a 3D humidity image in a confined environment, with µm-order resolution. In the case under study, this novel method automatically identifies the cavity center position, for an optimal insertion of the SNT inside the microfluidic meniscus.

4.4 SNT insertion inside the dynamic microfluidic cavity

4.4.1 Microchannel filling

The geometry of the dynamic microfluidic cavity (Figure 3.6) impacts on the filling of the microchannel. Therefore, a set of experiments was performed to evaluate the best dimensions, in order to be able to properly fill the cavity with the required solution. An example of the microchannel filling by DI water is illustrated in Figure 4.8. Depending on the height of the channels, the liquid volume inside the channel varied between 0.5 µl and 3 µl for the different devices used in the experiments. The majority of the experiments were performed in 1-µl channels. To change the solutions inside the channel, a pump applied a vacuum to generate a flow of 50±5 µl min^{-1} for 20 s. The flow corresponded to insertion of 15 µl of solution, which was 5 times the volume of the biggest channel. The applied vacuum depended on the channel and the size of the side-opening, varying by several mbar (~ -10 to -30 mbar).

For better understanding of the dynamic microfluidic cavity geometry, two pictures of the cavity in Figure 4.9 show the meniscus of the opening cavity, before and during the SNT positioning.

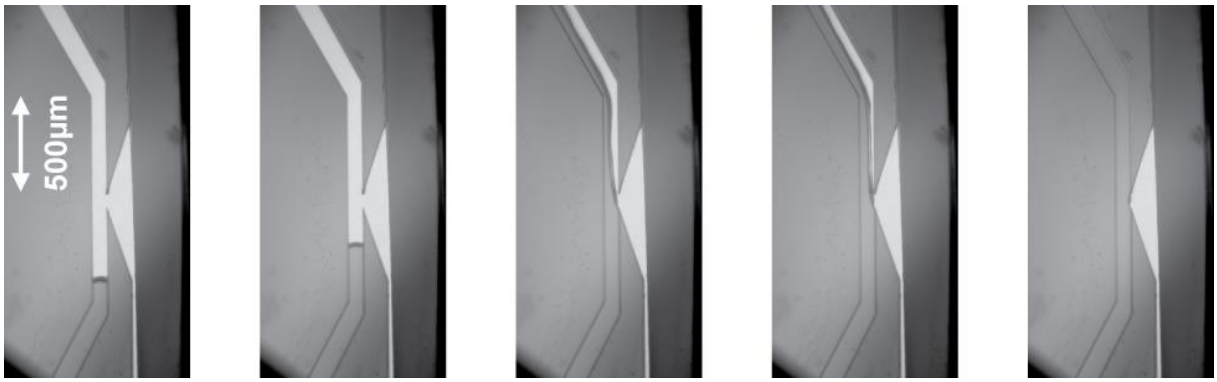

Figure 4.8: Pictures of the microchannel filling by DI water

4.4.2 Detection of the meniscus

The motion of the microfluidic device (on the XYZ stage) was controlled with the LabVIEW program, for the precise relative positioning of the SNT and cavity. To start the insertion protocol, illustrated by the schematic in Figure 4.10, the brimming PDMS is placed over the bare SNT. (a) The first step is to detect the relative position of the PDMS layer (top of the channel) and the SNT. The developed LabVIEW software run the XYZ stage (0.1 µm steps with a speed of 100 µm s^{-1}) while monitoring the resonance frequency F_R. When the PDMS

layer touches the mobile arm of the SNT, a lock-in-amplifier detects the sudden change in the frequency response (amplitude and phase) and stops the XYZ stage. The microfluidic device is then moved 30 µm away from tweezers, for safe insertion between the PDMS and glass layers. (b) After moving the microfluidic device toward the tweezers, the second step is to detect the top and bottom level position of the channel (PDMS and glass levels). The same detection technique is used, i.e. to follow the sudden changes in the frequency response. Finally, the device is placed at the middle of the aperture height, for stable operation (Figure 3.19) (c) The third step was to detect the air-liquid interface. By moving the microfluidic device toward the SNT, a sudden change in the frequency response was detected instantly when the tweezers touched the interface. Then, the device was moved back to a safe position (50 µm away from the tweezers).

The relative position of SNT tips with respect to the PDMS walls and the glass surface affects the stability of the detection. All the microfluidic devices used in the next experiments satisfy the design conditions for stable detection (i.e. w>110µm, h>90µm) established during the characterization of the dynamic microfluidic cavity (Chapter 3.7.1.3). All the experiments are performed at a 5-µm immersion depth.

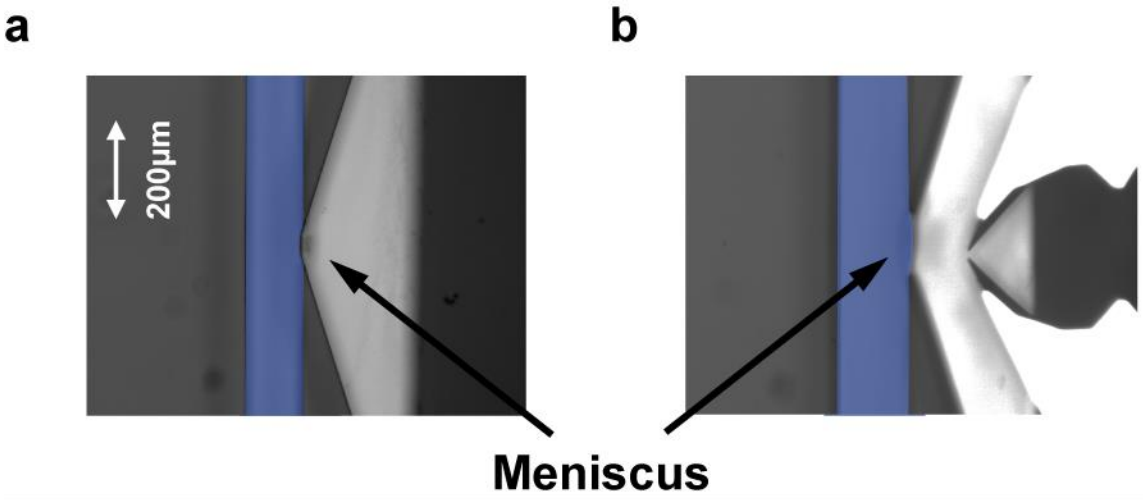

Figure 4.9: Pictures of the dynamic microfluidic cavity before and during the SNT positioning. The microchannel filled by DI water is highlight in blue for a better understanding.

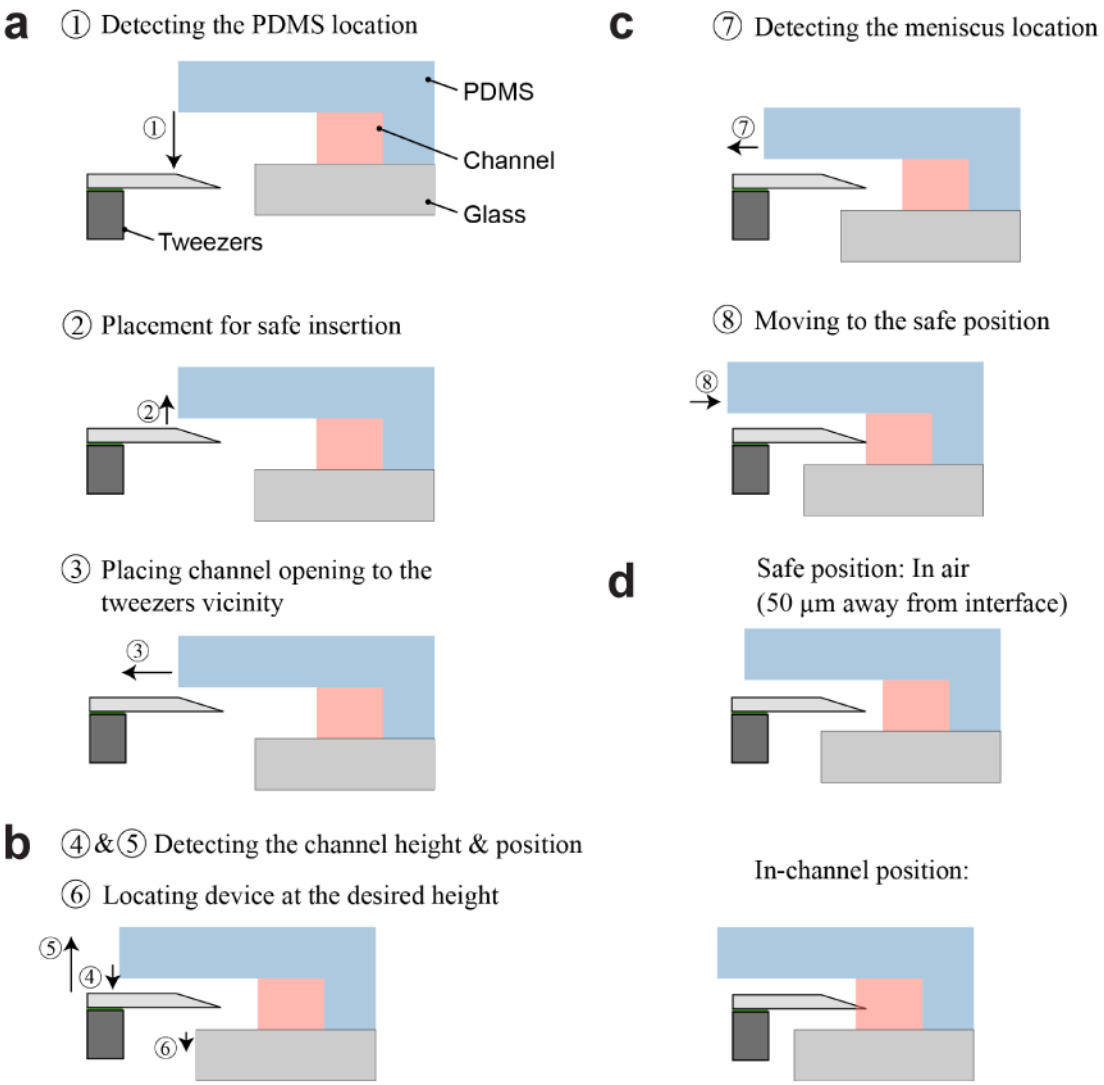

Figure 4.10: Tweezers insertion protocol is performed in three steps. **a.** Channel top-level detection (1,2) and tweezers is positioned close to the channel vicinity (3). **b.** Detection of the precise channel location (4,5) and positioning (6). **c.** Detection of the air-liquid meniscus (7) and safe positionning is saved before DNA trapping (8). **d.** Assays is performed inside channel at the desired immersion depth.[141]

4.5 Summary of the experimental protocol

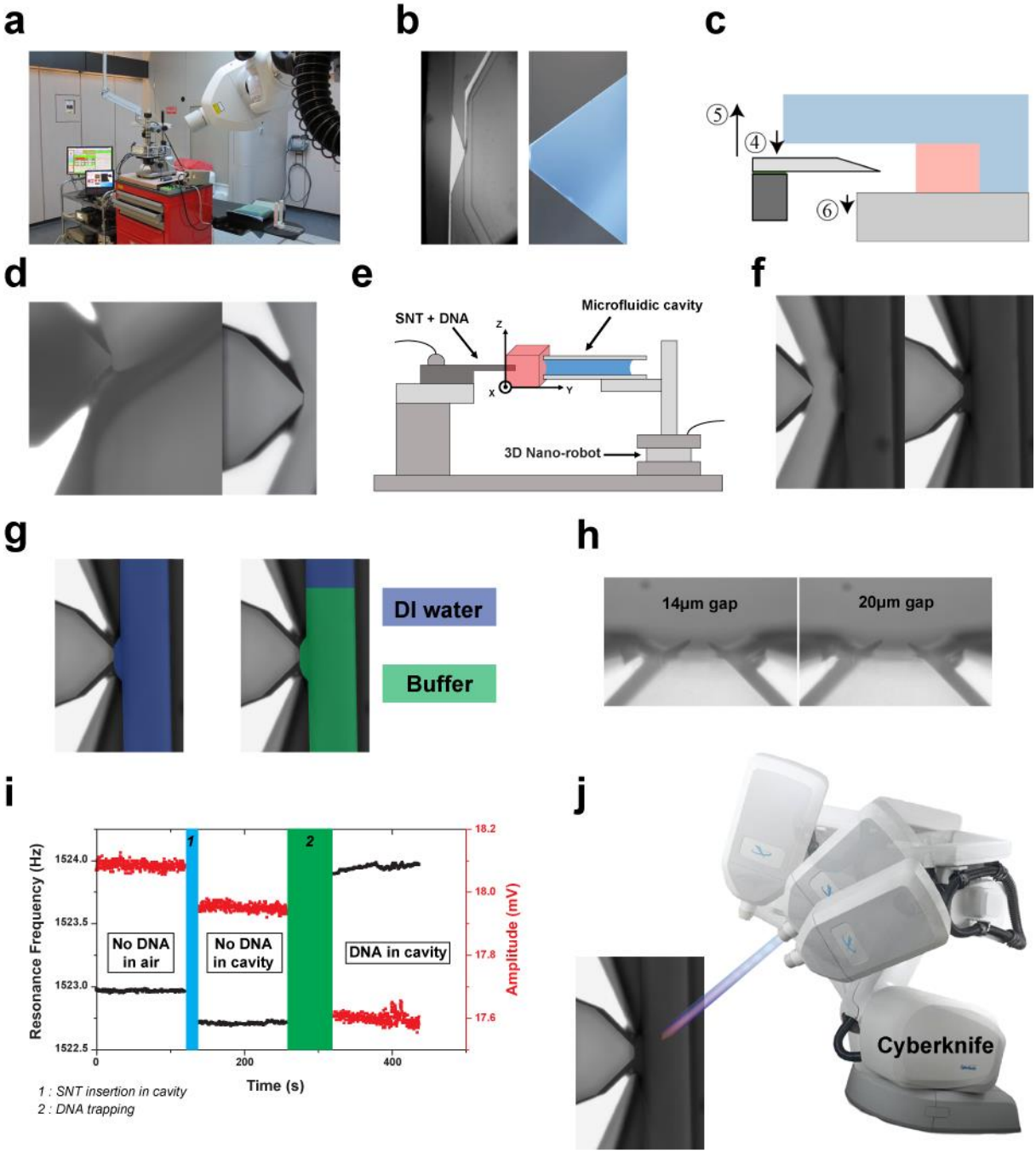

Figure 4.11: Resume of the experimental protocol

a. Installation of the set-up (hospital environment) (Chapter 3.8)
b. Filling the Microfluidic cavity (Chapter 4.4.1)
c. Meniscus detection: if dynamic microfluidic cavity (Chapter 4.4.2)
d. DNA trapping (Chapter 4.2)

e. Meniscus detection: if passive microfluidic cavity (Chapter 4.3.5)
f. Insertion of SNT + DNA inside the microfluidic cavity (Chapter 4.4.2 and 4.3.5)
g. Resuming of the protocol in terms of resonance frequency (Chapter 3.7.2.1)
h. Change the medium is possible if dynamic microfluidic cavity (Chapter 4.4.2)
i. DNA elongation is possible with D-A SNT (Chapter 2.3.2)
j. Ionizing irradiation by the Cyberknife (Chapter 3.2)

4.6 Conclusion

The SNT is able to trap DNA with either a manual or automatic protocol. The SNT tips are automatically inserted in the passive or the dynamic microfluidic cavity, thanks to two dedicated protocols. The setup is ready for the real-time mechanical characterization of a DNA bundle under the ionizing radiation beam of the radiotherapy machine. The DNA bundle environment conditions can be changed to evaluate their effect on DNA bundle mechanical properties evolution during an irradiation.

Based on this protocol, a set of irradiation experiments, in different medium, will be described and reported in the following chapter.

Chapter 5: Results and Discussions

5.1 Introduction

The ionizing radiation effect on the structural and mechanical properties of the DNA bundle is a complex process (Chapter 1.2.7). In every medium, the DNA bundle is equally damaged by the **direct** effect of the ionizing radiation. However, the **indirect** effects of the ionizing radiation on the DNA bundle depend on the medium (Chapter 1.3.1.3). In general, the global stiffness of the DNA bundle is expected to decrease, due to accumulation of SSB and DSB defects in DNA molecules. However, different types of aqueous medium may produce different kinetics of the degradation of the DNA bundle stiffness.

Before the DNA bundle irradiation, the resonance frequency F_R of the specific bare SNT used for the experiment is measured during an irradiation session, to provide a negative experiment in order to control that the SNT is not affected by the irradiation, and to provide the mechanical characteristics of the bare SNT as a reference for the DNA stiffness calculation.

The LINAC accelerator generates the γ-radiation beam with a photon energy spectrum centered around 6 MeV. The irradiation dose received by a DNA bundle is inversely proportional to the square of the distance between the source of the LINAC accelerator and the DNA bundle. Moreover the dose delivery depends obviously on the time of an irradiation period. In order to be able to compare different experimental results, the dose delivery during one period is always maintained around an arbitrary value of 30 Gy (around 10 times the dose of a session of a patient treatment). The time of an irradiation period can sometimes be different in the following experiments, in order to compensate the change of distance between the DNA bundle and the LINAC.

In the following of this Chapter, the real-time DNA bundle characterizations under ionizing radiation from a therapeutic machine (Cyberknife) will be performed in different mediums. Firstly in air, then in DI water, and finally in HNO_3 and Tris•HCl buffer.

In the final subsection of discussion, 5.3.2, the variation of the DNA bundle stiffness during its complete degradation in DI water will be interpreted by following a theoretical model developed in our research group [11], [79]. Finally, the limitations of the SNT method for the DNA damage characterizations under ionizing irradiation will also be discussed.

5.2 Results

5.2.1 DNA irradiation in Air

The first real-time DNA characterization by SNT was performed in air. Ambient air is not the most relevant environment, since it is very far from the cell environment. However, such a first important experiment allowed demonstrating the ability of the SNT to endure the harsh electromagnetic field of the Cyberknife, and measure simultaneously an appreciable variation of the DNA bundle mechanical properties.

The graph in Figure 5.1 shows the real-time measurement of the resonance frequency (F_R) of a SNT with trapped DNA bundle in air. The irradiation (green region in the plot) was performed for 220 seconds, delivering a nominal dose of 30 Gy. First, it can be noted that F_R is relatively stable before and after the ionizing irradiation. However, F_R ~~is~~ decreases during ionizing irradiation. Moreover, the reference shows a high stability of the bare SNT under irradiation and therefore the decrease of F_R should be ascribed to a change of the mechanical properties of the DNA bundle. Equation 2.17 connects the decrease of the resonance frequency F_R to the decrease of the DNA bundle stiffness k_{DNA}.

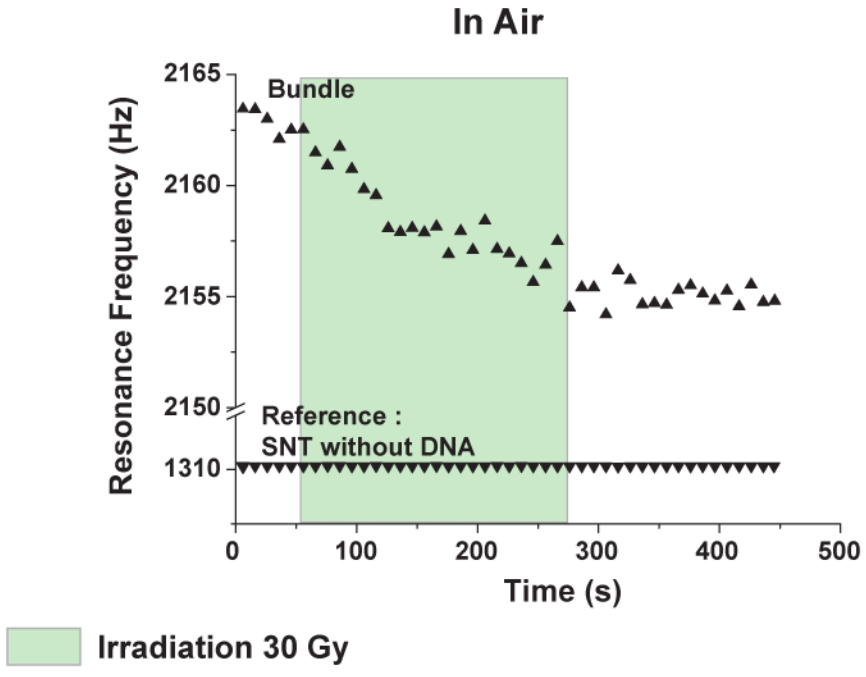

Figure 5.1: Variation of the resonance frequency of the SNT after DNA trapping under irradiation in Air. An irradiation in equivalent conditions but without DNA is performed to provide a reference.

From the Equation 2.19, the relative variation of a DNA bundle stiffness, $\frac{\Delta k_{DNA}}{k_{DNA\ init}}$, can be calculated, to normalize and compare different experiments:

Equation 5.1

$$\frac{\Delta k_{DNA}}{k_{DNA\ init}} = \frac{(F_{T+DNA\ init})^2 - \left(F_{T+DNA\ fin}\right)^2}{(F_{T+DNA\ init})^2 - (F_T)^2}$$

where Δk_{DNA} is the difference of the DNA bundle stiffness before and after the irradiation, and $k_{DNA\ init}$ is the DNA bundle stiffness before the irradiation. $F_{T+DNA\ init}$ and $F_{T+DNA\ fin}$ are respectively the resonance frequency of the SNT with trapped DNA bundle, before and after the irradiation; F_T is the resonance frequency of the bare SNT.

For this specific experiment in air, for example, the relative-variation of the DNA bundle stiffness is estimated: $\frac{\Delta k_{DNA}}{k_{DNA\ init}} = 1.2\%$

At this stage, it is impossible to correlate this change of DNA bundle stiffness with the accumulation of radiation-induced defects, such as SSB (single-strand break) and DSB (double-strand break). In fact, other parameter changes, the environment close to DNA bundle (humidity envelop), as well as other types of DNA degradation could also be at the origin of the observed decrease of the DNA bundle stiffness. Nevertheless, the direct correlation between the irradiation time and the decrease of the DNA bundle stiffness is evident.

5.2.2 DNA irradiation in DI water

As explained in chapter 0, environment modifies the ionizing irradiation effects on the DNA. During irradiation, a strong predominance of indirect damage has been demonstrated when compared to direct damage [134], as is explained in detail in Chapter 1.3.1.3. To generate both types of damage during the experiments, DNA is placed inside DI water to simulate the way in which DNA is damaged by water radiolysis products generated during irradiation of human cells.

5.2.2.1 Same SNT: 2 different bundles

The experiment in Figure 5.2 reports the mechanical characterization of DNA bundles trapped by SNT and placed in DI water. In order to establish the repeatability of the experiment, two different bundles are trapped by the same SNT and undergo the same ionizing irradiation protocol. The graph in Figure 5.2 compares the variation of the resonance frequency of the SNT

with these two bundles during the experiment. A reference is given by the irradiation of the bare SNT.

The initial resonance frequency of the SNT with both bundles is similar and around 0.3Hz higher than the reference measurement. For both bundles, the resonance frequency is stable before and after the 30Gy of irradiation. However, as in air, a significant decrease of the resonance frequency is observed during the intermittent irradiation (in green).

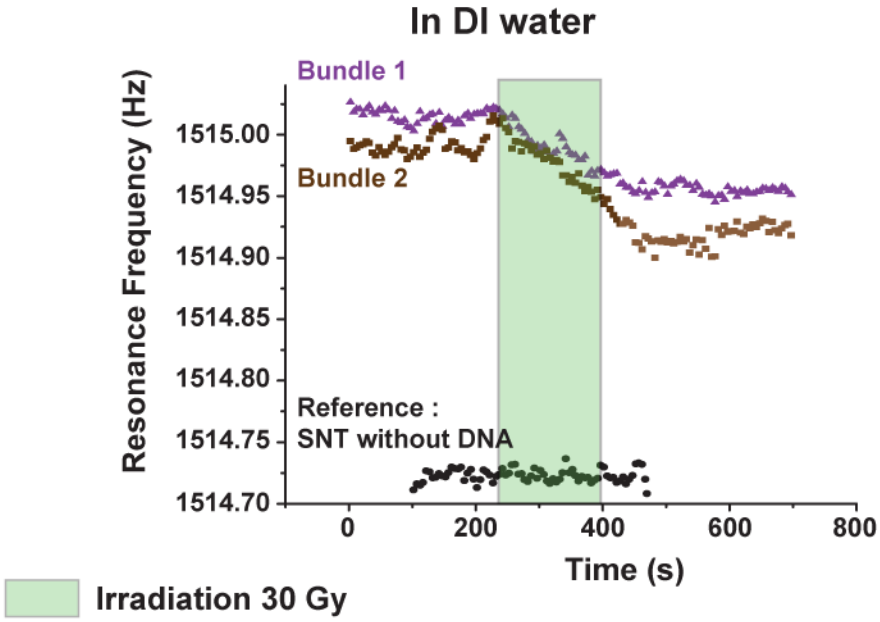

Figure 5.2: Comparison of the irradiation effect on the resonance frequency of 2 different DNA bundles in DI water trapped with the same SNT

In order to compare the effects of the irradiation on this two different bundles in DI water, the relative-variation of the DNA bundles is calculated in both cases,as:

$$\text{Bundle 1: } \frac{\Delta k_{DNA}}{k_{DNA\,init}} \cong 20\% \quad \text{and} \quad \text{Bundle 2: } \frac{\Delta k_{DNA}}{k_{DNA\,init}} \cong 25\%$$

The relative DNA bundle stiffness decrease during the 30 Gy of irradiation has the same order of magnitude for the two DNA bundles in DI water. However, this relative decrease of the bundle stiffness is much higher for these two DNA bundles in DI, than for the previous experiment in air.

This difference of relative variation of bundle stiffness during ionizing irradiation in air and in DI water, could be partly explained by the contribution from indirect effects during the irradiation in DI water. Nevertheless, at this stage, the correlation of the relative variation of

bundle stiffness with direct or indirect damage effects is still impossible. In fact, this strong difference in the relative DNA stiffness decrease during the ionizing irradiation could also be explained by entirely different phenomena. For example, when a DNA bundle is introduced in DI water, DNA molecules are relaxed, decreasing the DNA density, which therefore occupies a larger volume. This geometrical difference could modify the effects of the radiation on the relative stiffness variation, also allowing the relaxation of stress in damaged DNA to evolve in a quite different way in water compared to air.

For the same reason that for the experiment in air, it is impossible to correlate the relative variation of the DNA bundle stiffness with the accumulation of molecular-scale defects in DNA, although also in this case an evident correlation between the flux of ionizing radiation and the change in mechanical properties is evident.

5.2.2.2 Same bundle: Set of 4 irradiations

In order to establish the dependence on the irradiation dose of the radiation effects on the DNA bundle stiffness, a single DNA bundle was irradiated by a set of four 30 Gy irradiations, for a total dose of 120 Gy. This experiment was performed twice (Experiment 1 and Experiment 2), and shows different relative stiffness variation of the DNA bundle during the set of irradiations. The experimental conditions are necessarily different, due to the relatively weak control of the DNA trapping. The amount of DNA molecules and their arrangement are also poorly controlled.

5.2.2.2.1 Experiment 1

In this experiment, a DNA bundle is trapped and irradiated in DI water. The irradiation is divided in four runs of 30 Gy of 210 s each, spaced by a relaxation time of 180 s. The graphs in Figure 5.3 and Figure 5.4 plot the DNA bundle stiffness variation in two different manners, for a better understanding of the experiment.

In order to compare the Experiment 1 and 2, the DNA bundle stiffness is calculated from the resonance frequency of the SNT measured during the experiment, by the Equation 2.19. The plot in Figure 5.3 shows the variations of the DNA bundle stiffness all along the experiment. As before, the stiffness is seen to remain stable in the absence of irradiation, and decreases distinctly during the irradiation (in the green parts of the plot).

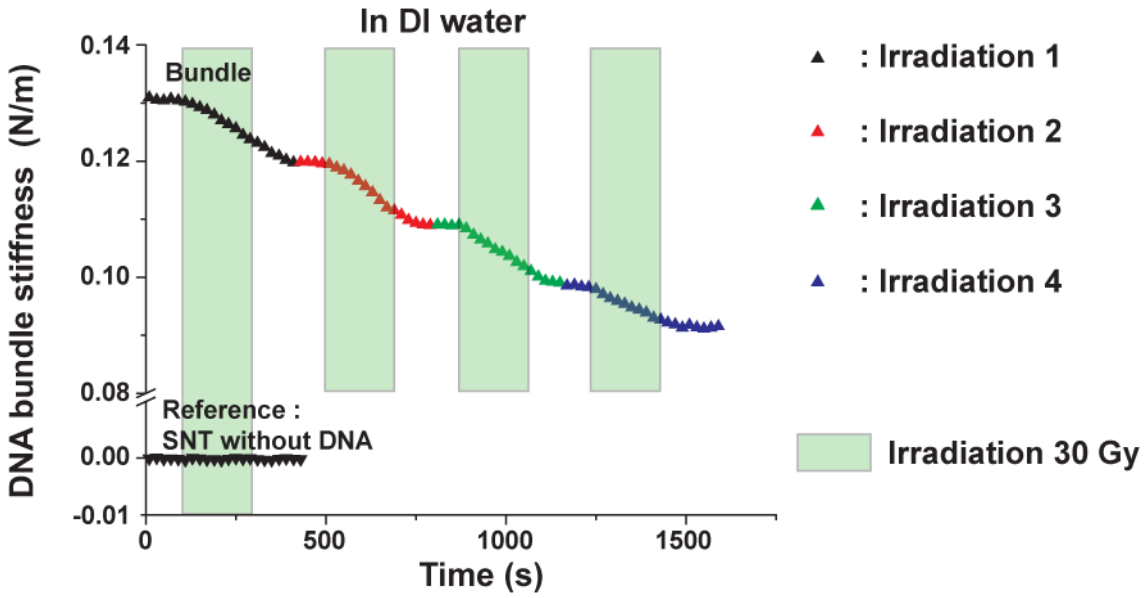

Figure 5.3: DNA bundle stiffness variation under a set of 4 irradiations in DI water: Experiment 1.

The initial DNA bundle stiffness in this case was equal to 0.13 N/m, and the stiffness decreased to 0.09 N/m. Therefore, the relative bundle stiffness variation is equal to 31% for the global experiment, under a total dose of 120 Gy.

For a more quantitative study, the four set of irradiations are compared in Figure 5.4, by shifting in time and superposing them in a same time scale. For the first three irradiations steps, the variation of the stiffness is very strictly reproducible. On the other hand, for the 4th irradiation step, the relative stiffness variation is smaller than in the first three. This "saturation" effect for the fourth irradiation could suggest that the DNA molecules are already strongly damaged, and the shape of the bundle itself is changing.

A simplified model of this process can be constructed by supposing that: (1) DNA bundle is composed by independent (i.e., non-interacting) DNA molecules, and (2) the bundle stiffness variations are only due to the breaking of molecule bridging between the SNT tips. Such hypotheses allow estimating an equivalent number of DNA molecules that composed the bundle, by knowing the stiffness of a single DNA molecule. Therefore, in this simple picture, the total stiffness of the bundle is just Nk, with N the (unknown) number of DNA molecules and k the equivalent stiffness of one DNA of 12µm length (width of the gap between the tips of the SNT used in this experiment). This calculation gives the data reported on the right axis of the same Figure 5.4.

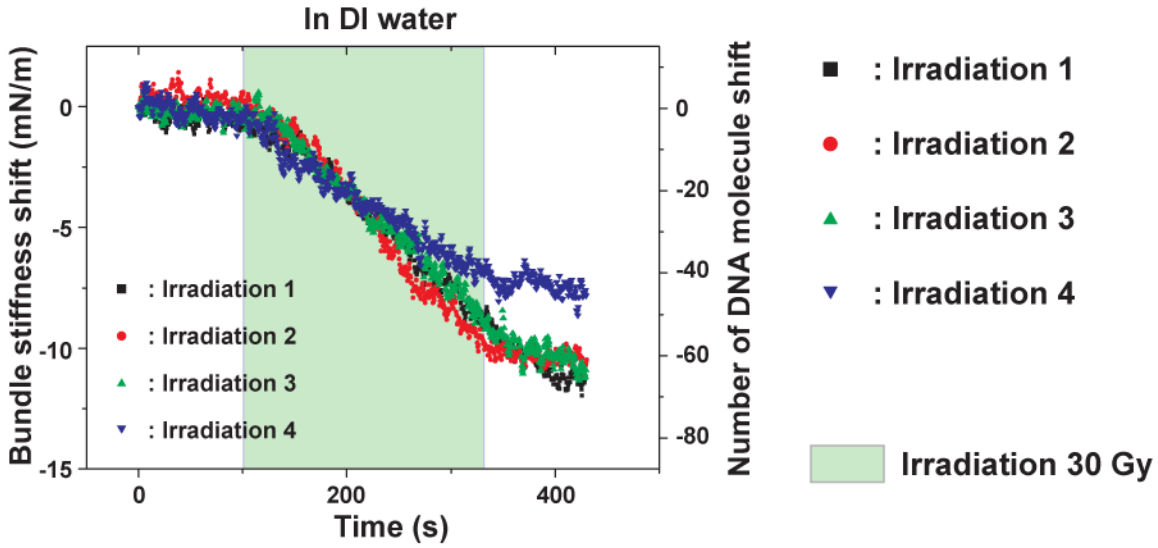

Figure 5.4: Comparison of the DNA bundle stiffness shift under a set of 4 irradiations in DI water. An equivalent number of DNA molecule which composed the bundle is proposed on the right axis

A more complex model to reanalyze these same data, also including lateral DNA interactions and viscous losses [11], [79], will be used in the discussion of Chapter 5.2.5.

5.2.2.2.2 Experiment 2

A similar Experiment 2 tested the repeatability of the Experiment 1. The experimental conditions are as close as possible in both experiments. Nevertheless, some conditions cannot be the same. Firstly, the SNT are not the same (fresh Al coating is necessary each time to ensure good trapping), however they come from the same run of fabrication, and their gap widths are similar (around 12µm). Secondly, the microfluidic cavity is replaced by a clean one. Third and the most important, the relatively poor control of the DNA trapping could provide very different bundles for the Experiment 1 and 2, with an amount and arrangement of DNA molecules unknown. In fact, already the initial DNA bundle stiffness is much higher in the Experiment 2 (0.205N/m) than in the Experiment 1 (0.130 N/m).

As a first comparison, we note that both experiment start with a stable DNA bundle stiffness in DI water. Nevertheless, the effect of the set of four irradiations on the bundle stiffness is clearly different in the two experiments. The relative DNA bundle stiffness variation is higher in the global Experiment 2 than in the global Experiment 1, with an overall decrease of 49% and 31% respectively. Moreover, in the Experiment 2, the bundle stiffness is no longer stable between

any two irradiations. Therefore, it is not possible to directly compare the effect of each irradiation on the DNA bundle stiffness, as we did for Experiment 1.

The instability of the DNA bundle stiffness between two irradiations is complicate to analyze, and unfortunately not repeatable. One possibility is that the DNA bundle of the Experiment 2 has a different inner arrangement on the tips of the SNT. Due to different trapping, the arrangements of the molecules inside the bundles are different. In Experiment 2 the molecule breakage during irradiation was sometimes followed by further rearrangement (i.e., F_R continuing to decrease) of the bundle even when irradiation was stopped. In order to elaborate a relevant scenario, more different experiments and simulation approaches are required.

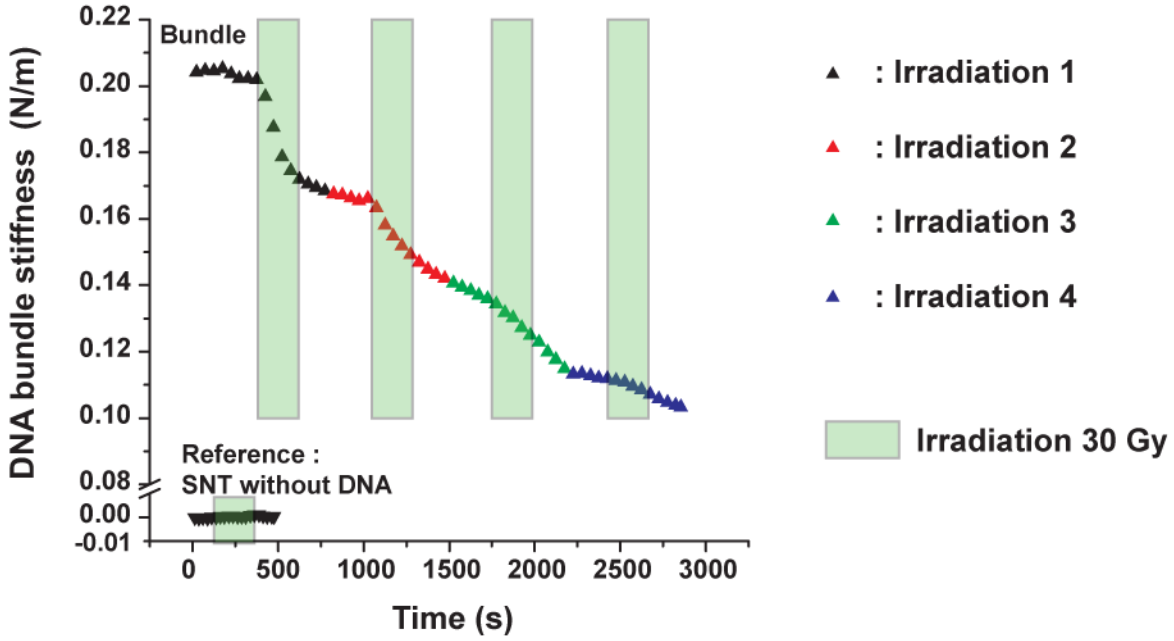

Figure 5.5: DNA bundle stiffness variation under a set of 4 irradiations in DI water: Experiment 2.

5.2.3 DNA irradiation in HNO_3 acid

The chapter 3.7.2.2 showed relevant effects of the pH on a DNA bundle stiffness. In fact, the stiffness was seen to increase when the pH of the solution was decreased (more acid). This increase of the DNA bundle stiffness could be a practical solution to amplify the difference between the resonance frequency of the bare SNT, and that of the SNT with trapped DNA inside liquid, thereby improving the resolution in the measurement of DNA bundle degradation. However, it should be noted that the effect of pH on DNA is questionable, several studies

having shown that among the main effects there can be depurination (cutting of purine bases), denaturation, and loss of structural integrity of the backbone.

In the experiment Figure 5.6, a DNA bundle is inserted into a HNO_3 solution with 1mM concentration (pH 3.1). In such a very low pH acid solution, the DNA bundle stiffness starts to increase as it was already found in our previous observations. After a waiting time for DNA bundle stabilization, a set of three irradiations is performed (green regions in the Figure). The stabilization was not complete before the irradiation (runtime of experiment is limited in hospital) and therefore the analysis of the bundle stiffness variation is complicated.

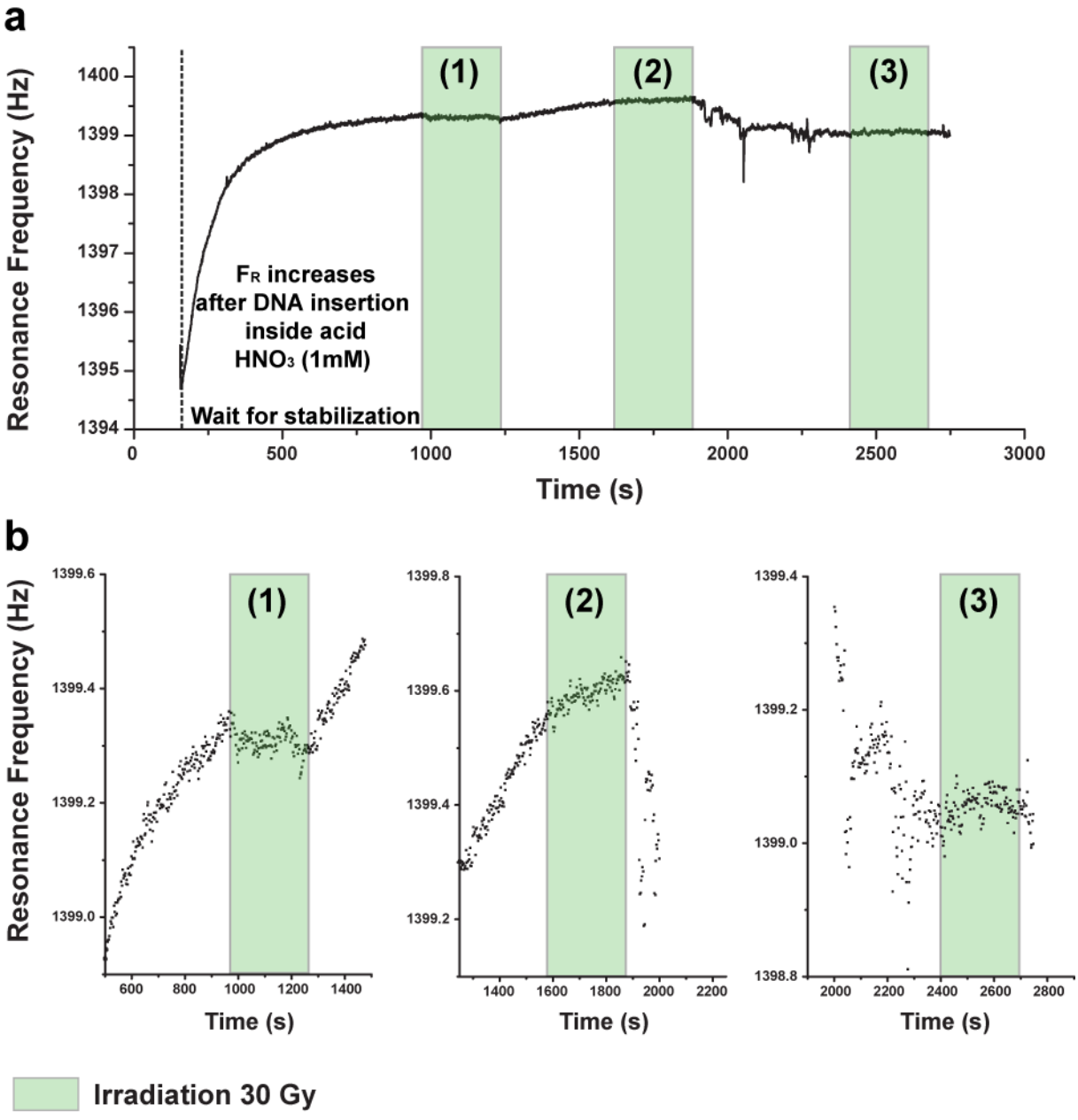

Figure 5.6: DNA irradiation in HNO_3 **a**. Set of Three irradiation. **b**. Zoom on this irradiation, just to show the different irradiations effect on the stiffness.

Nevertheless, the first and second irradiations seem to decrease the DNA bundle stiffness, which however continues to increase by the low pH effect. A possibility is that the pH increases in some way the rigidity of single molecules, while the radiation cuts some DNA bridges between the SNT tips. Each phenomenon has an opposite effect on the stiffness of the global bundle. The DNA bundle stiffness starts to be unstable after the second irradiation. After waiting for stabilization, a third irradiation was performed and did not show any effect on the DNA bundle stiffness. We have no means at this stage to be sure that DNA molecules are still in the configuration they had at the beginning of the experiment, therefore interpreting the evolution of F_R is practically impossible, without any other experimental information.

Other experiments in acid solutions were performed during the course of thesis. Nevertheless, any correlation between the ionizing irradiation dose and the DNA bundle stiffness variations could be extracted from this set of experiments. The DNA structure is likely to be so much altered at low pH, that irradiation has little effect on such configurations.

5.2.4 DNA irradiation in Tris•HCl buffer

In order to mimic the cell environment of DNA, and to work with an environment used in classical biological analysis, the DNA bundle in inserted inside a Tris•HCl buffer. Unfortunately, the length of the DNA molecules increases in the Tris•HCl buffer, and eventually the SNT is not able to sense the DNA bundle stiffness. In this subsection, we firstly report the failed experiment to evaluate the effect of irradiation on the DNA bundle stiffness in Tris•HCl buffer by the Single-Actuators SNT. Then, the Double-Actuators SNT was used to increase the gap between SNT tips, and therefore elongate the DNA bundle inside the Tris•HCl buffer before and during the irradiation.

5.2.4.1 Failed experiment with S-A SNT

The following experiment is reported to underline the advantage of using the D-A SNT for the mechanical characterization of a DNA bundle inside Tris•HCl buffer. In this experiment, the DNA bundle was inserted in Tris•HCl buffer. The resonance frequency of the SNT decreased, and finally stabilized at the bare SNT resonance frequency. Therefore, the DNA bundle stiffness is not sensed anymore by the SNT. Finally, the DNA bundle is irradiated, and obviously any possible effects of the ionizing radiation on the DNA bundle stiffness are not detected by the SNT.

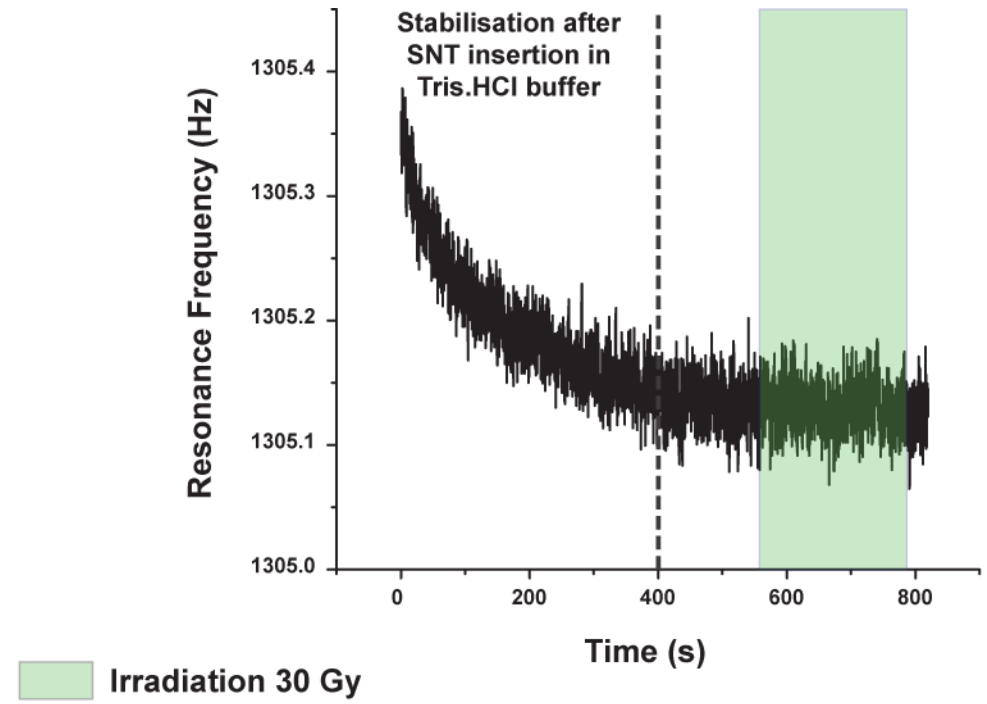

Figure 5.7: DNA irradiation inside Tris HCl buffer. No visible effect on the resonance frequency of the SNT.

5.2.4.2 DNA elongation by D-A SNT before irradiation

In the following experiment, the Double-Actuators SNT is used to adjust the DNA bundle to the elongation it gets inside the Tris•HCl buffer. In the experiment reported in Figure 5.8, a DNA bundle is elongated before and during two sessions of irradiation. Finally, the DNA bundle is relaxed to provide a reference in order to calculate the relative variation of the DNA bundle stiffness during the irradiation:

$$\text{Irradiation a} : \frac{\Delta k_{DNA}}{k_{DNA\,init}} \cong 10\% \quad \text{and} \quad \text{Irradiation b} : \frac{\Delta k_{DNA}}{k_{DNA\,init}} \cong 5\%$$

This experiment is a proof of concept that the D-A SNT can be used to adjust the DNA bundle to the elongation in Tris•HCl, thereby allowing the measurement of the variation DNA bundle stiffness also during an irradiation in this medium. However, this experiment was performed at the end of the thesis work, and could not be repeated because of technical issues (no more D-A SNT with good gap width were available). Therefore, the complex effects of the irradiation on DNA bundle with different elongations could not be properly analyzed.

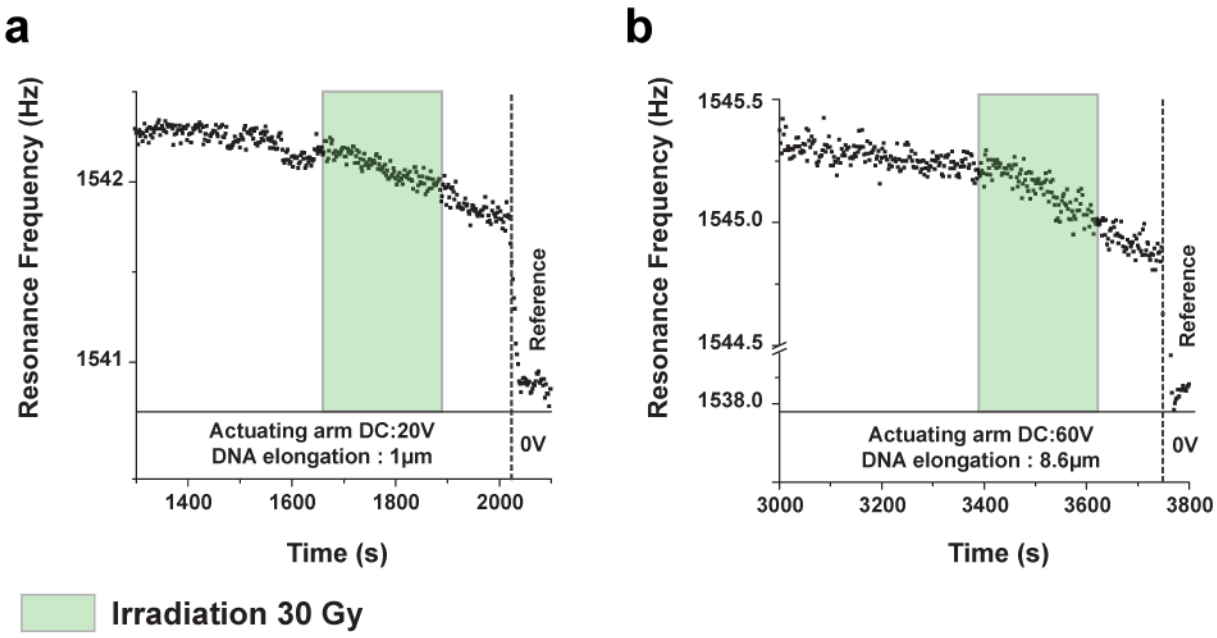

Figure 5.8: DNA irradiation inside Tris HCl **a.** DNA elongation (1µm) **b.** DNA elongation (8.6µm)

Further experiments are planned in the near future, thanks to the fabrication of a new set of D-A SNT by L.Jalabert and Y.Takayama.

5.2.5 Discussion: The Theoretical Model

The experimental results in the previous chapter underline the complexity of the ionizing radiation effects on the mechanical response of a DNA bundle. Moreover, it must be considered that the experimental conditions of the DNA molecules in the SNT experiments are very far from those of a human cell environment. Therefore, theoretical modeling of DNA degradation is a required condition for a scientific analysis of the experimental results obtained by Silicon Nano Tweezers, and in order to quantify protocols for clinical research objectives.

Firstly, we discuss a possible model for the kinetic breaks of the irradiated DNA bundle. It is assumed that in standard conditions, the irradiation generates a uniform DSB break rate b (breaks per second) in the whole structure composed of M parallel fibers each of length ℓ clamped at the ends (Figure 5.9.a). A living cell under irradiation experiences approximately 40 breaks (DSB) for 1 Gy of dose. Since the entire DNA is composed of about 3.10^9 bases, corresponding to a total length of 1 m (3.4 Angstrom per base pairs), in the case study the total length results to be $M\ell$ = 0.03m and, therefore, 1 Gy produces on average 1.2 breaks. Hence, with an irradiation of 120 Gy (4x30 Gy), the value of b should be 120•1.2/1375=0.1 breaks/s,

where *T*=1375 s is the total irradiation time. Nevertheless, this scaling of the rate would make sense only in living conditions, where the DNA is wrapped around the histones to form the chromatin fiber, and is protected by cell and nuclear membranes, and other cellular structures. For this reason, it seems reasonable that a completely free DNA bundle could experience a higher break rate *b*. Consequently, a value *b*=1 (1/sec) is adopted in the model.

In addition, a mechanism of self-healing of the DNA breaks could be taken into account. This mechanism may be represented by a kind of "collision" of some broken DNA fibers which make new links in the bundle, for example by knotting via dispersion forces. Such knotting increases the effective stiffness, so it can be represented like a new "repaired" molecule. If we imagine two pieces A that make a new link B, this reads like a reaction A+A→B. The reaction rate would read as -(1/2) dA/dt = +dB/dt (rate of disappearance of two A's equal to the rate of appearance of one B). The rate of disappearance of A's would be then proportional to -2 x the concentration of A, that is dA/dt = – w[A][A] = – w$[A]^2$, hence the second order term in the number of breaks N. This mechanism is described with second-order chemical kinetics:

Equation 5.2

$$\frac{dN}{dt} = b - \beta b N^2$$

where *N* is the number of breaks and the kinetics constant is written as $w = \beta b$. β represents a sort of "strand healing coefficient". This differential equation is able to account for a self-reparation mechanism, which possibly explains the saturation of the DNA bundle stiffness observed for long-irradiation times.

Equation 5.2 is solved by standard means, obtaining the solution:

Equation 5.3

$$N = \frac{1}{\sqrt{\beta}} \tanh(b\sqrt{\beta}t)$$

The limit of this solution at very long-irradiation times is:

Equation 5.4

$$\lim_{t\to\infty} N = \frac{1}{\sqrt{\beta}}$$

This equation shows that the number of breaks tends to a finite value, i.e. the breaking mechanism with "reparation" leads to a saturation of the decrease of the overall stiffness, which should approach as well a finite value, instead of going to zero.

On the other hand, the degradation of the mechanical stiffness E_{eff} (effective Young's modulus) in terms of the number of breaks N is written as:

Equation 5.5

$$k_{eff} = \frac{E_{eff}A}{l} = \frac{MEA}{l} e^{\left[-\varphi\left(\sqrt{\frac{k_{int}l^2}{E}}\right)\frac{N}{M}\right]}$$

as demonstrated in recent theoretical works from our research team [11], [79]. Here φ is a universal function, depending on the interaction coefficient k_{int} between the fibers of the bundle, as well as on the length l and the Young's modulus E of a single fiber.

The second-order kinetics can be combined with the exponential degradation, by replacing N in this equation with the solution (Equation 5.3), thus yielding the final result:

Equation 5.6

$$k_{eff} = \frac{MEA}{l} e^{\left[-\varphi\left(\sqrt{\frac{k_{int}l^2}{E}}\right)\frac{\tanh\left(b\sqrt{\beta}t\right)}{M\sqrt{\beta}}\right]}$$

Here, the fixed parameters are the Young modulus of one DNA chain (double strand), which is E=350 MPa, its average radius R=1nm, which corresponds to a cross-section area $A=\pi R^2$, the length of one DNA molecule ℓ=15μm (trapped between the tweezers arms), and the initial number of DNA molecules, set at M=1800. From this equation, the value of the unknown function φ taken at the argument ($k_{int}\,l^2/E$), and the value of the parameter β, can be determined.

For small N, i.e. in the limit $t\rightarrow 0$, the slope of Figure 5.9 is given by:

Equation 5.7

$$\frac{dk_{eff}}{dt}(t=0) = \frac{EA}{l}\varphi\left(\sqrt{\frac{k_{int}l^2}{E}}\right)\mathrm{b}$$

Therefore, this limit provides an estimate of the product $\varphi\left(\sqrt{\frac{k_{int}l^2}{E}}\right)\mathrm{b} = 0.7$ (in units of sec^{-1}). Since we have set $b = 1\ \mathrm{sec}^{-1}$, $\varphi\left(\sqrt{\frac{k_{int}l^2}{E}}\right) = 0.7$ is obtained. It is worth noting that such an

estimated value for the unknown function φ is consistent with the corresponding values derived in ([79],[11]) in various other conditions.

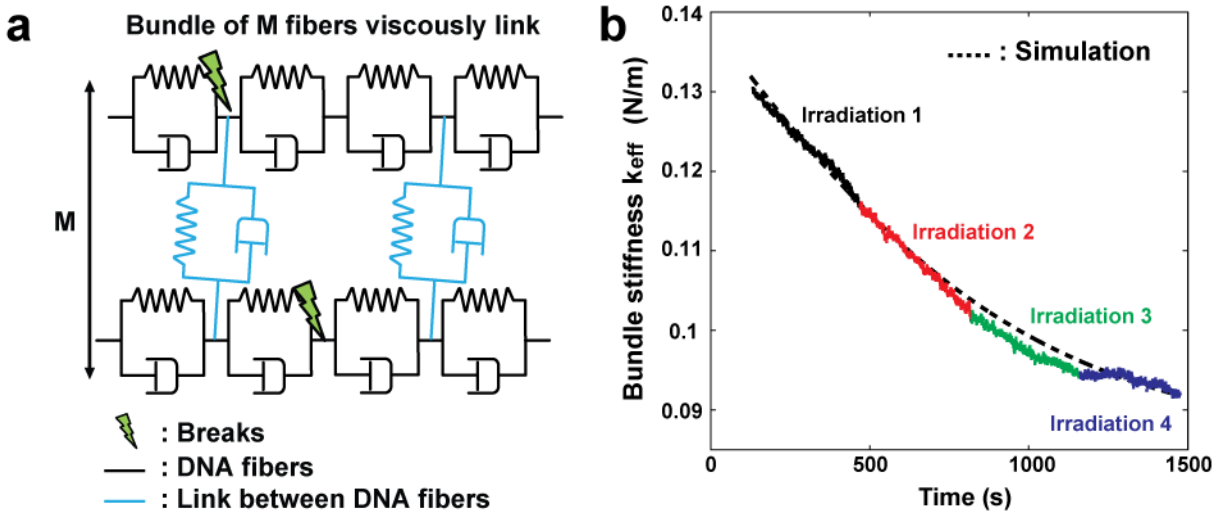

Figure 5.9: Comparison of the experiment Figure 5.3with the theoretical model. **a.** The DNA bundle is composed by M DNA molecule in parallel modeled with a series of visco-elastic dashpots. The confinement brings also a coupling between the molecules that is modeled by visco-elastic components in blue. The DNA breaks are simulated by breaks in the visco-elastic chain of a molecule (black). However, thanks to the lateral couplings, a broken molecule can still support stress. **b.** Comparison of the DNA bundle stiffness degradation during irradiation between the experiment in Figure 5.3 and the simulation based on the model (a).

The effective bundle stiffness k_{eff} from the experiments and the model is compared in Figure 5.9(b), as a function of the irradiation time. The multicolor curves are the experimental values from Experiment 1, after removing the discontinuities corresponding to the non-irradiation time windows. The black dashed curve is the theoretical bundle stiffness behavior predicted by Equation 5.6 with a fitted 'healing' coefficient $\beta = 8.1 \times 10^{-7}$. It can be seen that the model with second-order kinetics provides a very good interpretation of the experimental results, both for the decay time of the degradation, and for the saturation effect.

Conclusions and perspectives

Conclusion

In this thesis, a MEMS based device, the Silicon Nano Tweezers, has been used to perform, for the first time, real-time mechanical characterizations of a bundle of DNA molecules under a therapeutic radiation beam in different media.

The project started from a proof of concept realized in 2012 at the *Centre Oscar Lambret* where the first real-time DNA mechanical characterization was performed in air by the Silicon Nano Tweezers (SNT) under the γ-rays beam of a Cyberknife therapeutic LINAC. In this work, the endeavor of translating the irradiation from air to a realistic cellular-like medium was attacked, thereby facing the challenge of including both the direct and indirect ionizing irradiation effects on the DNA. To this end, the SNT and its complete setup had to be fully characterized and improved to allow DNA bundle mechanical characterization in different media at a high resolution.

This thesis introduced, in the Chapter 2, the design of two types of Silicon Nano Tweezers: the Single-Actuators SNT (S-A SNT) and the Double-Actuators SNT (D-A SNT). This design was carried out during my extended stages at the LIMMS Laboratory, in the University of Tokyo. Both devices were developed to allow easy DNA trapping and insertion in a microfluidic cavity (sharp tips). The D-A SNT, with two mobile arms, was specifically designed to be able to pre-elongate a trapped DNA bundle, and simultaneously measure its mechanical properties.

During the last three years, a complete setup around the SNT has been developed, to allow real-time DNA mechanical characterization in a microfluidic cavity with maximum control of the environment. In Chapter 3, I described the development and the full characterization of the setup, to evaluate the effects of all the parameters that could affect the measurements. The ionizing radiation effect on the bare SNT was quantified; and the ability of the setup to measure the mechanical response of DNA bundles, in air, in DI water, and also in others media, was demonstrated thanks to the dynamic microfluidic cavity and the D-A SNT. The stability of the setup was quantified prior to DNA trapping, and allowed to uncorrelate the effect of the irradiation on the bare SNT setup, and on the SNT with trapped DNA bundle.

New experimental protocols for this setup were developed. They optimized the repeatability and the runtime of the experiments under real conditions. Chapter 4 detailed the manual and automatic DNA trapping protocols, and the two novel protocols for the automatic positioning and insertion of the SNT tips inside the passive and dynamic microfluidic cavities. The specific protocol used for the positioning of the passive microfluidic cavity is based on the development

of a 3D humidity imager. During this development, the SNT was used to perform the initial characterization of the logarithmic relationship between DNA bundle stiffness and the relative humidity of its environment.

Chapter 5 reports the first real-time DNA bundle mechanical characterizations under ionizing radiation, performed under the γ-ray beam of the Cyberknife at the *Centre Oscar Lambret* of Lille. The experiments were performed with the DNA bundle inside different aqueous media, approaching a highly simplified condition of the cellular environment. The kinetics of DNA bundle degradation showed different time profiles, which depended on the medium. The quality of the DNA bundle degradation characterization by the SNT depended on the stability of the DNA bundle in the specific medium. It was demonstrated a clear correlation between the irradiation and the decrease of the resonance frequency, i.e. the effective stiffness, of the DNA bundle. However, it was not possible at this stage to deduce more microscopic information about the mechanisms of degradation, notably by correlating the reduction of stiffness with a degree of progressive breaking of the DNA molecules.

In the experimental and analytical conditions, the proposed DNA bundle geometry, which consists of parallel, fully extended strands between the arms of the SNT, is clearly different from the real-world conditions of tightly packed coiled DNA inside a cell nucleus. However, this partial lack of realism is compensated in part by the qualitative homogeneity, and the quantitative reproducibility of our experiments (in the same spirit as the irradiation experiments performed, for example, on crystallized DNA oligomers [142]). In an attempt to compensate for such a limitation, biophysical theoretical and numerical models were developed for this project, in order to support the experimental analysis, and to correlate the results obtained by the SNT and microfluidic setup with the *in vivo* DNA configurations. Indeed,it was only in DI water that the mechanical properties of DNA bundles were stable enough, to be compared and match the description of DNA bundle degradation under ionizing irradiation kinetics, developed in the biophysical model of Manca et al [11], [79]. However, this limited study further demonstrates that DNA damage modeling is a required condition, in order to quantify protocols for clinical research objectives.

Perspectives

This thesis represents a proof of concept of real-time biomechanical characterization of a DNA bundle under ionizing radiation in different aqueous mediums. Moreover, the SNT setup demonstrated a high ability to measure the mechanical properties of a DNA bundle in different mediums. Nevertheless, the effects of the true biological environment on the DNA mechanical properties are complex. In order to enhance the understanding of the effects of the properties of a specific medium on DNA bundle degradation under ionizing radiation, the project requires a scientific knowledge of biochemistry. From this knowledge, various mediums with different properties (pH, proteins, repair enzymes, free oxygen, etc) could be created, wherein the DNA bundle mechanical properties are stable. Moreover, a better understanding of the properties of the various mediums would permit a richer understanding of changes in DNA bundle mechanical properties under ionizing radiations. This thesis paves the way for long term and relevant clinical research possibilities, to quantify the effects of both healthy and tumor cell environments on the DNA degradation process under irradiation. The effects of the protocol of irradiation treatments (dose, dose rate, frequency…) could also be quantified, as well as the effects of additional drugs used before the irradiation. This clinical research could radically redefine the ideas of biologists and medical oncologists about the molecular–level connections between therapeutic irradiation and DNA damage, by allowing to establish, for the first time, a direct cause–effect experiment under ideally controlled and highly repeatable conditions. Moreover, the low-cost and large-scale integration of the experimental SNT apparatus, once the experimental research stage is completed, would represent a breakthrough in customized, patient-specific irradiation treatments, by extracting DNA samples, cell culturing, and SNT irradiation testing, before and during the radiotherapy.

Some additional perspectives, not directly related to radiotherapy, came to light thanks to the significant improvement to the SNT setup in the past two years. These changes allowed the SNT setup to turn into an easily-manipulable tool for mechanical characterization of DNA as well as other molecules.

The complete SNT setup (dynamic microfluidic cavity, Double-Actuators SNT …) provides a novel approach for the characterization of enzymatic reactions. Another indication of the SNT setup potential was demonstrated during a collaboration between the CNRS LIMMS laboratory and the CNRS *Laboratoire des Multimatériaux et Interfaces* (UMR 5615 in Lyon). This collaboration allowed the first real-time mechanical characterization of a DNA bundle during

enzymatic reactions (described in the Appendix). The proof of concept was elaborated during one week of experimentation with Yannick Tauran, a Cnrs researcher representing the UMR 5615. These additional experiments demonstrated that the application of the SNT setup could also be an excellent approach for a better understanding of DNA/enzyme interactions, and DNA/proteins interactions in a more general way.

Another near-future application envisaged for the SNT is the mechanical characterizations of whole cells. A new project was recently launched, to develop a prototype dedicated to the analysis of cell samples based on SNT technology. This prototype will be developed as a part of the SMMIL-E project of the LIMMS laboratory.

Bibliography

[1] C. Sonntag, *The Chemical Basis of Radiation Biology*, vol. 331, no. 6152. Taylor & Francis, 1987.

[2] S. G. Swarts, D. Becker, M. Sevilla, and K. T. Wheeler, "Radiation-induced DNA damage as a function of hydration. II. Base damage from electron-loss centers.," *Radiat. Res.*, vol. 145, no. 3, pp. 304–314, 1996.

[3] E. S. Henle, R. Roots, W. R. Holley, and A. Chatterjee, "DNA strand breakage is correlated with unaltered base release after gamma irradiation.," *Radiat. Res.*, vol. 143, no. 2, pp. 144–150, 1995.

[4] O. Ostling and K. J. Johanson, "Microelectrophoretic study of radiation-induced DNA damages in individual mammalian cells," *Biochem. Biophys. Res. Commun.*, vol. 123, no. 1, pp. 291–298, 1984.

[5] W. A. Bernhard, N. Mroczka, and J. Barnes, "Combination is the dominant free radical process initiated in DNA by ionizing radiation: an overview based on solid-state EPR studies.," *Int. J. Radiat. Biol.*, vol. 66, no. 5, pp. 491–497, 1994.

[6] G. U. Lee, L. A. Chrisey, and R. J. Colton, "Direct measurement of the forces between complementary strands of DNA.," *Science*, vol. 266, no. 5186, pp. 771–773, 1994.

[7] S. B. Smith, Y. Cui, and C. Bustamante, "Overstretching B-DNA: the elastic response of individual double- stranded and single-stranded DNA molecules," *Science (80-.).*, vol. 271, no. 5250, pp. 795–799, 1996.

[8] T. R. Strick, J. F. Allemand, D. Bensimon, A. Bensimon, and V. Croquette, "The elasticity of a single supercoiled DNA molecule.," *Science*, vol. 271, no. 5257, pp. 1835–1837, 1996.

[9] C. Yamahata, D. Collard, B. Legrand, T. Takekawa, M. Kumemura, G. Hashiguchi, and H. Fujita, "Silicon nanotweezers with subnanometer resolution for the micromanipulation of biomolecules," *J. Microelectromechanical Syst.*, vol. 17, no. 3, pp. 623–631, 2008.

[10] C. Yamahata, D. Collard, T. Takekawa, M. Kumemura, G. Hashiguchi, and H. Fujita, "Humidity dependence of charge transport through DNA revealed by silicon-based nanotweezers manipulation.," *Biophys. J.*, vol. 94, no. 1, pp. 63–70, 2008.

[11] F. Manca, S. Giordano, P. Palla, and F. Cleri, "Stochastic mechanical degradation of multi-cracked fiber bundles with elastic and viscous interactions," *Eur. Phys. J. E*, vol. 38, no. 5, pp. 1–21, 2015.

[12] K. D. Held, "Radiobiology for the Radiologist, 6th ed., by Eric J. Hall and Amato J. Giaccia," *Radiation Research*, vol. 166, no. 5. pp. 816–817, 2006.

[13] E. B. Podgorsak, *Chapter 6 External Photon Beams : Physical Aspects*. 2006.

[14] R. D. Evans and A. Noyau, *The atomic nucleus*, vol. 582. McGraw-Hill New York, 1955.

[15] S. Khaled and K. D. Held, “Radiation biology: a handbook for teachers and students,” *Int. J. Radiat. Biol.*, vol. 88, no. 11, pp. 858–859, 2012.

[16] E. B. Podgorsak and W. R. Hendee, “Radiation Physics for Medical Physicists,” *Med. Phys.*, vol. 33, no. 1, p. 249, 2006.

[17] T. Lindahl, “Instability and decay of the primary structure of DNA.,” *Nature*, vol. 362, pp. 709–715, 1993.

[18] O. T. Avery, C. M. Macleod, and M. McCarty, “Studies on the Chemical Nature of the Substance Inducing Transformation of Pneumococcal Types : Induction of Transformation By a Desoxyribonucleic Acid Fraction Isolated From Pneumococcus Type Iii.,” *J. Exp. Med.*, vol. 79, no. 2, pp. 137–58, Feb. 1944.

[19] J. D. Watson and F. H. Crick, “Molecular structure of nucleic acids. A structure for deoxyribose nucleic acid. 1953.,” *Rev. Invest. Clin.*, vol. 55, no. 2, pp. 108–109, 2003.

[20] G. Taborsky, “Some Recent Developments in the Chemistry of Phosphate Esters of Biological Interest,” *Yale J. Biol. Med.*, vol. 34, no. 2, pp. 153–154, 1961.

[21] M. Frankenberg-Schwager, “Induction, repair and biological relevance of radiation-induced DNA lesions in eukaryotic cells.,” *Radiat. Environ. Biophys.*, vol. 29, no. 4, pp. 273–292, 1990.

[22] R. Téoule, “Radiation-induced DNA Damage and Its Repair,” *Int. J. Radiat. Biol. Relat. Stud. Physics, Chem. Med.*, vol. 51, no. 4, pp. 573–589, Jan. 1987.

[23] R. V. Bensasson, E. J. Land, and T. G. Truscott, *Excited states and free radicals in biology and medicine*. Tokyo, 1993.

[24] K. W. Caldecott, “Single-strand break repair and genetic disease.,” *Nat. Rev. Genet.*, vol. 9, no. 8, pp. 619–631, 2008.

[25] M. a Siddiqi and E. Bothe, “Single- and double-strand break formation in DNA irradiated in aqueous solution: dependence on dose and OH radical scavenger concentration.,” *Radiat. Res.*, vol. 112, no. 3, pp. 449–463, 1987.

[26] J. F. Ward, “Biochemistry of DNA lesions.,” *Radiat. Res. Suppl.*, vol. 8, pp. S103–S111, 1985.

[27] S. P. Jackson, “Sensing and repairing DNA double-strand breaks.,” *Carcinogenesis*, vol. 23, no. 5, pp. 687–696, 2002.

[28] D. O. Ferguson and F. W. Alt, “DNA double strand break repair and chromosomal translocation: lessons from animal models.,” *Oncogene*, vol. 20, no. 40, pp. 5572–5579, 2001.

[29] M. L. Taverna Porro and M. M. Greenberg, “DNA double strand cleavage via interstrand hydrogen atom abstraction.,” *J. Am. Chem. Soc.*, vol. 135, no. 44, pp. 16368–71, 2013.

[30] M. Collado, J. Gil, A. Efeyan, C. Guerra, A. J. Schuhmacher, M. Barradas, A. Benguría, A. Zaballos, J. M. Flores, M. Barbacid, D. Beach, and M. Serrano, “Tumour biology: senescence in premalignant tumours.,” *Nature*, vol. 436, no. 7051, p. 642, 2005.

[31] Z. Chen, L. C. Trotman, D. Shaffer, H.-K. Lin, Z. A. Dotan, M. Niki, J. A. Koutcher, H. I. Scher, T. Ludwig, W. Gerald, C. Cordon-Cardo, and P. P. Pandolfi, “Crucial role of p53-dependent cellular senescence in suppression of Pten-deficient tumorigenesis.,” *Nature*, vol. 436, no. 7051, pp. 725–730, 2005.

[32] P. V Hariharan and P. A. Cerutti, “Formation and repair of γ-ray induced thymine damage in Micrococcus radiodurans,” *J. Mol. Biol.*, vol. 66, no. 1, pp. 65–81, Apr. 1972.

[33] R. C. Gupta, M. V. Reddy, and K. Randerath, “32P-postlabeling analysis of non-radioactive aromatic carcinogen - DNA adducts.,” *Carcinogenesis*, vol. 3, no. 9, pp. 1081–1092, 1982.

[34] K. Randerath, M. V Reddy, and R. C. Gupta, “32P-labeling test for DNA damage.,” *Proc. Natl. Acad. Sci. U. S. A.*, vol. 78, no. 10, pp. 6126–6129, 1981.

[35] S. A. Leadon, “Production and Repair of DNA Damage in Mammalian Cells.,” *Health Phys.*, vol. 59, no. 1, 1990.

[36] G. J. West and J. F. Ward, “Radioimmunoassay of a Thymine Glycol,” *Radiat. Res.*, vol. 90, no. 3, pp. 595–608, Jun. 1982.

[37] S. a Leadon and P. C. Hanawalt, “Monoclonal antibody to DNA containing thymine glycol.,” *Mutat. Res.*, vol. 112, no. 4, pp. 191–200, 1983.

[38] K. Hubbard, H. Huang, M. F. Laspia, H. Ide, B. F. Erlanger, and S. S. Wallace, “Immunochemical Quantitation of Thymine Glycol in Oxidized and X-Irradiated DNA,” *Radiat. Res.*, vol. 118, no. 2, pp. 257–268, May 1989.

[39] B. X. Chen, K. Hubbard, H. Ide, S. S. Wallace, and B. F. Erlanger, “Characterization of a monoclonal antibody to thymidine glycol monophosphate.,” *Radiat. Res.*, vol. 124, no. 2, pp. 131–136, 1990.

[40] R. Greferath and P. Nehls, “Monoclonal Antibodies to Thymidine Glycol Generated by Different Immunization Techniques,” *Hybridoma*, vol. 16, no. 2, pp. 189–193, Apr. 1997.

[41] P. Jaruga, T. H. Zastawny, J. Skokowski, M. Dizdaroglu, and R. Olinski, “Oxidative DNA base damage and antioxidant enzyme activities in human lung cancer.,” *FEBS Lett.*, vol. 341, pp. 59–64, 1994.

[42] M. Dizdaroglu, E. Coskun, and P. Jaruga, “Measurement of oxidatively induced DNA damage and its repair, by mass spectrometric techniques,” *Free Radic. Res.*, vol. 49, no. 5, pp. 525–548, Mar. 2015.

[43] T. Mori and M. Dizdaroglu, “Ionizing radiation causes greater DNA base damage in radiation-sensitive mutant M10 cells than in parent mouse lymphoma L5178Y cells.,” *Radiat. Res.*, vol. 140, no. 1, pp. 85–90, 1994.

[44] M. Dizdaroglu, “Application of capillary gas chromatography-mass spectrometry to chemical characterization of radiation-induced base damage of DNA: implications for assessing DNA repair processes.,” *Anal. Biochem.*, vol. 144, no. 2, pp. 593–603, 1985.

[45] M. Dizdaroglu, P. Jaruga, M. Birincioglu, and H. Rodriguez, “Free radical-induced damage to DNA: mechanisms and measurement,” *Free Radic. Biol. Med.*, vol. 32, no. 11, pp. 1102–1115, 2002.

[46] M. Dizdaroglu, M. L. Dirksen, H. X. Jiang, and J. H. Robbins, “Ionizing-radiation-induced damage in the DNA of cultured human cells. Identification of 8,5-cyclo-2-deoxyguanosine.,” *Biochem. J.*, vol. 241, pp. 929–932, 1987.

[47] S. Z. Hussain and K. Maqbool, “GC-MS : Principle , Technique and its application in Food Science,” *Int. J. Curr. Sci.*, 2014.

[48] J. a. McCloskey, *[45] Electron ionization mass spectra of trimethylsilyl derivatives of nucleosides*, vol. 193. Elsevier, 1990.

[49] H. Pang, K. H. Schram, D. L. Smith, S. P. Gupta, L. B. Townsend, and J. A. Mccloskey, “Mass Spectrometry of Nucleic Acid Constituents. Trimethylsilyl Derivatives of Nucleosides1p2,” *J. Org. Chem.*, vol. 366, no. 17, pp. 3923–3932, 1982.

[50] P. Mallick and B. Kuster, “Proteomics: a pragmatic perspective.,” *Nat. Biotechnol.*, vol. 28, no. 7, pp. 695–709, 2010.

[51] J. Cadet, T. Douki, S. Frelon, S. Sauvaigo, J.-P. Pouget, and J.-L. Ravanat, “Assessment of oxidative base damage to isolated and cellular DNA by HPLC-MS/MS measurement1,2 1This article is part of a series of reviews on ‘Oxidative DNA Damage and Repair.’ The full list of papers may be found on the homepage of the journal. 2Guest Ed,” *Free Radic. Biol. Med.*, vol. 33, no. 4, pp. 441–449, Aug. 2002.

[52] P. J. Taylor, “Matrix effects: the Achilles heel of quantitative high-performance liquid chromatography–electrospray–tandem mass spectrometry,” *Clin. Biochem.*, vol. 38, no. 4, pp. 328–334, Apr. 2005.

[53] G. Ahnstrom, “Techniques to measure DNA single-strand breaks in cells: A review,” *Int. J. Radiat. Biol.*, vol. 54, no. 5, pp. 695–707, 1988.

[54] R. a. McGrath and R. W. Williams, “Reconstruction in vivo of Irradiated Escherichia coli Deoxyribonucleic Acid; the Rejoining of Broken Pieces,” *Nature*, vol. 212, no. 5061, pp. 534–535, Oct. 1966.

[55] S. J. Whitaker, S. N. Powell, and T. J. McMillan, “Molecular assays of radiation-induced DNA damage,” *Eur. J. Cancer Clin. Oncol.*, vol. 27, no. 7, pp. 922–928, Jul. 1991.

[56] G. Ahnström and K.-A. Edvardsson, “Radiation-induced Single-strand Breaks in DNA Determined by Rate of Alkaline Strand Separation and Hydroxylapatite Chromatography: An Alternative to Velocity Sedimentation,” *Int. J. Radiat. Biol.*, vol. 26, no. 5, pp. 493–497, Jan. 1974.

[57] B. Rydberg and K. J. Johanson, “Estimation of DNA Strand Breaks in Single Mammalian Cells,” in *DNA Repair Mechanisms*, 1978, pp. 465–468.

[58] A. E. Kiltie and A. J. Ryan, “SYBR Green I staining of pulsed field agarose gels is a sensitive and inexpensive way of quantitating DNA double-strand breaks in mammalian cells.,” *Nucleic Acids Res.*, vol. 25, no. 14, pp. 2945–6, 1997.

[59] K. W. Kohn and R. A. Grimek-Ewig, “Alkaline Elution Analysis, a New Approach to the Study of DNA Single-Strand Interruptions in Cells,” *Cancer Res.*, vol. 33, no. 8, pp. 1849–1853, 1973.

[60] M. O. Bradley and K. W. Kohn, “X-ray induced DNA double strand break production and repair in mammalian cells as measured by neutral filter elution,” *Nucleic acids Res.*, vol. 7, no. 3, pp. 793–804, 1979.

[61] H. H. Evans, M. Ricanati, and M. F. Horng, “Deficiency in DNA repair in mouse lymphoma strain L5178Y-S,” *Proc. Natl. Acad. Sci.* , vol. 84 , no. 21 , pp. 7562–7566, Nov. 1987.

[62] T. M. Koval and E. R. Kazmar, “Eluting solution composition affects DNA double-strand break analysis by filter elution,” *Int J Radiat Biol*, vol. 54, no. 5, pp. 739–747, 1988.

[63] R. Okayasu, D. Bloecher, and G. Iliakis, “Variation through the cell cycle in the dose-response of DNA neutral filter elution in X-irradiated synchronous CHO-cells.,” *Int. J. Radiat. Biol. Relat. Stud. Phys. Chem. Med.*, vol. 53, no. 5, pp. 729–47, 1988.

[64] F. Hutchinson, “On the Measurement of DNA Double-Strand Breaks by Neutral Elution,” *Radiat. Res.*, vol. 120, no. 1, p. 182, Oct. 1989.

[65] N. P. Singh, M. T. McCoy, R. R. Tice, and E. L. Schneider, “A simple technique for quantitation of low levels of DNA damage in individual cells.,” *Exp. Cell Res.*, vol. 175, no. 1, pp. 184–191, 1988.

[66] C. Alapetite, P. Thirion, A. De La Rochefordière, J. M. Cosset, and E. Moustacchi, “Analysis by alkaline comet assay of cancer patients with severe reactions to radiotherapy: Defective rejoining of radioinduced DNA strand breaks in lymphocytes of breast cancer patients,” *Int. J. Cancer*, vol. 83, no. May, pp. 83–90, 1999.

[67] M. Wojewódzka, M. Kruszewski, T. Iwaneñko, A. R. Collins, and I. Szumiel, “Application of the comet assay for monitoring DNA damage in workers exposed to chronic low-dose irradiation I. Strand breakage,” *Mutat. Res. - Genet. Toxicol. Environ. Mutagen.*, vol. 416, pp. 21–35, 1998.

[68] J. T. Lett, E. S. Klucis, and C. Sun, “On the Size of the DNA in the Mammalian Chromosome: Structural Subunits,” *Biophys. J.*, vol. 10, no. 3, pp. 277–292, Mar. 1970.

[69] B. Rydberg, “Detection of Induced DNA Strand Breaks with Improved Sensitivity in Human Cells,” *Radiat. Res.*, vol. 81, pp. 492–495, 1980.

[70] S. E. Freeman, a D. Blackett, D. C. Monteleone, R. B. Setlow, B. M. Sutherland, and J. C. Sutherland, “Quantitation of radiation-, chemical-, or enzyme-induced single strand breaks in nonradioactive DNA by alkaline gel electrophoresis: application to pyrimidine dimers.,” *Anal. Biochem.*, vol. 158, no. 1, pp. 119–129, 1986.

[71] K. W. Kohn, L. C. Erickson, R. a Ewig, and C. a Friedman, “Fractionation of DNA from mammalian cells by alkaline elution.,” *Biochemistry*, vol. 15, no. 21, pp. 4629–37, 1976.

[72] N. P. Singh, R. E. Stephens, and E. L. Schneider, “Modifications of alkaline microgel electrophoresis for sensitive detection of DNA damage.,” *Int. J. Radiat. Biol.*, vol. 66, no. 1, pp. 23–28, 1994.

[73] E. C. Friedberg and E. C. Friedberg, “DNA damage and repair.,” *Nature*, vol. 421, no. 6921, pp. 436–40, 2003.

[74] C. Dekker and M. Ratner, “Electronic properties of DNA,” *Physics World*, vol. 14. pp. 29–33, 2001.

[75] C. Bustamante, Z. Bryant, and S. B. Smith, “Ten years of tension: single-molecule DNA mechanics.,” *Nature*, vol. 421, no. January, pp. 423–427, 2003.

[76] C. J. Benham and S. P. Mielke, “DNA mechanics.,” *Annu. Rev. Biomed. Eng.*, vol. 7, pp. 21–53, 2005.

[77] F. Manca, S. Giordano, P. L. Palla, F. Cleri, and L. Colombo, “Two-state theory of single-molecule stretching experiments,” *Phys. Rev. E*, vol. 87, no. 3, p. 32705, 2013.

[78] S. Nath, T. Modi, R. K. Mishra, D. Giri, B. P. Mandal, and S. Kumar, “Statistical mechanics of DNA rupture: theory and simulations.,” *J. Chem. Phys.*, vol. 139, no. 16, p. 165101, 2013.

[79] F. Manca, S. Giordano, P. L. Palla, and F. Cleri, “Scaling Shift in Multicracked Fiber Bundles,” *Phys. Rev. Lett.*, vol. 113, no. 25, p. 255501, 2014.

[80] H. Craighead, “Future lab-on-a-chip technologies for interrogating individual molecules,” *Nature*, vol. 442, no. 7101, pp. 387–393, Jul. 2006.

[81] A. Ashkin, J. M. Dziedzic, J. E. Bjorkholm, and S. Chu, “Observation of a single-beam gradient force optical trap for dielectric particles.,” *Opt. Lett.*, vol. 11, no. 5, p. 288, 1986.

[82] J. Van Mameren, M. Modesti, R. Kanaar, C. Wyman, G. J. L. Wuite, and E. J. G. Peterman, “Dissecting elastic heterogeneity along DNA molecules coated partly with

Rad51 using concurrent fluorescence microscopy and optical tweezers.," *Biophys. J.*, vol. 91, no. 8, pp. L78–L80, 2006.

[83] Y. Arai, R. Yasuda, K. Akashi, Y. Harada, H. Miyata, K. Kinosita, and H. Itoh, "Tying a molecular knot with optical tweezers.," *Nature*, vol. 399, no. 6735, pp. 446–448, 1999.

[84] K. Svoboda, C. F. Schmidt, B. J. Schnapp, and S. M. Block, "Direct observation of kinesin stepping by optical trapping interferometry.," *Nature*, vol. 365, no. 6448, pp. 721–727, 1993.

[85] S. M. Block, L. S. Goldstein, and B. J. Schnapp, "Bead movement by single kinesin molecules studied with optical tweezers.," *Nature*, vol. 348, no. 6299, pp. 348–52, 1990.

[86] M. Mammen, K. Helmerson, R. Kishore, S. K. Choi, W. D. Phillips, and G. M. Whitesides, "Optically controlled collisions of biological objects to evaluate potent polyvalent inhibitors of virus-cell adhesion.," *Chem. Biol.*, vol. 3, no. 9, pp. 757–63, 1996.

[87] S. M. Block, D. F. Blair, and H. C. Berg, "Compliance of bacterial flagella measured with optical tweezers.," *Nature*, vol. 338, no. 6215, pp. 514–518, 1989.

[88] A. Rohrbach and E. H. K. Stelzer, "Trapping Force, Force Constant, and Potential Depths for Dielectric Spheres in the Presence of Spherical Aberrations," *Appl. Opt.*, vol. 41, no. 13, pp. 2494–2507, 2002.

[89] K. C. Neuman and S. M. Block, "Optical trapping," *Rev. Sci. Instrum.*, vol. 75, no. 9, pp. 2787–2809, 2004.

[90] F. Ritort, S. Mihardja, S. B. Smith, and C. Bustamante, "Condensation transition in DNA-polyaminoamide dendrimer fibers studied using optical tweezers," *Phys. Rev. Lett.*, vol. 96, no. 11, p. 118301, 2006.

[91] T. R. Strick, V. Croquette, and D. Bensimon, "Single-molecule analysis of DNA uncoiling by a type II topoisomerase.," *Nature*, vol. 404, no. 6780, pp. 901–904, 2000.

[92] H. Itoh, A. Takahashi, K. Adachi, H. Noji, R. Yasuda, M. Yoshida, and K. Kinosita, "Mechanically driven ATP synthesis by F1-ATPase.," *Nature*, vol. 427, no. 6973, pp. 465–8, 2004.

[93] C. Gosse and V. Croquette, "Magnetic tweezers: micromanipulation and force measurement at the molecular level.," *Biophys. J.*, vol. 82, no. 6, pp. 3314–3329, 2002.

[94] J. Lipfert, J. W. J. Kerssemakers, T. Jager, and N. H. Dekker, "Magnetic torque tweezers: measuring torsional stiffness in DNA and RecA-DNA filaments.," *Nat. Methods*, vol. 7, no. 12, pp. 977–980, 2010.

[95] G. Binnig, C. Quate, and C. Gerber, "Atomic Force Microscope," *Physical Review Letters*, vol. 56, no. 9. pp. 930–933, 1986.

[96] L. Grebikova, P. Maroni, B. Zhang, a. D. Schlüter, and M. Borkovec, "Single-molecule force measurements by nano-handling of individual dendronized polymers," *ACS Nano*, vol. 8, no. 3, pp. 2237–2245, 2014.

[97] H. Clausen-Schaumann, M. Rief, C. Tolksdorf, and H. E. Gaub, "Mechanical stability of single DNA molecules.," *Biophys. J.*, vol. 78, no. 4, pp. 1997–2007, 2000.

[98] P. C. Weber, D. H. Ohlendorf, J. J. Wendoloski, and F. R. Salemme, "Structural origins of high-affinity biotin binding to streptavidin.," *Science*, vol. 243, no. 4887, pp. 85–88, 1989.

[99] A. Engel, "Biological Applications of Scanning Probe Microscopes," *Annu. Rev. Biophys. Biophys. Chem.*, vol. 20, no. 1, pp. 79–108, Jun. 1991.

[100] J. O. O. Bustamante, a. Liepins, R. a. A. Prendergast, J. a. A. Hanover, and H. Oberleithner, "Patch clamp and atomic force microscopy demonstrate TATA-binding protein (TBP) interactions with the nuclear pore complex," *J. Membr. Biol.*, vol. 146, no. 3, pp. 263–272, 1995.

[101] Z. Shao, J. Yang, and A. P. Somlyo, "Biological atomic force microscopy: from microns to nanometers and beyond.," *Annu. Rev. Cell Dev. Biol.*, vol. 11, pp. 241–65, 1995.

[102] M. Ueda, Y. Baba, H. Iwasaki, O. Kurosawa, and M. Washizu, "Direct measurement of DNA by means of AFM," *Nucleic Acids Symp. Ser.*, no. 42, pp. 245–246, 1999.

[103] A. V Krasnoslobodtsev, L. S. Shlyakhtenko, and Y. L. Lyubchenko, "Probing Interactions within the Synaptic DNA-SfiI Complex by AFM Force Spectroscopy," *J. Mol. Biol.*, vol. 365, no. 5, pp. 1407–1416, 2007.

[104] H. C. Nathanson, W. E. Newell, R. A. Wickstrom, and J. R. Davis, "The resonant gate transistor," *IEEE Trans. Electron Devices*, vol. 14, no. 3, pp. 117–133, 1967.

[105] K. E. Petersen, "Silicon As a Mechanical Material.," *Proc. IEEE*, vol. 70, no. 5, pp. 420–457, 1982.

[106] M. Mehregany, K. Gabriel, and W. S. Trimmer, "Integrated Fabrication of Polysilicon Mechanisms," *IEEE Trans. Electron Devices*, vol. 35, no. 6, pp. 719–723, 1988.

[107] E. Sarajlic, C. Yamahata, M. Cordero, and H. Fujita, "Three-Phase Electrostatic Rotary Stepper Micromotor With a Flexural Pivot Bearing," *J. Microelectromechanical Syst.*, vol. 19, no. 2, pp. 338–349, 2010.

[108] Y.-C. Tai and R. S. Muller, "IC-processed electrostatic synchronous micromotors," *Sensors and Actuators*, vol. 20, no. 1, pp. 49–55, 1989.

[109] W. C. Tang, T.-C. H. Nguyen, and R. T. Howe, "Laterally driven polysilicon resonant microstructures," *IEEE Micro Electro Mech. Syst. , Proceedings, 'An Investig. Micro Struct. Sensors, Actuators, Mach. Robot.*, vol. 20, pp. 25–32, 1989.

[110] H. Cai, X. M. Zhang, C. Lu, A. Q. Liu, and E. H. Khoo, "Linear MEMS variable optical attenuator using reflective elliptical mirror," *IEEE Photonics Technol. Lett.*, vol. 17, no. 2, pp. 402–404, 2005.

[111] Y. Lu and C.-J. K. C.-J. Kim, "Micro-finger articulation by pneumatic parylene balloons," *TRANSDUCERS '03. 12th Int. Conf. Solid-State Sensors, Actuators Microsystems. Dig. Tech. Pap. (Cat. No.03TH8664)*, vol. 1, no. JULY, 2003.

[112] K. Mølhave, T. M. Hansen, D. N. Madsen, and P. Bøggild, "Towards pick-and-place assembly of nanostructures.," *J. Nanosci. Nanotechnol.*, vol. 4, no. 3, pp. 279–282, 2004.

[113] B. E. Volland, H. Heerlein, and I. W. Rangelow, "Electrostatically driven microgripper," *Microelectron. Eng.*, vol. 61–62, pp. 1015–1023, 2002.

[114] D.-H. Kim, M. G. Lee, B. Kim, and Y. Sun, "A superelastic alloy microgripper with embedded electromagnetic actuators and piezoelectric force sensors: a numerical and experimental study," *Smart Mater. Struct.*, vol. 14, no. 6, pp. 1265–1272, 2005.

[115] K. Mølhave and O. Hansen, "Electro-thermally actuated microgrippers with integrated force-feedback," *J. Micromechanics Microengineering*, vol. 15, no. 6, pp. 1265–1270, 2005.

[116] N. Chronis and L. P. Lee, "Electrothermally activated SU-8 microgripper for single cell manipulation in solution," *J. Microelectromechanical Syst.*, vol. 14, no. 4, pp. 857–863, 2005.

[117] F. Arai, D. Andou, Y. Nonoda, T. Fukuda, H. Iwata, and K. Itoigawa, "Integrated microendeffector for micromanipulation," *IEEE/ASME Trans. Mechatronics*, 1998.

[118] I. Roch, P. Bidaud, D. Collard, and L. Buchaillot, "Fabrication and characterization of an SU-8 gripper actuated by a shape memory alloy thin film," *J. Micromechanics Microengineering*, vol. 13, pp. 330–336, 2003.

[119] M. Kohl, E. Just, W. Pfleging, and S. Miyazaki, "SMA microgripper with integrated antagonism," *Sensors Actuators, A Phys.*, vol. 83, pp. 208–213, 2000.

[120] O. Millet, P. Bernardoni, S. Régnier, P. Bidaud, E. Tsitsiris, D. Collard, and L. Buchaillot, "Electrostatic actuated micro gripper using an amplification mechanism," *Sensors Actuators, A Phys.*, vol. 114, no. 2–3, pp. 371–378, 2004.

[121] D. Collard, S. Takeuchi, and H. Fujita, "MEMS technology for nanobio research," *Drug Discov. Today*, vol. 13, no. November, pp. 989–996, 2008.

[122] N. Lafitte, "Modeling and control of MEMS tweezers for the characterizations of enzymateic reactions on DNA molecules," Université de Franche-Comté, 2012.

[123] P. V Cornish and T. Ha, "A survey of single-molecule techniques in chemical biology.," *ACS Chem. Biol.*, vol. 2, no. 1, pp. 53–61, 2007.

[124] G. Zhou and P. Dowd, "Tilted folded-beam suspension for extending the stable travel range of comb-drive actuators," *Journal of Micromechanics and Microengineering*, vol. 13, no. 2. pp. 178–183, 2002.

[125] C. T. C. Nguyen and R. T. Howe, "Integrated CMOS micromechanical resonator high-Q oscillator," *IEEE J. Solid-State Circuits*, vol. 34, no. 4, pp. 440–455, 1999.

[126] R. Legtenberg, A. W. Groeneveld, and M. Elwenspoek, "Comb-drive actuators for large displacements," *J. Micromechanics Microengineering*, vol. 6, no. 3, pp. 320–329, 1996.

[127] W. a. Johnson and L. K. Warne, "Electrophysics of micromechanical comb actuators," *J. Microelectromechanical Syst.*, vol. 4, no. 1, pp. 49–59, 1995.

[128] Y. S. Y. Sun, S. N. Fry, D. P. Potasek, D. J. Bell, and B. J. Nelson, "Characterizing fruit fly flight behavior using a microforce sensor with a new comb-drive configuration," *J. Microelectromechanical Syst.*, vol. 14, no. 1, pp. 4–11, 2005.

[129] M. Despont, G. A. Racine, P. Renaud, and N. F. de Rooij, "New design of micromachined capacitive force sensor," *J. Micromechanics Microengineering*, vol. 3, no. 4, p. 239, 1993.

[130] N. Lafitte, Y. Haddab, Y. Le Gorrec, H. Guillou, M. Kumemura, L. Jalabert, D. Collard, and H. Fujita, "Improvement of Silicon Nanotweezers Sensitivity for Mechanical Characterization of Biomolecules Using Closed-Loop Control," *IEEE/ASME Trans. Mechatronics*, vol. 20, no. 3, pp. 1418–1427, 2015.

[131] G. Hashiguchi, T. Goda, M. Hosogi, K. Hirano, N. Kaji, Y. Baba, K. Kakushima, and H. Fujita, "DNA manipulation and retrieval from an aqueous solution with micromachined nanotweezers," *Anal. Chem.*, vol. 75, no. 17, pp. 4347–4350, 2003.

[132] D. Collard, N. Lafitte, H. Guillou, M. Kumemura, L. Jalabert, and H. Fujita, *Silicon Nano Tweezers for molecules and cells manipulation and characterization*, Wiley-VCH. 2014.

[133] N. Lafitte, C. M. Tarhan, G. Perret, T. Lacornerie, M. Kumemura, L. Jalabert, F. Cleri, E. Lartigau, H. Fujita, and D. Collard, "Silicon Nano Tweezers are reaching clinical research," *Seisan Kenkyu*, vol. 67, no. 5, pp. 565–571, 2015.

[134] R. E. Krisch, M. B. Flick, and C. N. Trumbore, "Radiation chemical mechanisms of single- and double-strand break formation in irradiated SV40 DNA.," *Radiat. Res.*, vol. 126, no. 2, pp. 251–259, 1991.

[135] M. C. Tarhan, N. Lafitte, Y. Tauran, L. Jalabert, M. Kumemura, G. Perret, B. Kim, A. Coleman, H. Fujita, and D. Collard, "A rapid and practical technique for real-time monitoring of biomolecular interactions using mechanical responses of macromolecules," *(submitted)*.

[136] H. a Tajmir-Riahi, J. F. Neault, and M. Naoui, "Does DNA acid fixation produce left-handed Z structure?," *FEBS Lett.*, vol. 370, pp. 105–108, 1995.

[137] M. Washizu and O. Kurosawa, “Electrostatic manipulation of DNA in microfabricated structures,” *IEEE Trans. Ind. Appl.*, vol. 26, no. 6, pp. 1165–1172, 1990.

[138] M. H. and G. H. and M. H. and T. Y. and K. K. and H. Fujita, “Electrical Conductivity of Lambda DNA–Pd Wire,” *Jpn. J. Appl. Phys.*, vol. 44, no. 7L, p. L955, 2005.

[139] D. Han Ha, H. Nham, K.-H. Yoo, H. So, H.-Y. Lee, and T. Kawai, “Humidity effects on the conductance of the assembly of DNA molecules,” *Chem. Phys. Lett.*, vol. 355, no. 5–6, pp. 405–409, 2002.

[140] T. Kleine-Ostmann, C. Jördens, K. Baaske, T. Weimann, M. H. de Angelis, and M. Koch, “Conductivity of single-stranded and double-stranded deoxyribose nucleic acid under ambient conditions: The dominance of water,” *Appl. Phys. Lett.*, vol. 88, no. 10, p. 102102, 2006.

[141] M. C. Tarhan, N. Lafitte, H. Fujita, and D. Collard, “Molecule detecting system,” Patent ID 07085 (under process).

[142] Y. Razskazovskiy, M. G. Debije, and W. a Bernhard, “Direct radiation damage to crystalline DNA: what is the source of unaltered base release?,” *Radiat. Res.*, vol. 153, no. 4, pp. 436–441, 2000.